LBL-26362
UC-403

Annual Report 1988

Earth Sciences Division

August 1989

LAWRENCE BERKELEY LABORATORY
UNIVERSITY OF CALIFORNIA
BERKELEY, CALIFORNIA 94720

Prepared for the U.S. Department of Energy under Contract No. DE-AC03-

DISCLAIMER

EARTH SCIENCES DIVISION ANNUAL REPORT 1988

Lawrence Berkeley Laboratory
1 Cyclotron Road
Berkeley, CA 94720

August 1989

Prepared for the U.S Department of Energy under Contract No. DE-AC03-76SF00098

ACKNOWLEDGMENTS

This work was supported through U.S. Department of Energy Contract No. DE-AC03-76SF00098 by (1) the DOE Assistant Secretary for Energy Research, Office of Basic Energy Sciences and Office of Health and Environmental Research; (2) the DOE Office of Civilian Radioactive Waste Management, Office of Systems Integration and Regulation; (3) the DOE Assistant Secretary for Conservation and Renewable Energy, Office of Renewable Technologies; (4) the DOE Assistant Secretary for Fossil Energy, Office of Oil, Gas, Shale and Special Technologies; (5) the Environmental Protection Agency; (6) the U.S. Department of Interior; (7) the U.S. Department of Defense; (8) the National Science Foundation through the University of California at Berkeley; (9) the University of California; (10) the California Consortium for Crustal Studies; (11) the Gas Research Institute; and (12) the Chevron Oil Company.

CONTENTS

INTRODUCTION

Scientists and engineers of the Earth Sciences Division, following the mission of a multipurpose National Laboratory, conduct research on a wide variety of topics relevant to the nation's energy development programs. This report summarizes the activities for 1988. The Earth Sciences Division has developed unique expertise in several research areas. This expertise is due in part to the special resources and facilities available to researchers at the Lawrence Berkeley Laboratory and in part to the Laboratory's commitment to technical and scientific excellence. In addition to the permanent Laboratory staff, University faculty members, postdoctoral fellows, students, and visiting scientists participate in many investigations. Each year, several Ph.D. and Masters theses are founded in research within the Division. Interlaboratory cooperation within the U.S. Department of Energy system and collaboration with other research institutions provide access to unmatched intellectual and technological resources for the study of complex problems.

Much of the Division's research deals with the physical and chemical properties and processes in the Earth's crust, from the partially saturated, low-temperature near-surface environment to the high-temperature environments characteristic of regions where magmatic-hydrothermal processes are active. Strengths in laboratory and field instrumentation, numerical modeling, and in situ measurement allow study of the transport of mass and heat through geologic media—studies that now include the appropriate chemical reactions and the hydraulic-mechanical complexities of fractured rock systems. Related and parallel laboratory and field investigations address the effects of temperature, pressure, stresses, pore fluids, and fractures on the elastic and electrical properties of rock masses. These studies are concerned with rock behavior in the brittle and ductile crustal regimes, and they drive the development of improved geomechanical and geophysical tools and techniques for mapping and characterizing heterogeneity in the subsurface. Recent initiatives in special areas of research have been generated in response to needs perceived by Congress, by DOE, by industry, or by the scientific community at large. Of particular note are three major new Division efforts addressing problems in the discovery and recovery of petroleum, the application of isotope geochemistry to the study of geodynamic processes and earth history, and the development of borehole methods for high-resolution imaging of the subsurface using seismic and electromagnetic waves.

This Annual Report presents summaries of selected representative research activities grouped according to the principal disciplines of the Earth Sciences Division: Geophysics and Geomechanics, Reservoir Engineering and Hydrogeology, and Geology and Geochemistry. We are proud to be able to bring you this report, which we hope will convey not only a description of the Division's scientific activities but also a sense of the enthusiasm and excitement present today in the Earth Sciences.

GEOPHYSICS AND GEOMECHANICS

The Geophysics and Geomechanics group conducts basic and applied research relevant to the nation's energy development programs and helps train the next generation of scientists and engineers in the geosciences. The research utilizes unique facilities at Lawrence Berkeley Laboratory and is directed toward the solution of problems in geothermal energy development, nuclear and toxic waste disposal, fossil fuels, and the definition of fundamental properties and processes in the earth's crust. The aim is to address not only today's needs, but also needs that will arise from the ever-increasing pressures placed upon the earth's resources. The group has focused, and will continue to focus, on a collaborative approach, not only between geophysical and geomechanical disciplines, but with other disciplines in government and industry as well. The thrust is for a strong theoretical foundation coupled with laboratory, numerical, and field-based studies. The overall philosophy is to address broad research bases rather than individual program areas. The group draws upon the unique resources within other divisions at the Laboratory and the various earth sciences departments on the U.C. Berkeley campus. Current emphasis is on the development of techniques for characterizing and monitoring processes in fractured, heterogeneous rock using high-resolution geophysical imaging. Future growth will come about only through a coordinated and balanced program based on solid research principles—one that can respond to changing needs in the earth sciences and new objectives of DOE programs in a timely and efficient manner.

Facilities for Supporting Research in Geophysics and Geomechanics

E.L. Majer, T.V. McEvilly, and L.R. Myer

Over the years Lawrence Berkeley Laboratory (LBL) has had extensive involvement in the collection and processing of data used to support research activities in many different areas of the earth sciences. Because of the research nature of this work we have found it necessary to enhance in-house capabilities in order to collect and process specialized data sets. Given below is a brief description of these facilities that we use on a daily basis to carry out our research.

CENTER FOR COMPUTATIONAL SEISMOLOGY

The Center for Computational Seismology (CCS) has now been in existence for 5 years. It has expanded from a several-user facility occupying 10 to 25 percent of a VAX/780 to a 20- to 30-member user community. For this reason CCS has upgraded its facilities to accommodate the load. The purpose of CCS has been to provide a facility with a wide range of computational tools to serve DOE programs in the basic energy sciences and other areas of energy research. Research over the entire spectrum of seismology is carried out at CCS, from basic studies in earthquake-source mechanisms to the applied work of reflection seismology. The software base is made up of 5 years' of our own efforts in coding internal analysis routines in addition to processing tools of DISCO™ (Digicon Inc), SierraSEIS™ (Sierra Geophysics), INGRES™ (Relational Technology), the Geoquest Inc. AIMS package, and the most recent addition, the Geowell package from Spectrum Geophysics.

During the last quarter of 1987 the CONVEX C-1/XP computer was installed and tested at CCS. The CONVEX is a UNIX™ (Bell Labs) based machine that runs 4.2 BSD. It is a 64-bit vector machine. Benchmarks to date indicate that in straight scalar mode it is 6 to 8 times faster than our previous system, a VAX 11/780, and if the calculations vectorize, we have observed speed increases of up to 20 times. For some very specialized uses, i.e., FFT's, the speed is the same as that of a Cray-1. In addition to the new hardware installed, CCS will be running the SierraSEIS seismic-reflection processing package. This package is a complete processing package that replaces the DISCO package. The graphics system will be the NCAR package running on top of the ATC GKS package. The present configuration of CCS and networking is shown in Fig. 1.

We now have the ability to address research topics that we were previously not capable of embarking upon. The principal areas of research are, of course, various programs in the DOE involving seismic projects relating to basic and applied research. During the past year this has involved work for the Office of Basic Energy Sciences in the Salton Sea project and the Long Valley data synthesis. Another area of work has been for geothermal programs. Vertical seismic profiling (VSP) for fracture detection and microearthquake studies for reservoir management are two examples. We are also carrying out work for the DOE nuclear waste program. This involves relating the seismic response of fractured media to the hydrologic response. This program will soon involve field work, but the main thrust of the present study is to develop 2- and 3-D models for ray-tracing *P*-, *SV*-, and *SH*-waves through fractured rock. The goal is to use seismic tomography for mapping fracture density, spacing, and orientation. It is hoped that sufficient resolution can be achieved to aid the hydrologist/reservoir engineer in predicting fluid flow. Last but not least we are still carrying out work related to mapping fluid flow in natural and induced (hydrofracture) fractures.

Overall, CCS has grown into a mature research unit carrying out a broad range of research topics. We have grown to the point where we will soon have to expand our facilities. During the next year we hope to implement a hardware upgrade that will greatly enhance our computational capabilities. At the present time we are leaning toward a semidistributed workstation system. We feel that to stay on the edge of the research projects we are involved in, we must also have modern facilities.

LABORATORY FACILITIES

Rock physics laboratory facilities are located in two buildings on the U.C. Berkeley campus. A general-purpose laboratory is housed in the Hearst Mining Building. In this laboratory is an electro-servo-controlled system with two 600,000-lb capacity stiff frames. The system is linked to a computer for both control and data acquisition. Four other test frames of smaller capacity are also available. A

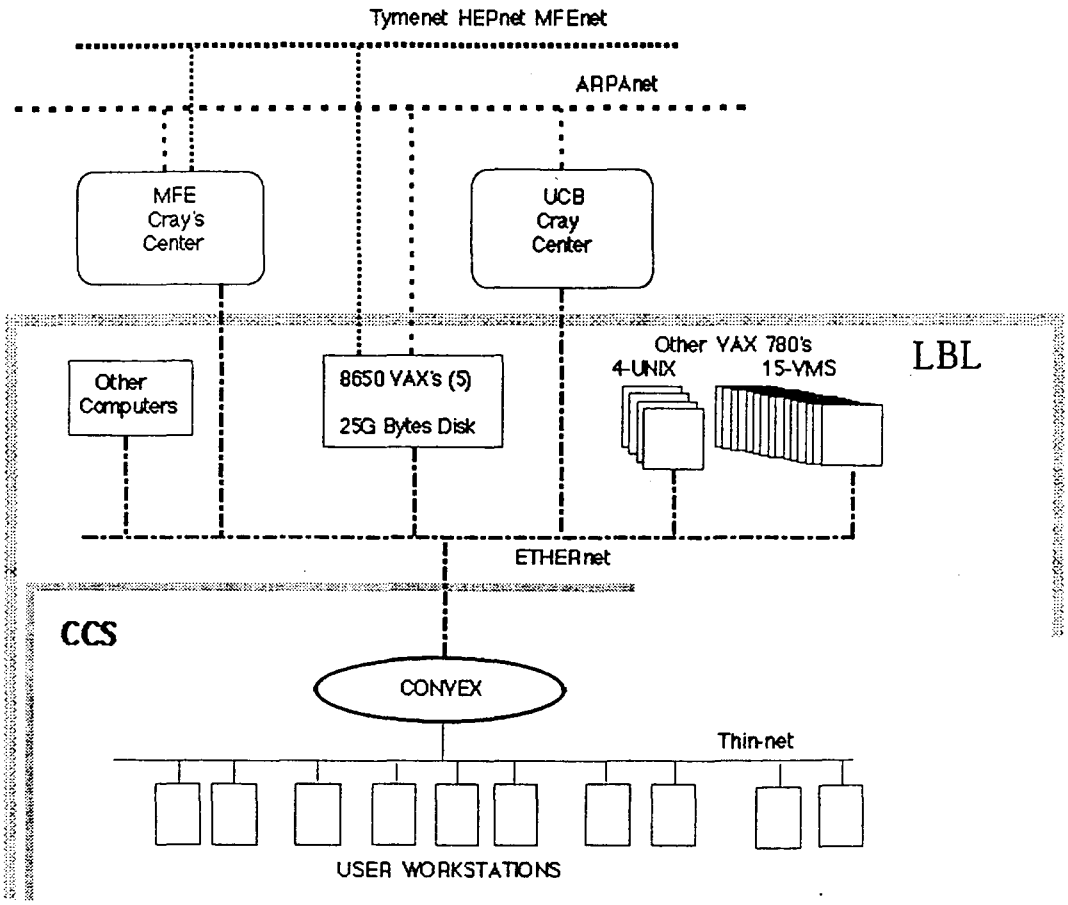

Figure 1. Configuration of the CCS facilities and the networking associated with other on-site computers. [XBL 886-2291]

variety of hydraulic jacks, which can be operated either manually or connected to the servo-controlled test system, is available for testing over a wider range of loads. Ancillary equipment includes a variety of heaters for elevated temperature tests and equipment to perform Wood's metal and mercury porosimetry tests. A clean box is available for assembly of apparatus in an atmosphere with minimum particulate concentrations. Two waveform-acquisition systems are available. A single-channel input system incorporates a Tektronics digital oscilloscope linked to an LSI-11 computer. A more-flexible two-channel system incorporates a LeCroy 120-MHz transient recorder with an IBM PC for display and control. Both systems have software for routine spectral analysis. A Velonex 2-kV pulse generator, with variable amplitude and pulse, supplies a high-voltage pulse to a variety of piezoelectric transducers. Transducers with center frequencies from about 200 KHz to 1 MHz are available. These transducers produce compressional and polarized shear waves.

A second facility located in the Hesse Building is devoted primarily to fluid-flow measurements. A large test vessel with 6-in. inside diameter and 40-in. length is available for use at pressures up to 2500 psi. A gas pressurization system is used with two single-stage compressors in series. The first low-pressure compressor is used for tests below 5000 psi. Ancillary apparatus includes internal heaters and apparatus for pulse permeability tests of rock with permeabilities as low as 0.1 nanodarcy. Data acquisition is via computer.

GEOPHYSICAL MEASUREMENT FACILITY

The Geophysical Measurements Facility (GMF) was established at LBL to maximize the use of field

instrumentation and to put in place a facility that would maintain the equipment in a field-ready state. Many projects that involve field measurements often spend a large proportion of the funds refurbishing, renting, and/or buying equipment in order to carry out the field experiment. The concept behind GMF was to minimize the costs associated with the collection of field data. By sharing equipment, and properly maintaining the existing instrumentation, the overall field costs should be minimized. GMF is not intended to serve only LBL programs. It is meant to be used by all agencies participating in DOE programs. For example, Sandia National Laboratories has placed a portable drill rig at GMF.

The list of equipment at GMF is too long to detail here, but in general it includes a variety of equipment for use with seismic methods (two automated seismic recorders (ASP), 17 three-channel digital recorders, two seismic vibrators, a VSP recording and processing system, and an acoustic-emission system) and electrical methods (controlled-source EM and DC resisitivity system, and SQUID magnetometers). There is also a large variety of general field and test equipment (meters, scopes, etc.) at GMF. The most recent additions are a complete VSP recording and in-field processing system and two complete well-logging trucks. The well-logging trucks were donated by Dresser-Atlas. One truck is outfitted with 18,000 ft of new high-temperature (300°C) seven-conductor cable. The other truck has a split reel with 3000 ft of seven-conductor cable on one side and room on the other half for specialized cable. In 1988 GMF moved into new facilities that expanded its shop and milling capabilities and provided space for large-scale block testing. GMF is now serving many DOE programs (Basic Energy Sciences, Geothermal, Waste Isolation) and has succeeded in its goal of providing a state-of-the-art pool of field-ready equipment for the collection of field data.

Seismic Field Experiments for Characterizing Anisotropic Inhomogeneous Materials

*E.L. Majer, T.V. McEvilly, J.E. Peterson, T.M. Daley, and R.W. Clymer**

During the past several years seismologists at Lawrence Berkeley Laboratory (LBL) have been working in several different field areas to investigate the use of seismic techniques for mapping critical parameters of the earth that may control such processes as geothermal and petroleum reservoir production, hydrologic behavior of underground toxic and nuclear waste repositories, and the relation between stress distribution and earthquake occurrence. The scale of this work has varied from a few meters, such as the work at the Grimsel Rock Laboratory in Switzerland, to tens of kilometers at the Parkfield field study area, which is designed to monitor stress release along the San Andreas fault. Described below are some of the main field efforts undertaken in the last year by LBL in these areas of interest.

*Department of Geology and Geophysics, Seismographic Stations, University of California, Berkeley, CA.

CROSS-HOLE SEISMIC IMAGING IN FRACTURED ROCK

In 1987 work was started at the Grimsel Rock Laboratory in Switzerland as part of a joint DOE/NAGRA research program. NAGRA is a Swiss cooperative formed to address the storage and disposal of nuclear waste generated in Switzerland. The Grimsel rock laboratory, located in the Swiss alps in a granitic rock, consists of a series of tunnels that have been excavated into the side of a mountain using a 3.5-m-diameter tunnel-boring machine (TBM). The field work is designed to answer questions regarding the fundamental nature of seismic-wave propagation in fractured rock and to aid in the development of seismic-imaging methods for defining fracture characteristics (density, orientation, spacing). A layout of the field site with the significant mapped fracture sets is shown in Fig. 1. As can be seen, two parallel boreholes 10 m apart extend between two tunnels. This configuration allows access to all four sides of the rock mass under investigation. A fracture set in this zone is the target of

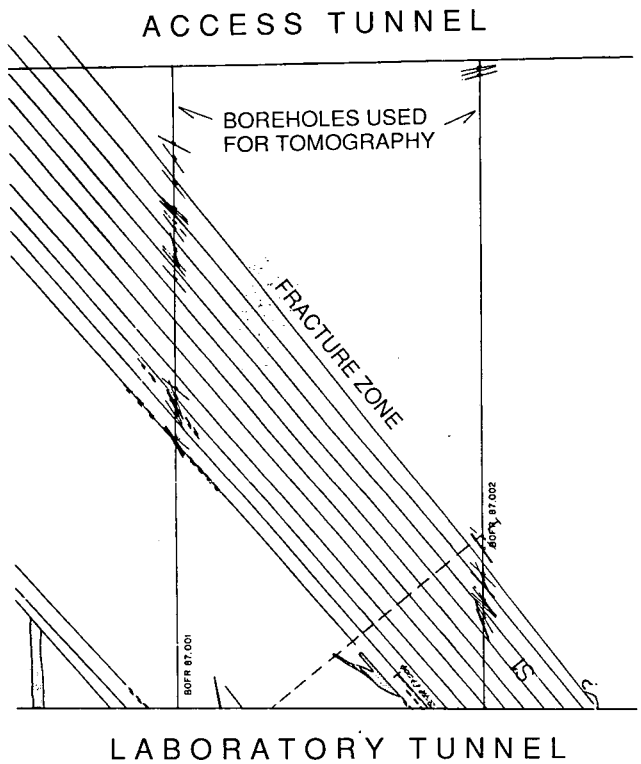

Figure 1. Plan view of the boreholes and access tunnels around the FRI zone at the Grimsel Rock laboratory in Switzerland. Also shown are the fractures mapped from the core and tunnel walls. [XBL 894-1359]

the investigations. The goal is to image the area tomographically using three-component sources and receivers. One of the principle aims of the project is to investigate the effect of fractures and anisotropy on *P*-, *SV*-, and *SH*-waves. The project is a 3-year field experiment with different phases being carried out each year. In 1987 we used primarily *P*-waves in the frequency range of 2 to 5 kHz to image the structure. In 1988 a new piezoelectric source with new electronics was used that produced *P*-waves with a frequency content to 10 kHz and improved shear-wave transmission as well.

To date, processing has been completed on the *P*-wave data, but only preliminary results are available for the shear waves. The zone mapped between the boreholes in the study area exhibited significant anisotropy and complexity in fracture structure and content. The shear waves were most significantly affected by the fractures. Shear-wave arrival would be quickly damped out in areas of fractures. Although the piezoelectric source was designed to generate *S*-waves as well as *P*-waves, it is obvious that the *S*-waves being generated by the present source should be much stronger to penetrate the same distance as the *P*-waves. Shown in Figs. 2 and 3 are the final results of the *P*-wave travel-time data for the 1987 and 1988 surveys, respectively. As can be seen, there are significant differences between the 1987 and 1988 results. Shown in Fig. 1 are the features compiled from examining the core in the holes and from mapping the fractures on the mine walls. The 1988 results of the seismic tomography show better resolution of the significant fracture sets and also define in more detail the fracture set running from the access tunnel to hole 87.001. In addition, the "damage zone" of the tunnel walls has disappeared as well. The results of the field work to date indicate that the original premise of using *P*- and *S*-waves for mapping fracture content is valid. The dramatic effect of the fractures on the shear waves indicates that if strong enough shear waves could be generated, the data would be very useful in mapping the locations of fractures. Future work should focus on using improved shear-wave data to increase the resolution of the technique and to define such parameters as fracture density and spacing. The results indicate that features such as significant fracture zones and changes in rock type are very distinguishable by using *P*-wave seismic tomography.

Figure 2. The results of the *P*-wave tomographic imaging using data acquired in 1987. [XBL 894-1360]

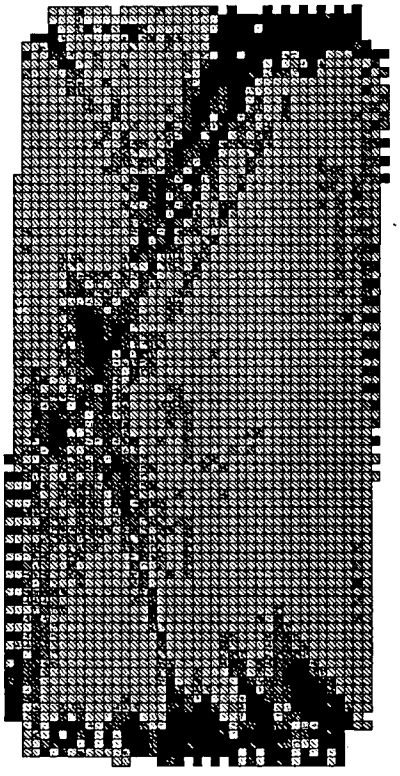

Figure 3. The results of the *P*-wave tomographic imaging using data acquired in 1988. [XBL 894-1361]

PASSIVE SEISMIC MONITORING OF HYDROFRACTURES IN A SHALLOW PETROLEUM RESERVOIR

A unique field experiment to monitor the seismic signals associated with the propagation of a hydrofracture in a shallow commercial petroleum reservoir was carried out in the Central Valley of California in the summer of 1988. The experiment was supported by Chevron USA. The study was part of a larger effort to use VSP, crosshole seismic, pressure monitoring, and tiltmeters to determine the principle stress directions and the path of hydrofracture. The hydrofracture was a normal production job with injection rates up to 50 barrels/min at pressures up to 1200 psi. The results of these field tests indicate that there is usable discrete seismic energy between 100 and 1000 Hz. There are basically two types of events: discrete seismic events (acoustic emission) and, in some cases, increases in continuous seismic energy that appear to be associated with the fluid sheet when very viscous fluids are used. A new high-frequency data-acquisition and processing system was used to carry out an experiment that is capable of locating seismic activity in close to real time. The objective of the experiment is to determine if passive seismic monitoring can be used to map the progress of a hydrofracture in a petroleum source-rock environment.

During the last several years LBL, with the support of the U.S. Army Corps of Engineers and the U.S. Department of Energy Civilian Radioactive Waste Management program, has been evaluating and developing seismological techniques for mapping the location of fluid injections in real time. This project is an outgrowth of the work that LBL has carried out using acoustic emissions for the characterization of hydrofracture propagation. As applied to the petroleum industry it was unknown if the same techniques that were developed for hard rock could be applied to mapping hydrofractures in real time. The project was designed to answer some questions regarding the use of passive seismic techniques for the characterization of hydrofractures in soft rock.

In a petroleum application it is much more difficult to detect seismic activity associated with hydrofracturing because of the lower differential stress values than in most hard rock sites and also because of the relatively high attenuation values in petroleum source rocks. The ultimate purpose of the seismic field experiments was to use seismic signals to map the path of the hydrofracture in detail using a 3-D array of seismic sensors surrounding the injection zone.

Figure 4 is the layout of the field experiment carried out in central California. The experiment was

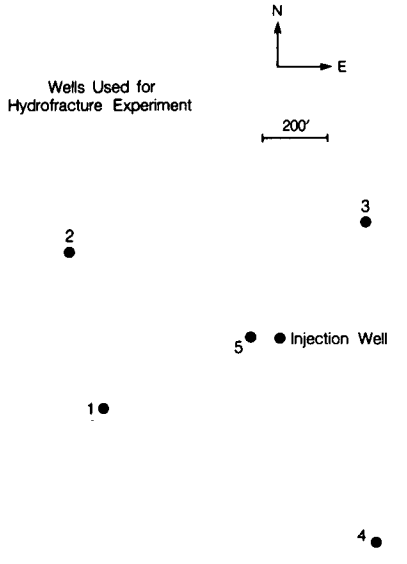

Figure 4. Layout of the hydrofracture monitoring experiments in a central California oil field, showing the wells in which geophones were placed, at the depth of the hydrofracture, and the hydrofracture well. [XBL 891-7449]

carried out in a shallow 1500- to 2500-ft reservoir in a soft rock. Geophones were emplaced in five wells at different elevations to record seismic signals associated with the hydrofracture. The wells all penetrate a shallow oil reservoir with limited permeability. Hydrofracturing is routinely used in this area to stimulate production and to prepare for waterflooding. Three-component geophones were used in wells 1, 2, 3, and 4, and a two-component (one vertical and one horizontal) geophone, with the two components tied together, was used in well 5. The sample rate selected for data collection was 5000 samples/s. The field system is a 16-channel system that digitizes at up to 100,000 samples/s on each channel (12-bit), saves the waveforms, picks *P*-wave times, locates the events, and plots the results in close to real time using 3-D color graphics. It has over one MIPS processing capability from a 20-MFLOP array processor and also has variable gain amplifiers on the input channels. This system was developed for monitoring the seismic activity associated with the injection of grout in hard rock for the U.S. Army Corps of Engineers at the Waterways Experimental Station in Vicksburg, Mississippi. In addition to performing discrete-event analysis this system has been programmed to use frequency/wave-number analysis to locate energy that is not discrete and may be coming from the fluid flow. To perform in this fashion, however, spatial aliasing must be avoided in the signal recording. This usually dictates the use of arrays in the wells rather than single-point geophones. The system is based on IBM/AT technology and, except for the array processor, is programmed in FORTRAN. This PC-based system allows flexibility and expandability. The front end to this system is an intelligent transient-waveform analyzer. This front end digitizes, captures one megasample of data, and transfers the data to the PCs for processing. One PC performs the event detection, FK analysis, and the timing of the *P*-wave picks. The other PC carries out the location of seismic energy and plotting of the data.

Listed below are the main conclusions to be reached from these two field experiments.

1. There is acoustic-emission activity at the pressure and injection rates used. This is a very surprising and important result. The rock in which the hydrofracture was carried out is a very soft rock, and for this rock to break or fail in such a manner as to produce detectable seismic energy is very significant. Plotted in Fig. 5 is the rate of seismic activity as a function of time for one of the injections. The event rate is shown for each of the monitor wells. The pumping was not constant, and the seismic activity was sporadic, but there is no doubt that detectable seismic energy was being produced at all wells. Very little of this activity was detectable on enough wells to be accurately located. The only means of locating the activity was to look at the relative occurrence of the activity as a function of time. In all the hydrofracture jobs the most activity was detected at wells 1 and 2. This would tend to indicate that the propagation of the hydrofracture was asymmetric and larger in the direction of wells 1 and 2 compared with wells 3 and 4.
2. Events continued after pumping had ceased and pressure on the injection well was reduced. This seems to indicate that the rock around the injection well was slowly inflated during pumping. Upon reduction of pressure there was a more-rapid deflation of the rock, thus releasing the stored energy in larger events.
3. There was also identifiable continuous activity, which became more dominant as the viscosity of the fluid increased.
4. The frequency content of events in both shallow and deep application was 100–1000 Hz for discrete events and 50–200 Hz for continuous activity.

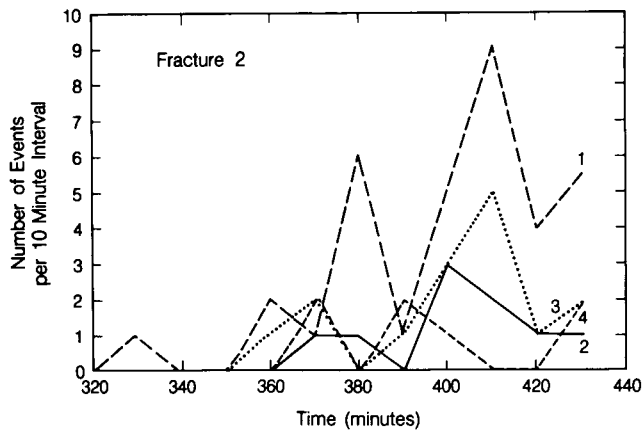

Figure 5. Seismic activity as a function of time for one of the main hydrofracture treatments. [XBL 891-7448]

In summary, much work remains to done before seismic techniques can be reliably used for hydrofracture monitoring in petroleum source rocks. There does seem to be hope for the method, however, and with the advent of new technology it will be easier to perform meaningful field experiments using the necessary high-frequency content.

MULTICOMPONENT VSP SURVEYS AT THE CAJON PASS DEEP WELL

Another example of using seismological data for characterizing earth structure is vertical seismic profiling (VSP)—a proven tool for studying the seismic-wave properties near a well and detailing subsurface structure. The usefulness of the VSP method has been increased by the acquisition of multicomponent data using a three-component borehole geophone in conjunction with both *P*-wave and *S*-wave seismic sources. The three-component geophone allows recording of the entire wave field, and the *S*-wave source (usually a seismic-vibrator truck) allows control of the shear-wave polarization. Among the possible uses of such data is fracture detection and characterization via seismic anisotropy measurements. During the past year final processing of VSP data from a deep hole near the San Andreas fault at Cajon Pass, California, has yielded some very interesting results. Use of a three-component geophone, along with careful rotation of the recorded data traces into a wavefront-based coordinate system, allowed analysis of many aspects of the seismic-wave propagation properties around the well. In this survey the shear-wave vibrator occupied one offset position for three runs of the borehole geophone, allowing *S*-wave polarizations to be obtained at three orientations in relation to a line from the well: 0°, 90°, and 45°, called *SV*, *SH*, and *S45*, respectively. Complete data sets were obtained for the *SV* and *SH* polarizations (from surface to 1800 m, with 10-m spacing), but the third run was not finished, giving coverage with the *S45* source from 1040 m to 1630 m. By rotating the data from the *P*, *SV*, and *SH* sources into the radial, *SH*, and *SV* components, a nine-component display could be produced for the VSP (Fig. 6). The variation of events seen on each of these nine components shows the details that multicomponent VSPs produce compared with standard VSPs, which have one source and one receiver component (such as the *P*-source, radial-component data shown in Fig. 6).

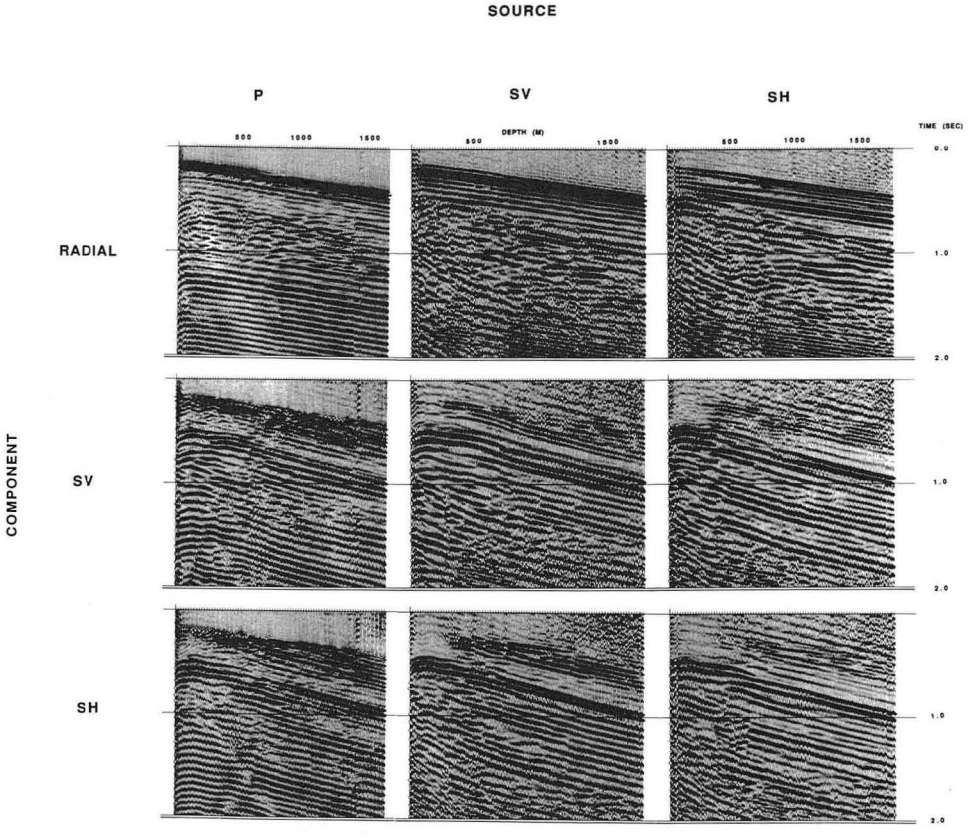

Figure 6. Nine-component display of Cajon Pass VSP data. Each section is a depth-versus-time display of the data from one source type (*P*, *SH*, or *SV*) recorded on one geophone component (radial, *SH*, or *SV*). The data have been rotated into radial, *SH*, and *SV* components from the original, randomly rotated geophone recordings using the first *P*-wave arrival. [XBL 8710-4019]

The three shear-wave data sets are shown in Fig. 7 for the *SH* and *SV* components. Anisotropic effects are clearly seen on the *SH* components, where the *S45*-generated arrival between 0.7 and 1.1 s has a split waveform and a less coherent arrival. The nearby San Andreas fault is expected to cause microfracturing, which will affect the orientation of the shear-wave particle motion. This type of particle-motion analysis of the data shows that factors other than the San Andreas fault are affecting the seismic anisotropy.

PARKFIELD EARTHQUAKE-PREDICTION EXPERIMENT

The Parkfield experiment is being conducted along along a central California segment of the San Andreas fault that has had a magnitude 6 earthquake approximately once every 20 years for the past 100 years. We are now within a 5-year window in which the next magnitude 6 should occur if the 20-year cycle is correct. The present program at Parkfield follows the developing awareness of the potential for

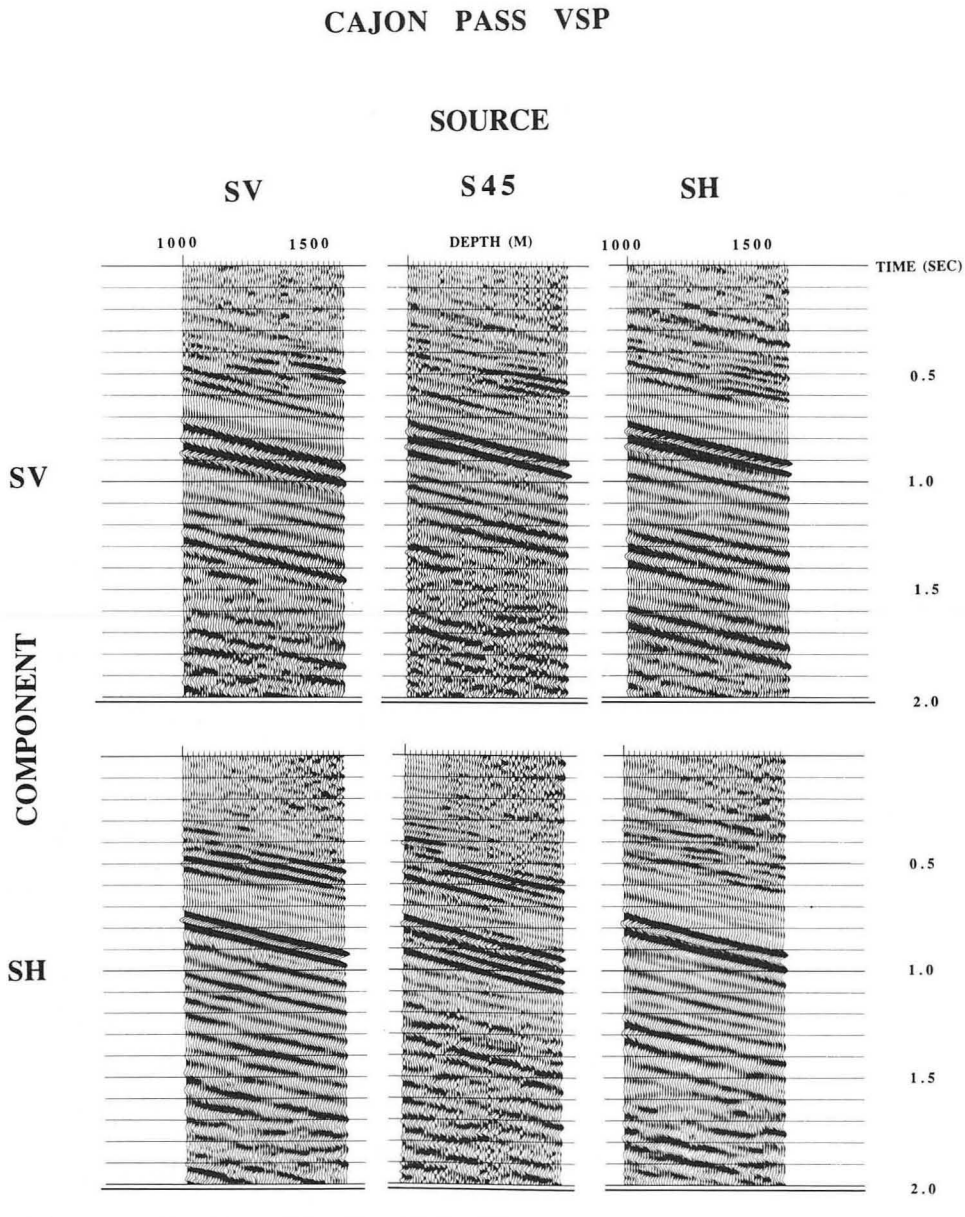

Figure 7. Shear-wave data from Cajon Pass VSP. The *SV*, *SH*, and *S45* sources are three polarizations of a shear-wave vibrator. The borehole geophone data have been rotated into *SH* and *SV* components. The variation in observed arrivals between sources can be used to study seismic anisotropy. [XBL 8712-5118]

S-wave monitoring in earthquake prediction, based in part upon new observations of the effects of fractures and stress on *S*-wave anisotropy. In our previous work at a site near Hollister, California, we had already established a precision for travel-time monitoring (10^{-3} -10^{-4} of total path time) of crustal *P*-waves using Vibroseis. Furthermore, our experience in using a newly acquired shear-wave Vibroseis in direct measurement of anisotropy in the field encouraged us to incorporate *S*-wave studies into our monitoring for earthquake prediction. Finally, our Parkfield earthquake study and the subsequent full-scale field experiment in the U.S. Geological Survey program led us in FY 1986 to shift our research emphasis to Parkfield and to incorporate major changes in experimental methods and instrumentation based on our previous work. The research is a direct test, with all that 1989 technology (equipment and data processing) can bring to the problem, of two hypotheses:

1. The earthquake nucleation process produces stress-driven perturbations in physical properties (velocity, Q, anisotropy) of the rocks in the incipient focal region, and these are measurable by high-precision observations of seismic waves (particularly *S*) in the affected zone.
2. The nucleation process involves progressive failure of local high-strength "asperities" in the fault zone, and this process should be observable in the zero-magnitude microseismicity, given sufficiently high resolution on earthquake locations and mechanisms.

The plan of attack has been to emplace in the anticipated nucleation zone a state-of-the-art high-resolution seismic network (HRSN) of 10 stations and a vertical array in a deep well (Varian borehole) for the purpose of monitoring both controlled-source events (*S*-wave vibrator, variable polarization) and natural events (microearthquakes to $M_L \approx -0.5$) to test the hypotheses set out above. We have produced the needed significant technical advances in several areas:

1. High-accuracy (0.2-ms) timing of similar trace.
2. Fully 3-D hypocenter locations with a data-determined (joint 3-D inversion) velocity model.
3. Polarization analyses for the study of *S*-wave anisotropy (VSP and microearthquakes) and its variation.
4. A computing/data base management/archiving environment for routine handling of some 600–700 earthquakes and 10 controlled-source field sessions annually (about 50 gigabytes of data).

In 1988 the work consisted of three basic tasks:

1. Operation of the 32-channel, 10-station HRSN for both microearthquake and controlled-source monitoring, which includes a $200K+ state-of-the-art telemetered digital data acquisition system, for near-field source studies and VSP surveys.
2. Monthly illumination of the network (by the *S*-wave Vibroseis owned by UC, maintained and operated by LBL's Geophysical Measurements Facility) with controlled-polarization *S*-waves from 24 source configurations at 8 locations throughout the Parkfield study zone.
3. VSP monitoring of the Varian well from three offsets in addition to the 8 source points used to illuminate the 10-station network.

Each monthly field session of full data acquisition with the Vibroseis produces about 4 gigabytes of prestacked data. This is in addition to the triggered network operation of our (quite versatile) data-acquisition system in its unattended mode, collecting events as small as magnitude -1.0. The Vibroseis and microearthquake data are stored permanently in the seismic data archive of the Center for Computational Seismology at LBL.

We are just entering, after little more than 2 years, that third stage of the project in which the exciting research is getting underway. Phase one covered the installation of the network and the subsequent year's debugging. Phase two covers the tools-development (computational as well as instrumentation) era, begun as soon as we saw the potential in the data (late 1987) being acquired and realized that standard processing and analysis methods would be inadequate to the task of dealing with either the microearthquake or controlled source/VSP data. We are embarking now on phase three, which includes the systematic full relocation task for the 1987–1988 Parkfield microearthquakes (current uncertainties in relative positions of nearby hypocenters are demonstrably as much as 1 km, regardless of formally calculated statistical values). This will yield an unprecedented view of the fault-zone process. Differential measurements on the vibrator data are being applied to extract sensitive parameters characterizing the wave-propagation properties of the focal region.

The research on Parkfield microseismicity in this project has two main objectives: (1) observation of the mode of stress release in the fault zone, at length

scales up to 20 km, and (2) description of fault-zone structure at the scale of intermediate to small asperities (tens of meters) to relate the surface and subsurface geology by establishing connections between different modes of stress release and the properties in the fault zone. In addition, the controlled-source *S*-wave research monitors velocity, attenuation, and anistropy. Anisotropy in the nucleation zone can result from several physical mechanisms (e.g., preferred crack orientation, fabric of sheared material, the acting stress field). Changes in stress or pore pressure can affect shear-wave propagation. To date, monthly field trips are made to image the fault using controlled vibrator sources. Microearthquakes are being located in the fault zone using new 3-D location software to an accuracy of about 10 m. It is hoped that with data of this quality the earthquake nucleation process can be monitored and understood so that someday useful predictions can be made.

Anisotropy in Seismic Velocities and Amplitudes from Multiple Parallel Fractures

L.R. Myer, N.G.W. Cook, and L.J. Pyrak-Nolte

Many rock structures include multiple sets of near-parallel, planar nonwelded interfaces, such as bedding planes or joints. Because these features often control the hydraulic and mechanical behavior of a rock mass, knowledge of their orientation and spacing is of great importance in many instances, including development of petroleum reservoirs and hazardous and nuclear waste disposal. Considerable emphasis has and will continue to be placed on the use of seismic methods for characterization of such features.

The effects of multiple nonwelded interfaces on seismic-wave propagation are often analyzed using effective moduli, in which case it is assumed that wave propagation is independent of frequency and that the medium causes no loss in amplitude. An alternative approach is to treat these interfaces as a boundary condition in the seismic wave equation, which states that seismic-stresses are continuous across the interface but particle displacements are not. The ratio of the stress to the displacement discontinuity is the specific stiffness of the interface. These two approaches have been compared by analytical computation and laboratory tests on idealized transversely isotropic media.

THEORY

To apply the effective-moduli method, a rock mass containing a single set of parallel fractures or nonwelded interfaces is represented by a transversely isotropic medium described by five elastic constants (Schoenberg, 1980; Majer et al., 1988). The phase and group velocities have been calculated as a function of propagation direction in such a medium by Crampin (1981, 1984a,b), as well as by others.

In an elastic medium the velocities of compressional (*P*) and shear (*S*) waves are independent of propagation direction. However, in an anisotropic medium seismic velocities are dependent upon propagation direction. In addition to this directional dependence, the shear wave propagates as two components, designated as S_1 and S_2. Figure 1 illustrates the angular dependence of the group velocity of *P*-, S_1-, and S_2-waves for a particular value of the

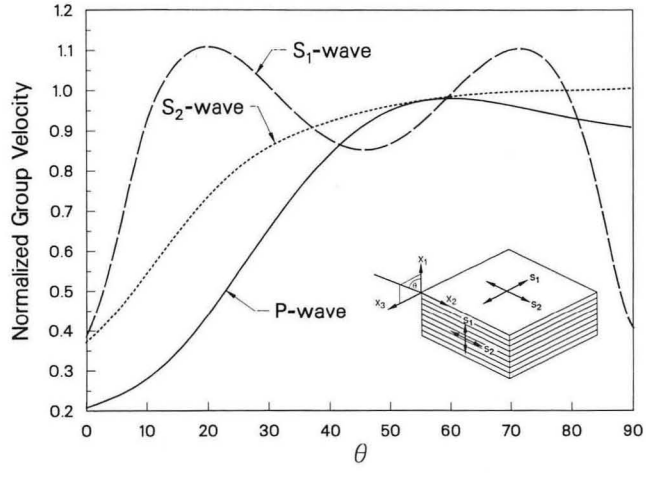

Figure 1. Dependence of the group velocity (normalized with respect to the group velocity in intact material) on propagation direction for *P*-, S_1-, and S_2-waves based on effective-moduli theory. Insert shows propagation direction and particle motion in layered medium. [XGC 891-4617]

material parameters E_T and E_N, where $E_T = \mu/H\kappa_T$ and $E_N = \mu/H\kappa_N$ and μ = the shear moduli of the intact material, H = the interface spacing, and κ_T,κ_N = the shear and normal stiffness of an interface.

To apply the displacement-discontinuity model, it is assumed that the effects of each interface are independent of all others. The solution of the wave equation for compressional and shear waves obliquely incident upon a nonwelded interface is given by Schoenberg (1980). Subsequently Myer et al. (1986) showed that the displacement-discontinuity theory correctly predicts the behavior of waves propagated across single interfaces of calculable stiffness, and Pyrak-Nolte (1988) showed that the model correctly predicts the seismic response of single, dry, natural fractures in rock.

Figure 2 illustrates the angular dependence of group velocity of P-, S_1-, and S_2-waves predicted by the displacement-discontinuity model for a particular value of $\omega Z/k$, where ω is circular frequency, Z is seismic impedance, and κ_N and κ_T are interface stiffnesses. Comparing Fig. 2 with Fig. 1 shows that the two theories predict similar changes in group velocity with propagation direction for P- and S_2-waves; that is, the velocities are a minimum in the 0° propagation directions and increase with the angle of propagation. The predicted behavior of the S_1-wave, however, is quite different for the two theories. The effective-modulus theory predicts that the S_1-wave group velocity at 0° and 90° will be equal and a minimum, whereas the displacement-discontinuity model predicts that the S_1-wave group velocity will approach that of the intact material at 90°. In addition an abrupt shift is predicted at the critical angle of incidence.

The effective-moduli theory predicts propagation without loss of amplitude unless complex moduli are assumed. However, the displacement-discontinuity theory predicts amplitude loss in the propagating wave without any assumption of inelasticity. Figure 3 shows the normalized amplitude of the transmitted P-, S_1-, and S_2-wave as a function of propagation direction for the same material properties used in the group-velocity calculations. (The number of fractures was selected to correspond to the experimental specimen.) The displacement-discontinuity theory predicts that the S_2-wave amplitude will increase with propagation direction, approaching, at 90°, the amplitude of a wave in intact material. For P- and S_1-waves, the amplitude of the transmitted wave is substantially reduced in the 0° direction compared with that in intact material. At 90° the theory predicts that the amplitude of both waves should approach zero.

EXPERIMENTAL RESULTS

In the laboratory, compressional and polarized shear waves were propagated through a laminated block of 31 mild steel plates, each about 3 mm in thickness. Waveforms were collected in the 0° pro-

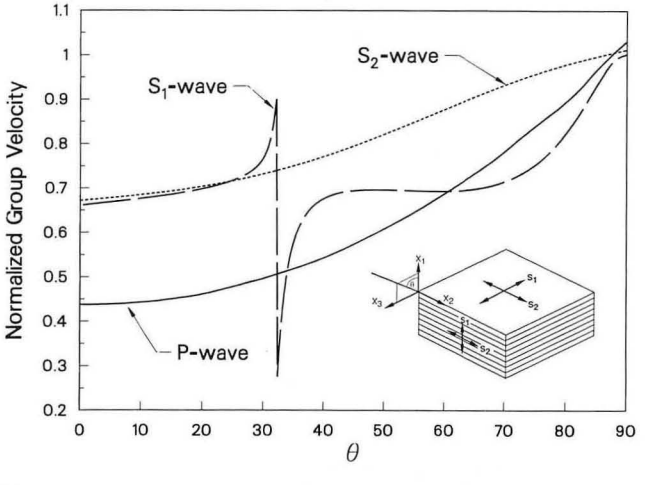

Figure 2. Dependence of group velocity (normalized with respect to that in intact material) on propagation direction for P-, S_1-, and S_2-waves based on displacement-discontinuity model. Insert shows propagation direction and particle motion. [XGC 891-4618]

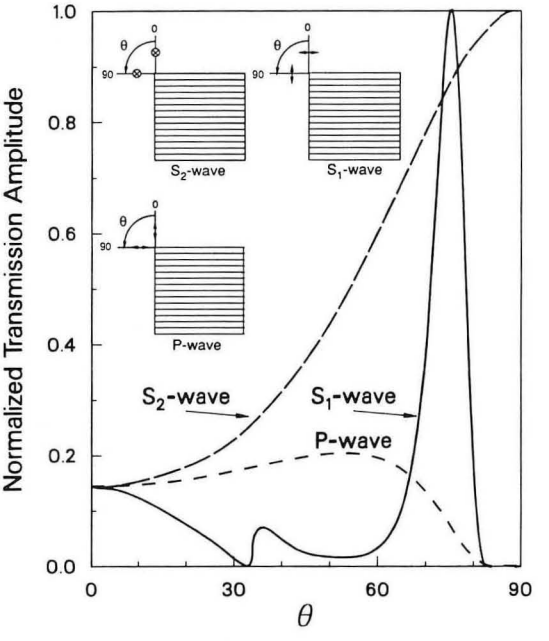

Figure 3. Transmitted wave amplitude (normalized with respect to that in intact material) as a function of propagation direction for P-, S_1-, and S_2-waves. Insert shows propagation direction and particle motion. [XCG 891-4611]

pagation direction (perpendicular to the interfaces) and the 90° direction. In the 90° propagation direction measurements were made with shear-wave particle motion both parallel and perpendicular to the interfaces (Fig. 4).

Table 1 summarizes the results of the velocity and amplitude measurements on the laminated block and compares these with results from an intact piece of steel. Amplitudes measured using the first-arriving pulse were determined from the difference between the trough and peak. Table 1 shows that both the velocities and amplitudes of the received pulses for the 0° propagation directions in the laminated block were much reduced compared with those in the intact block. This behavior is in accordance with the displacement-discontinuity model. The effective-modulus model also predicts that the velocities in the laminated block would be lower, but under assumptions of elastic material properties it predicts no difference in amplitude. Values of fracture stiffness obtained from the laboratory velocity measurements and using the effective-moduli theory were similar in magnitude to those obtained from the amplitude measurements and using the displacement-discontinuity model.

For propagation in the 90° direction P- and S_2-wave velocities were as expected from both theories. The S_1-wave velocity was, however, nearly the same as the S_2-wave velocity, contrary to the effective-moduli theory. Though the velocity of the S_2-wave was in accordance with the displacement-discontinuity model, the observed amplitudes were too large. It is believed that the first-arriving S_2-wave may have been an interface wave, as described by Pyrak-Nolte and Cook (1987).

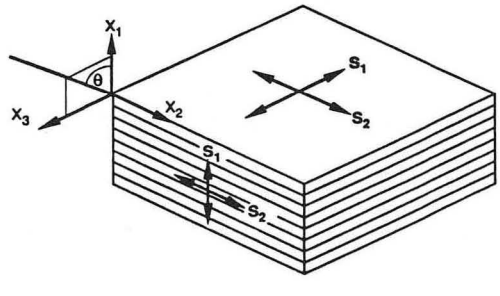

Figure 4. Block diagram showing S_1- and S_2-wave propagation directions and particle motion in laminated block. [XCG-891-4615]

Table 1. Measured velocities and amplitudes at 0° and 90° incidence.

P(0°)	
Vel. (m/s)	3845
Amp. (mV)	14
S(0°)	
Vel. (m/s)	2056
Amp. (mV)	520
P(90°)*	
Vel. (m/s)	5876/5899
Amp. (mV)	300/295
S_1 (90°)	
Vel. (m/s)	3284
Amp. (mV)	1200/348
S_2 (90°)	
Vel. (m/s)	3274
Amp. (mV)	4200
P(solid steel)	
Vel. (m/s)	6023
Amp. (mV)	460
S(solid steel)	
Vel. (m/s)	3254
Amp. (mV)	3600

*P-wave velocities and amplitudes corresponding to the two tests required to obtain the different S-wave polarizations.

REFERENCES

Crampin, S., 1981. A review of wave motion in anisotropic and cracked elastic media. Wave Motion, v. 3, p. 343–391.

Crampin, S., 1984a. An introduction to wave propagation in anisotropic media. Geophys. J. R. Astron. Soc., v. 76, p. 17–28.

Crampin, S., 1984b. Effective anisotropic elastic constants for wave propagation through cracked solids. Geophys. J. R. Astron. Soc., v. 76, p. 135–145.

Majer, E.L., McEvilly, T.V., Eastwood, F.S., and Myer, L.R., 1988. Fracture detection using P- and S-wave VSP at The Geysers geothermal field. Geophys., v. 53, no. 1, p. 76–84.

Pyrak-Nolte, L.J., and Cook, N.G.W., 1987. Elastic interface waves along a fracture. Geophys. Res. Lett., v. 14, no. 11, p. 1107–1110.

Pyrak-Nolte, L.J., 1988. Seismic visibility of fracture (Ph.D. Thesis). University of California, Berkeley.

Schoenberg, M., 1980. Elastic wave behavior across linear slip interfaces. J. Acoust. Soc. Am., v. 68, no. 5, p. 1516.

Design and Development of a Downhole Seismic-Wave Source

L.R. Myer, N.G.W. Cook, E.L. Majer, T.V. McEvilly, and P.A. Witherspoon

Beginning in FY1986 a project was funded to design and develop an innovative downhole shear and compressional seismic-wave source. The device will have wide application in petroleum and geothermal reservoir studies, toxic and nuclear waste disposal site investigations, and many other studies requiring subsurface imaging or seismic tomographic reconstruction of rock-mass characteristics. The device will generate shear (*S*) waves of two polarizations and compressional (*P*) waves over the frequency range of 0.1 kHz to 0.5 kHz and will rely on the swept-frequency-signal principles for analysis by correlation techniques commonly used in seismic exploration methods. The goal is a working prototype borehole tool demonstrating proof of concept and potential for realization of a unit with an effective signal range of 1 km and an operating depth to 5 km.

The proposed device was divided into four main units for purposes of design and preliminary testing. These four units are (1) *S*-wave source with axial vibratory motion (*SV*); (2) *S*-wave source with torsional/rotational vibratory motion, (*SH*); (3) *P*-wave source with radially directed vibratory motion, and (4) borehole clamp. To date, unit one has received the primary emphasis, resulting, as described below, in a prototype device that has been bench tested. Alternative designs for unit two are being studied.

LINEAR AXIAL (*SV*) SHEAR-WAVE SOURCE

The design concept for this device is illustrated in Fig. 1, which is a schematic cross section of the central portion of the unit. The vibratory motion is produced by interaction of the coil with the magnetic field produced by samarium cobalt magnets mounted on the core. The magnets are radially magnetized so that the magnetic flux lines are perpendicular to the direction of the current flowing in the coil. The magnetic circuit is completed through the

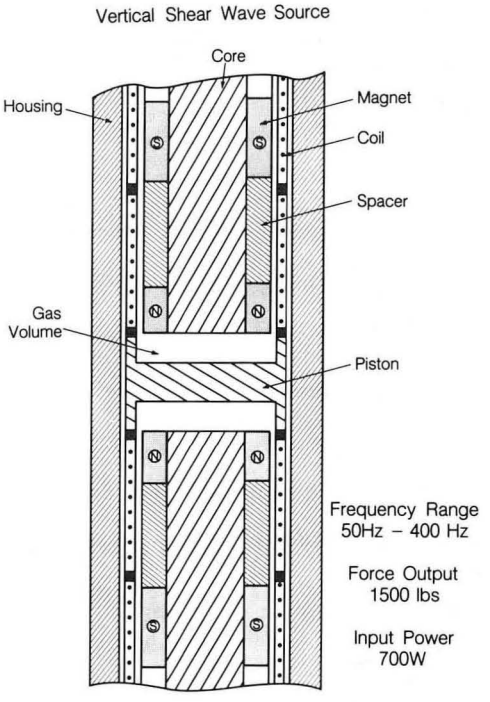

Figure 1. Schematic cross section of *SV* source. [XBL 8612-5972]

housing and the central core. Applying an alternating current to the coil produces vibratory motion of the same frequency. A symmetric component configuration was chosen, as shown in Fig. 1, with each magnet-core assembly holding five ring magnets. With an input power of 700 W the total static-force output of the magnet-coil system was calculated to be about 130 lb.

To increase the force transmitted to the borehole wall, a design was adapted that enables the device to operate in a resonant condition at all frequencies. This is achieved by a pneumatic spring of variable stiffness. The spring action is provided by compression of the gas volume, as shown in Fig. 1. Movement of the coil-piston assembly compresses the gas.

The resistance of the gas to compression translates into a force that acts on the magnet-core assembly and is ultimately transmitted to the borehole wall. Varying either the volume of gas or its pressure results in a change in the stiffness of the pneumatic spring. The stiffness is adjusted to achieve resonant motion of the coil-piston assembly as the driving frequency is swept over the desired bandwidth. Assuming a reasonable damping factor, a peak force output of 1300 lb was calculated for the configuration described above.

Figure 2 shows the *SV*-source components: coil-piston assembly, magnet assemblies, probe assemblies, and housing. The coil-piston assembly is the vibratory element, as described above. One of the magnet assemblies bolts to the housing. The other assembly slides inside the housing and is used to control the volume of gas in the pneumatic spring; motion is sensed by a linear variable differential transformer located in the housing. The probe assemblies contain tubes for the gas supply to the pneumatic springs and the electrical leads for the coil. Current flows from the probe to the flexible spring, shown on the end of the magnet assemblies, into the piston and to the coil. Each probe assembly also houses a pressure transducer that monitors the gas pressure in the pneumatic spring.

Initial performance testing was carried out by securely fastening the source to the floor of the laboratory and monitoring the cyclic pressure response of the pneumatic spring at resonant conditions. Figure 3 shows results of tests at gas pressures of 200 psi and 500 psi. Resonant frequencies for these pressures were 68 Hz and 115 Hz, respectively. Values of Q from a half-power calculation were found to be 7 and 13 for these conditions. Transducer output is proportional to the force output of the device.

In addition to assembly and testing, analysis was also carried out for conceptual design of a control system for the source. This design is based on using the drive current as the resonance indicator in a phase-locked loop system. When the coil is vibrating in a resonant mode, the drive current is at a minimum and the phase is also zero, increasing or decreasing monotonically on either side of resonance. Hence the control system would change the pneumatic spring pressure or volume to keep the phase "locked" at zero as the frequency of the vibrating motion changes.

TORSIONAL SHEAR-WAVE SOURCE

Two conceptual designs have been considered for the torsional (*SH*) wave source: (1) a system based on rotating eccentric masses, and (2) an electromagnetically actuated system. Preliminary engineering studies were completed for the rotating-mass systems. Figure 4 is a schematic cross section illustrating the principal components of the device. Torsional forces are produced by rotating eccentric masses. The masses are attached to two shafts, as illustrated in the figure. The shafts rotate in the same angular direction so that a force couple is produced when the masses are located 180° apart in the plane of rotation. Resulting torque is transmitted through the source housing to the rock as shear motion in the horizontal plane. Variable frequency response is achieved by controlling the speed of the motor driving the shafts. Vibratory motion in the range of 50–400 Hz is provided by a high-speed motor capable of speeds of 24,000 rpm. Because a rotating body of constant mass would generate inadequate torque at low frequencies and excessive torque at high frequencies, it was necessary to design a system that would permit variation of the mass of

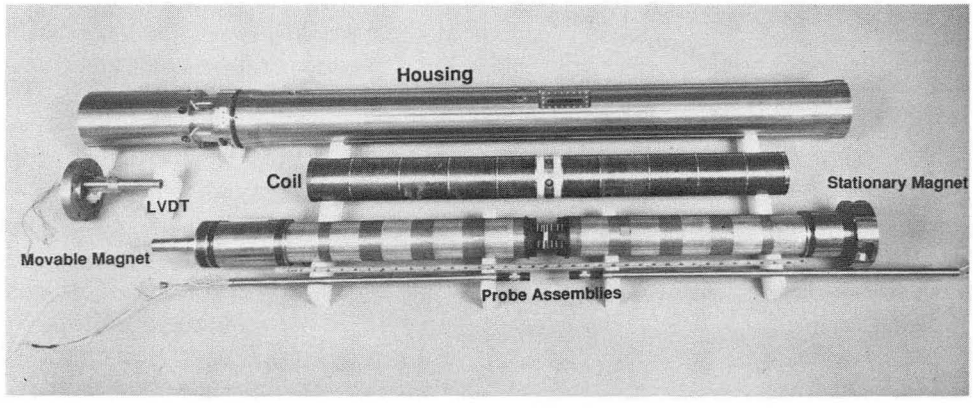

Figure 2. Principal components of *SV* source. [CBB 870-10700A]

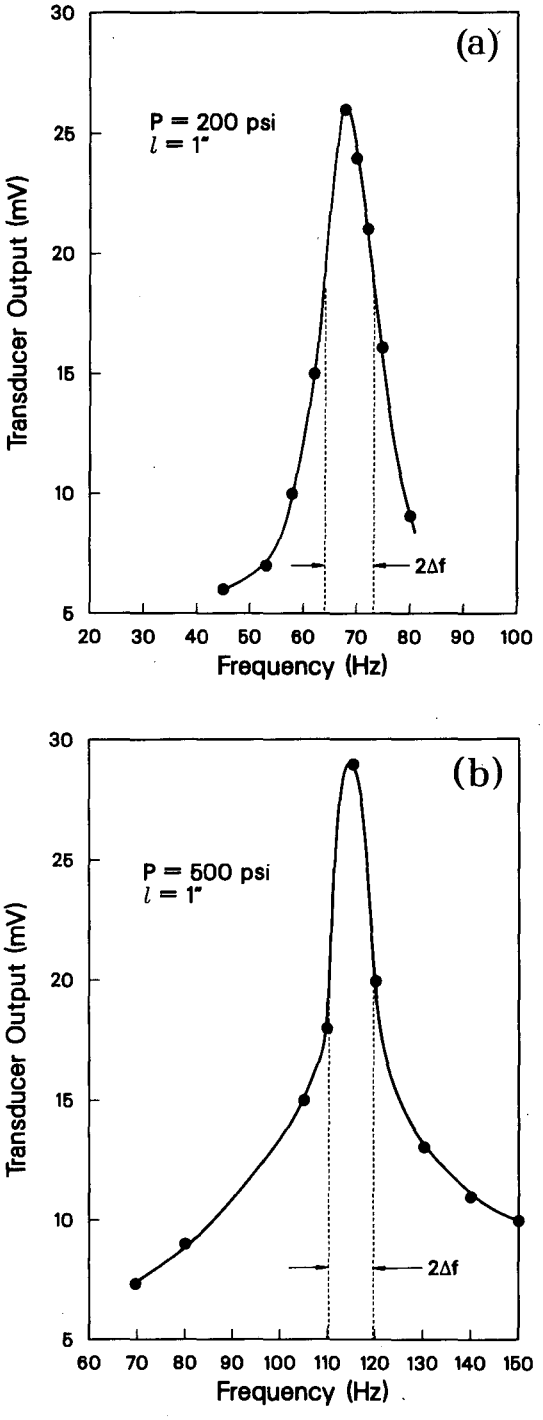

Figure 3. Results of bench tests showing resonant behavior of the *SV* source at gas pressures of **(a)** 200 psi, and **(b)** 500 psi. Gas volume is constant in each test, as indicated by l = 1″. [Part a, XCG 883-6570; part b, XCG 883-6571]

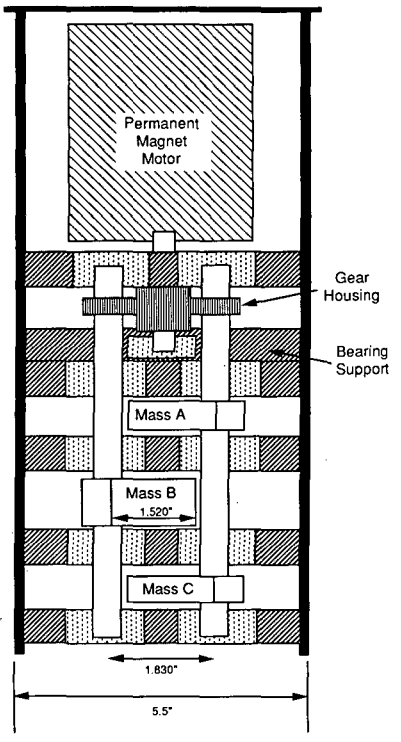

Figure 4. Schematic cross section of rotating eccentric mass system for *SH* source. [XCG 891-4619]

rotating bodies. The mass of these bodies will be varied by injection or withdrawal of mercury. Preliminary engineering specifications were completed for the principal components, including motors, gearing, bearings, and configuration of the rotating masses. The calculated torque output of the device is a minimum of about 1000 ft-lb at 50 Hz. Higher torques can be achieved at higher frequencies, depending on the volume of mercury in the rotating masses.

The second conceptual design configuration, using an electromagnetic actuator, is currently being evaluated. The principal of operation is similar in concept to that of the *SV* source. The magnet-coil configuration would be altered so that an imposed alternating current would result in torsional motion of the coil instead of vertical motion. The piston in this case would be mounted in the plane containing the long axes of the device. It would sweep through an angular displacement, compressing gas in a confined volume. Resonant motion would be achieved by adjusting the volume and pressure of the gas.

Diffraction and Diffusion Tomography: A Comparative Study

A. Tura and Q. Zhou

With the advancement of medical tomography (e.g., Mersereau and Oppenheim, 1974; Huesman et al., 1977; Slaney and Kak, 1985), applications of these techniques to geophysical inverse problems, including seismic-ray tomography, diffraction tomography in an acoustic medium, and electromagnetic ray tomography in a resistive background medium, have followed. Ray tomography in both seismic (e.g., Bois et al., 1972; Peterson, 1986) and electromagnetic (e.g., Dines and Lytle, 1979) exploration have been studied widely. Diffraction tomography for subsurface seismic applications has been discussed by Devaney (1984) and Wu and Toksöz (1987), whereas diffusion tomography for the low-frequency electromagnetic case is currently being developed by Zhou and Morrison (1988). Diffraction tomography (acoustic case) and diffusion tomography (audio-frequency electromagnetic case) differ from ray tomography in that they use the full wave field rather than the high-frequency approximation to the wave field; we will therefore refer to this class of methods as full-wave-field tomography. Although each class of methods has distinct advantages, they will not be compared here. We will instead concentrate on the characteristics of diffraction and diffusion tomography.

The reconstructed images of velocity (diffraction case) and conductivity (diffusion case) provide information additional to that obtained with other techniques for subsurface formation evaluation. Potential applications of these methods include the evaluation of petroleum or geothermal reservoirs and fracture-zone characterizations of nuclear and other waste repositories.

THEORY

To demonstrate the basic principles of full-wave-field tomography, a simple two-dimensional case is considered. The background medium is assumed to be a homogeneous medium with two-dimensional velocity inhomogeneities (diffraction case) or conductivity inhomogeneities (diffusion case) embedded in it (Fig. 1). An acoustic (pressure) line-source or an electrical (current) line-source along the strike (this source would be perpendicular to the page in Fig. 1) is harmonic in time and is operated at a fixed audio frequency. Under these conditions the acoustic field satisfies the scalar wave equation and the electric field satisfies the scalar diffusion equation. A relation between the secondary acoustic or electric field and the velocity or conductivity anomaly to be imaged can be deduced from the integral formulation

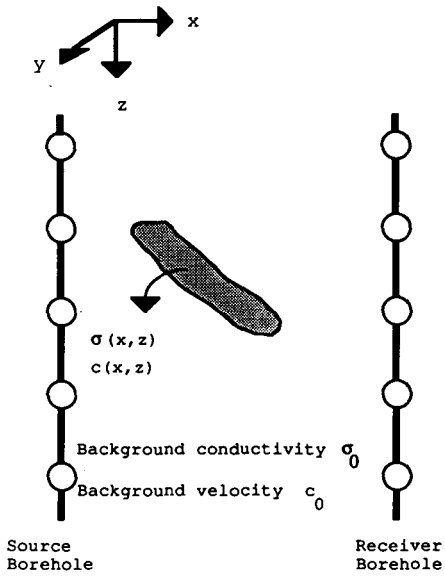

Figure 1. The geometry of cross-hole measurements. [XBL 894-1433]

$$U^s(\mathbf{r}_r,\mathbf{r}_s) = -\int k_0^2\, O(\mathbf{r})\, U(\mathbf{r},\mathbf{r}_s)\, G(\mathbf{r}_r,\mathbf{r})\, dxdz, \quad (1)$$

where $U^s(\mathbf{r}_r,\mathbf{r}_s)$ is the secondary acoustic or electric field at $\mathbf{r}_r$, $U(\mathbf{r},\mathbf{r}_s)$ is the total acoustic or electric field at r, both due to a source at $\mathbf{r}_s$. $G(\mathbf{r}_r,\mathbf{r})$ is the two-dimensional (2-D) Green's function. The object function $O(\mathbf{r})$ is defined as $1 - k^2(\mathbf{r})/k_0^2$. Here, $k(\mathbf{r}) = \omega/c(\mathbf{r})$ and $k_0 = \omega/c_0$ in the acoustic case, and $k^2(\mathbf{r}) = -i\omega\mu\sigma(\mathbf{r})$ and $k_0^2 = -i\omega\mu\sigma_0$ in the electrical case, with ω denoting angular frequency, $c(\mathbf{r})$ velocity, $\sigma(\mathbf{r})$ conductivity, and μ magnetic permeability; c_0 is the background velocity, σ_0 is the background conductivity, and k_0 is the background wave number, used as reference.

In order to simplify this nonlinear equation, a weak-scattering Born approximation,

$$U(\mathbf{r},\mathbf{r}_s) = G(\mathbf{r},\mathbf{r}_s),$$

is employed to linearize Eq. (1):

$$U^s(\mathbf{r}_r,\mathbf{r}_s) = -\int k_0^2\, O(\mathbf{r})\, G(\mathbf{r},\mathbf{r}_s)\, G(\mathbf{r}_r,\mathbf{r})\, dxdz. \quad (2)$$

If one takes Fourier transforms along the source and receiver lines for the geometry shown in Fig. 1, Eq. (2) becomes

$$V^s(k_r,k_s) = \int O(\mathbf{r}) \times \exp[-i(\gamma_s - \gamma_r)x - i(k_s + k_r)z]\,dxdz, \quad (3)$$

where V^s represents the filtered secondary responses in the wave-number domain, k_s and k_r are the wave numbers along source and receiver lines, and

$$\gamma_s^2 = k_0^2 - k_s^2, \qquad \gamma_r^2 = k_0^2 - k_r^2. \quad (4)$$

Although the seismic case is based on the use of real wave number k_0^2, the electromagnetic problem requires their complex equivalent. Note that in the seismic application, γ_s and γ_r are real numbers as long as k_0 is real and k_s and k_r are smaller than k_0. If one lets

$$\gamma_s - \gamma_r = k_x, \qquad k_s + k_r = k_z, \quad (5a)$$

then Eq. (3) states that the object function $O(\mathbf{r})$ can be derived by performing a double inverse Fourier transform on both sides of Eq. (3).

For the electromagnetic field in a conductive medium, k_s and k_r are still real but k_0 is complex. Therefore, the following substitutions are found to be proper:

$$k_s + k_r = k_z, \qquad i(\gamma_s - \gamma_r) = s_x. \quad (5b)$$

Equation (3) now becomes

$$V^s(k_r,k_s) = \int O(\mathbf{r}) \exp[-s_x x - ik_z z]\,dxdz, \quad (6)$$

which means that one can get $O(\mathbf{r})$ by doing an inverse Fourier transform in z and an inverse Laplace transform in x for this cross-hole electromagnetic problem.

INVERSION

Obtaining the object function is the solution of the inverse problem and is our ultimate aim. It is also important to notice that the model medium constructed for this theory may not be the actual medium that we want to image. In such cases research is needed concerning the extent and reduction of the errors produced by representing the actual medium with the model medium. For example, attenuation of the medium has not been included in the seismic case, and the Born approximation utilized could be inappropriate for a medium with high contrast in physical parameters.

Wave-number Domain Coverage and Resolution

The inverse Laplace and inverse Fourier transform representations of the object function provide the convenience of studying the system coverage. The wave-number-domain coverage of the source-receiver configuration shown in Fig. 1 is presented in Fig. 2, based on examination of Eqs. (5a) and (5b). In Fig. 2 the vertical axis is the Fourier domain wave number k_z. In Fig. 2a the horizontal axis is the Fourier domain wave number k_x; in Fig. 2b,c the horizontal axis is either the real or the imaginary part of the Laplace domain wave number s_x. Figure 2b represents the attenuation of electromagnetic waves. The seismic case has only a real component because the seismic model does not include attenuation, which in reality is quite small, especially when compared with the electromagnetic case.

If every point in this wave-number domain were known, the transform of the object function could be determined exactly and the inversion would yield the unique object function. However, this is not possible for several reasons. The first reason is that the sources and receivers are discrete in the transform direction (in the z direction in Fig. 1). Therefore, we have discrete samples of the object function in its transform domain. The second and more-important reason is that the maximum coverage we can obtain is determined by a circle of radius $2k_0$ (Fig. 2a, broken line) in the seismic problem. This means that as the frequency at which the data are collected increases, the inversion will become sharper because it will contain higher wave numbers of the object function's transform. In the electromagnetic problem, although the circle radius is not totally determined by the background wave number, the high attenuation corresponding to the high wave number limits the resolution. On the other hand, the choice of frequency is constrained by spatial aliasing considerations and by the high-frequency nature of the noise spectrum. This suggests that inversions at different frequencies can be done and then averaged in order to increase coverage in the transform domain.

The full circle we have mentioned above can be obtained only if we have sources and receivers all around the object to be imaged. This is usually not the case in geophysical applications, where we are constrained to boreholes or the free surface. Cover-

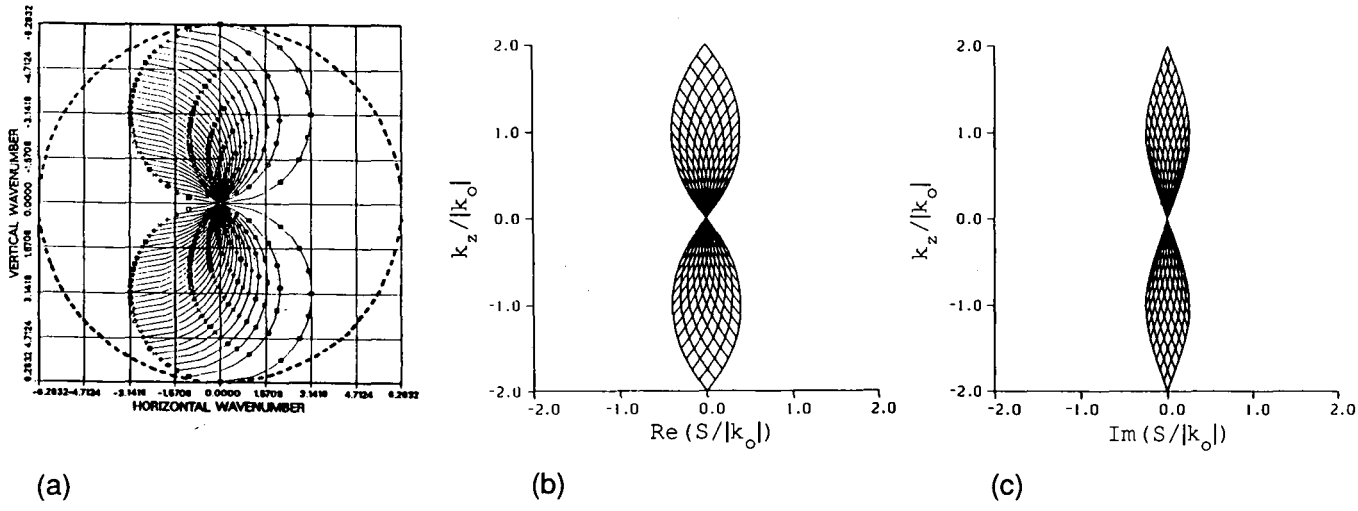

Figure 2. Wave-number domain coverage of the cross-hole configuration. **(a)** Seismic case. **(b)** Electromagnetic case, real part. **(c)** Electromagnetic case, imaginary part. [XBL 894-1434]

age for the cross-hole case is shown in Fig. 2 (continuous line). This figure suggests that in both the seismic and electromagnetic cases, poor resolution in the lateral x direction is expected for the cross-hole configuration. One important thing to point out from Fig. 2 is that, for the same geometry, the coverage of the object function in the transform domain is less in the electromagnetic case due to attenuation effects. This leads us to conclude that electromagnetic inversion produces poorer images than seismic inversion. The coverages of source-receiver configurations other than cross-hole can also be studied in the same fashion.

Inversion Algorithm and Examples

For the acoustic case the method outlined in the previous section can be carried out exactly as formulated. The inversion is done by backpropagating the recorded waves into their correct locations (Devaney, 1984; Wu and Toksöz, 1987). For the electrical case, although Eq. (6) provides a way of solving for the object function, the numerical inverse Laplace transform is extremely unstable. Because of the strong effects of attenuation in the electrical case, precautions have been taken to ensure that a stable solution is obtained for the conductivity structure. Here, the integral in Eq. (6) is discretized over the area between the boreholes. This results in a linear system of equations that relate the electrical conductivity anomaly, or the object function, to the measured secondary field. This linear system of equations is similar in concept to that used in ray tomography except that now a full matrix is required to describe the process. To solve such equations, conventional methods (such as the ART algorithm in Huesman et al., 1977) do not work well because the matrix equation is also quite unstable. Thus a constrained least-squares method (Lawson and Hanson, 1974) is introduced to ensure stability. In other words, one considers only the case with conductivity anomaly greater than the reference background or only the case with conductivity anomaly smaller than the background.

Figure 3 (seismic case) and Fig. 4 (electromagnetic case) show a numerical example in which the output data are obtained by a two-dimensional program that generates the exact synthetic response of the models. These models represent a fracture zone in a 2-D medium. In the seismic case (Fig. 3), the inversion is done at 25 frequencies ranging from 2440 to 5490 Hz with 122-Hz intervals, and the results are averaged. The background velocity is 5500 m/s, and the inhomogeneity is 4500 m/s; 40 sources and 40 receivers are used with 0.5-m separation. The area between the boreholes is discretized into 20 × 40 pixels. In the electromagnetic case (Fig. 4), the operating frequency is 5000 Hz, background conductivity is 0.01/ohm-m, and the conductor has a conductivity-thickness product of 0.1 S; 32 sources and 32 receivers are used with equal separation. The area between the boreholes is discretized into 10 × 16 pixels. As shown in the figures, both tomographic methods provide a fairly good estimation of the velocity and conductivity distributions.

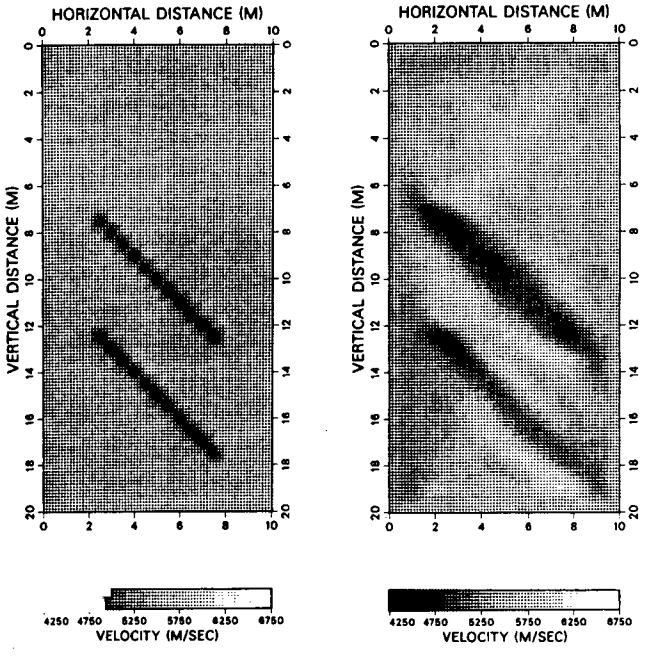

Figure 3. Fracture model and tomographic image; cross-hole 2-D seismic example. [XBL 894-1435]

CONCLUSIONS

A comparative study of diffraction and diffusion tomography has been carried out. Diffraction tomography cannot be applied directly to the electromagnetic case because of the attenuating nature of the electromagnetic field in a conductive medium. A similar approach to diffraction tomography is developed, but it deals with diffusion phenomena, which has a complex background wave number instead of a real one. Thus the problem has to be studied in the Laplace transform domain rather than the Fourier transform domain. For the seismic case this is usually not necessary because the seismic attenuation is quite small. Because attenuation is high, the coverage in the wave number domain in the electromagnetic case is less than in the seismic case, which should produce a smeared image of the conductivity. Using the constrained least-squares reconstruction not only provides the necessary stability but also gives a higher resolution image than expected. In return, the backpropagation algorithm for diffraction tomography is computationally efficient and easy to implement.

REFERENCES

Bois, P., LaPorte, M., Lavergne, M., and Thoms, G., 1972. Well to well seismic measurements. Geophysics, v. 37, p. 471–480.

Devaney, A.J., 1984. Geophysical diffraction tomography. IEEE Trans. Geosci. Remote Sensing, v. GE-22, no. 1, p. 3–13.

Dines, K.A., and Lytle, R.J., 1979. Computerized geophysical tomography. Proc. IEEE, v. 67, no. 7, p. 1065–1073.

Huesman, R.H., Gullberg, G.T., Greenberg, W.L., and Budinger, T.F., 1977. Users manual: Donner algorithms for reconstruction tomogra-

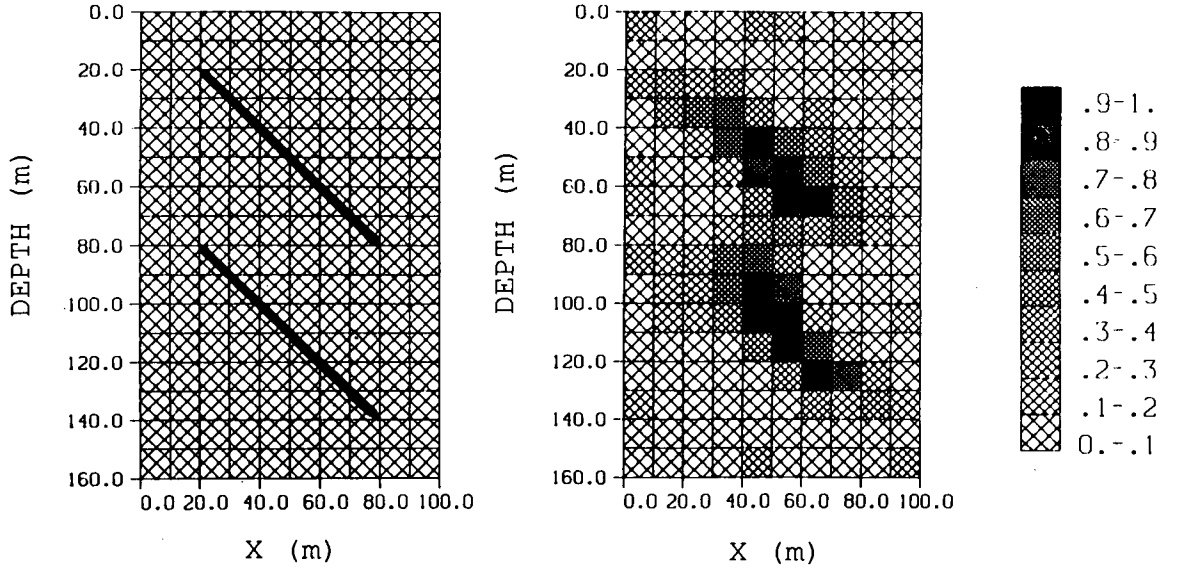

Figure 4. Fracture model and tomographic image; cross-hole 2-D electromagnetic example. [XBL 894-1436]

phy. Lawrence Berkeley Laboratory Report PUB-214, 285 p.
Lawson, C.L., and Hanson, R. J., 1974. Solving least squares problems. Prentice-Hall, Englewood Cliffs, N.J., Chapter 23.
Mersereau, R.M., and Oppenheim, A., 1974. Digital reconstruction of multidimensional signals from their projections. Proc. IEEE, v. 62, no. 10, p. 1319–1338.
Peterson, J.E., Jr., 1986. The application of algebraic reconstruction techniques to geophysical problems (Ph.D. Thesis). University of California, 188 p.
Slaney, M., and Kak, A.C., 1985. Imaging with diffraction tomography. Purdue University, School of Electrical Engineering, Report TR-EE 85-5, 211 p.
Wu, R., and Toksöz, M.N., 1987. Diffraction tomography and multisource holography applied to seismic imaging. Geophysics, v. 52, no. 1, p. 11–25.
Zhou, Q., and Morrison, F., 1988. Cross borehole audio frequency electromagnetic tomography. Presented at the Ninth Workshop on Electromagnetic Induction in the Earth and Moon, USSR, October 24–31, 1988.

A New Approach to Interpreting Electromagnetic-Sounding Data

K.H. Lee

Electomagnetic (EM) methods in geophysics have been used for many years to determine the electrical-conductivity distribution in the ground. The major application has been in the search for mineral deposits, with lesser applications in groundwater, petroleum exploration, and crustal studies. In most of these applications the depth of interest requires low frequencies, usually below 30 kHz, and for typical earth conductivities the conduction current is orders of magnitude greater than the displacement currents. The resulting partial differential equation describing the behavior of the fields is in fact a diffusion equation, whose solution is quite different from that of the more-familiar wave equation encountered in seismic-wave propagation or radar. The concepts of pulse or wavelet propagation, pulse travel time, and the construction of reflectivity images of subsurface structure are not possible for solutions that do not allow the definition of group velocity. The difficulty of depicting the solutions for the diffusion equation in all but simple, elementary situations is one very practical reason for the slow acceptance of EM conductivity mapping in new applications.

Several studies in the past have implied an interesting parallelism between the mathematical form for the EM diffusion equation and the seismic-wave equation (Kunetz, 1972; Weidelt, 1972; and Levy et al., 1988). The subject of these studies has been essentially limited to the magnetotelluric (MT) problems in a layered (1-D) medium. For practical situations, typically involving a multidimensional space and an arbitrary source, Lee et al. (1988) have presented a more-fundamental relationship between fields satisfying a diffusion and the corresponding wave equations. The relationship is defined by an integral transform that is completely independent of space variables. In this relationship the diffusive field—the electric field **E**, for example—is uniquely represented by an integral of a corresponding wave field **U** weighted by an exponentially damped kernel. This fictitious field **U** would be dispersionless and would have a well-defined phase, as well as group, velocity.

It has been demonstrated (Lee et al., 1988) that the transform technique can be used for modeling EM fields. In this application the wave field is first computed numerically, and then the EM field is calculated using the integral. It is also shown later in this article that an inverse transform could be used to transform field data measured in time (or in frequency) to the wave field in a time-like variable q. The inverse transform requires that the data be of wide band to yield waveforms of a reasonable resolution. The other important factor that determines the resolution of the constructed wave field is the level of estimated noise contained in the data. For stability reasons a stochastic approach has been used to construct the wave field. This constructed wave field can then be used for further analysis in conductivity mapping using migration techniques or even the more-sophisticated wave-equation imaging or tomographic-reconstruction techniques.

THEORY

To begin, let us write Maxwell's equations in the presence of a current source, $\mathbf{J}^s$,

$$\nabla \times \mathbf{E}(\mathbf{r},t) = -\mu\frac{\partial}{\partial t}\mathbf{H}(\mathbf{r},t), \tag{1}$$

$$\nabla \times \mathbf{H}(\mathbf{r},t) = \sigma(\mathbf{r})\mathbf{E}(\mathbf{r},t) + \epsilon(\mathbf{r})\frac{\partial}{\partial t}\mathbf{E}(\mathbf{r},t) + \mathbf{J}^s(\mathbf{r},t). \tag{2}$$

At low frequencies the displacement current may be neglected, resulting in the following second-order differential equation for the electric field:

$$\nabla \times \nabla \times \mathbf{E}(\mathbf{r},t) + \mu\sigma(\mathbf{r})\frac{\partial}{\partial t}\mathbf{E}(\mathbf{r},t) = \mathbf{S}(\mathbf{r},t), \tag{3}$$

where the source term, $\mathbf{S}(\mathbf{r},t)$, is given by

$$\mathbf{S}(\mathbf{r},t) = -\mu\frac{\partial}{\partial t}\mathbf{J}^s(\mathbf{r},t).$$

Introducing the functions $\mathbf{U}(\mathbf{r},q)$ and $\mathbf{F}(\mathbf{r},q)$, such that

$$\nabla \times \nabla \times \mathbf{U}(\mathbf{r},q) + \mu\sigma(\mathbf{r})\frac{\partial^2}{\partial q^2}\mathbf{U}(\mathbf{r},q) = \mathbf{F}(\mathbf{r},q), \tag{4}$$

Lee et al. (1989) have shown that the diffusive electric field $\mathbf{E}$ in Eq. (3) and the wave field $\mathbf{U}$ in Eq. (4) are uniquely related by

$$\mathbf{E}(t) = \frac{1}{2\sqrt{\pi t^3}}\int_0^\infty \exp(-q^2/4t)q\mathbf{U}(q)dq \tag{5}$$

As a necessary condition the same relationship should hold between the source terms $\mathbf{S}$ and $\mathbf{F}$. The wave equation (4) implies that each component of the wave field $\mathbf{U}$ would have a velocity of $(\mu\sigma)^{-1/2}$ m/q. Throughout the study the magnetic permeability is assumed to be equal to that of the free space. The position vector r has been dropped from the expression, since the transformation is independent of it.

The integral transform can be used for numerical modeling of EM fields. In this application we first obtain the wave field $\mathbf{U}(q)$ numerically for a corresponding source $\mathbf{F}(q)$. The next step is straightforward, using the integral given by Eq. (5). This numerical modeling scheme is particularly attractive, not only because many efficient wave-equation algorithms are readily available, but because it is easy to implement these algorithms on modern computers, especially on those with parallel-processing capabilities.

Perhaps the other, more-important application of this integral transform can be found in the construction of the fictitious wave field $\mathbf{U}(q)$ from the field data $\mathbf{E}(t)$. This process is essentially an inverse problem. An algorithm for the closed-form solution to this problem is described below. We first Fourier transform (from t to ω) both sides of Eq. (5) to yield

$$\tilde{\mathbf{E}}(\omega) = \int_0^\infty \exp[-(i\omega)^{-1/2}q]\,\mathbf{U}(q)\,dq. \tag{6}$$

If we take only the imaginary part, this equation becomes

$$\mathrm{Im}\{\tilde{\mathbf{E}}(\omega)\} = -\int_0^\infty \exp[-(\omega/2)^{1/2}\,q] \times \sin[(\omega/2)^{1/2}q]\,\mathbf{U}(q)\,dq.$$

Applying a change of variables,

$$\omega = 2e^{2u}, \qquad q = e^{-v},$$

and multiplying both sides by e^v, we finally obtain

$$\mathbf{D}(u) = -\int_{-\infty}^{\infty} H(u-v)\mathbf{W}(v)dv, \tag{7}$$

where

$$\mathbf{D}(u) = e^u\,\mathrm{Im}\{\tilde{\mathbf{E}}(2e^{2u})\},$$

$$H(u) = \exp(-e^u)\sin(e^u)e^u,$$

and

$$\mathbf{W}(v) = \mathbf{U}(e^{-v}).$$

Equation (7) is a convolution integral, for which the solution for $\mathbf{W}$ can be formally written as

$$\mathbf{W}(v) = -\frac{1}{2\pi}\int_{-\infty}^{\infty}\frac{\tilde{\mathbf{D}}(\eta)}{\tilde{H}(\eta)}e^{i\eta v}d\eta, \tag{8}$$

where $\tilde{\mathbf{D}}(\eta)$ and $\tilde{H}(\eta)$ are Fourier transforms (from u to η) of functions $\mathbf{D}(u)$ and $H(u)$, respectively.

The formal solution given by Eq. (8) has been presented by Lee (1987), but it is numerically unstable when applied to real field data. Because the deconvolution kernel $\tilde{H}(\eta)$ is exponentially damped in η, the distributed noise spectrum contained in the data $\tilde{\mathbf{D}}(\eta)$ will be amplified. This is to be expected, since the original linear inverse problem for the wave field $\mathbf{U}$ in Eq. (5) is ill-posed. A practically useful

solution would involve a stochastic approach to the given problem (Franklin, 1970; Aki and Richards, 1980). The approach requires that the original convolution integral be modified to

$$\mathbf{D}^*(u) = -\int_{-\infty}^{\infty} H(u - v)\mathbf{W}^*(v)dv + \mathbf{N}(u). \quad (9)$$

The additional term $\mathbf{N}(u)$ is an estimated noise. If the noise is statistically unrelated to the model (wave field), the solution for the modified equation is simply

$$\mathbf{W}^*(v) = -\frac{1}{2\pi}\int_{-\infty}^{\infty} \tilde{G}(\eta)\frac{\tilde{\mathbf{D}}^*(\eta)}{\tilde{H}(\eta)}e^{i\eta v}d\eta, \quad (10)$$

with its optimum inverse filter $\tilde{G}(\eta)$ given by

$$\tilde{G}(\eta) = \frac{|\tilde{H}(\eta)|^2}{\frac{\sigma_N(\eta)}{\sigma_W(\eta)} + |\tilde{H}(\eta)|^2}. \quad (11)$$

Here $\sigma_N(\eta)$ and $\sigma_W(\eta)$ are the estimated power spectra of noise and signal, respectively. When there is no noise, Eq. (10) becomes identical to Eq. (8). But with noise, the deconvolution integral becomes a low-pass operation. The inverse filter renders the deconvolution integral stable by effectively cutting off those harmonic contributions from below the specified noise level. This feature is in fact similar to that of the generalized inverse scheme, in which contributions associated with those eigenvalues below a threshold are selectively eliminated at the expense of reduced resolutions. The impulse response of $G(v)$ can therefore be considered as the upper limit of the resolution for the constructed wave field. Figure 1 shows the impulse response in $\log(q)$ for different levels of percent noise. As is expected, the higher the noise level, the lower the resolution. In the constructed wave fields shown here, we also notice that the wave form is preserved not in q but in $\log(q)$. This phenomenon is rather physical in origin and puts the limit in resolution for those waves at late q. The reason for this is that the impulse response of the inverse filter is symmetric across the origin in $\log(q)$—a consequence of the required change of variables and subsequent contractions in space and time dimensions. The limited resolution at late q also means that as we seek deeper targets, the resolution will get progressively poorer. This fact is consistent with what we can expect from the analysis of the original diffusive EM fields.

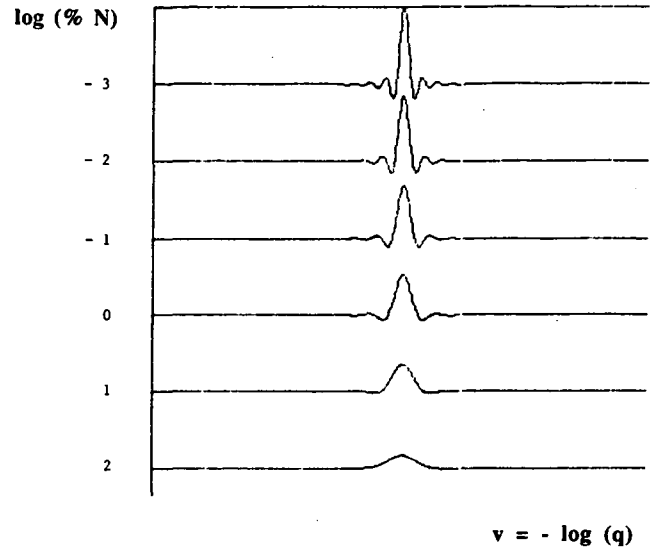

Figure 1. Impulse response of the filter function $G(v)$ for different noise levels $N(v)$ expressed in log of percent noise. [XBL 894-1355]

NUMERICAL EXAMPLE

A numerical test for the construction of wave fields has been made using the model shown in Fig. 2. The model consists of a circular cylinder in a whole space of conductivity 0.01 S/m. The cylinder is a 0.5-S/m conductor with a radius of 100 m. A line source is located at 200 m to the left of the center of the cylinder, and the voltage induced in a vertical coil is computed at positions along the receiving borehole 200 m to the right of the center of the cylinder. The computed frequency-domain voltage corresponds to the line source whose current has been abruptly turned off. A wide-band frequency response (more than 4 decades) has been used to construct wave fields in the receiving borehole. The numerically constructed wave fields are shown in Fig. 3 at every 20-m intervals. An inverse filter with an estimated noise level of 1% has been used for this exercise. By inspection one can now visualize the propagation of the wave field from the source to each receiver position. For example, at the first receiver position opposite the source, the first arrival seems to be made up of waves that propagate around the cylinder with the higher velocity of the surrounding medium. After a pronounced delay, the direct wave transmitted through the conductor arrives at this position with its amplitude much larger than that of the first arrival. As the receiver is moved down the borehole, the effect of diffraction by the cylinder gradually disappears, and the higher-velocity

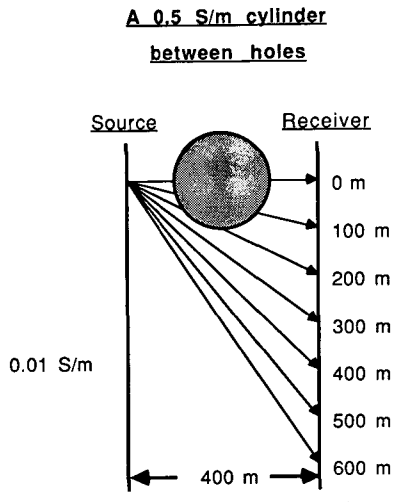

Figure 2. A cross-well configuration in a uniform whole space of 0.01 S/m. The transmitting and receiving boreholes are separated by 400 m. A conductive cylinder (0.5 S/m) of radius 100 m is located at the center between boreholes. [XBL 894-1356]

direct wave begins to dominate. The other commonly used configuration involves a moving source and a receiver right at the source position (zero offset). The field is usually measured after the current is turned off, so that the measurement would consist entirely of back-scattered field in this case. The constructed wave field simulated for the zero-offset configuration is shown in Fig. 4. The single hole is located 200 m to the left of the center of the cylinder. Strong reflections can be observed when

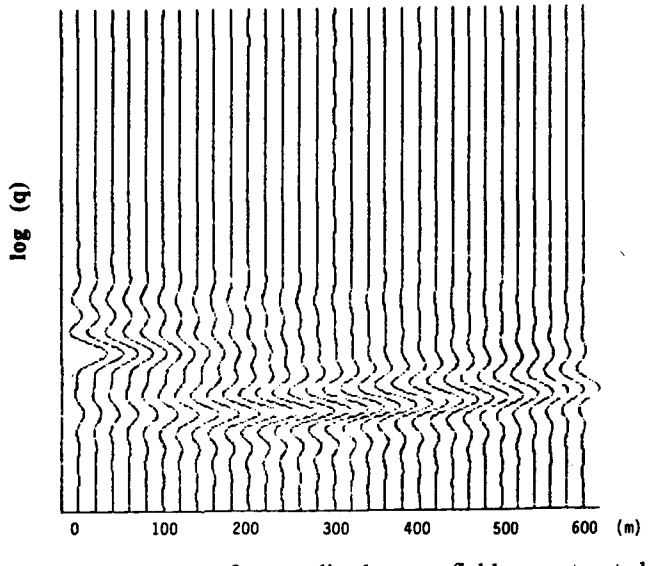

Figure 3. Traces of normalized wave fields constructed from voltages measured in the receiving borehole across the cylinder. The source is fixed. [XBL 894-1357]

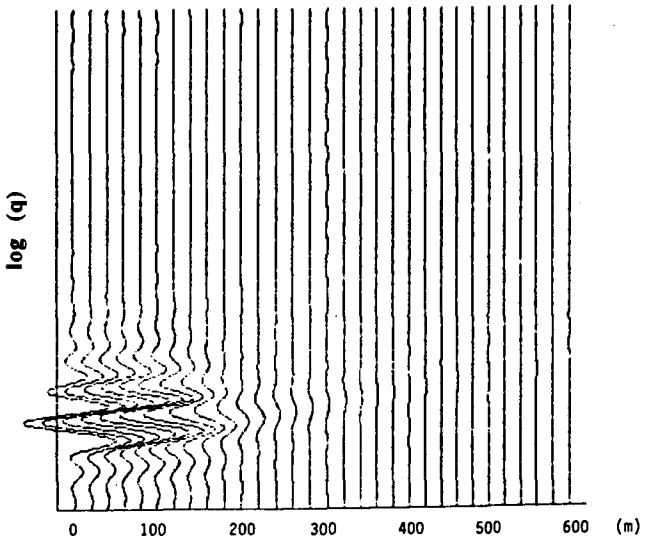

Figure 4. Traces of normalized wave fields constructed from voltages measured in a single hole. The measurement is made at the source (zero offset), and this source-receiver pair is moved down at the same time. [XBL 894-1358]

the source-receiver pair is near the cylinder. The amplitude of the reflected wave decreases very fast because both the source and the receiver are moved down the borehole at the same time.

REFERENCES

Aki, K., and Richards, P.G., 1980. Quantitative Seismology: Theory and Methods (Vol. II, p. 695). W.H. Freeman and Company, San Francisco.

Franklin, J.N., 1970. Well-posed stochastic extension of ill-posed linear problems. J. Math. Anal. Appl., v. 31, p. 682–716.

Kunetz, G., 1972. Processing and interpretation of magnetotelluric soundings. Geophysics, v. 37, p. 1005–1021.

Lee, K.H., 1987. A new approach to modeling and interpreting electromagnetic sounding data. Lawrence Berkeley Laboratory Report LBL-23544.

Lee, K.H., Guimin, L., and Morrison, H.F., 1989. A new approach to modeling the electromagnetic response of conductive media. Geophysics, in press.

Levy, S., Oldenburg, D., and Wang, J., 1988. Subsurface imaging using magnetotelluric data. Geophysics, v. 53, p. 104–117.

Weidelt, P., 1972. The inverse problem of geomagnetic induction. Zeit. Geophys., v. 38, p. 257–298.

Subsurface Electromagnetic Responses of Multiple Thin Conductors

Q. Zhou, A. Becker, and N.E. Goldstein

As a continuation of the investigation into the electromagnetic (EM) response of a single thin conductor (Zhou et al., 1987), the EM response of multiple thin conductors embedded in a conductive host rock was studied by means of a similar-integral-equation approach. This more realistic model can be used to simulate the cross-hole EM effects due to water-filled fracture zones or vein-type mineral deposits missed by drilling.

By examining the calculated electromagnetic responses for a variety of source-receiver arrangements, we can evaluate and compare their response characteristics. The results from these experiments provide the basis for designing field experiments to obtain enough information for data-interpretation purposes.

Current research in geothermal energy development, enhanced oil recovery, and waste repository evaluation has greatly increased the level of interest in new techniques capable of mapping hydraulically important fracture zones at depth. These major conduits may also be electrically conductive and therefore resolvable by means of electromagnetic surveys. Although there are a number of general three-dimensional numerical modeling programs available for studying this problem (Lee et al., 1981; Xiong et al., 1986, to name a few), they are usually not economical because of the enormous computing time involved. In addition, most of those programs can only deal with a single conductor and one source and one receiver at the surface.

Tabular conductors, such as fracture zones or vein-type mineral deposits, may be tens of meters in length. They are generally thin, sheet-like, with thickness-conductivity products ranging from a fraction of a siemen to several hundred siemens. The host rock usually has a resistivity of a hundred ohm-meters or more. As a way of reducing computer time, we use a thin-sheet approximation in which the target is described by its conductivity-thickness product (Weidelt, 1981).

THE MATHEMATICAL FORMULATION AND NUMERICAL CALCULATION

The Thin-Conductor Model

Simplified models that represent the geologic situation are used for numerical calculation (Fig. 1). The conductors are represented by rectangular thin-sheet targets (two in this illustrative model). They are assumed to be thin, so that only their conductances (i.e., the thickness-conductivity products) are important. This simplification is justified if the electric field on the thin-sheet conductor varies slightly across its full thickness. The conductors, with different strike (γ) and dip (β) angles, are located in a space of conductivity σ. The displacement current is neglected, and the magnetic permeability, μ_0, is assumed to have the free-space value. The boreholes are considered to be vertical, but their effects are not accounted for in the calculations.

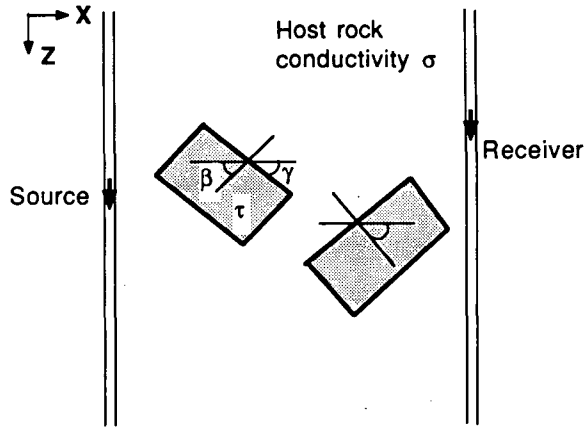

Figure 1. Schematic of cross-hole EM study. One or more nonintersecting planar conductive fracture zones lie between source and receiver holes. [XBL 894-1437]

The Integral Equations

Our approach for calculating the frequency-domain magnetic-field response is similar to the algorithm developed by Weidelt (1981), who calculated the magnetic field anomaly due to a thin conductor with magnetic dipole source and receiver on or above the ground. For a time-harmonic source ($e^{i\omega t}$), the tangential electric fields on the ith thin conductor satisfies the integral equation

$$\mathbf{E}_{si}(\mathbf{r}_0) = \mathbf{E}_{nsi}(\mathbf{r}_0) - i\omega\mu_0 \sum_{j=1}^{ns} \int_{s_j} \tau_j(\mathbf{r})\, \mathbf{g}_{sji}(\mathbf{r}_0/\mathbf{r}) \cdot \mathbf{E}_{sj}(\mathbf{r})\, ds \ , \tag{1}$$

where $\mathbf{g}_{sji}$ is the Green's dyadic function relating the electric field on the ith and jth thin conductors, $\mathbf{E}_s$ is the tangential electric field on the target, and $\mathbf{E}_{ns}$

is the incident tangential electric field on it. The conductance $\tau(\mathbf{r})$ is the conductivity-thickness product, which is assumed to be constant for each conductor. Similarly, the magnetic field at any point in the space is given by

$$\mathbf{H}(\mathbf{r}) = \mathbf{H}_n(\mathbf{r}) + \sum_{j=1}^{ns} \int_{sj} \tau_j(\mathbf{r}_0)\, \mathbf{E}_{sj}(\mathbf{r}_0) \cdot \nabla \times g(\mathbf{r}/\mathbf{r}_0)\, ds_0 \,. \tag{2}$$

Here, $\mathbf{H}$ is the total magnetic field, $\mathbf{H}_n$ is the incident magnetic field at the point of observation, and $g(\mathbf{r}/\mathbf{r}_0)$ is the Green's dyadic function relating the tangential current distribution on the sheet to the electric field everywhere.

Solution of the Integral Equations

Both the incident fields $\mathbf{E}_{ns}$ and $\mathbf{H}_n$ and the Green's dyadic functions g and g_s are related to the dipole fields in a whole space or a layered medium and are easy to evaluate (Johansen and Sorensen, 1979; Weidelt, 1981). After the targets are discretized and $\mathbf{E}_{ns}$ and g_s are calculated, Eq. (1) is then solved for $\mathbf{E}_s$, which is then used in Eq. (2) together with the calculated $\mathbf{H}_n$ and $\nabla \times g$ to obtain $\mathbf{H}$ at the receiver sites.

EXPERIMENTS ON SOURCE-RECEIVER ARRANGEMENTS

We have attempted to determine which source-receiver arrangement is best for resolving the conductors and obtaining the necessary information for data interpretation. In this summary we limit ourselves to the vertical magnetic dipole source and a vertical magnetic field detector. This arrangement is also highly practical for borehole conditions. The basic model consists of one or two thin vertical conductors between two boreholes; the targets are perpendicular to and symmetrical about the plane defined by the boreholes. Each conductor measures 100 m × 100 m and has a conductance of 10 S. The background conductivity is 0.01 S/m. The frequency used is 1 kHz. The boreholes are separated by 150 m. Only the response amplitudes are plotted, although similar analyses can be done using phase information.

In the first cross-hole case the source and receiver move in tandem in separate holes (Fig. 2). The response curve is normalized by the primary vertical magnetic field amplitude at the receiver. We find that the two curves for source-target separations (X_s) of 50 m and 100 m are identical, a result that can be explained by reciprocity. However, the

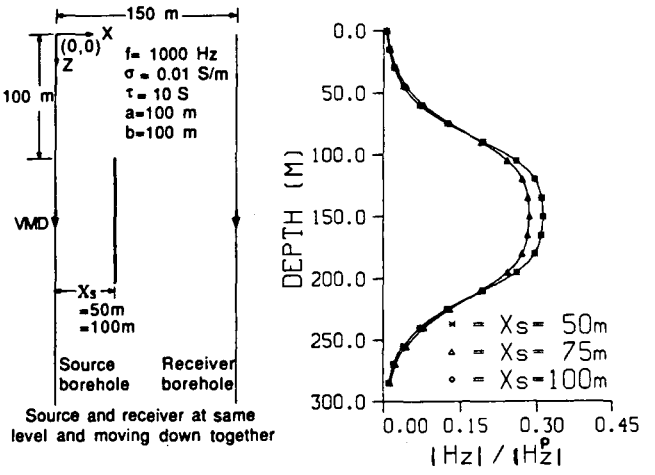

Figure 2. Schematic diagram and numerical results for source (vertical magnetic dipole or VMD) and receiver (a vertical-component magnetic-field detector) moving in tandem in their respective holes past a finite vertical conductor located at distances X_s from the source borehole. The normalized response, $|H_z|/|H_z^p|$, is shown for a 1-kHz signal. [XBL 894-1438]

response remains about the same for other target positions, and thus this source-receiver arrangement is poor for resolving the lateral position of a fracture.

Next we look at the case of a fixed dipole source in one hole and a moving receiver in another borehole (Fig. 3). The primary field amplitude at the source level is chosen as the normalization factor. Although the maximum peak-to-peak amplitudes are

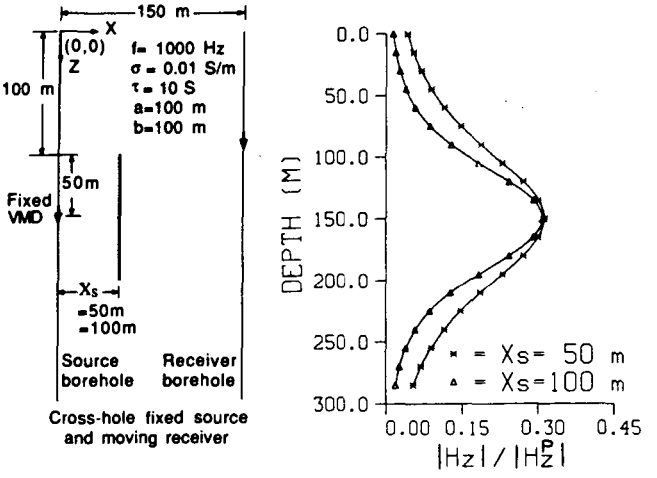

Figure 3. Cross-hole numerical results for conditions similar to those for Fig. 2, except that here the VMD source remains fixed at 150 m and only the receiver moves. [XBL 894-1439]

the same for the source-target separations of 50 and 100 m, the overall curve shapes are different. The broader curve for the 50-m case is due to a shielding effect that occurs when the detector is in the shadow of the target. The example shows that the shape of the response is very important if one inverts the data.

Treating now the case of two parallel and identical thin conductors, we can determine whether the cross-hole measurements still contain the information on target position. For vertical thin conductors separated by 50 m and 30 m, two source-receiver arrangements were tested: source and receiver moving in tandem and fixed source with moving receiver. The results are shown in Figs. 4 and 5, respectively. Some difference is observed for 50-m and 30-m conductor separations. The normalization in Figs. 4 and 5 is the same as for the corresponding arrangements in Figs. 2 and 3.

Finally, we look at the moving source-receiver, separated by 15 m in a single hole (Fig. 6). The responses show a much clearer difference for the 50-m and 30-m conductor separations. As the curve is normalized by the primary vertical magnetic field when the source is 15 m away, the relative response is very small, although $|H_z|$ has about the same amplitude as in other cases. This example shows the sensitivity of the back-scattered fields to conductor position.

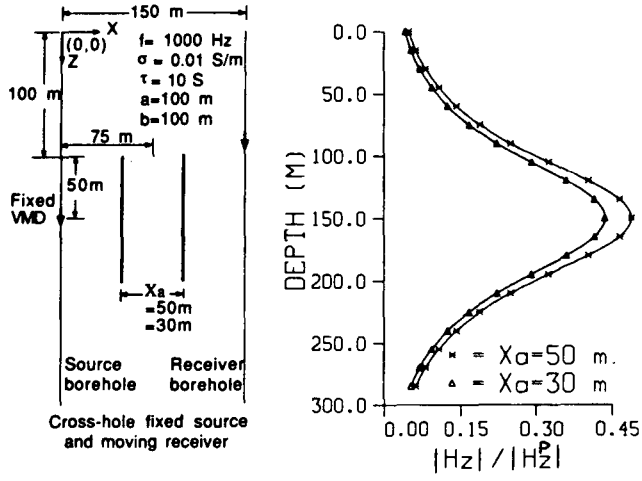

Figure 5. Cross-hole numerical results for the case shown in Fig. 4, except that here the source is fixed at 150 m. [XBL 894-1441]

CONCLUSIONS

A number of tests, both physical and numerical, have been applied, and the code has been found to be accurate. The computing time for 20 cross-hole source-receiver positions in a model of two thin conductors buried in a conductive homogeneous space is about 30 s on an IBM 3090 computer. The developed code can also handle thin conductors embedded in a conductive half-space capped by an overburden layer.

A number of experiments on the various source-receiver arrangements show that: (1) both the shape

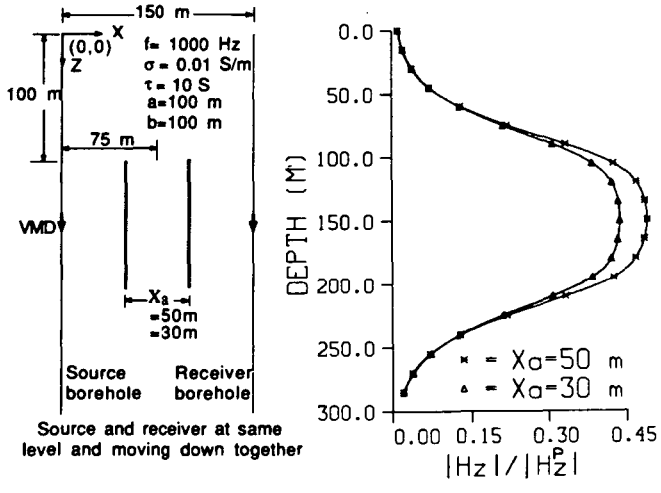

Figure 4. Schematic diagram and numerical results for source and receiver moving in tandem in their respective holes past two parallel conductive fractures separated by 30 and 50 m. [XBL 894-1440]

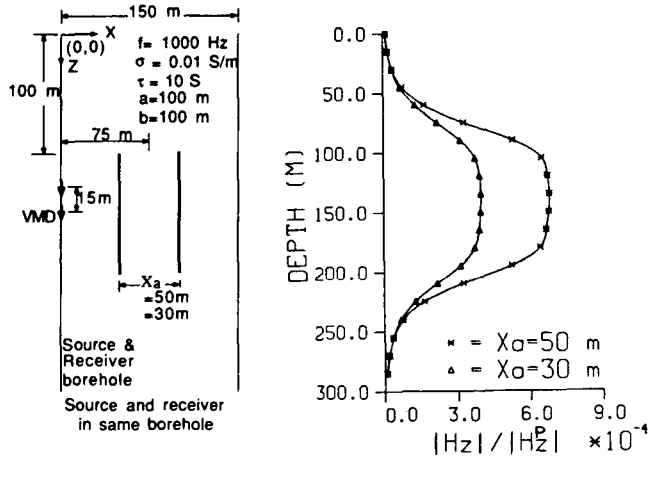

Figure 6. Schematic diagram and numerical results for the in-hole electromagnetic response due to two sheet-like conductors 30 and 50 m apart. Here both source and receiver are in the same hole and 15 m apart. [XBL 894-1442]

and peak-to-peak values of the measured responses are needed for interpretation; (2) the cross-hole source-receiver pair moving in tandem has poor lateral resolution; (3) for better resolution of lateral variation, the back scattered field should also be measured (i.e., source and receiver in a single hole).

Though EM waves at audio frequencies have deep penetration, the response cannot be interpreted easily because of their diffusive nature in a conductive medium. Multi-frequency and multi-component data collection are mandatory for interpretation.

REFERENCES

Johannsen, H.K., and Sorensen, K., 1979. Fast Hankel transforms. Geophysical Prospecting, v. 27, p. 876–901.

Lee, K.H., Pridmore, D.F., and Morrison, H.F., 1981. A hybrid three-dimensional electromagnetic modeling scheme. Geophysics, v. 46, p. 796–805.

Weidelt, P., 1981. Report on dipole induction by a thin plate in a conductive half-space with an overburden. Federal Institute for Earth Science and Raw Materials, Hannover, Germany.

Xiong, Z., Luo, Y., Wang, S., and Wu, G., 1986. Induced-polarization and electromagnetic modeling of a three-dimensional body buried in a two-layered anisotropic earth. Geophysics, v. 51, p. 2235–2246.

Zhou, Q., Becker, A., Goldstein, N.E., Morrison, H.F., and Lee, K.H., 1987. Fracture detection using subsurface electromagnetic techniques. *In* I.W. Farmer et al., Proceedings, 28th U.S. Rock Mechanics Symposium. A.A. Balkema, Rotterdam, Netherlands, p. 5–17.

Mapping a Saline Groundwater Plume with Electromagnetics

N.E. Goldstein, S.M. Benson, and D. Alumbaugh

A detailed ground-conductivity survey was carried out over private ranch land immediately east of the Kesterson Reservoir, Merced County, California. The measurements were made to map a plume of saline drainage water believed to have moved from the flooded ponds into the underlying shallow alluvial aquifer. For this purpose we used two direct-reading ground-conductivity instruments, the Geonics EM31 and EM34-3. Multiple intercoil separations are needed to help distinguish between shallow conductors due to saline soil conditions and the deeper saline plume (Goldstein et al., 1988).

BACKGROUND AND HYDROLOGY

The Kesterson area (Fig. 1) is the site of a chemical contamination problem that became highly publicized after waterfowl deformities were traced to high levels of selenium entering the food chain. Beginning in 1981, agricultural drainwater containing trace amounts of selenium and other toxic elements was discharged into the Reservoir, which consisted of 12 unlined storage ponds covering 1280 acres. These ponds provided a habitat to both migratory and resident waterfowl. Once the source of the problem was recognized in 1986, the flow of contaminated agricultural drainwater was ordered stopped. A program was initiated by the U.S. Bureau of Reclamation to find ways to neutralize the selenium already present and to remediate the area. During 1986–1987 several of the ponds were flooded with uncontaminated groundwater.

Chemical analysis of water and core samples taken from many shallow holes in the ponds showed that the selenium was chemically immobilized in the bottom sediments, but more-soluble chemical species were being discharged into the shallow aquifer underlying the Reservoir. Conductivities of the native groundwater are in the range of 300 to 400 mS/m, whereas conductivities of contaminated groundwater below the ponds rise into the 1000 to 1700 mS/m range, largely as a result of increased Na, Cl, and SO_4. During 1986 and 1987, extensive sampling of groundwater beneath the Reservoir showed that drainage water had infiltrated to depths ranging from less than 6 m to as much as 40 m, with an average depth of approximately 20 m. Because of the lack of off-site monitoring boreholes, only limited data were available for tracking lateral movement of the plume.

Computer-modeling studies were carried out to determine the approximate rate of plume movement (LBL, 1987). These simulations indicated that Reservoir operations caused the formation of a

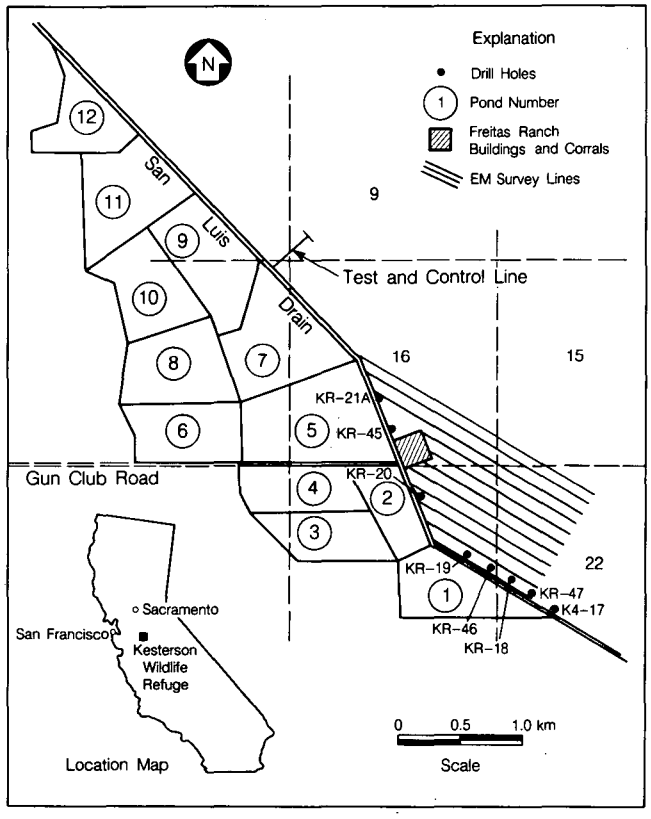

Figure 1. Location map of the Kesterson ponds and the ground conductivity survey area and lines adjacent to Ponds 1, 2, and 5. [XBL 8811-10473]

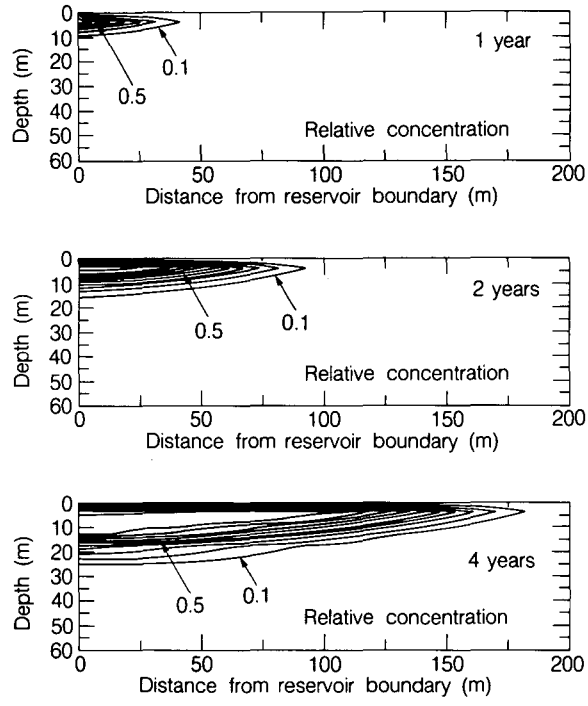

Figure 2. Calculated migration of a conservative chemical species in the groundwater 1, 2, and 4 years after pond filling begins. Contours are normalized by the initial concentration of the species in the ponds. [XBL 887-8497]

groundwater mound that dominated the local flow regime. Prior to pond construction groundwater flowed primarily horizontally from the south and southwest to the northeast at an average estimated rate of 10 m/yr. When the ponds were flooded drainwater moved radially away from the groundwater mound. The net flow velocities were greatest in the direction of the prevailing natural flow. Calculated lateral and vertical changes in the extent of the plume for the vicinity of the EM survey area are shown in Fig. 2 for the period 1981 to 1985. The simulations predict that the plume front moved northeastward at a rate of 45 m/yr and vertically at 4.5 m/yr.

THE SURVEY AREA

The average elevation of the area is 70 ft above mean sea level, and the surface varies from flat to slightly undulating. Drainage features in the survey area include a system of man-made canals that once distributed waters to the area and an intermittent stream that cuts across the southeast part of the area. The stream, dry during the survey, carries seasonal runoff in a northerly direction into Salt Slough. An oxbow lake, presumed to be a relict feature of the ancestral San Joaquin River, exists at the south end of the survey area. Salt crystals and desiccation cracks suggest that this area, dry at the time of the survey, is subject to periodic inundation and evaporation.

Color aerial photographs were taken of the Reservoir area by CH2M-Hill at monthly intervals from late November 1987 through mid-March 1988. During this period the area received most of its annual rainfall, and the new vegetation created color contrasts that were helpful in identifying ground conductivity anomalies associated with high-salinity soil conditions. A number of small areas that never acquired a normal grass vegetation during the rainy season were found to correlate well with high surface conductivities.

INSTRUMENTATION

The EM31 and the EM34-3 are inductively coupled EM systems whose operating frequencies span the range 0.4 to 10 kHz (McNeill, 1986). Eddy currents generated in the earth by a primary electromagnetic field, H_p, produce a secondary magnetic field, H_s. In practice, it is possible to determine ter-

rain conductivity directly, because under usual conditions H_s is 90° out of phase with H_p and ground conductivity is linearly proportional to the ratio H_s/H_p.

The EM31 consists of two coplanar coils mounted on a rigid boom and is carried on a shoulder sling. The coil axes are vertical in this configuration, referred to as the vertical dipole (VD) mode. The VD mode provides a nominal depth of exploration of 6.0 m (Table 1). The EM34-3 uses two circular coils, 0.63 m in diameter, connected by cable to the electronics. Intercoil separations of 10, 20, or 40 m are allowed and are switch selectable. We used coil separations of 20 and 40 m to achieve a greater depth of exploration than possible with the EM31. The EM34-3 coils may be oriented with both axes vertical (the VD mode) or horizontal (the HD mode). The HD mode was used because the VD mode is highly susceptible to coil misalignment and gives erroneous readings in highly conductive environments, such as in the survey area.

The ground conductivity measurements were made on a regular grid, along 11 lines, 100 m apart, trending approximately N60°W. These lines are roughly parallel to the San Luis Drain where it borders Pond 1. Readings were taken at 20-m intervals in the belief that this close spacing would detect saline groundwater flow guided by narrow paleochannels.

DATA REDUCTION AND INTERPRETATION

Because conductivities in the survey area are uniformly high the data had to be corrected for slightly nonlinear instrument response (McNeill, 1980). The corrected conductivities are for a homogeneous-earth model.

Both the EM31 and the EM34-3 HD-mode readings are highly sensitive to near-surface conductivities, and these may mask the effects of deeper variations. To help resolve subsurface conditions we followed two approaches. First, all of the EM34-3 data were numerically transformed to obtain a new apparent ground conductivity (σ_{an}) at each station;

$$\sigma_{an} = 2\,\sigma_{40} - \sigma_{20}\,,$$

where σ_{40} and σ_{20} are the apparent conductivities at the 40- and 20-m intercoil spacings, respectively (McNeill, 1985).

This operation alters the effective depth-response function to one that has zero sensitivity at the surface and maximum sensitivity to conditions at depths of about 0.25 times the larger intercoil separation. The procedure yields a ground-conductivity map (Fig. 3) emphasizing conductivities in the saturated zone. This operation produces isolated negative values of conductivity, but these have no physical meaning other than to indicate where

Table 1. Depths of exploration used for the survey.

Instrument	Intercoil spacing (m)	Approximate depth of exploration (m)
EM31	3.7	6.0
EM34-3	20	15
EM34-3	40	30

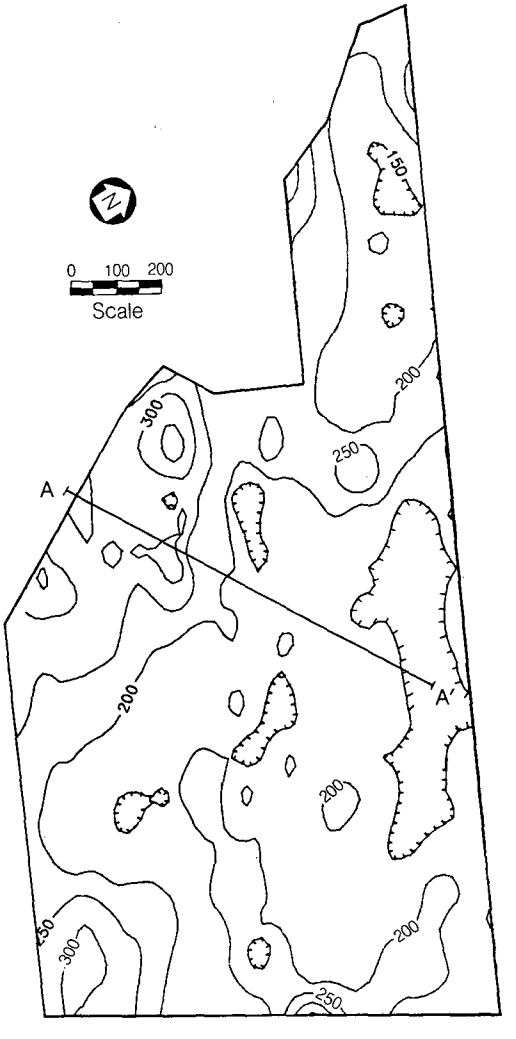

Figure 3. Calculated ground conductivity using EM34 data at coil separations of 20 and 40 m to accentuate conductivities in the saturated zone. [XBL 8812-10606]

ground conductivity varies abruptly over distances of less than 40 m. Because of its close resemblance to the VD-mode response, we refer to Fig. 3 as a pseudo-VD isoconductivity map.

The second approach is to find a layered-earth model that fits the data at selected stations. Using EM31 and EM34-3 data at stations close to profile $A-A'$ (Fig. 3), we obtained the numerical solutions shown in Fig. 4. Notice that we see evidence for a shallow conductive feature extending more than 200 m from Pond 2, but its precise dimensions cannot be determined. We cannot determine the thickness of the saline feature, and it is difficult to map the leading edge of the conductor using sounding data taken at 100-m station intervals. However, if we define the position of the leading edge of the plume as the point where ground conductivity measured with the EM34 (40-m coil separation) declines to background values, it would appear that the leading edge of the plume has moved about 350 m from the San Luis Drain. The average amount of movement (defined as the point where the conductivity is midway between the highest and background levels) is about 200 m, which is in general agreement with the layered-earth conductivity calculations.

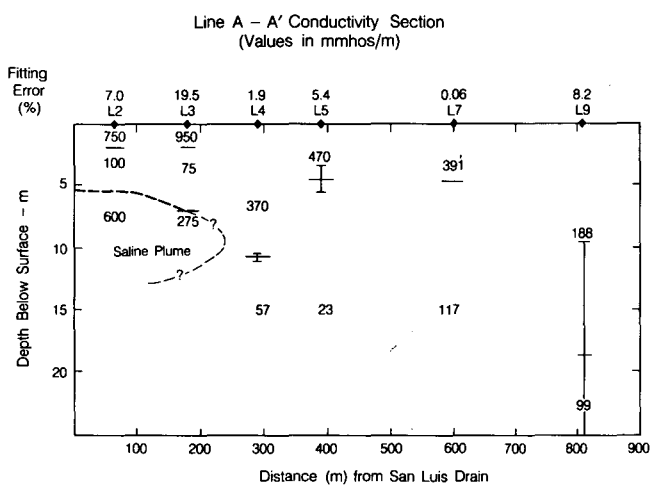

Figure 4. Conceptual model of saline groundwater feature adjacent to Pond 2 based on forward and inverse modeling using the EM31 and EM34 data. [XBL 8811-10572]

ACKNOWLEDGMENTS

This work was supported by the U.S. Bureau of Reclamation. The authors would like to thank the Freitas family for allowing LBL onto their ranch for the survey. We would also like to thank Ray Solbau, Don Lippert, Alex Becker, Cliff Schenkel, Kurt Nihei, Cindy Yates, and Chang Zhou for their assistance in planning and carrying out the survey.

REFERENCES

Goldstein, N.E., Alumbaugh, D., and Benson, S.M., 1988. Ground conductivity measurements adjacent to the Kesterson Ponds 1, 2 and 5. Lawrence Berkeley Laboratory Report LBL-24657, 25 p.

LBL, 1987. Hydrological, geochemical, and ecological characterization of Kesterson Reservoir, Fourth Progress Report. Lawrence Berkeley Laboratory Report LBID-1250, 92 p.

McNeill, J.D., 1980. EM 34-3 Survey interpretation techniques. Geonics Limited, Technical Note TN-8 (Rev. 1983), Mississauga, Ontario.

McNeill, J.D., 1985. EM 34-3 Measurements at two inter-coil spacings to reduce sensitivity to near-surface material. Geonics Limited, Technical Note TN-19, Mississauga, Ontario.

McNeill, J.D., 1986. Rapid, accurate mapping of soil salinity using electromagnetic ground conductivity meters. Geonics Limited, Technical Note TN-18, Mississauga, Ontario.

Transmission of *S*-Waves across a Thin Liquid Layer

F.R. Suárez, L.J. Pyrak-Nolte, N.G.W. Cook, F. Doyle, and L.R. Myer

Liquid-filled fractures in rock are of fundamental and practical interest in connection with many problems in geology and geophysics, mining and petroleum engineering, and waste isolation. To study the effects of such fractures on seismic waves, we have conducted idealized laboratory experiments. These consisted of measuring the transmission of compressional and shear pulses across thin layers of different liquids between two disks of fused quartz. Pyrak-Nolte (1988) has analyzed the transmission,

reflection, and conversion of seismic waves by a thin layer of liquid, treating this layer as a velocity-discontinuity boundary condition in the seismic-wave equation. According to this theory, the absolute value of the transmission coefficient for shear waves normally incident on the layer is as illustrated in Fig. 1. The value of the transmission coefficient is independent of frequency and varies as the ratio of the specific liquid viscosity to the seismic impedance of the adjacent solid material. The specific viscosity, defined as the ratio between the seismic stress and the difference between the seismic particle velocities across the layer, should be equal to the viscosity of the liquid divided by the thickness of the layer.

EXPERIMENTAL SETUP

Figure 2 is a schematic representation of the experimental setup, which consists of two fused quartz cylindrical disks, 90 mm in diameter, each bonded with a thin layer of epoxy resin to a seismic transducer. The two transducers, made of aluminum, each contain piezoelectric crystals for the transmission and reception of *P*-wave and *S*-wave pulses. The two free surfaces of the quartz disks are optically flat with a surface roughness on the order of 10 Å. These surfaces are separated from one another by three circular Mylar spacers 2 mm in diameter and 12.5 μm thick located near the edges of the disks. The whole assembly is placed in a carefully aligned load frame. By varying the load, the separation between the two optically flat surfaces can be controlled with high precision from 12.5 μm (the thickness of the Mylar spacers) at no load to "zero" at 2 kN, when the surfaces come into contact. The elastic deformation of the quartz is largely confined to the vicinity of the Mylar spacers. Interference

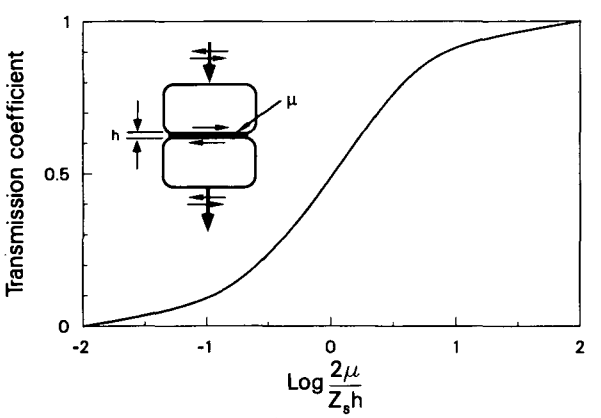

Figure 1. Theoretical transmission coefficients for *S*-waves as a function of specific viscosity (Pyrak-Nolte, 1988). [XCG 8811-6811]

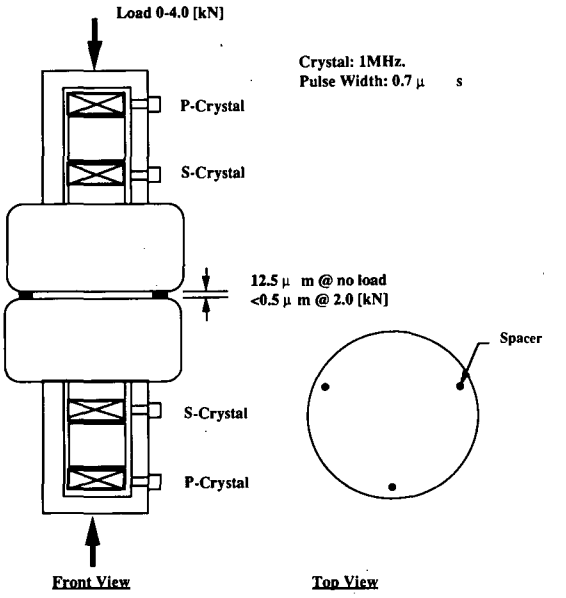

Figure 2. Experimental setup for measurement of transmitted seismic pulses across thin liquid layers. [XBL 894-1430]

fringes have shown that over a central area 30 mm in diameter, the surfaces are parallel to within the wavelength of light. The space between surfaces is filled with selected liquids either by imbibition or by placing a spherical droplet, 1 mm in diameter, on one of the surfaces before mounting the assembly. At each load during the experiment, corresponding to different thicknesses of the liquid layer, measurements of the transmitted shear and compressional pulses are recorded for analysis.

EXPERIMENTAL RESULTS

A summary of the experimental results is shown in Fig. 3, where the transmitted shear-pulse amplitude is plotted as a function of applied load. Several liquids were selected for these tests: three polar liquids, glycerol (1500 cP), honey (100,000 cP), water (1 cP), and three nonpolar, hexadecane (10 cP) and two silicone oils of different viscosities (100,000 cP and 10 cP). This selection provided us with a wide range of viscosities as well as liquids with the same viscosities but different chemical characteristics.

The vertical line at 2 kN marks the point at which contact between the two quartz surfaces occurs when the test is carried out with air between the solid surfaces. For this case, transmission is zero up to the point where solid-to-solid contact is established, increasing thereafter as the contact surface area increases with increasing load. Honey and glycerol are the only two liquids that show a consistent

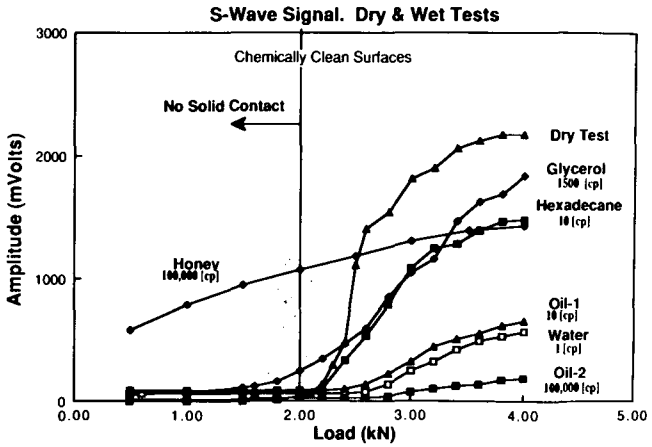

Figure 3. Summary of experimental results. Amplitude of *S*-pulses transmitted across liquid layer as a function of load (thickness of layer). [XBL 894-1431]

increase in transmission with decreasing liquid film thickness before any contact between the solid surfaces occurs. Surprisingly, high-viscosity silicon oil, although of the same viscosity as honey, does not follow the behavior of honey but instead shows a very poor transmission over the full range of film thicknesses.

Above 2 kN, in the presence of liquids, solid-to-solid contact might occur due to puncture of the liquid film by the asperities. However, it is believed that even under this condition, at least a monolayer of liquid remains adsorbed on the silica surface, thus affecting the degree of contact. A clear example of this phenomenon is presented in Fig. 4. Two sets of curves for *P*- and *S*-pulses are shown as a function of load. Both experiments were carried out under dry

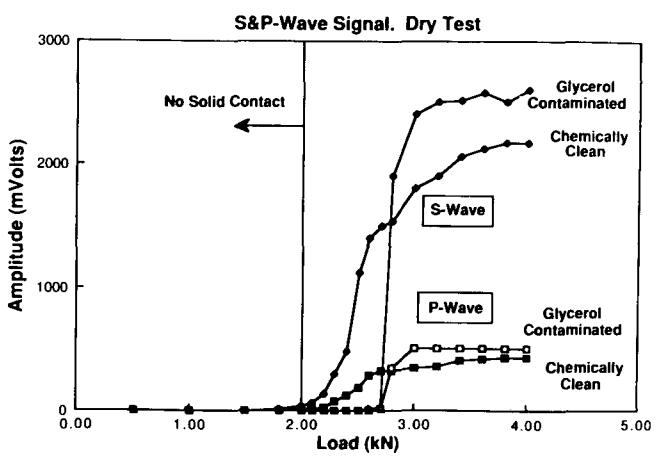

Figure 4. Effect of surface contamination on amplitudes of seismic pulse transmission. Dry test. [XBL 894-1432]

conditions; however, for the first one, the silica surface was wetted with glycerol prior to the test. Although the surface was then washed with water and dried, some glycerol molecules still remained adsorbed on the solid surface. This condition is referred to as glycerol contamination. The second set of curves was obtained using silica surfaces that had been chemically cleaned with an oxidizing agent, then well rinsed. As can be observed, a small amount of liquid, no more than a few monolayers, has a pronounced effect on the transmission of *S*-pulses. The amplitude of the transmitted signal is somewhat higher for the contaminated surfaces, and its rate of increase with loading is abrupt, in contrast with the chemically clean case, in which transmission gradually increases with loading. The behavior in the contaminated case possibly reflects improved coupling between the mating surfaces once contact has been established. The solid-to-solid contact point for glycerol-contaminated surfaces seems to be established at 2.7 kN. This shift might be associated with interactions between the solid surface and the adsorbed liquid.

For loads larger than 2 kN we observe that glycerol and hexadecane transmit *S*-pulses (at the highest load) more efficiently than honey, although honey is 66 times more viscous than glycerol and 10,000 times more viscous than hexadecane. A possible explanation for this behavior is that solid-to-solid contact may never develop with honey. (The smoothness of the curve for honey seems to confirm this hypothesis.) However, for glycerol and hexadecane solid-to-solid contact is established and increases with load. High-viscosity silicone oil transmitted *S*-pulses very poorly, although the film thicknesses for honey and oil were probably similar, given that both have the same viscosity. An explanation of this behavior is provided below.

MODIFIED PHYSICAL MODEL

The velocity-discontinuity model assumes that there is no relative motion across the interface between the thin liquid layer and the adjacent solid material. Under these conditions, the transmission of the seismic wave is determined completely by the viscosity of the liquid and the thickness of the layer. In our experiments we observed very different amplitudes for shear pulses transmitted across layers of liquids of similar viscosity but different chemical characteristics, such as honey (100,000 cP) and silicone oil (100,000 cP), over the full range of layer thicknesses. We ascribe this difference to slippage across the solid-liquid interfaces. Slippage appears to be prevented when the solid and the liquid surfaces

have strong affinities for each other. In these experiments those liquids giving good transmission are polar and would probably be associated with the silica through hydrogen bonds. These affinities are due to a common type of Lewis acid-base interaction. The enhancement of adhesion by interfacial Lewis acid-base bonds has been discussed at length by Fowkes (personal communication, 1985). When the liquid is nonpolar and Lewis acid-base association does not occur, the interfacial coupling is weak, there is slippage across the interface, and consequently shear-pulse transmission is curtailed at the solid-liquid interface, irrespective of the liquid viscosity and the film thickness. One additional mechanism affects overall *S*-pulse transmission when the liquid film thickness approaches the magnitude of the surface roughness. At this point, solid contact may develop, either as a result of puncture of the liquid film by asperities or by rupture of the liquid film itself. Under these circumstances, *S*-pulses are transmitted by a complex interaction of viscous coupling, interfacial solid-liquid coupling, and asperity-contact effects. A more complete model for shear-wave transmission across a thin layer of liquid would include the solid-liquid interface.

CONCLUSIONS

One can re-evaluate the experimental results (Fig. 3) from the perspective of the modified physical model for shear-wave transmission, described above, in which slippage can occur across the liquid-solid interface and solid-solid contact may develop at high loads. As noted before, only two liquids transmitted *S*-pulses in the absence of solid contact: honey and glycerol. These liquids both have a high viscosity and are sufficiently polar to develop hydrogen bonds with the silica surfaces. As a result, there is an effective coupling at the solid-liquid interface, equally effective viscous coupling within the liquid, and transmission is high. Water also has a very strong affinity for the quartz surface, but its low viscosity limits transmission to very small film thicknesses. Neither hexadecane nor any of the silicone oils wills develop strong bonds with the quartz surfaces, and thus slippage occurs at the solid-liquid interface at all loads. Slippage at the interface is the main reason why transmission is poor for high-viscosity oil. At loads higher than 2 kN, the actual transmission, for all the liquids, is affected by a complex combination of their viscosities, their bonding with the solid surface, and their degree of solid-to-solid contact across a film of liquid. We speculate that at the final load of 4 kN, the transmission for honey is mostly due to viscous coupling, whereas the transmission for hexadecane, and to a lesser extent glycerol, is mostly due to solid-to-solid contact. The transmission across high-viscosity silicone oil is mostly restricted by slippage at the solid-liquid interface, since very little, if any, solid-to-solid contact develops.

REFERENCE

Pyrak-Nolte, L.J., 1988. Seismic visibility of fractures (Ph.D. Thesis). Department of Materials Science and Mineral Engineering, University of California at Berkeley.

Fluid Percolation through Single Fractures

*L.J. Pyrak-Nolte, G. Yang, N.G.W. Cook, and D.D. Nolte**

The flow of fluids through fractures in rock masses is of considerable fundamental and practical importance in connection with problems in geology and geophysics, mining and petroleum engineering, and waste disposal. In particular the dependence of fluid flow on changes in the aperture of the void space between the fracture surfaces as a result of changes in stress or fluid pressure is of considerable interest. To the lowest order, flow through fractures has been approximated as laminar flow between parallel plates, leading to a flow that is proportional to the cube of the aperture. Some experimental evidence supports the cubic relationship (e.g., Witherspoon et al., 1980), but experiments on natural fractures suggest that the exponent may be much greater than 3 and that there exists also an irreducible component of flow at the highest stress (e.g., Raven and Gale, 1985; Pyrak-Nolte et al., 1987). We have sought to simulate numerically the distribution of

*Center for Advanced Materials, Materials and Chemical Sciences Division, Lawrence Berkeley Laboratory.

apertures in the void space between the two rough surfaces of a fracture and the fluid flow through that space in an endeavor to shed some light on the discrepancy between the high exponents measured in laboratory experiments and the cubic law.

STRATIFIED PERCOLATION MODEL

To model fracture contact area and local apertures, including correlations, a stratified percolation model has been developed (Nolte et al., 1989). This model is a hybrid between the standard random-continuum percolation construction (in which small void areas are randomly positioned within a given area; see Pike and Seager, 1974) and the recursive structures called fractals (see Mandelbrot, 1983). In the stratified percolation model, the procedure begins by randomly distributing N sites within a given square region, called a tier. Each site defines the center of a new tier, which is smaller, by a scale factor, than the parent tier. Within each of the new, smaller tiers, N sites are randomly distributed, defining the centers of yet another set of tiers that are also reduced in size by the same scale factor from the immediately preceding tier. The procedure continues for as many iterations as is necessary. The squares plotted in the last iteration are reduced in size from that of the original square by the scale factor raised to a power equal to the number of tiers. For five tiers with a scale factor of 2.37 between tiers and nine areas per tier, the total number of squares is $(9)^5 = 59{,}049$. The void area fraction for this pattern is 83%, and has an approximate fractal dimension of $D = 1.94$. As the final squares are randomly plotted, many squares will overlap. The aperture at a given site is taken to be directly proportional to the number of times a black square was positioned over that site during the construction of the pattern. The aperture distribution that results is displayed in the contour plot of Fig. 1.

Percolation studies of networks of nodes connected with strongly inhomogeneous conductances (Ambegaokar et al., 1971; Shklovskii and Efros, 1971; Pollak, 1972) have shown that the macroscopic conductivity of these networks is determined by the element of least conductance along the critical path; that is, the *critical neck*. To satisfy the criterion of strong inhomogeneity, the conductances must vary by four orders of magnitude (Seager and Pike, 1974). This criterion is satisfied in our model because the fluid conductance depends on the cube of the aperture, and the apertures are distributed over two orders of magnitude.

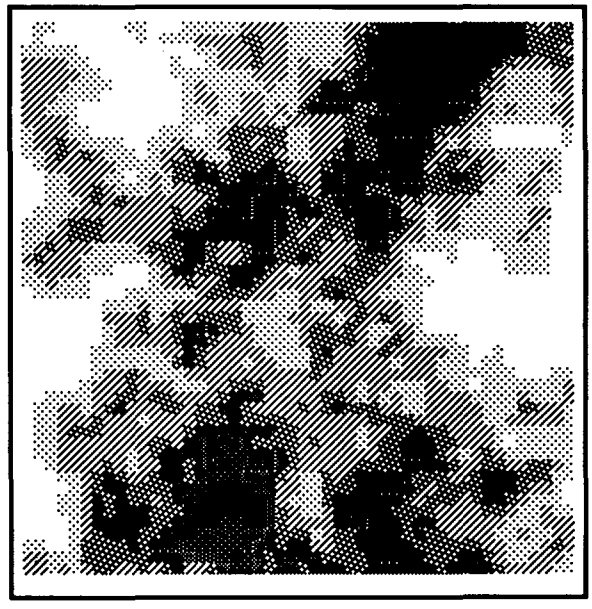

Figure 1. Distribution of apertures derived from the stratified percolation model. White represents areas of contact and black the largest apertures. [XBL 888-2961]

RELATIONSHIP BETWEEN FLOW AND APERTURE

In experiments to study the relationship between fluid flow and changes in fracture aperture brought about by changes in effective stress, displacements are measured across a gauge length of rock containing the fracture, d_t, and across the same gauge length of intact rock, d_r, as functions of the effective stress. The displacement induced by the stress across the fracture itself is given by the difference between these two measurements $(d_r - d_r) = d_{mech}$ at every stress. This difference is frequently referred to as the fracture deformation or closure. Curves of closure against stress are typically nonlinear and approach to a maximum constant value, d_{max}, at the highest stress. The difference between this maximum value and the closure is taken to be the apparent aperture of the fracture,

$$\overline{b} = d_{max} - (d_r - d_r) \mid d_{max} - d_{mech} . \qquad (1)$$

However, the reduction in the actual aperture of the void space is not equal to the fracture closure, or the change in apparent fracture aperture. The deformations associated with the concentrations of stress and strain adjacent to the areas of contact, and void

spaces between the two surfaces of a fracture are isovolumetric (Cook, 1989). Accordingly, the incremental change in fracture closure $\delta(d_t - d_r)$ is related to the corresponding decrement in the aperture of the void space δd_v by

$$A\,\delta(d_t - d_r) = A_v \delta d_v \ , \qquad (2)$$

where A is the projected area of the whole fracture plane and A_v is the area of that plane occupied by voids at any particular value of the effective stress. Integration of Eq. (2), a statement of conservation of volume, yields

$$A(d_t - d_r) = \int_0^{d_v} A_v(y)dy \ . \qquad (3)$$

To determine the relationship between apparent fracture aperture and fluid flow, we diminish all the apertures uniformly to simulate increasing stress, determine the apparent fracture aperture from Eqs. (1) and (3), and assume that the full pressure difference occurs across the critical neck, producing a flow that locally follows the cubic law. The resulting relationship is plotted logarithmically in Fig. 2, from which it can be seen that the exponent relating aperture to flow is not a constant and has tangent values much greater than 3.

NETWORK MODEL

As an independent check on the assumption that macroscopic fluid flow through a fracture is dominated by the critical neck, we have constructed a full network model of flow through the void spaces given by this stratified percolation model. A rectangular fracture plane is divided into 100 × 100 elements, the apertures of which are given by the fractal construction described above. At each of 100 cross sections normal to the plane of the fracture and to the direction of the overall pressure gradient, sections through the nonzero local aperture are approximated by elliptical holes. Whenever holes in adjacent cross sections overlap, they are connected from one cross section to the next to form networks of intersecting elliptical tubes. The hydraulic resistance of each elliptical tubular element is calculated on the assumption that flow is laminar.

In most engineering systems, the network is well connected and the topological structure is given. However, the network that results from the method just described includes many dead-end branches and dead loops, with only one end connected to the rest of the network. We have developed a computer program to remove dead-ends and dead loops. Using Graph Theory, minimum trees are formed and chords are chosen as the branches of greatest resistance that form meshes so as to facilitate solution by Hardy-Cross iteration (Cross, 1936).

The effects of stress on fracture closure are simulated as described above. As the stress is increased, the limit of percolation is reached when all the flow must pass through a single critical segment. The network for this condition is illustrated in Fig. 3. For

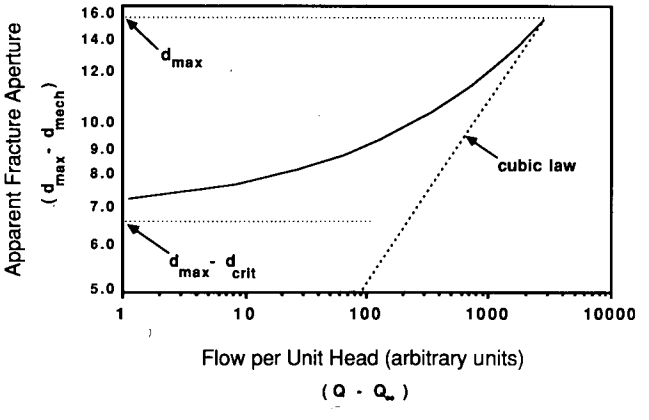

Figure 2. Relationship between fluid flow ($Q - Q_\infty$) and apparent fracture aperture ($d_{max} - d_{mech}$). [XBL 888-2960]

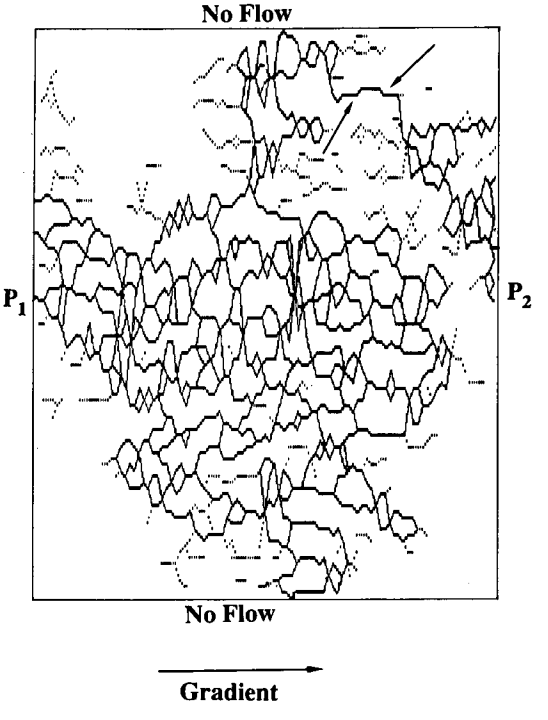

Figure 3. Network of flow tubes at the limit of percolation, showing the critical segment across an area of contact. [XBL 894-1429]

this realization we find that 30% of the total pressure difference exists across this critical segment, which also contains the critical neck. Thus, although flow may be dominated by the critical neck, it does depend upon the whole network. Elsewhere, flow occurs through a complex network of intersecting elements that are important in terms of storage and dispersion. The results of simulations at different stresses, corresponding to different apparent fracture apertures, show that flow tends to vary as a function of the apparent aperture raised to a constant power of about 6 (Yang et al., 1989).

CONCLUSIONS

We have shown that the relationship between the laminar flow of fluid between the two rough surfaces of a fracture should depend upon the apparent fracture aperture raised to a much greater power than 3 given by the cubic law. This arises mainly from two effects. First, increases in stress reduce the actual apertures of the voids through which fluid flows more than the average apparent fracture aperture. This is a consequence of the areas of contact between fracture surfaces and conservation of the volume of rock in deformations adjacent to the fracture plane. Second, increasing stress also reduces the number of parallel channels (or width of the fracture) through which fluid can flow. Although flow is dominated by the critical neck—that is, the point of smallest aperture along the critical flow path—most of the pressure drop occurs throughout the whole fracture plane.

REFERENCES

Ambegaokar, V., Halperin, B.I., and Langer, J.S., 1971. Hopping conductivity in disordered systems. Phys. Rev., v. B4, p. 2612–2620.

Cook, N.G.W., 1989. Natural joints in rock: Mechanical, hydraulic and seismic behavior and properties under normal stress. Int. J. Rock Mech. Min. Sci. Geomech., in press.

Cross, H., 1936. Analysis of flows in networks or conduits of conductors. Bulletin 286, Engineering Experimental Station, University of Illinois.

Mandelbrot, B.B., 1983. The Fractal Geometry of Nature. W.H. Freeman and Company, San Francisco.

Nolte, D.D., Pyrak-Nolte, L.J., and Cook, N.G.W., 1989. Fractal geometry of the flow paths in natural fractures in rock and approach to percolation. Pure Appl. Geophys., v. 131, in press.

Pike, G.E., and Seager, C.H., 1974. Percolation and conductivity: A computer study. I. Phys. Rev., v. B10, p. 1421–1434.

Pollak, M., 1972. A percolation treatment of D.C. hopping conduction. J. Non-Crystal. Solids, v. 11, p. 1–24.

Pyrak-Nolte, L.J., Myer, L.R., Cook, N.G.W., and Witherspoon, P.A., 1987. Hydraulic and mechanical properties of natural fractures in low-permeability rock. *In* G. Herget and S. Vongpaisal (eds.), Proceedings, Sixth International Conference on Rock Mechanics, Montreal, Quebec, Canada, August 3–September 3, 1987. A.A. Balkema, Rotterdam, Netherlands, p. 225–231.

Raven, K.G., and Gale, J.E., 1985. Water flow in a natural rock fracture. Int. J. Rock Mech. Min. Sci. Geomech., v. 22, p. 251–261.

Seager, C.H., and Pike, G.E., 1974. Percolation and conductivity: A Computer Study. II. Phys. Rev., v. B10, p. 1435–1446.

Shklovskii, B.I., and Efros, A.L., 1971. Impurity band and conductivity of compensated semiconductors. Sov. Phys. – JETP, v. 33, p. 468–474.

Witherspoon, P.A., Wang, Y.S., Iwai, K., and Gale, J.E., 1980. Validity of cubic law for fluid flow in a deformable rock fracture. Water Resour. Res., v. 10, p. 1016–1024.

Yang, G., Cook, N.G.W., and Myer, L.R., 1989. Network modeling of flow in natural fractures. Presented at the 30th U.S. Symposium on Rock Mechanics, Morgantown, West Virginia, June 19–22, 1989.

RESERVOIR ENGINEERING AND HYDROGEOLOGY

The scientists and engineers in the Reservoir Engineering and Hydrogeology group are primarily concerned with several different approaches to the fundamental problem of the movement of mass and energy through rocks. For a number of years, we have been striving to understand geothermal systems and to unravel the complex physics that controls such systems. This has required the perfection of mathematical models and their application to rather large and complicated field projects. Several articles in this section present the results of recent developments and serve to illustrate the level of sophistication that has been attained in geothermal reservoir modeling.

Several years ago we began to investigate the phenomenon of flow in fractured rocks, and this has now become a major effort. The importance of fractures in fluid flow arose in connection with our work on geothermal systems and has become a central theme in our investigations of problems related to the isolation of radioactive and toxic wastes. One of these problems is to be able to characterize the fracture system of a rock mass; several articles discuss the difficulties in the evaluation of field data and the use of well tests. Another problem is to develop models that are appropriate to use in evaluating the factors that control fluid movement in fractures; different approaches are being pursued in this area, and they address a vast range of spatial scales, from small (cored) sections of individual rough-walled fractures to three-dimensional fracture networks in the field. Single- and multiphase flow as well as chemical transport in fractures are being studied.

High-level radioactive wastes generate substantial amounts of heat, and once the waste is placed underground the dissipation of this thermal energy and its effects on the rock mass must be understood. Our previous work on geothermal systems has provided us with an excellent background for confronting this problem; the results of several investigations are included here. Another problem of great practical importance concerns the migration of chemical species in groundwater systems. Our studies in this area involve the development and field application of quantitative techniques for monitoring and predicting the behavior of organic as well as inorganic contaminants in the subsurface.

Recently there has been considerable interest in utilizing the unusual properties of foam to improve the efficiency of oil recovery and underground gas storage. Results of our laboratory experiments and theoretical attempts to understand foam flow in porous media are reported.

Our research program is rounded out by a number of topical studies. These relate to the design and interpretation of hydrologic tests and to the improvement of mathematical-modeling capabilities.

Reservoir Analysis of the Ahuachapan Geothermal Field, El Salvador

Z. Aunzo, G.S. Bodvarsson, C. Laky, M.J. Lippmann, B. Steingrimsson, and A.H. Truesdell†*

As part of the reservoir-evaluation effort in cooperation with the Comision Ejecutiva Hidroelectrica del Rio Lempa (CEL) and the Los Alamos National Laboratory, various studies have been conducted during this first year of the project. The work has focused on understanding the available data and the development of a conceptual model for the field. This involved the development of a geologic model of the geothermal system, analysis of geochemical data, interpretation of pressure and temperature logs, and evaluation of well data and the observed pressure drawdown. In addition, a natural-state model of the field has been developed. Details of this work are given in Laky et al. (1989), Truesdell et al. (1989), Steingrimsson et al. (1989), and Aunzo et al. (1989a,b).

HYDROGEOLOGY

The known lithologic column at Ahuachapan consists mostly of the San Salvador formation with only the basement rock from the Balsamo. Four major units have been defined, including the Surficial Material (SM), Young Agglomerates (YA), Ahuachapan Andesites (AA), and Older Agglomerates (OA). The Surficial Material is composed of colluvium and a series of altered pyroclastics. The Young Agglomerates, found below the SM, are composed of pyroclastics and andesites ranging from 300 to 800 m in thickness. The Ahuachapan Andesites are a highly fractured unit that hosts the hot geothermal fluids. The underlying Older Agglomerates are a combination of dense breccias and andesites, with low matrix permeability but some fracturing. The structure of the Ahuachapan field appears to be dominated by seven major and five minor faults (Fig. 1). Identified on the basis of lithologic logs, aerial photographs, and existing structural maps, these faults control the heat and fluid recharge and the flow within the reservoir. Three aquifers identified in the field appear to coincide with individual lithologic units. These are the Shallow Aquifer (found in SM), the Regional Saturated Aquifer (found in YA), and the Saline Aquifer (found in AA and OA).

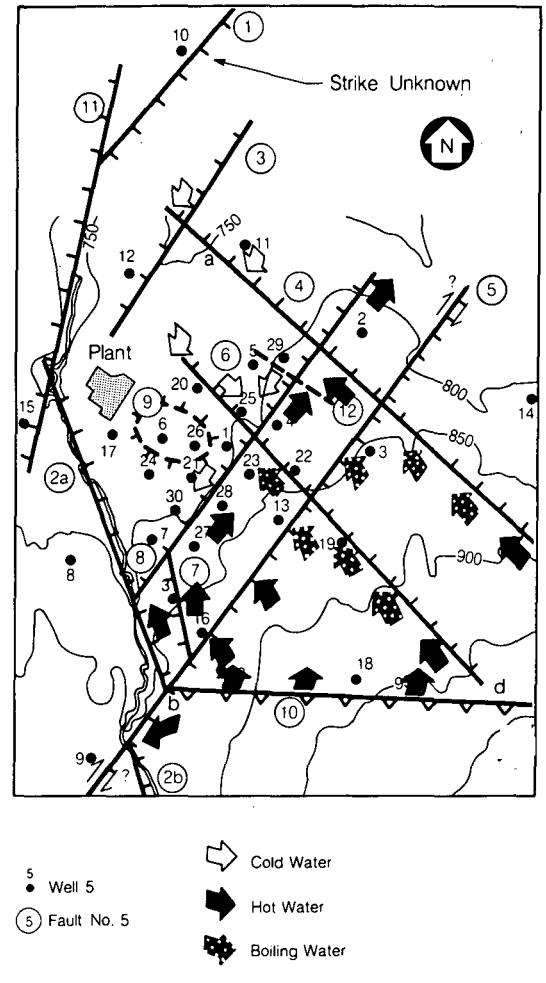

Figure 1. The faults and inferred flow channels in the Ahuachapan field. [XBL 894-1539]

INITIAL THERMODYNAMIC CONDITIONS

Initial pressures in the various aquifers in Ahuachapan suggest that hydraulic communication between them is limited, as their hydraulic potentials are different. The hydraulic potential is lowest in the Saline Aquifer. Within the geothermal reservoir there is no significant variation in hydraulic potential, and at the 200-masl reference level the pressure is about 36 bar gage. Temperatures exceeding 240°C are found in the AA, and temperature inversions are observed in most wells when entering the OA. All productive wells show similar profiles, with the top

*National Energy Authority, Iceland.
†U.S. Geological Survey, Menlo Park, CA.

of the convective zone coinciding with the top of the AA. Temperatures are observed to increase toward the southeast, where the highest reservoir temperature (245°C) has been measured. This suggests hot fluid recharge from the southeast. Analyses of well discharges from Ahuachapan yield valuable data on the initial reservoir conditions and processes. Geochemical temperature and aquifer chloride concentrations show increase from east to west. This suggests mixing between a more-saline, higher-temperature water and a more-dilute, lower-temperature water.

CONCEPTUAL MODEL

Our present understanding of Ahuachapan suggests that the field is only an outflow of a deeper and much larger system and that the reservoir extends much farther to the east and southeast (Fig. 2). The system has the following main characteristics:

1. The Ahuachapan and nearby Chipilapa systems are recharged by an upflow zone southeast of the Ahuachapan wellfield, probably beneath the Laguna Verde volcanic complex, located southeast of Ahuachapan. The temperature of this upwelling fluid is believed to be 250°C or higher, as suggested by geochemical temperatures of the discharged fluid.
2. Most of the upwelling fluids flow to the north, with the main outflow for this system being in the El Salitre springs area, located about 7 km north of the wellfield. The discharge is a mixture of geothermal and Regional Saturated Aquifer fluids; the mixing is believed to occur in the vicinity of the springs rather than close to the geothermal field.
3. Colder fluids recharge the Ahuachapan reservoir, as evidenced by variation in chloride concentrations in the field. The cold water inflow is either laterally from the north or vertically downward from the Regional Saturated Aquifer, which overlies the main reservoir and has a higher pressure potential.
4. The main reservoir rocks are the Ahuachapan Andesites and the underlying Older Agglomerates. Most of the produced fluids come from the andesites although the permeability of the Older Agglomerates is significant, as evidenced by several feed zones encountered in this unit.
5. Faults limit the extent of the Ahuachapan reservoir toward the north and the west. The extent of the field is also limited toward the south.
6. The Ahuachapan and Chipilapa fields seem to communicate at depth and to be outflow zones of a large geothermal system.

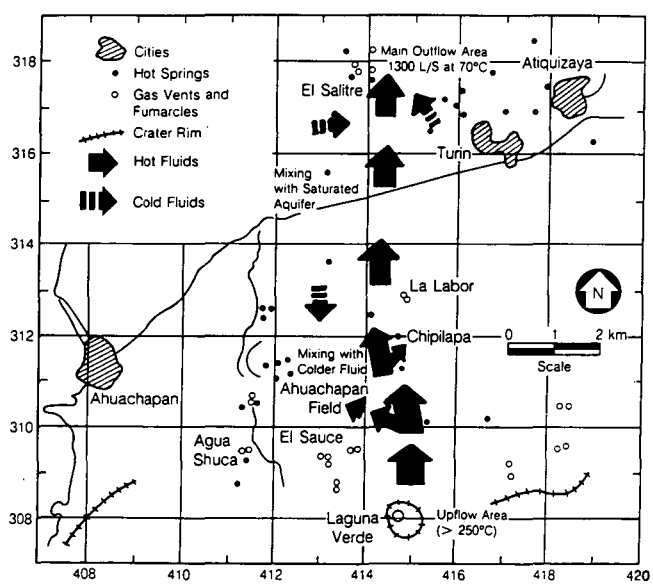

Figure 2. Fluid flow in the Ahuachapan/Chipilapa geothermal system. [XBL 894-1540]

EXPLOITATION EFFECTS

Since large-scale exploitation began in 1975, pressure drawdowns of up to 15 bars have developed and significant temperature changes have been observed. Cooling of up to 15°C has been observed. The temperature history of Ahuachapan is complicated and has been influenced by several factors:

1. Gradual cooling of the upper part of the reservoir due to boiling as a result of pressure decline.
2. Progressive cooling of the liquid region in the Ahuachapan Andesites within the main production area. This cooling is due to recharge of boiling fluid (two-phase) to the production area.
3. Temporal cooling in the vicinity of injectors during the (1975–1982) reinjection period. This cooling, however, did not cause significant detrimental temperature declines in producing wells.
4. Cooling in the northern and western parts of the field due to increasing cold-water recharge in response to reservoir drawdown.
5. Heating in the southeastern part of the field due to increasing geothermal (hot) fluid recharge to the production area.

MODELING STUDIES

Various modeling studies have been conducted on the Ahuachapan field data, including the analysis of interference test data, analysis of the average reservoir-drawdown history, and development of a natural-state model.

Interference Tests

Several interference tests were conducted at Ahuachapan. One such test was carried out during the period from May 6 to August 19, 1982. In the analysis of the data, the computer model VARFLOW (EG&G and LBL, 1982) was used. The best match between the observed and the computed pressure yielded a reservoir transmissivity of 25 darcy-m and a storativity of 2.5×10^{-6} m/Pa.

Pressure-Drawdown History Match

Pressures in Ahuachapan wells were fairly uniform prior to exploitation; production has caused significant drawdown (approximately 15 bars). Drawdown has been monitored by annual pressure surveys in all wells accessible to logging and by daily pressure measurement at 200 masl in well AH25. In this study a simple model was used to match the pressure history. The model assumes an isothermal, horizontal, homogeneous, fully saturated porous-medium reservoir of constant thickness and infinite areal extent with a N–S boundary near well AH-15. The data were analyzed using the VARFLOW code. Figure 3 shows the best match. A transmissivity of 35 darcy-m and storativity of 3.5×10^{-6} m/Pa were estimated. In order to estimate the effect of the reinjection from 1975 to 1982 on the pressure drawdown, the pressure history was simulated using the above model without any reinjection. The results indicate that reinjection provided significant pressure support.

Natural-State Model

The computational mesh used in this study consists of a three-dimensional three-layer grid (Fig. 4). The simulation work was carried out using MULKOM (Pruess, 1983). The best model indicates that

1. The horizontal permeability of the Ahuachapan Andesites is estimated to be about 80 mdarcies and vertical permeability 16 mdarcies.
2. The permeability of the Older Agglomerates is estimated to be 20 mdarcies horizontal and 4 mdarcies vertical.

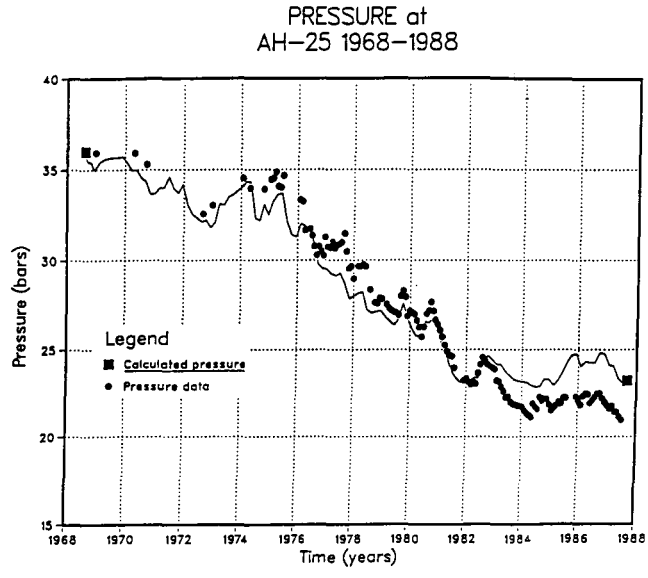

Figure 3. Pressure-history match for well AH-25. [XBL 894-1541]

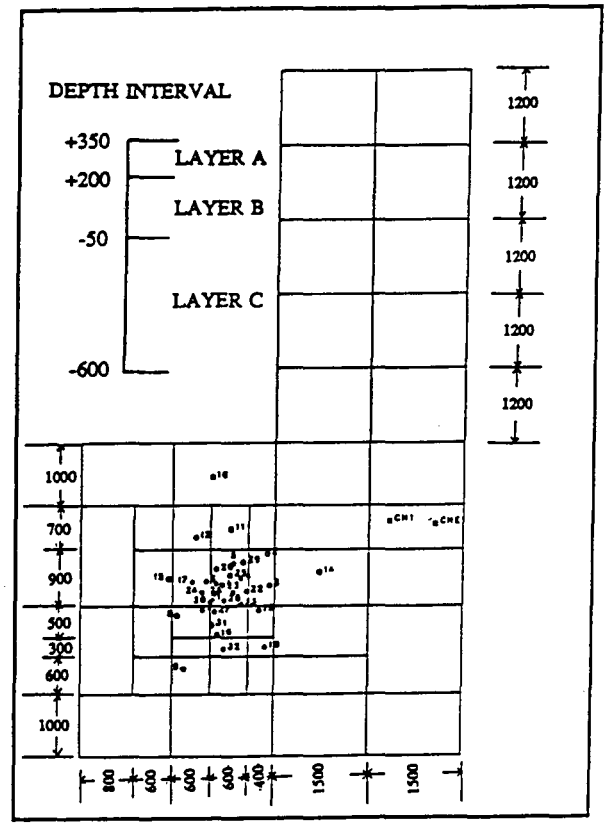

Figure 4. Grid blocks and well locations. [XBL 894-1542]

3. The total recharge to the Ahuachapan/Chipilapa geothermal system is estimated to 225 kg/s of 255°C fluids, yielding a total thermal throughflow of 250 MW_t. Most of these fluids discharge in El Salitre springs (170 kg/s), but significant energy is lost through surface springs in the Ahuachapan/Chipilapa areas (60 MW_t) and through conduction to the ground surface (20 MW_t).

REFERENCES

Aunzo, Z., Steingrimsson, B., Bodvarsson, G.S., Escobar, C., and Quintanilla, A., 1989a. Modeling studies of the Ahuachapan geothermal field, El Salvador. Presented at the Fourteenth Workshop on Geothermal Reservoir Engineering, Stanford, California, January 21–24, 1989.

Aunzo, Z., Bodvarsson, G.S., Laky, C., Lippmann, M.J., Steingrimsson, B., and Truesdell, A.H., 1989b. The Ahuachapan geothermal field, El Salvador: Reservoir analysis. Lawrence Berkeley Laboratory Report LBL-26612.

EG&G Idaho, Inc. and Lawrence Berkeley Laboratory, 1982. Low-to- moderate temperature hydrothermal reservoir engineering handbook. Report IDO-10099.

Laky, C., Lippmann, M.J., Bodvarsson, G.S., Retana, M., and Cuellar, G., 1989. A hydrologic model of Ahuachapan geothermal field, El Salvador. Presented at the Fourteenth Workshop on Geothermal Reservoir Engineering, Stanford, California, January 21–24, 1989.

Pruess, K., 1983. Development of the general purpose simulator MULKOM. *In* Earth Sciences Division Annual Report 1982. Lawrence Berkeley Laboratory Report LBL-15500, p. 133–134.

Steingrimsson, B., Bodvarsson, G.S., Cuellar, G., and Escobar, C., 1989. Changes in thermodynamic conditions of the Ahuachapan reservoir due to production and injection. Presented at the Fourteenth Workshop on Geothermal Reservoir Engineering, Stanford, California, January 21–24, 1989.

Truesdell, A.H., Aunzo, Z., Bodvarsson, G.S., Alonso, J., and Campos, A., 1989. The use of Ahuachapan fluid chemistry to indicate natural state conditions and reservoir processes during exploitation. Presented at the Fourteenth Workshop on Geothermal Reservoir Engineering, Stanford, California, January 21–24, 1989.

Geochemical, Biological, and Hydrological Research at Kesterson Reservoir: An Update

S.M. Benson, A. Horne, O. Weres, T.K. Tokunaga, and A. Yee*

Kesterson Reservoir, located in Merced County, California, was used as a facility for the disposal of selenium-tainted subsurface drainage from agricultural lands in the Westlands Water District from 1978 to 1986. By 1984 elevated levels of selenium became suspect as the cause of water-bird death and embyonic deformity. In response to this concern the U. S. Bureau of Reclamation (USBR) made plans to stop deliveries of drainage water and to find a cost-effective means to deal with the selenium that had accumulated in the soils, vegetation, and biota at the Reservoir. Over the past 3 years scientists and engineers at Lawrence Berkeley Laboratory (LBL) and the Sanitary Engineering and Environmental Health Research Laboratory (SEEHRL) have worked with the USBR to define the extent of the problem and to find a reasonable approach to eliminating risks to wildlife resulting from exposure to hazardous levels of selenium.

Our early studies were guided by the observation that even though 50% of the water was seeping though the bottom of the Reservoir into an underlying aquifer, most of the selenium was concentrated in a thin layer of organic detritus and mineral soil on the bottom of the ponds (Weres et al., 1985). Thermodynamic data indicated that under chemically reducing conditions, selenium would be converted from the highly soluble selenate and selenite species present in drainage water to the more insoluble forms, such as elemental selenium (Geering et al., 1968). Field observations confirmed that both the

*Department of Sanitary Engineering, University of California, Berkeley.

pond-bottom soils (when flooded) and native groundwater were chemically reducing, thus explaining the high concentration of practically insoluble selenium in the pond-bottom sediments and the lack of widespread selenium contamination in the upper aquifer.

Motivated by the observation that selenium could be geochemically immobilized in the pond-bottom sediments, we hypothesized that by keeping the ponds submerged with a selenium-free water supply, selenium concentrations in food-chain items would decline to acceptable levels while the groundwater remained free of undesirably high concentrations of selenium. Early data showing the promise of this hypothesis were used as the technical basis for proposing the Wet-Flex cleanup plan, a scheme that involved keeping the selenium geochemically immobilized by permanently flooding the Reservoir with selenium-free water. In 1985 laboratory and field experiments were initiated to test the effectiveness of this approach.

In March 1987, because of scientific uncertainty as to if and when a sufficient level of cleanup would be achieved with the Wet-Flex plan, the California State Water Resources Control Board rejected this plan in favor of the On-Site Disposal Plan (ODP), a more-conventional excavation scheme. As a result of this decision the focus of our research shifted to include evaluation of post-ODP conditions at the Reservoir. During these investigations we identified several issues that demonstrated that the proposed excavation scheme would not be effective for eliminating risks to wildlife at the Reservoir. Subsequently, the State Board reversed its earlier order to implement the On-Site Disposal Plan and ordered the USBR to fill all of the low-lying areas of the Reservoir with soil.

A brief summary of the results of these investigations is provided in the following paragraphs.

RESEARCH ON CONTROLLED FLOODING: WET-FLEX

Research on the effectiveness of the Wet-Flex plan was conducted on three scales: laboratory microcosms, a 1-acre mesocosm, and on a Reservoir scale using three of the ponds at the Reservoir (LBL, 1987, 1988b). In each case, selenium levels in the water, biota, and sediments were monitored periodically following permanent application of selenium-free water to the sediments. Results from all three types of experiments were similar in character, although the time scales over which changes in the selenium concentrations occurred were progressively slower for systems of larger physical size. The results are demonstrated best by the mesocosm study, where the environment was most representative of the ideal conditions for the Wet-Flex plan.

As illustrated in Fig. 1, following application of selenium-free water to the mesocosm (average water depth is approximately 1 m), selenium concentrations in the water quickly dropped to below 5 ppb, the upper range of acceptable concentrations (USBR, 1986). Similar rapid declines were observed in the macroalga *Chara* and aufwuch, the community of microscopic organisms attached to the alga. During the first year of the experiment selenium concentrations in these items at the bottom of the food web dropped to about 10 to 15 ppm, a decline of 80 to 90% of their original concentrations. In spite of the rapid and large decline, selenium levels did not reach the target goal of 3 ppm (on a dry-weight basis in the biota) that year or, as illustrated in Fig. 1, over the next several years. A similar pattern was observed for aquatic invertebrates. Apparently internal recycling processes transport selenium from the sediments to the biota, without significantly increasing the aqueous concentrations above what are believed to be safe levels for wildlife. Because of the slow rate of decline observed during 1987 and 1988, is not possible to predict if and when safe levels can be achieved with this remediation technique. Management practices that may improve the rate and efficiency of this cleanup technique have been identified, such as lowering the pH and/or increasing the productivity of the system by providing nutrients, but they are not being implemented at this time.

DRY LAND AND ODP INVESTIGATIONS

In January 1987 test plots were established to measure the concentration of selenium in the biota,

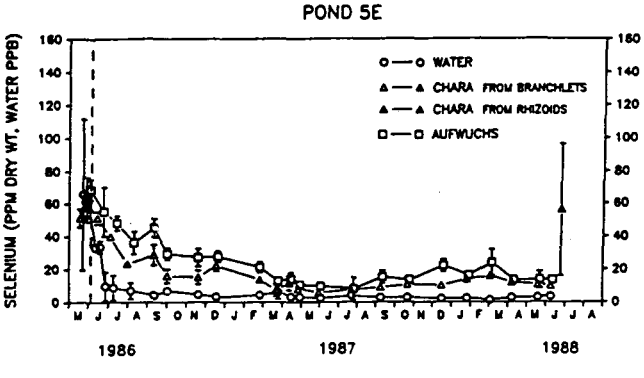

Figure 1. Selenium concentrations in water, Chara, and aufwuchs in Pond 5E, 1986–1988. The vertical broken line indicates when the Pond 5E was first isolated from the main pond. Error bars represent ± 1 standard errors. [XBL 894-1543]

soil, and groundwater in the areas of the Reservoir that were not flooded. In addition, several test plots were also established to test the efficacy of the proposed excavation plan. Installations at each of the test plots included soil-water samplers to measure solute concentrations in the vadose zone and tensiometers from which the direction of soil-water movement may be inferred.

Contrary to prior perceptions that elevated levels of selenium were confined to the top 0.15 m of soil, data from the test plots demonstrated that pore-water selenium concentrations ranged from 1000s of ppb at 0.15 m to 100s of ppb at a depth of 1 m (LBL, 1987). As illustrated in Fig. 2, soil-water samples from 31 locations throughout the Reservoir confirmed the widespread occurrence of high concentrations of dissolved selenium in the vadose zone. These concentrations are far in excess of the drinking water standard of 10 ppb and surface water goal of 2 to 5 ppb.

There are three areas of concern with regard to the high concentration of soluble selenium in the vadose zone. First, and most obvious, this large pool of soluble selenium will be available for plant uptake and thereby become biologically available. The other two concerns stem from the hydrologic setting. Each winter the water table rises to within a short distance of the ground surface. In low-lying areas, the water table rises above the ground surface, creating ephemeral pools. When these pools form, the seleniferous waters in the vadose zone rise to the surface, creating extremely high surface-water selenium concentrations. In addition to the continually changing geochemical and biological regimes

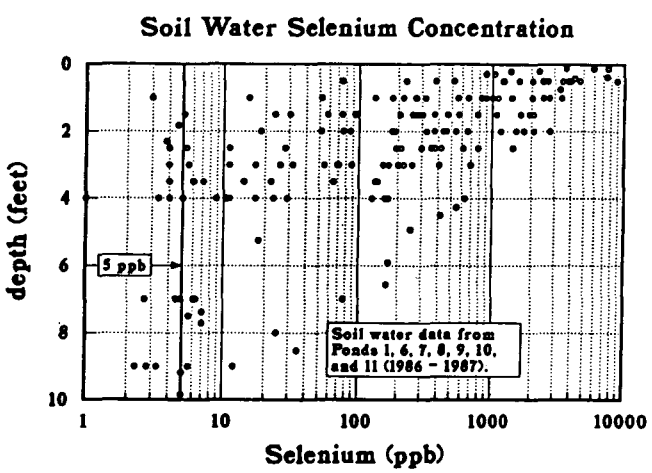

Figure 2. Depth distribution of soil-water selenium from various monitoring sites at Kesterson Reservoir. Data are from Ponds 1, 6, 7, 8, 9, 10, and 11. [XBL 894-1544]

created by the fluctuating water table, the shallow depth of the water table facilitates evaporative accumulation of salts and soluble selenium in near-surface soils. Recent measurements indicate that the mass of salts and selenium in the surficial soils increased by at least 16% over the past summer as a result of evaporative transport of the salts and selenium dissolved in the pore water (LBL, 1988b).

These results indicate that the ODP or any other cleanup method that removes only the surficial accumulation of selenium will not solve either of these problems. For example, at an experimental plot where the top 0.3 m of soil was removed, ephemeral pool water concentrations ranged from 700 to 6000 ppb. Biotic contamination in this pool was as high as had been observed at the Reservoir, even while the seleniferous drain water was being delivered to the site (LBL, 1988a). Besides failing to lower the surface-water selenium concentrations significantly, the ODP would exacerbate this problem by increasing the areal extent and persistence of the ephemeral pools. Lowering the ground surface would also accelerate evapotranspirative accumulation of salts and selenium in the near-surface soils.

As a result of these considerations the ODP was abandoned and the State Board ordered the USBR to fill the estimated 400 acres of low-lying areas where ephemeral pools were expected to form each year due to the seasonal rise in the water table.

GROUNDWATER INVESTIGATIONS

Ongoing and extensive groundwater sampling and analysis from many monitoring wells located adjacent to the ponds has demonstrated that for the most part, even though drainage water seeped into the underlying groundwater aquifer, selenium concentrations remain at background levels in the underlying groundwater aquifer. However, several exceptions to this observation led to a concern that this problem could become more widespread. During 1985, in the southern part of the Reservoir, many wells located within a 75 × 75 m area had elevated concentrations of selenium. Similar isolated plumes were identified mainly along the eastern edge of the Reservoir. When these plumes were first discovered, the factors controlling the mobility of selenium in groundwater were not well understood. To identify the factors controlling selenium mobility in the various geochemical environments, we collected a large body of water-quality data, conducted an extensive set of laboratory-column experiments, and performed three different types of field-scale tracer experiments. A brief description of all of these is provided below.

Extensive monitoring during 1985 and 1986 revealed that concentrations of selenium and nitrate had increased and that redox potentials exceeded 300 mV (LBL, 1987). After deliveries of selenium and nitrate-rich drainage water ceased in 1986, selenium and nitrate concentrations quickly declined to near background values in the majority of monitoring wells (LBL, 1988a). The rate of decline was far too rapid to be explained by migration and dilution of the seleniferous and nitrate-bearing waters, indicating that chemical and/or microbial processes were removing these constituents from the water.

Laboratory-column experiments indicated that the factors contributing to migration of selenium into the aquifer include higher-than-average seepage rates, elevated concentrations of nitrate, and lower-than-average organic content in the detrital layer and/or mineral soils (LBL, 1987; Weres et al., 1989). The experiments also indicated that transformation and immobilization of selenium were possible under appropriate conditions.

Three types of tracer experiments were conducted to confirm that such processes were acting in the aquifer and to quantify the rate at which immobilization occurred, including single-well injection-withdrawal tests, two-well recirculating tests with multiple observation wells, and a pond-reflooding experiment (LBL, 1987, 1988; Benson, 1988; Long, 1988; Long et al., 1989). Results of all these experiments demonstrated that chemically and/or biologically mediated reduction processes transform selenate into insoluble forms within weeks of its introduction into the aquifer. For example, as illustrated in Fig. 3, within 4 weeks after flooding a pond and establishing fully saturated conditions, 80% of the soluble selenium originally residing in the vadose zone was transformed to insoluble and/or strongly sorbed species and removed from solution. Rapid denitrification was also observed in the two-well recirculating test. Results from the two-well recirculating test also confirmed the important role that nitrate plays in inhibiting transformation and immobilization of selenate.

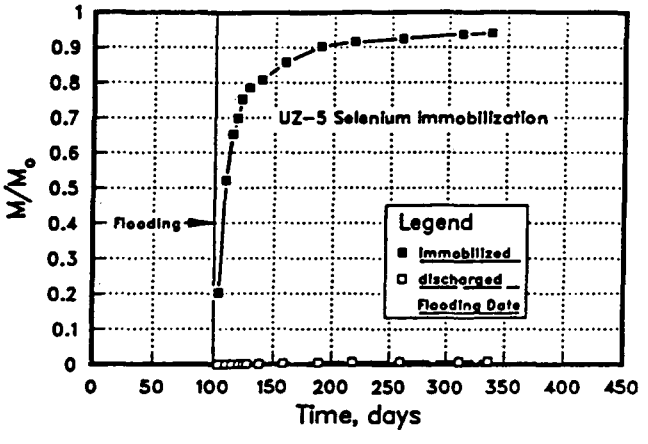

Figure 3. Results of selenium immobilization calculations at site UZ-5. Quantities plotted are normalized to the initial inventory of soluble selenium, M_0, in the 1.22-m-thick study block. [XBL 894-1545]

As a result of these investigations and a large body of groundwater-monitoring data, concerns for groundwater pollution have subsided. At Kesterson, in the absence of applied surface water, the combined effects of the shallow water table and the large excess of potential evaporation relative to rainfall create a soil environment where natural leaching of selenium and other salts is nearly impossible. This environment, together with the chemical conditions that limit the mobility of selenium, protects the groundwater from selenium contamination.

FUTURE PLANS

Research activities are continuing in order to address ongoing concerns regarding the effects of selenium contamination at Kesterson Reservoir. Specific issues of importance include the rate and potential effects of evaporative accumulation of salts and selenium in near-surface soils, the rate and effects of remobilization of the pool of insoluble selenium residing in the Reservoir soils, and control of the biological availability of selenium-contaminated biota at the Reservoir.

REFERENCES

Benson, S.M., 1988. Characterization of the hydrogeologic and transport properties of the shallow aquifer under Kesterson Reservoir (Ph.D. Thesis). University of California, Berkeley.

Geering, H.R., Cary, E.E., Jones, H.P., and Allaway, W.H., 1968. Solubility and redox criteria for the possible forms of selenium in soils. Soil Sci. Soc. Am. Proc., v. 32, p. 35–40.

LBL, 1987. Hydrological, geochemical, and ecological characterization of Kesterson Reservoir. Annual Report. Lawrence Berkeley Laboratory Report LBL-24250.

LBL, 1988a. Kesterson Reservoir progress report No. 7. LBID-1404.

LBL, 1988b. Hydrological, geochemical, and ecological characterization of Kesterson Reservoir. Annual Report. Lawrence Berkeley Laboratory Report LBL-26438.

Long, R.H., 1988. Analysis of selenium and chloride movement through a shallow pond bottom soil at Kesterson Reservoir (M.S. Thesis). University of California, Berkeley.

Long, R.H., Benson, S.M., and Tokunaga, T., 1989. Selenium immobilization in a pond bottom sediment at Kesterson Reservoir. J. Environ. Qual., in press.

USBR, 1986. Environmental impact statement for Kesterson Reservoir. U.S. Bureau of Reclamation, Mid-Pacific Region, Sacramento, California.

Weres et al., 1985. Geochemistry of selenium at Kesterson Reservoir: Possible remedial measures. Earth Sciences, v. 8, no. 3. Lawrence Berkeley Laboratory PUB-431, 8p.

Weres, O., Bowman, H.R., Goldstein, A., Smith, E.C., and Tsao, L., 1989. Nitrate and organic matter control the mobility of selenium in groundwater. Lawrence Berkeley Laboratory Report LBL-23499.

The Effect of Contact Area on the Permeability of Fractures

D.W. Chen, R.W. Zimmerman, and N.G.W. Cook

The permeability of a naturally occurring rock fracture depends principally on the geometry of the void space. The geometry of a typical fracture consists of regions where the two rock surfaces are in contact (asperities), surrounded by regions where the two surfaces are separated by a distance (known as the aperture, h) that may vary from point to point. When fluid flows through such a fracture, it not only must flow around the contact areas but also has a tendency to flow preferentially through the channels with the largest apertures (Brown, 1987), since hydraulic conductance is proportional to h^3. To model this process successfully, both effects must be taken into account. In this work, however, attention is focused on the tortuosity induced by the contact regions. We therefore consider idealized fractures consisting of two parallel surfaces with isolated regions of contact. Numerical and analytical methods will be used to relate the decrease in permeability (relative to that of unobstructed flow between parallel plates) to the amount of contact area and the geometrical structure of the contact areas.

FORMULATION OF PROBLEM

The flow of a Newtonian fluid (such as water) through a fracture is governed by the Navier-Stokes equations. Exact solutions for specific geometries are extremely difficult to obtain; for flow between two parallel plates under a uniform pressure gradient, however, the exact solution is known (Schlichting, 1968). The velocity profile for this flow is parabolic, with zero velocity at the upper and lower surfaces to satisfy the no-slip boundary condition. The total fluid flux Q is found by integrating the velocity across the thickness of the channel. This leads to the familiar cubic law $Q = h^3 G/12\mu$, where $G = |\nabla P|$ is the magnitude of the pressure gradient and μ is the viscosity of the fluid.

For a fracture that is modeled as two parallel plates propped open by discrete areas of contact, the flow cannot be everywhere parallel to the overall pressure gradient, since the fluid must follow a tortuous path as it circumvents the obstacles. If the flow rates are suitably low, and if the aperture h is small relative to the characteristic distance L between the contact areas, the flow can be well approximated by "Hele-Shaw" flow (Schlichting, 1968). In Hele-Shaw flow, the fluid still has a parabolic velocity profile, and the velocity vector $\vec{u}$ at each point is still in the direction of decreasing pressure, but the local pressure gradient is not necessarily the same as the overall macroscopic pressure gradient. The velocity profile for this type of flow is given by

$$\vec{u} = \frac{-\nabla P}{2\mu} z\,(z - h)\,, \qquad (1)$$

where z is the transverse coordinate measured from the bottom wall. The pressure is found by solving the two-dimensional Laplace equation in the region of the $x-y$ plane exterior to the obstacles, i.e.

$$\nabla^2 P(x,y) = 0. \qquad (2)$$

Since there can be no flow into or out of the obstacles, the pressure field must satisfy $\partial P/\partial n = 0$ along the obstacle boundaries, where n is the outward unit normal vector. The external boundaries are typically either no-flow or constant-pressure boundaries.

METHODS OF ANALYSIS

Boundary-Element Analysis

We have used a boundary-element method to solve the Laplace equation in square regions containing contact areas of various shapes. Fixed pressures are maintained on two opposing edges of the region, and the other two sides are taken to be no-flow boundaries. Details of this method, and some computer programs, can be found in Brebbia (1978). The boundary-element calculations yield the pressure distribution throughout the flow region. The velocity vector can be found from Eq. (1), after which the total flux through the region is found by integrating the normal component of the velocity vector across one of the constant-pressure boundaries.

Analogue Measurements

Since the fluid flow is described by Laplace's equation, with the contact areas serving as impermeable boundaries, this problem is analogous to the flow of electrical current in a thin sheet with holes punched in it. Experiments were therefore carried out on such sheets to measure the overall electrical conductivity (which is the analogue of the fracture permeability) in order to validate our numerical code. For these experiments, a thin sheet of conductive paper is cut into a square and a strip of metallic paint is applied to two opposing edges. Since the conductivity of the paint is much higher than that of the paper, these edges will therefore be lines of constant potential. Holes that have the desired shapes, sizes, and locations are cut out of the sheet, and the overall conductance is measured with an ohmmeter.

Effective-Medium Theory

The problem outlined above is a typical one in the area of effective properties of heterogeneous media. The unobstructed areas between the obstacles are regions of permeability K_o (say) whereas the obstacles are regions of zero permeability, and it is desired to determine the effective macroscopic permeability K^* that can represent flow through the fracture on a length scale large enough to cover many asperities. Since this problem is governed by Laplace's equation, the method introduced by Maxwell (Carslaw and Jaeger, 1959) to predict the overall electrical conductivity of composite media can be applied. This method considers the decrease in flux due to a single obstacle of known size and shape, averages this effect over all shapes and orientations of the obstacles, and then equates the resulting decrease in flux to that which would be caused by a single circular "obstruction" that has some effective permeability K^*.

RESULTS

Circular Obstructions

Walsh (1981) used Maxwell's effective-medium approach to derive the following expression for the effective permeability of a fracture with randomly oriented circular obstructions:

$$\frac{K^*}{K_o} = \frac{1-c}{1+c}, \tag{3}$$

where c is the fractional contact area of the fracture. We have performed boundary-element calculations for fractures with circular obstructions arranged in both hexagonal (Fig. 1) and square arrays for values of c ranging from 0 to 0.25, which is the range of values encountered in rock fractures (Tsang and Witherspoon, 1981). Perhaps surprisingly, in light of its approximate nature, Walsh's expression was found to be extremely accurate. In addition to the

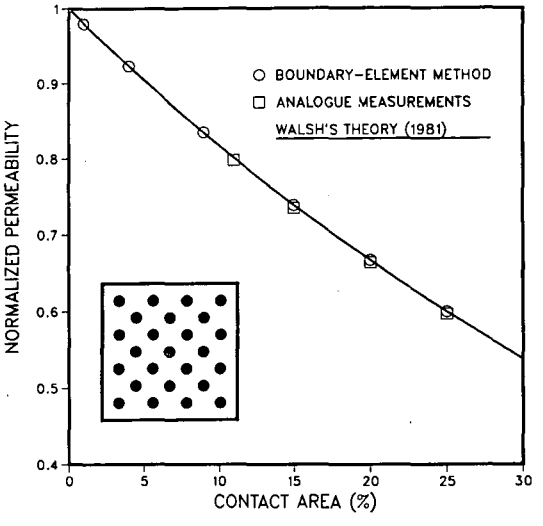

Figure 1. Normalized permeability of a fracture with circular asperities; typical asperity geometry shown in inset. [XBL 891-131]

boundary-element calculations, analogue electrical conductivity measurements were also carried out (Fig. 1); these also agreed very closely with Eq. (3).

Elliptical Obstructions

We have extended the Walsh-Maxwell effective-medium approach to fractures with elliptical obstructions (Chen et al., 1989). The ellipse is often used in modeling the physical properties of rocks (Zimmerman, 1984), in part because by varying the aspect ratio, different values of the perimeter-to-area ratio can be obtained. The basic problem that must be solved in order to apply this approach to elliptical obstructions is Laplace's equation in the region exterior to an ellipse, with a uniform potential gradient at infinity and no flow across the boundary of the ellipse. The solution to this problem can be found in Batchelor (1967), where it was derived in the mathematically equivalent but physically different context of inviscid flow across an ellipse. After averaging over all (equally likely) orientations of the obstruction with respect to the overall pressure gradient, the resulting expression for the effective permeability is

$$\frac{K^*}{K_o} = \frac{1-\beta c}{1+\beta c}, \qquad (4)$$

where $\beta = (1+\alpha)^2/4\alpha$, and the aspect ratio α (≤ 1) is defined as the ratio of the minor to major axis.

The predictions of the effective medium theory for $\alpha = 0.2$ are shown in Fig. 2, where they are compared to boundary-element calculations. The elliptical obstacles were generated by placing them on a hexagonal array and then assigning to each a randomly chosen angular orientation. Over the range of contact areas shown, the effective medium estimates are very accurate. Because cutting out the elliptical holes in the conductive sheet is an extremely laborious and painstaking procedure, only one analogue measurement was made; this value (Fig. 2) was also in relatively close agreement with the predictions of Eq. (4).

Irregular Obstructions

The shapes of asperity obstructions found in real rock fractures are of course more irregular than circles or ellipses. We have therefore used our boundary-element code to study flow around irregularly shaped obstacles such as that shown in Fig. 3. These patterns are generated by breaking up the square into a 64 × 64 rectangular grid and assigning

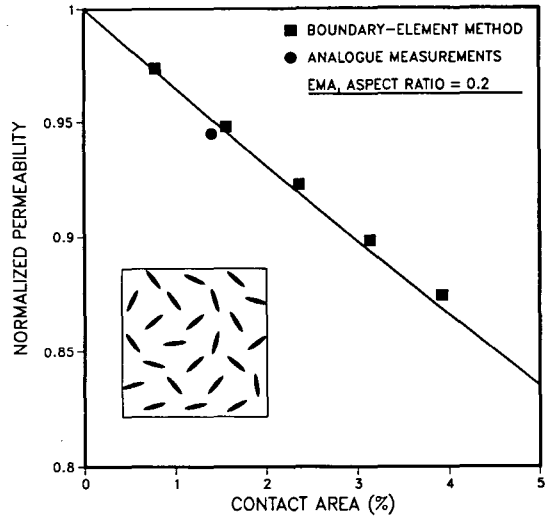

Figure 2. Normalized permeability of a fracture with elliptical asperities; typical asperity geometry shown in inset. [XBL 891-132]

each grid block to be either an obstruction zone or a flow zone. The parameter that can be altered when generating these patterns is the correlation-length parameter. The calculated permeabilities can be fit fairly well by using the elliptical-obstruction model (Eq. 4) and a value of $\alpha = 0.25$. It can be conjectured that this value of α is somehow related to the perimeter-to-area ratio of the irregular obstruction pattern; this possibility is currently being investigated.

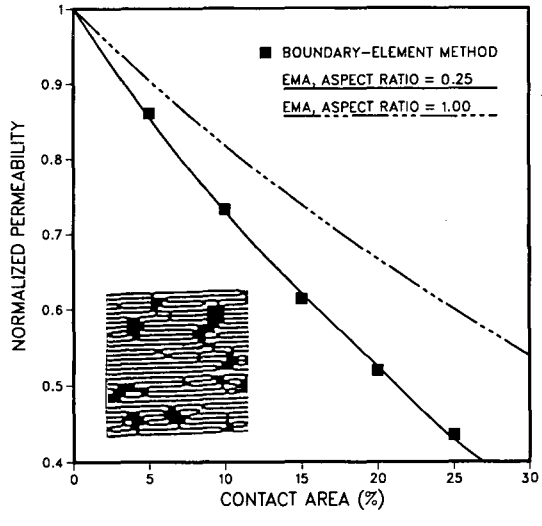

Figure 3. Normalized permeability of a fracture with irregular asperities; typical asperity geometry shown in inset. [XBL 891-133]

REFERENCES

Batchelor, G.K., 1967. Introduction to Fluid Dynamics. Cambridge University Press, New York.

Brebbia, C.A., 1978. The Boundary Element Method for Engineers. Pentech Press, London.

Brown, S.R., 1987. Fluid flow through rock joints: The effect of surface roughness. J. Geophys. Res., v. 92, p. 1337–1347.

Carslaw, H.S., and Jaeger, J.C., 1959. Conduction of Heat in Solids. The Clarendon Press, Oxford, p. 425.

Chen, D.W., Zimmerman, R.W., and Cook, N.G.W., 1989. The effect of contact area on the permeability of fractures. Presented at the 30th U.S. Symposium on Rock Mechanics, Morgantown, W.V., June 19–22, 1989.

Schlichting, H., 1968. Boundary-Layer Theory (6th ed.) McGraw-Hill, New York, p. 114.

Tsang, Y.W., and Witherspoon, P.A., 1981. Hydromechanical behavior of a deformable rock fracture subject to normal stress. J. Geophys. Res., v. 86, p. 9287–9298.

Walsh, J.B., 1981. The effect of pore pressure and confining pressure on fracture permeability. Int. J. Rock Mech. Min. Sci & Geomech. Abstr., v. 18, p. 429–435.

Zimmerman, R.W., 1984. The effect of pore structure on the pore and bulk compressibilities of consolidated sandstones (Ph.D. Thesis). University of California, Berkeley.

Analysis of Heat Transfer in a Porous Medium Due to the Natural Convection of Water near the Critical Point

B.L. Cox and K. Pruess

Fluid conditions near the critical point (374°C, 221 bars for pure water; higher temperatures and pressures for brines) may be encountered in deep zones of geothermal systems and above cooling magma bodies. Laboratory experiments have demonstrated strong enhancements in heat transfer at supercritical conditions (Dunn and Hardee, 1981). We developed special numerical techniques for modeling porous flow at near-critical conditions, which can handle the extreme nonlinearities in water properties near the critical point. Our original objective was to use the data from the Dunn and Hardee experiment to validate our simulator. Our numerical results showed strong enhancement of heat transfer at supercritical conditions; however, the heat-transfer rates obtained in the numerical simulations were considerably smaller than those reported for the laboratory experiments by Dunn and Hardee. After careful scrutiny of their experimental procedure, we concluded that the experimental conditions were not sufficiently controlled to permit quantitative comparison. We then conducted a series of numerical experiments to gain insight into conditions and parameters controlling near-critical heat transfer (Cox et al., 1988; Cox and Pruess, 1988).

NUMERICAL-SIMULATOR MODIFICATIONS

Simulations were performed with the geothermal reservoir simulator MULKOM (Pruess, 1983, 1988), utilizing the Haar equation of state for water (Haar et al., 1984). Because the full Haar et al. formulation involves many highly nonlinear terms with significant numerical cancellation in the near-critical region, we did not use it directly in the simulation. Instead, we calculated from the formulation given by Haar et al. a two-dimensional table of densities and internal energies as functions of temperature and pressure in the critical region. A bilinear interpolation scheme was used to estimate values between table values. Numerical cancellation problems from the presence of large pressures and small pressure differentials near the critical point were overcome by measuring pressure relative to a floating reference pressure. Attainment of steady-state conditions was facilitated by initializing the simulations with a set of temperatures corresponding to pure conduction between heat source and outer constant-temperature boundary.

EXPERIMENTAL DATA

The only available experimental work on heat transfer in near-critical porous convection of water is that performed at Sandia National Laboratories (Dunn and Hardee, 1981). A conceptual sketch of the experimental setup is shown in Fig. 1. A 1-liter cylindrical vessel filled with a fine silica sand (fully saturated with distilled water) was heated with electrical tape heaters on the cylinder mantle and along a thin platinum wire in the center of the vessel. The outside of the cylinder was kept at a lower temperature than the wire (approximately 2°C temperature difference), and the top and bottom of the cylinder were insulated. The steady-state temperatures were measured with embedded thermocouples. Pressures ranged from 225 to 248 bars (22.5 to 24.8 MPa), so that single-phase fluid conditions were maintained. The experimenters found an enhancement in heat transfer over a broad temperature range from 360 to 400°C, which near the critical point reached a peak of about 70 times that for pure conduction. This enhancement is expressed as the Nusselt number (Nu), a ratio of the total heat transfer to that which would be attributed to pure conduction. The method of estimating Nu in the experiment may have given misleading results. The precise location of the temperature sensors was not given, but from the sketch in their paper, it appears that the measurements were made at the mid-height of the vessel, at some distance from the heater wire. When convection occurs, a thin boundary layer forms next to the wire, and the pattern of convection is asymmetrical in the vertical direction, so that these temperature measurements would not permit a quantitatively accurate estimate of the Nusselt number.

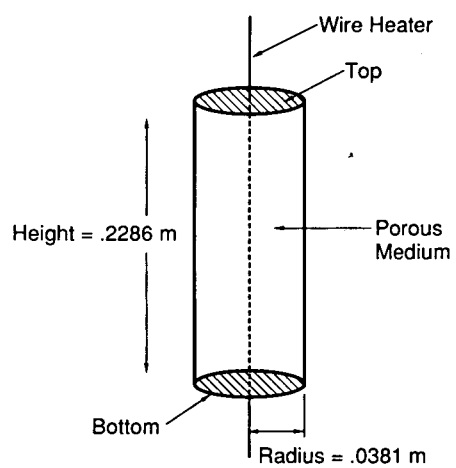

Figure 1. Cylindrical geometry for heat-transfer study. [XBL 881-10016]

NUMERICAL SIMULATIONS

Using the flow geometry and parameters shown in Fig. 1 and Table 1, we performed a series of numerical experiments to study various issues relating to near-critical heat transfer. We then examined effects of boundary conditions, aspect ratio of convecting cells, space discretization, average temperature, temperature interval, thermal dispersion, and flow channeling (Table 2). We used permeabilities up to 20 times greater than that reported in the laboratory experiments, yet the enhancements seen in the simulations (up to a factor of 5 over pure conduction) are substantially smaller than those reported from the laboratory experiment (up to a factor of 70). Furthermore, the simulations predict significant heat-transfer enhancement only for a narrow temperature interval (a few°C) whereas Dunn and Hardee reported enhancement over a broad range (20°C). None of the effects we investigated could increase heat transfer to values nearly as large as those reported by the experimenters.

CONCLUSIONS

Numerical simulations predict substantial convective enhancement of heat transfer near the critical point. Carefully controlled and instrumented laboratory experiments should be undertaken to better define the physical conditions and mechanisms for near-critical heat transfer. The possible occurrence of thick zones with near-critical heat transfer in hydrothermal convection systems deserves further study.

Table 1. Parameters used in reference case.

Temperature of wire, T	377°C
Temperature of outer wall, T_o	375°C
Average pressure, $\overline{P}$	225 bars (22.5 MPa)
Permeability, k	40 darcies
	$(40 \times 10^{-12}\,m^2)$
Porosity, ϕ	0.25
Cylinder radius, R	0.0381 m
Cylinder height, H	0.2286 m
Aspect ratio (R:H)	1:6
Rock properties	
Rock heat capacity, C_{pR}	960 kJ/kg-°C
Rock density, ρ_R	2400 kg/m^3
Rock thermal conductivity, λ_R	3.35 W/m°C

Table 2. Discretization and boundary effects.

Case	Description	Permeability, darcies (1 darcy = 1×10^{-12} m^2)	Nusselt number, Nu
1	Reference case; see Table 1. Average pressure = 225.5 bars Temperature interval = 375–377°C Table interval = 0.1°C × 0.1 bar Mesh = 21 × 15	20	1.831
		40	2.227
2	Same as case 1, but table interval = 1 bar × 0.05°C	20	1.854
		40	2.056
3	Same as case 2, but top and bottom boundaries are at constant T of 375°C	20	1.738
		40	2.077
A1	Aspect ratio = 1:3	10	1.795
		20	2.182
		40	2.742
A2	Aspect ratio = 1:2	10	1.945
		20	2.428
		40	3.150
A3	Aspect ratio = 1:1	10	2.198
		20	2.895
		40	3.956
A4	Aspect ratio = 2:1	10	2.313
		20	3.227
		40	4.794
T10	Temperature interval = 370–80°C	20	1.290
		40	1.531
T1	Temperature interval = 375.3–376.3°C	20	1.732
		40	2.153
D1	w/Dispersion	40	2.580
FC1	w/Flow channeling	40	2.609
DFC1	w/Dispersion and flow channeling	40	3.170

REFERENCES

Cox, B.L., Pruess, K., and McKibbin, R., 1988. Mathematical modeling of near-critical convection. Presented at the Thirteenth Workshop on Geothermal Reservoir Engineering, Stanford, California, January 19–21, 1988.

Cox, B.L., and Pruess, K., 1988. Numerical experiments on convective heat transfer in water-saturated porous media at near-critical conditions. Lawrence Berkeley Laboratory Report LBL-26060, preprint.

Dunn, J.C., and Hardee, H.C., 1981. Superconvecting geothermal zones. J. Volcanol. Geotherm. Res., v. 11, p. 189–201.

Haar, L., Gallagher, J.S., and Kell, G.S., 1984. NBS/NRC Steam Tables, Hemisphere Publishing Corp., Washington, D.C.

Pruess, K., 1983. Development of the general purpose simulator MULKOM. Earth Sciences Division Annual Report 1982. Lawrence Berkeley Laboratory Report LBL-15500.

Pruess, K., 1988. SHAFT, MULKOM, TOUGH: A Set of numerical Simulators for multiphase fluid and heat flow. Geotermia, Rev. Mex. Geoenergia, v. 4, no. 1, p. 185–202.

Simulated Annealing: A New Technique for Hydrologic Inversion

A. Davey, K. Hestir, K. Karasaki, J.C.S. Long, K. Nihei, M. Landsfeld, and J.E. Peterson

Site characterization uses diverse and incomplete information from geology, geophysics, and hydrology. Integration of this information into a consistent model is a major problem. In addition, the sketchy information available means that it is not possible to specify a unique model.

Lawrence Berkeley Laboratory has been developing an inversion technique that can be used to construct a system that is functionally equivalent to the observed system: its behavior matches recorded observations. This equivalent system is nonunique, which allows us to find a range of systems that behave the same way the real system behaves. We describe here how to build such a model using hydrologic well-test data. Work is in progress to incorporate additional types of information, particularly geophysical tomographic data.

The fracture-network model is built by continually modifying a base model called a "template" such that the modifications behave more and more like the observed system. For instance, we may observe real well-test behavior in the field and try to modify our model such that the equivalent well tests simulated on the model have the same results. The modifications are accomplished through a process called simulated annealing, which is a statistical technique for finding near-optimal solutions on a complicated function with many possible solutions and local minima. When we are satisfied with the modifications, new well tests can be simulated on the model as a validation.

First, the template model is developed; for example, a simple grid of line elements might be used, although the technique can be used with any configuration of conducting elements. The most efficient way to construct a template is to include in it as much a priori information as you can about the possible paths for water flow. In the case of a fractured rock, the fracture zones may dominate the hydrologic behavior, so the template should include these zones explicitly. A simple template for each fracture zone might be a plane with a square or triangular grid of conducting elements. To start with, each of these elements would be assigned the same arbitrary transmissivity and storativity. The resolution of the template is limited by computational considerations and the density of available well-test results.

The well tests can then be simulated on the model using TRINET, an advection-dispersion code developed by Karasaki (1987). This finite-element code simulates transient flow in a fracture network and is used to solve for the head distribution as a function of time in the fracture mesh created by the mesh generator. For example, the head measurements from transient constant-flux well tests can be simulated with TRINET.

We now examine the curves for head versus time obtained from the simulated well tests and scale the values of transmissivity and storativity assigned to the elements in order to achieve as good a match as possible to the observed drawdown curves. This corresponds to shifting the well-test data to match the Theis curve. We then define the "energy," Q_C, of our current model configuration (referred to as C) as the squared sum of the differences between the measured and simulated heads, taken at a set of locations at discrete time intervals as done in Carrera and Neuman (1986).

Next we change the model by switching a randomly chosen channel "on" (i.e., conducting) if it is "off" (i.e., nonconducting) or vice versa and then repeat the well-test simulation. If the changed model gives simulated well-test data closer to the real observed test values—i.e., if Q_C is decreased—then the changed model is kept. However, if Q_C is increased by the change, then the change will be kept with a certain probability, p, that is a function of a weighting factor, T (called the "temperature"), and Q_C. The temperature is decreased as the number of iterations increases to make it more and more unlikely that an unfavorable change will be accepted. At first, a high value of T allows the algorithm to jump up out of local minima and continue searching for a better region of the function. Later, lowering the temperature tends to confine the search for a minima so the algorithm can converge.

This process of accepting changes in the model is called simulated annealing. This optimization technique employs an analogy between optimizing a function with many local minima and the process of annealing a metal to reach its lowest energy state. Thus simulated annealing can be viewed as a process of minimizing an energy function over a set of possible configurations of elements.

THEORY OF ANNEALING

Simulated annealing is defined in analogy with the thermodynamic process of cooling or annealing

of a metal (Kilpatrick et al., 1983; Tarantola, 1987). We define Q as an energy function, C as a configuration of elements, and M as the finite set of all possible elements, ordered from 1 to M. A system composed of atoms of a metal in thermal equilibrium at a temperature T has a range of possible energies that depend on the configuration. One possible probability distribution for the range of energies is the Boltzmann distribution,

$$P(Q(C)) \propto e^{-Q(C)/bT},$$

where b is the Boltzman constant.

Thermodynamically, low energy states are more likely, but at any temperature there is still some chance of being in a high energy state. Metropolis et al. (1953) used this conception of energy states to simulate changes in a thermodynamic system. The system was assumed to have the option to change from C_1 to C_2 with probability P:

$$P = \begin{cases} 1 & \text{if } Q(C_1) - Q(C_2) > 0, \\ \exp\{-[Q(C_2) - Q(C_1)]/T\} & \text{if } Q(C_1) - Q(C_2) < 0. \end{cases}$$

Thus the system would always move to a new configuration if it was of lower energy and would sometimes move to a new configuration of higher energy. This allowed the system to move out of a local or global minima in the energy function. Simulated annealing uses an analogy with these thermodynamic systems to search for a global minima.

To use simulated annealing on a general problem, one needs a set of possible configurations, a way of randomly changing the configurations, a function one would like to minimize, and an annealing schedule (sequence of temperature changes) (Press et al., 1986). The algorithm can be written in four steps.

1. Randomly select a beginning configuration C from the set.
2. Randomly select a pipe, p, from M. If p is in C, delete it; if p is not in C, add it. This is the new configuration C'.
3. Calculate $Q(C)$ and $Q(C')$.
   If $Q(C) > Q(C')$, then keep C' with probability 1 if $Q(C) - Q(C') > 0$ or with probability

   $$\exp\{-[Q(C_2) - Q(C_1)]/T\}$$

   if $Q(C) - Q(C') < 0$; otherwise, keep C.
4. If the end of stage k of the annealing schedule has not been reached, return to step 2, and continue. If the last iteration of stage k was reached, reduce T to T', return to step 2, and continue. If the last stage of the annealing schedule was reached, stop if no change was made in the configuration after some large number of iterations.

RESULTS

To test this technique, we made up a "real" fracture network, shown in Fig. 1a. Then we simulated "real" well tests by pumping from well A and observing heads at wells B through G. These cross-hole well-test results were used as our observed hydrological response. Then a square mesh (Fig. 1b) was used as a template model for the simulated annealing inversion. A resulting equivalent system channel model is given in Fig. 1c; the curve for energy function versus iteration number for the simulated system is shown in Fig. 2.

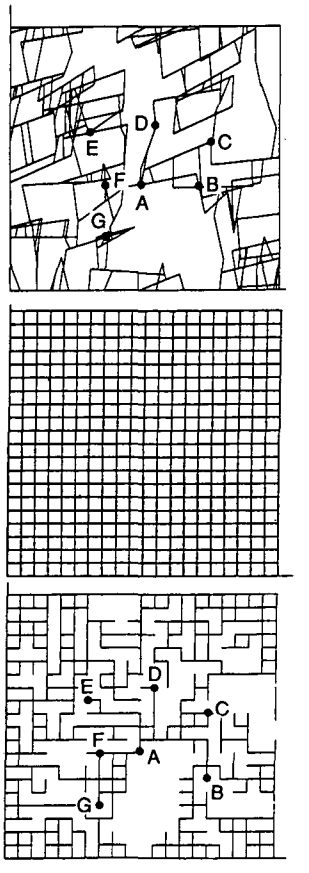

Figure 1. **(a)** A "real" fracture network, for which "real" data have been generated on a well test in hole A and monitoring in holes B through G. **(b)** The template model. **(c)** The pattern of conductors resulting from annealing. [XBL 891-6142]

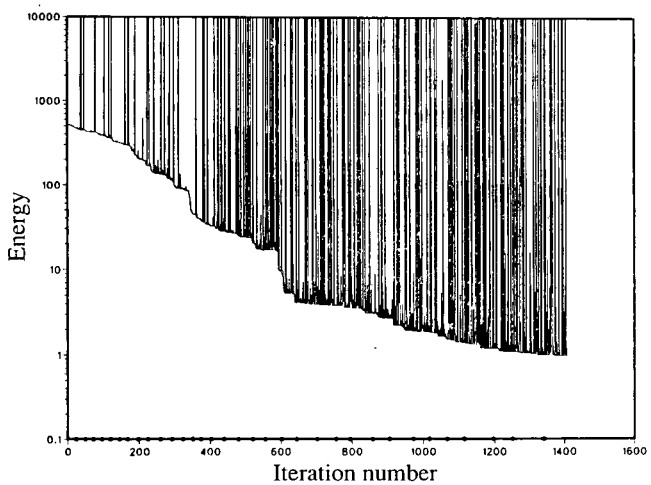

Figure 2. Energy as a function of iteration number. [XBL 895-2032]

Examination of Fig. 1c shows that the basic pattern of connectivity between the wells has been reproduced. By repeating the process it would be possible to come up with another possible configuration that matched the data. In this way it would be possible to study how well we have been able to define the system with the available tests. Moreover, given new tests not included in the annealing process would allow us to validate a model such as that in Fig. 1c. We could simulate this new test and see if our model predicts the observed response.

Preliminary results for using steady-state cross-hole well tests in annealing are good. However, much additional work must be done before equivalent discontinuum modeling, using discrete channel networks and simulated annealing, can integrate the wide variety of information available into one consistent set of models. We are currently working to incorporate tracer test results, which should offer a large advantage over diffusive pressure tests.

We also are incorporating geological and geophysical data into the inversion process. This is most straightforwardly done by controlling the construction of the base model. However, it is also possible to construct an energy function that is a weighted combination of energy functions for different phenomena. The practical limitation is that we must be able to forward-model the phenomena. For example, if we were to forward-model the seismic travel times, we would include a term in the energy function to account for the delay experienced by an acoustic wave passing from one point in the rock to another, assuming that the wave is delayed by each conductor through which it passes. Thus the energy of the system would be the sum of the squared differences between observed and predicted delays. As this delay has more to do with the elastic properties of the medium than the fluid conductance, we would probably not weight this term of the energy function very high. However, this technique does allow us to include certain data, such as seismic profiling data, directly into the inversion.

REFERENCES

Carrera, J., and Neuman, S.P., 1986. Estimation of aquifer parameters under transient and steady state conditions. 2. Water Resour. Res., v. 22, no. 2, p. 199–210.

Karasaki, K., 1987. A new advection-dispersion code for calculating transport in fracture networks. *In* Earth Sciences Division Annual Report 1986. Lawrence Berkeley Laboratory Report LBL-22090, p. 55–58.

Kilpatrick, S., Gelatt, D.C., and Vecchi, M.P., 1983. Optimization by simulated annealing. Science, v. 220, p. 671–680.

Metropolis, N., Rosenbluth, A., Rosenbluth, M., Teller, A., and Teller, M., 1953. Equations of state calculations by fast computing machines. J. Chem. Phys., v. 21, 1953.

Press, W.H., Flannery, B.P., Teukolsky, S.A., and Vetterling, W.T., 1986. Numerical Recipes. Cambridge University Press, p. 326–334.

Tarantola, A., 1987. Inverse Problem Theory. Elsevier, New York.

Design Considerations for the Dixie Valley Tracer Test

C. Doughty and G.S. Bodvarsson

A tracer test for the Dixie Valley, Nevada, geothermal resource was conducted in order to study the fluid-flow paths that will develop under typical operating conditions. During the test six production wells provided the power plant with steam sufficient for generation of 60 MW_e, requiring fluid production at a rate of approximately 600 kg/s. About 75% by mass of the extracted fluid was reinjected into the reservoir, using four injection wells. Tracer was added to the injected fluid for a 20-minute period, and the produced fluid was subsequently monitored for the tracer.

During the design phase of the tracer test we made calculations to help determine the quantity of tracer to inject and where and when to look for breakthrough. The calculations involved mathematically modeling the test using a three-dimensional porous-medium model developed in 1986 and 1987 by the Oxbow Geothermal Corporation (Oxbow, 1986, 1987). The mathematical model assumes that fluid flow at the Dixie Valley geothermal field is primarily through high-permeability channels associated with the SW-NE trending range-front fault that separates Dixie Valley from the adjacent Stillwater Range. The model was developed from an integrated analysis of geological, geochemical, and seismological data, natural-state modeling of the system, and modeling of two extensive flow tests. The rather coarse spatial discretization, which is deemed appropriate for natural-state, flow-test, and production modeling, is less accurate for tracer-test modeling, so the following results should be viewed as general estimates of future behavior rather than detailed predictions.

The computer program MULKOM (Pruess, 1983), developed at Lawrence Berkeley Laboratory, was used for the calculations. MULKOM uses the integral-finite-difference method to calculate coupled flows of water, carbon dioxide (in liquid and vapor phases), and heat in fractured/porous media. For the modeling of the proposed Dixie Valley tracer tests we introduced carbon dioxide as a conservative tracer dissolved in the liquid phase. Under natural-state and expected exploitation conditions at Dixie Valley, water will remain single-phase liquid, so that CO_2 in liquid is an acceptable and simple way to simulate a tracer. Further details of this work may be found in Doughty and Bodvarsson (1988).

POROUS-MEDIUM VERSUS FRACTURED/POROUS-MEDIUM MODELS

The first case considered used the porous-medium model described above. A 5-year simulation was carried out in which a 51-MW_e power production rate was prescribed. MULKOM calculated that an extraction rate of 503 kg/s of fluid would be required to generate power at that rate; 75% of the fluid produced was reinjected. After 1 month of production a 10-day slug of tracer was injected at a constant concentration C_0 into each of the four injection wells. Figure 1 shows the tracer concentrations in the injection and production wells as a function of time. The large volume of the elements containing the wells resulted in a large dilution of concentration, and there were still appreciable level of tracer in these elements after several years. This variation should be viewed as representing the region around the well rather than the well itself. With the above considerations in mind, the most valid interpretation of the modeled tracer concentrations is not to believe absolute values of either the breakthrough times or concentration levels but to consider the responses of the different production wells relative to one another. In production well 76-7, tracer breakthrough occurred about 2 months after tracer injection with a maximum concentration occurring after about 3 years (Fig. 1b). Tracer breakthrough in wells 84-7 and 74-7 occurs about 4 to 6 months after tracer injection but at very low concentrations; the breakthrough in well 73-7 occurs after about 1.5 years (Fig. 1c). In wells 84-7, 74-7, and 73-7 tracer concentration was still increasing after 5 years. Although these times are fictitious because of the coarse mesh used, the earlier response to the tracer pulse indicates that well 76-7 is better connected to the injection wells. Our calculations show no noticeable tracer in wells 27-33 and 45-33, indicating low connectivity.

After the above preliminary calculation was made, further details of the tracer test were incorporated in the model: the duration of the tracer injection was decreased from 10 days to 20 minutes, and power generation was increased from 51 to 60 MW_e. With the increase in power generation, a total fluid production rate of 592 kg/s was required; total injection-well capacity limited reinjection to 61% of

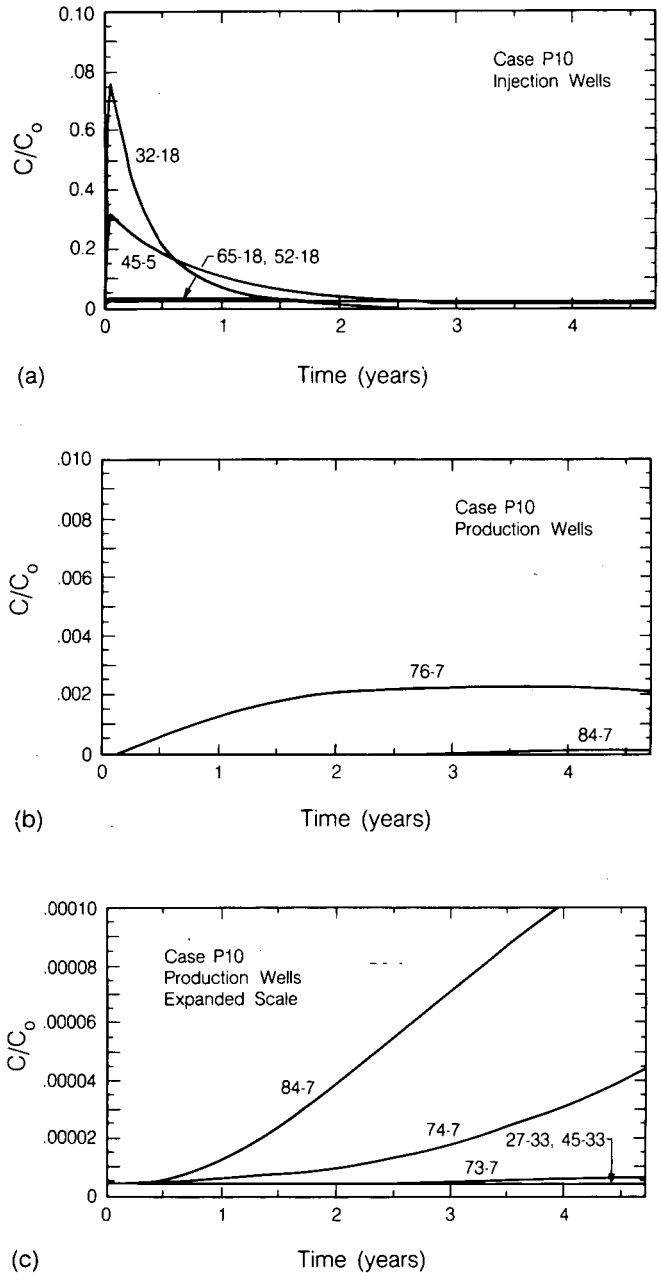

Figure 1. Tracer concentration calculated using the porous-medium model for the injection wells (**a**) and the production wells (**b** and **c**). [XBL 896-5815]

the fluid produced. With the shorter tracer injection period, far less tracer was injected and the porous-medium model showed such a small tracer response in the producing wells that the use of a more realistic fractured/porous-medium model was necessary.

A simplified fractured/porous-medium model was derived from the porous-medium model as follows. Assuming a fracture porosity of 1%, the volume of all elements was decreased by a factor of 100, total compressibility (rock plus water) was increased by a factor of 100, and rock heat capacity was increased by a factor of 100. This allows an approximate calculation of fracture flow, maintaining the appropriate pressure decline and thermal front movement. However, it is important to note that the assumption of 1% fracture porosity is only a first-order estimate, which greatly affects the results obtained. Thus all results should be considered only as first-order estimates.

The fractured/porous-medium model was used to calculate a 6-month 60 MW_e production period with 61% injection. A 20-minute tracer slug was added to all injection wells after 31 days of production. Figure 2a shows the tracer concentrations in the injection wells. Figured 2b shows the tracer concentrations in the production wells. All production wells showed some tracer within 6 months, although for well 73-7 the level was very low. Figure 2c shows early-time behavior at the production wells. Tracer breakthrough times of 1, 4, and 6 days after tracer injection are estimated for wells 76-7, 84-7, and 74-7, respectively. Tracer breakthroughs in wells 45-33 and 27-33 occur after a much longer time, about 30 days after tracer injection. Tracer breakthrough in well 73-7 is estimated to be the slowest and tracer concentration the lowest.

To better study the connectivity between individual injection and production wells, simulations were done in which tracer was injected into only one injection well at a time. These simulations are carried out for a 1-year period. Results are summarized in Table 1.

ESTIMATION OF AMOUNT OF TRACER NEEDED

Besides predicting breakthrough times, these modeling studies may be used to estimate the minimum amount of tracer necessary for detection. The mass of tracer injected in the numerical model is M_{inj}^N. The peak concentration at a production well is C_{pk}^N; it occurs at time t_{pk}^N. The time at which tracer is first observed at a production well is t_{bt}^N. Times are measured relative to the start of tracer injection. The quantities M_{inj}^N and C_{pk}^N can be used to determine maximum dilution M_w, which is defined as the mass of water in the region swept by the tracer at breakthrough,

$$M_w = \frac{M_{inj}^N}{C_{pk}^N}.$$

The tracer detection limit, C_{dl}, is considered to be 60 ppb, although in reality the actual detection limit of

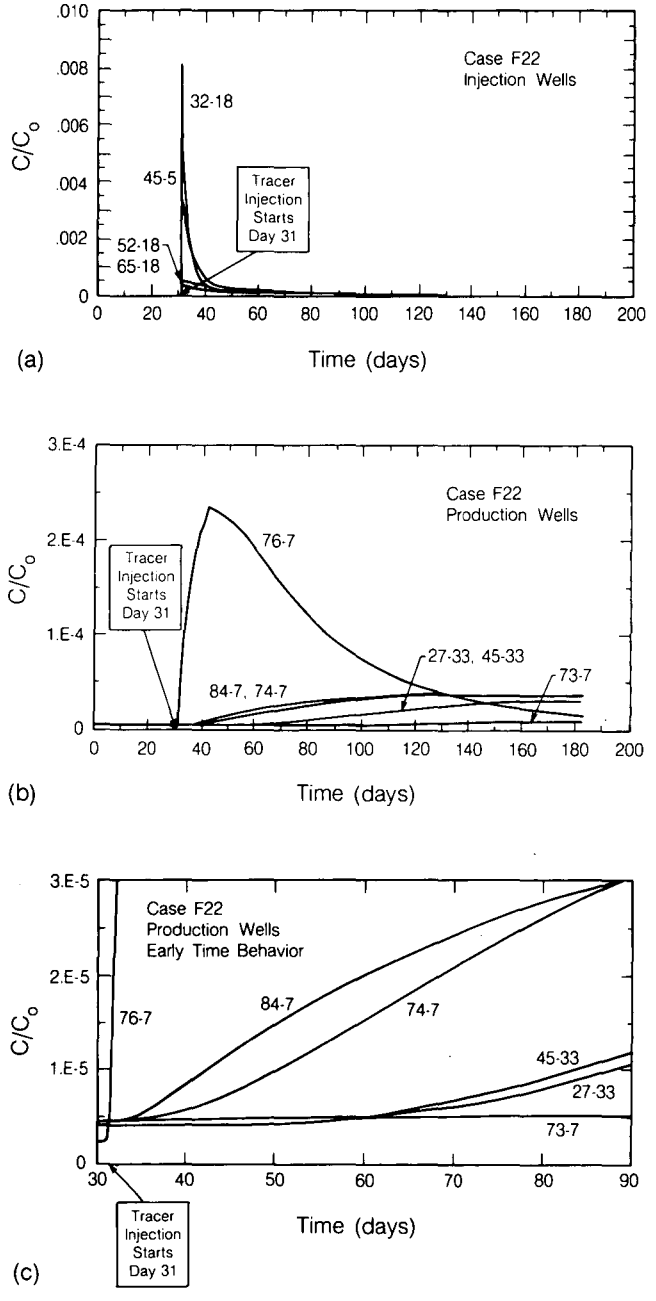

Figure 2. Tracer concentration calculated using the fractured-porous medium model for the injection wells (**a**) and the production wells (**b** and **c**). [XBL 896-5814]

most of the tracers planned for Dixie Valley is about 3 times lower. Thus the results and analyses include a safety factor of 3. The required injected mass to obtain a peak tracer concentration of C_{dl} = 60 ppb (= 6×10^{-8}) is

$$M_{inj} = C_{dl} M_w = C_{dl} \frac{M_{inj}^N}{C_{pk}^N}.$$

Table 1. Summary of model results.

Inj. well	Prod. well	t_{bt}^N (days)	t_{pk}^N (days)	M_w (10^9 kg)	M_{inj} (kg)
65-18	76-7	11	102	6.4	382
	84-7	15	148	7.7	460
	74-7	12	125	7.3	439
	73-7	34	171	427.0	25,600
	27-33	–	–		
	45-33	–	–		
45-5	76-7	–	–		
	84-7	49	216	25.1	1,506
	74-7	49	193	21.4	1,284
	73-7	49	273	13.9	837
	27-33	19	171	4.5	270
	45-33	19	159	4.4	265
32-18	76-7	1	11	0.539	32
	84-7	4	45	10.0	602
	74-7	9	114	71.4	4,283
	73-7	5	57	206.0	12,370
	27-33	–	–		
	45-33	–	–		
52-18	76-7	3	51	2.7	162
	84-7	6	91	4.2	250
	74-7	4	68	3.5	208
	73-7	9	91	347.0	20,810
	27-33	–	–		
	45-33	–	–		

DISCUSSION

The wide range of values of M_{inj} for each injection well, listed in Table 1, shows that the amount of tracer required for 60 ppb detection depends strongly on which production well is being monitored. For example, the results obtained suggest that for tracer injected into well 45-5 to be detected at wells 84-7, 74-7, and 73-7, about 1500 kg of tracer should be injected. However, the same tracer may be detected in wells 27-33 and 45-33 with only 300 kg of tracer injected. Thus one must weigh the cost of the tracer versus the number of wells that will detect it to obtain the best estimate for the amount of tracer that should be injected.

One must recognize the uncertainties involved with these calculations. The relationship between fracture porosity and both tracer breakthrough time and peak concentration is approximately linear. That is, a fracture porosity of 5% instead of 1% would yield tracer breakthrough times about 5 times longer and peak concentrations about 5 times smaller than those given here. Thus the estimates given are very uncertain and should only be used as relative guidelines.

Even if fracture porosity were known accurately, the present results would have to be used with caution because numerical codes tend to smear out chemical fronts due to numerical dispersion, causing the calculated peak concentrations to be many times too low. This smearing is rather obvious when one inspects the computed tracer curves, which show very diffuse maxima.

REFERENCES

Doughty, C., and Bodvarsson, G.S, 1988. Some design considerations for the proposed Dixie Valley tracer test. Lawrence Berkeley Laboratory Report LBL-25971.

Oxbow, 1986. Dixie Valley reservoir assessment. Oxbow Geothermal Corporation, Reno, Nevada.

Oxbow, 1987. Six-well flow test, Dixie Valley, Nevada July 23, 1986–July 1, 1987. Oxbow Geothermal Corporation, Reno, Nevada.

Pruess, K., 1983. Development of the general purpose simulator MULKOM. *In* Earth Sciences Division Annual Report 1982. Lawrence Berkeley Laboratory Report LBL-15500.

Development and Use of CPT—A Coupled Fluid and Heat-Flow Code with Simplified Chemical Transport and Reactions

C. Doughty, D.C. Mangold, and C.F. Tsang

A series of hydrochemical modeling studies have been carried out to investigate the effects on fluid flow of permeability changes caused by chemical reactions between injected fluid and the aquifer formation. Such effects may be important in a number of practical groundwater projects, such as the safety analysis of disposal of toxic liquid waste by deep underground injection.

CODE DEVELOPMENT

The numerical model CPT (Mangold and Tsang, 1984) was modified and used for these studies. Model CPT is an extension of the well-verified, well-validated, and much-used code PT (Bodvarsson, 1982). Code PT calculates fully coupled fluid and heat flow in water-saturated three-dimensional porous or fractured/porous media. The integral-finite-difference method is used for space discretization, and time stepping is done implicitly. In CPT solute transport is calculated explicitly with full upstream weighting, using the fluid-flow field at each time step. Chemical reactions and permeability changes are calculated schematically. The original version of CPT considered solute transport by advection only. The present version incorporates diffusion and longitudinal dispersion as well.

Model CPT has been verified against two one-dimensional analytical solutions, one for radial geometry and one for linear geometry (Javandel et al., 1984). Figure 1 shows CPT results and the linear-geometry solution. In this problem a steady fluid flow of 1 m/d in the positive x direction passes a chemical source of concentration C_0 at $x = 0$. The dispersivity of the system is assumed to be 10 m. The mesh spacing used in CPT is 2 m. The agreement between the CPT-calculated profile and the analytical solution is excellent.

Figure 1 also shows the CPT-calculated profile for a hypothetical "advection-only" case where dispersivity is zero. The comparable analytical solution would be a step function, so the spread in the calculated curve is solely due to numerical dispersion. Mesh spacings of 5, 15, 20, 30, 50, and 100 m have been used to examine the sensitivity of the results to numerical dispersion. The 5-m mesh results are very similar to the 2-m mesh results shown above. As mesh spacing increases beyond 5 m, the concentration profiles become more diffuse, but the dependence on mesh size is much smaller for cases with nonzero values of dispersivity than for advection-only cases.

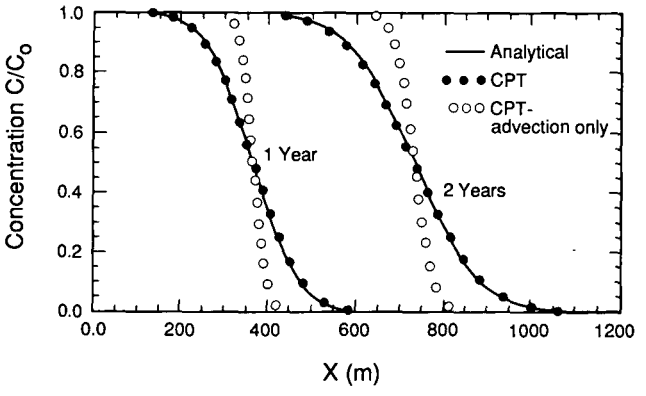

Figure 1. Comparison of dimensionless concentration profiles calculated by CPT and an analytical solution. [XBL 891-7447]

CASE STUDIES

A series of two-dimensional ($r - z$) calculations have been made to examine some of the interesting possibilities in deep injection of toxic wastes. Table 1 outlines the calculations made. In each case two hypothetical chemicals, C_1 and C_2, are injected into a 100-m-thick layer overlain by a layer with 100 times lower permeability and underlain by an impermeable layer. The injected water has a temperature of 20°C, and the average aquifer temperature is 80°C. Chemical C_1 is nonreactive, so it acts as an ideal tracer, delineating the hydrodynamic front. Chemical C_2 reacts with C_3, an immobile species initially present in various parts of the system, to form C_4, an immobile species that changes permeability.

Case 1 is a base case in which no C_3 is initially present in the system, so C_2 does not react.

Case 2 considers a uniform initial distribution of C_3 in the upper layer and a product C_4 that increases permeability by a factor of 100. Figure 2 shows the concentration distribution of C_1 and C_2 after 6 years of injection. We see that the injected fluid has penetrated about 65 m into the upper layer. This is a great increase over the base case, in which fluid penetrates only 30 m during the same time period.

Table 1. Two-dimensional calculations made with CPT.

Case	Upper layer	Lower layer
1	No R and no PC	No R and no PC
2	Reactive, $k \rightarrow k \cdot 100$	No R and no PC
3	Reactive, $k \rightarrow k/100$	No R and no PC
4	No R and no PC	Reactive lens 20-m-thick, $k \rightarrow k \cdot 10$

Note: R = reactions between injected fluid and formation. PC = permeability changes; k = permeability value.

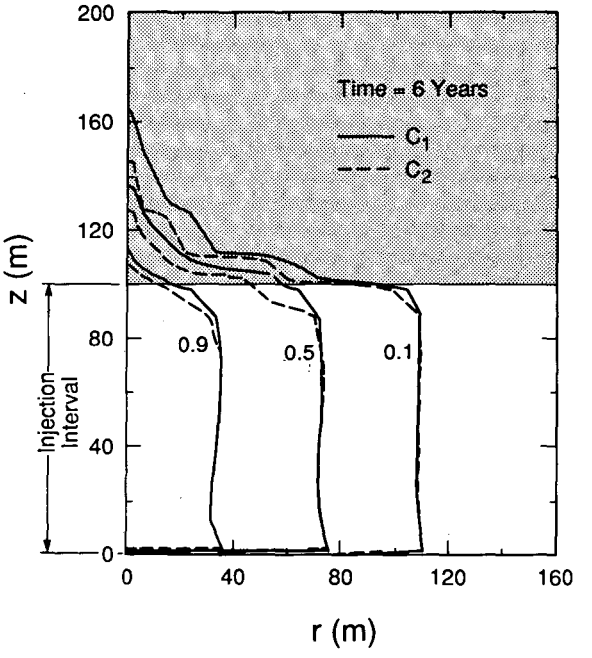

Figure 2. Dimensionless concentration contours after 6 years of injection for Case 2. The shaded region shows the initial distribution of C_3. [XBL 891-7446]

Case 3 considers the same initial distribution of C_3 as in Case 2, but product C_4 decreases permeability by a factor of 100 rather than increasing it. The penetration of the injected fluid into the upper layer is decreased to about 10 m after 6 years of injection.

Case 4 considers a uniform initial distribution of C_3 in a 20-m-thick lens in the lower layer and a product C_4 that increases permeability by a factor of 10. A wellbore model must be used to correctly partition injected flow into various rows of the lower layer. When the reaction occurs, flow into the lens is enhanced by the permeability increase. Not only does increased flow from the well enter the lens, but flow from above and below the lens enters the lens. Because this fluid contains C_2 (unreacted, since there is no C_3 outside the lens), the $C_2 - C_3$ reaction is enhanced at the upper and lower edges of the lens, with a corresponding permeability increase as more C_4 is produced there. Subsequently, greater injected flow enters the lens at the edges, leading to the concentration distribution shown in Fig. 3.

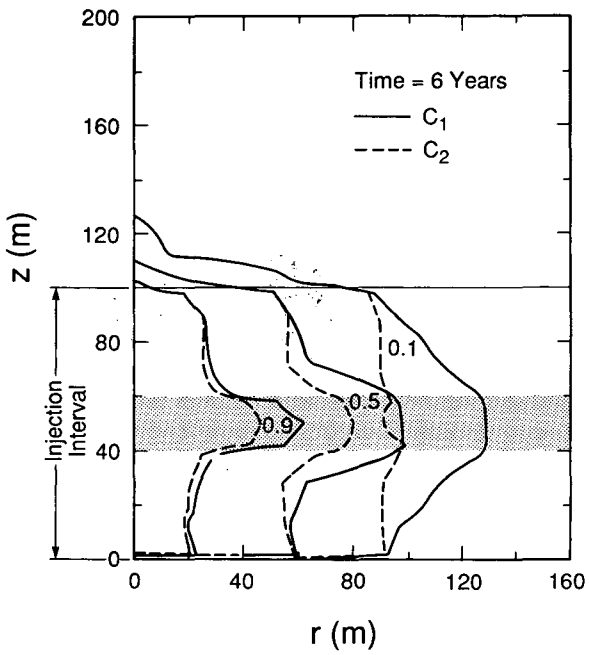

Figure 3. Dimensionless concentration contours after 6 years of injection for Case 4. The shaded region shows the initial distribution of C_3. [XBL 891-7445]

REFERENCES

Bodvarsson, G.S., 1982. Mathematical modeling of the behavior of geothermal systems under exploitation (Ph.D. thesis). Lawrence Berkeley Laboratory Report LBL-13937.

Javandel, I., Doughty, C., and Tsang, C.F., 1984. Groundwater Transport: Handbook of Mathematical Models. Water Resources Monograph 10, American Geophysical Union, Washington, D.C.

Mangold, D.C., and Tsang, C.F., 1984. A study of nonisothermal chemical transport in geothermal systems by a three-dimensional, coupled, thermal and hydrologic parcel model. *In* Earth Sciences Division Annual Report 1983. Lawrence Berkeley Laboratory Report LBL-16920.

A Similarity Solution for Two-Phase Fluid and Heat Flow near Buried Nuclear Waste Packages

C. Doughty and K. Pruess

The Nevada Nuclear Waste Site Investigations (NNWSI) project is investigating the feasibility of constructing a geologic repository for high-level nuclear waste at Yucca Mountain, Nevada, in a partially saturated, highly fractured volcanic formation. Several recent mathematical modeling studies (Pruess et al., 1985; Doughty and Pruess, 1988) have examined the thermohydrologic behavior surrounding a repository in this geologic setting. Undisturbed conditions are such that temperature is well below the saturation temperature, so water is primarily in the liquid phase, and the initial heat transfer from a waste package is mainly conductive. As temperatures around the repository increase to the saturation temperature, evaporation increases and vapor partial pressure becomes appreciable. Heat-pipe effects may contribute to or even dominate heat transfer in this regime. With time the heat pipe moves away from the waste packages, leaving a gas-phase zone in which heat transfer is again conduction-dominated. The conditions surrounding a waste package at some time after emplacement are shown schematically in Fig. 1.

In the heat-pipe region, heat transfer is primarily convective. Near the heat source liquid water vaporizes, causing pressurization of the gas phase and flow of the gas phase away from the heat source. The water vapor condenses in cooler regions away from the heat source, where it deposits its latent heat of vaporization. This sets up a saturation profile, with liquid saturation increasing away from the heat source. The saturation gradient drives the backflow of the liquid phase toward the heat source by means of capillary forces. The liquid then vaporizes again and repeats the cycle. This convective heat transfer is very efficient compared with conduction, so it is accompanied by very small temperature gradients.

This article summarizes a semianalytical solution to an idealized version of the problem of fluid and heat flow near high-level nuclear waste packages

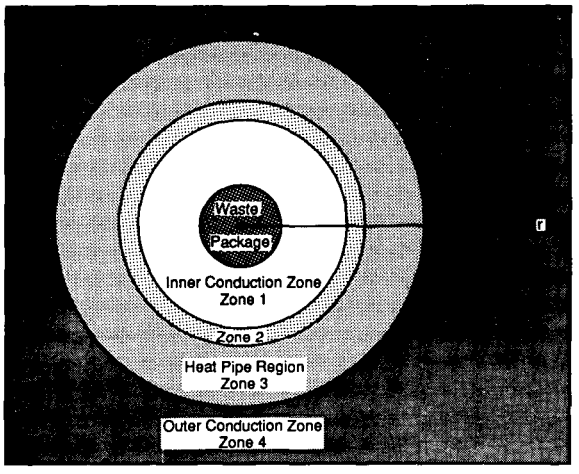

Figure 1. Schematic of the conditions achieved at some time after waste emplacement (not to scale). Water is primarily in the liquid phase in zone 4, because $T < T_{sat}$; two-phase conditions prevail in zones 2 and 3, with $T \approx T_{sat}$; fluid in zone 1 is in the gas phase, with $T > T_{sat}$. [XBL 8611-12738B]

(Doughty and Pruess, 1989). We are interested in how an infinite homogeneous porous medium with uniform initial conditions will behave in response to the emplacement of an infinitely long linear heat source of constant (time-independent) strength. Gravity effects are neglected, so that the system has a one-dimensional radial symmetry. With these simplifications, the coupled partial differential equations governing fluid and heat flow for radial geometry can be transformed into simpler ordinary differential equations through the use of a similarity variable, $\eta = r/\sqrt{t}$. This change of variable is known as the Boltzmann transformation in heat-conduction problems. It has been applied to the thermohydrologic behavior of geologic media by O'Sullivan (1981), who used it to analyze geothermal well-test data. Other researchers also have used the similarity concept for this purpose but limited themselves to simplified thermodynamic relationships to allow quasianalytic solutions.

Following O'Sullivan (1981), we consider the fully nonlinear problem with realistic thermodynamic relationships, which requires a numerical integration of the coupled differential equations. The main difference from O'Sullivan's treatment is that the mass-flux boundary condition at $r = 0$, appropriate for geothermal production or injection wells, is here replaced by a heat-flux boundary condition. Furthermore, we include capillary pressure and heat-conduction effects. These are unimportant for the geothermal well-test problem but are essential for the heat-driven problem considered here. Our general mathematical treatment includes two fluid components, water and air, although the specific solutions implemented so far are for water only.

After the similarity transformation, the problem is posed as a set of four coupled ordinary differential equations. Solution of the equations is straightforward in principle, by numerically integrating from $\eta = 0$ to $\eta = \infty$, but in practice several complications arise that require special numerical techniques. One difficulty is posed by the nature of the boundary conditions, which specify the value of some variables at $\eta = 0$ and others at $\eta = \infty$; thus no complete set of starting values is available for integration. The solution to this problem is to use an iterative integration scheme, known as the shooting method (Press et al., 1986). At the lower limit of the integration, values are guessed for the missing boundary conditions, and the numerical integration is carried out. At the upper limit of the integration the values of the variables are compared with the specified boundary conditions. A Newton-Raphson iteration is used to find improved values for the missing boundary conditions at $\eta = 0$, and the integration is repeated. This procedure continues until the value of each variable at $\eta = \infty$ matches the specified boundary condition there.

Figure 2 shows an example of the output of the similarity solution. The boundary conditions and some of the material properties used are shown in Table 1. The horizontal axis is $z = \ln(\eta) = \ln(r/\sqrt{t})$, so these profiles may be thought of as spatial profiles for a given time, with radial distance increasing from left to right, or as a time sequence for a given point in space, with time increasing from right to left. Figure 2a shows temperature, pressure, and liquid-saturation profiles. The near-isothermal two-phase zone ($-12 < z < -9.5$) indicates that convective heat transfer (the heat pipe) accounts for most of the heat transfer there, whereas the larger linear temperature gradients in the single-phase zones show that heat transfer is conduction-dominated there.

Figure 2b shows the mass and heat flows. Heat flow, Q_e, is specified to be 200 W/m at $z = -\infty$. Total mass flow, Q_w, consists of liquid and gas-phase flows, $Q_w = Q_l + Q_g$. In the gas-phase zone ($z < -12$) there is essentially no mass flow. In the two-phase zone there is little net mass flow, but large, balanced liquid and vapor counterflow. In the liquid-phase region beyond the heat pipe ($z > -7$) there is liquid flow away from the heat source, which arises because the vapor forming near the heat source is much less dense than the liquid water it replaces, requiring a net outflow from the system.

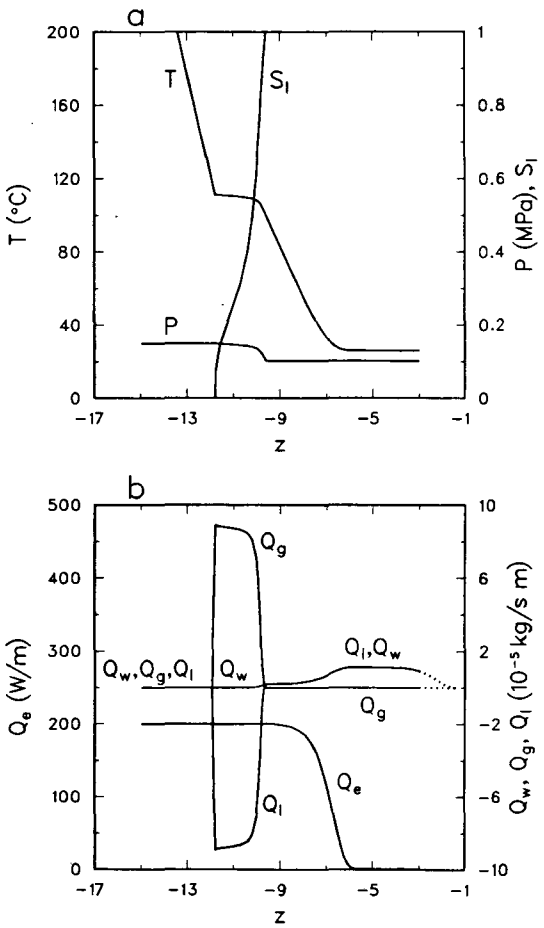

Figure 2. Temperature, pressure, and saturation profiles (**a**) and heat, mass, liquid, and gas-flow profiles (**b**) for the problem described in Table 1. [XBL 8811-4029]

Table 1. Boundary conditions and material properties used for the similarity-solution results shown in Fig. 2.

Boundary conditions	
$z = \ln(\eta) = -\infty$	$Q_{w0} = 0$
	$Q_{e0} = 200$ W/m
$z = \ln(\eta) = +\infty$	$P_0 = 101325$ Pa
	$T_0 = 26$°C
Material properties	
Intrinsic permeability	10^{-13} m^2
Porosity	0.40
Relative permeability	
liquid	S_l^3
vapor	S_g^3

The semianalytical similarity solution has been compared favorably with results of the numerical model TOUGH (Pruess, 1987), as shown in Fig. 3. The intrinsic permeability used for this case is 100 times smaller than that shown in Table 1, and linear rather than cubic relative-permeability curves have been used. The smaller value of intrinsic permeability increases the pressure and temperature of the heat pipe and increases the relative importance of conduction to convection, as evidenced by the larger temperature gradient in the heat-pipe region as compared with that in Fig. 2. Lower intrinsic permeability also tends to shorten heat-pipe length, but in this case the effect is counteracted by the linear relative-permeability curves, which increase heat-pipe length as compared with the cubic relative-permeability curves.

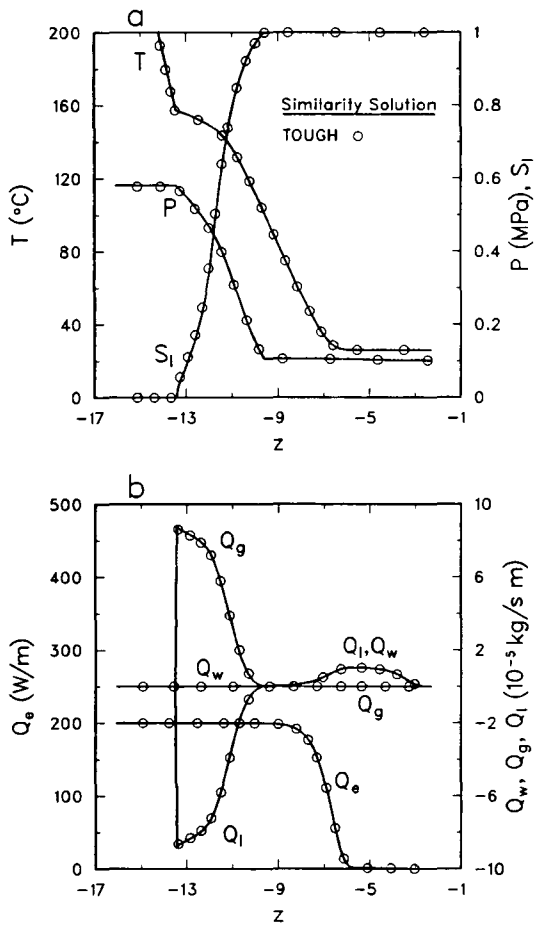

Figure 3. Temperature, pressure, and saturation profiles (**a**) and heat, mass, liquid, and gas-flow profiles (**b**) calculated using the similarity solution and the numerical model TOUGH. [XBL 8811-4025]

REFERENCES

Doughty, C., and Pruess, K., 1988. A semianalytical solution for heat pipe effects near high-level nuclear waste packages buried in partially saturated geological media. Int. J. Heat Mass Transfer, v. 31, no. 1, p. 79–90.

Doughty, C., and Pruess, K., 1989. A similarity solution for two-phase fluid and heat flow near high-level nuclear waste packages emplaced in porous media. Submitted to Int. J. Heat Mass Transfer.

O'Sullivan, M.J., 1981. A similarity method for geothermal well test analysis. Water Resour. Res. v. 17, no. 2, p. 390–398.

Press, W.H., Flannery, B.P., Teukolsky, S.A., and Vetterling, W.T., 1986. Numerical Recipes: The Art of Scientific Computing. Cambridge University Press, New Rochelle, New York, Chapter 16.

Pruess, K., 1987. TOUGH user's guide. U.S. Nuclear Regulatory Commission Report NUREG/CR-4645, Washington, D.C. (Also available as Lawrence Berkeley Laboratory Report LBL-20700.)

Pruess, K., Tsang, Y.W., and Wang, J.S.Y., 1985. Modeling of strongly heat driven flow in partially saturated fractured porous media. *In* Memoirs, International Association of Hydrogeologists, v. XVII, p. 486–497.

Buoyancy-Driven Flow of Gas in the Unsaturated Zone Due to the Evaporation of Volatile Organic Compounds

R.W. Falta, I. Javandel, K. Pruess, and P.A. Witherspoon

At many sites in the United States and other countries, groundwater supplies are threatened by contamination from volatile organic compounds (VOC), such as solvents and hydrocarbon fuels. These contaminants may enter the ground as separate-phase liquids as a result of chemical spills, chemical waste burials, or leaking storage tanks.

During the migration of these liquids through the unsaturated zone, a certain amount of the liquid will be retained in the soil by capillary forces. This trapped fraction, known as the residual saturation, may occupy from about 4 to 20% or more of the available pore space. The fate of this trapped liquid in the unsaturated zone is determined by the degree of evaporation and transport in the gas phase, dissolution and transport in the aqueous phase, and chemical and biological reactions. Although the organic liquid may be trapped in the unsaturated zone above the water table, chemical transport in the gas and aqueous phases may result in contamination of the underlying groundwater. In locations where the depth to the water table is large and the amount of infiltration is small, gas-phase chemical transport may be the dominant process by which the groundwater becomes contaminated.

To evaluate the potential for groundwater contamination from residual saturations of VOC in the unsaturated zone and to interpret the results of soil-gas surveys, an understanding of the mechanisms of gas-phase chemical transport is necessary. The transport of contaminants in the gas phase may result from both advection and diffusion and is influenced by phase partitioning into the water and solid phases. Gas-phase advection may result from gas-pressure or gas-density gradients.

As organic liquids with high vapor pressures and molecular weights evaporate, the density of the gas in contact with the liquid changes with respect to the ambient soil gas. This density contrast results in an advective gas flow, the magnitude of which is dependent on the properties of the evaporating chemical and the porous medium. Under certain conditions, this buoyancy flow may dominate the transport of contaminants in the gas phase. In this article, we focus attention on the relative importance of evaporation and buoyancy-driven flow in gas-phase contaminant transport in the vadose zone.

NUMERICAL SIMULATIONS

In order to simulate the evaporation of organic liquids and transient buoyancy flow, an existing code (TOUGH) was modified. Developed by Pruess (1987), TOUGH is a three-dimensional numerical code for simulating the coupled transport of water, water vapor, air, and heat in porous and fractured

media. The modified version of TOUGH used in the present application, which will be referred to as TOUGH-VOC, simulates the coupled transport of a volatile organic compound (VOC) in the liquid and gas phases and the transport of air. Both the gas phase and the liquid VOC phase are mobile. An immobile water phase is included, and the VOC is partitioned between the liquid VOC phase, the gas phase, the water phase, and the solid phase by assuming local chemical equilibrium between the phases. Details of the mass-balance equations used in TOUGH-VOC may be found in Falta et al. (1989).

For the purpose of better understanding how evaporation and gas-phase transport of VOCs occur in natural systems, a series of two-dimensional radially symmetric simulations were performed. A conceptual diagram of the system to be modeled is shown in Fig. 1. In this figure, a liquid VOC has been released into the subsurface by a spill from a chemical tank car. Similar releases of organic liquids could result from leaking underground storage tanks, industrial accidents, or improper disposal of organic liquid wastes. It is assumed that the volume of this spill was large enough so that a significant volume of soil has become contaminated but not so large that the liquid has migrated down to the water table. Within this contaminated volume of soil, the organic liquid is present at some residual saturation.

To isolate the importance of certain parameters on the gas-phase transport of a VOC, several simplifying assumptions are made. The unsaturated porous medium is assumed to be homogeneous and isotropic and to contain a uniform water saturation and fraction of organic carbon. The system is assumed to be isothermal, with no water infiltration from the ground surface. For simplicity, the gas-phase relative permeability, k_{rg}, is taken to be S_g^3. The liquid VOC phase is assumed to be immobile ($k_{rL} = 0$), as is the water phase. It is assumed that diffusion of the VOC through the water phase is negligible compared with diffusion of the VOC in the gas phase and that the gas-phase viscosity is constant, not a function of composition. Partitioning of the VOC between the liquid VOC, water, gas, and solid phases is calculated according to local chemical equilibrium.

To illustrate the effect of buoyancy-driven gas flow on gas-phase transport, two types of simulations were performed, one in which transport is due to evaporation, diffusion, and buoyancy flow and one in which buoyancy effects are suppressed. The problem geometry and boundary conditions for the cases in which buoyancy flow is considered are shown in Fig. 2. Initially, the liquid VOC occupies a cylindrical region centered at $r = 0$ with a radius of 4 m, a thickness of 4 m, and a saturation (S_L) of 0.1. For a porosity of 0.4, this corresponds to a liquid VOC volume of 8.042 m^3. The depth from the ground surface to the top of the contaminated zone is 3.5 m. The initial condition on the VOC mass fraction in the gas phase is $\omega_g^{(1)} = 0$ everywhere except in the region occupied by the liquid VOC, where the mass fraction in the gas phase is determined by chemical equilibrium with the liquid VOC. The initial pressure distribution reflects the static equilibrium of pure air, $P = P_{atm} + \rho_{air} gz$. The boundary conditions for the simulations in which buoyancy flow is not considered are similar to those shown in Fig. 2, except that the pressure at the outer radial boundary is atmospheric, $\partial P/\partial z = 0$ at the lower boundary, and the initial pressure is atmospheric everywhere. Problem specifications for the simulations are listed in Table 1.

Simulations were performed for two different compounds, carbon tetrachloride and toluene. The

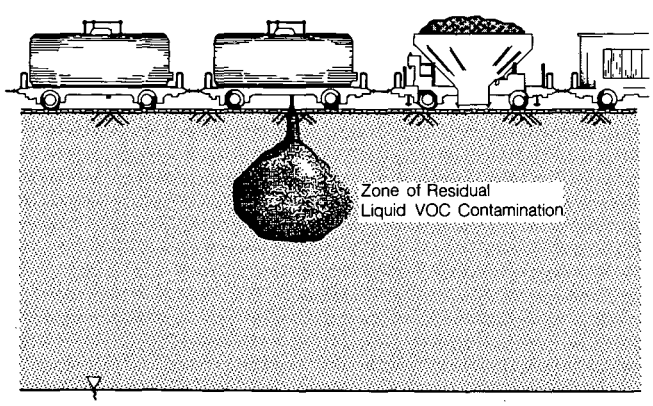

Figure 1. Schematic diagram of the system to be modeled. [XBL 8811-10564]

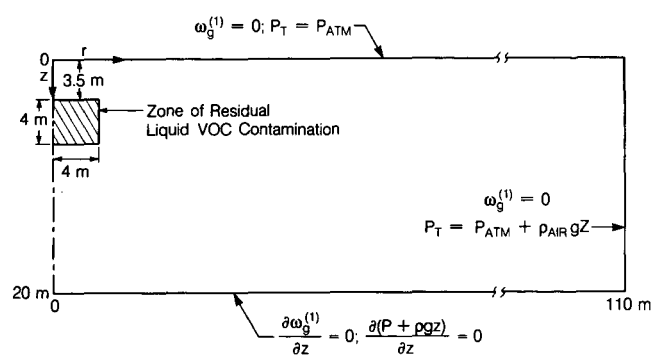

Figure 2. Geometry and boundary conditions for numerical simulations considering buoyancy flow. [XBL 8811-10563]

Table 1. Problem specifications.

Parameter	Value
Air diffusion constant	$D_g = 1 \times 10^{-5}$ m^2/s
Porosity	$\phi = 0.4$
Water saturation	$S_w = 0.25$
Initial liquid VOC saturation in contaminated zone	$S_L = 0.1$
Fraction of organic carbon	F_{oc} 0.001
Soil dry bulk density	ρ_b = 1,500 kg/m^3
Gas viscosity	$\mu_g = 1.81 \times 10^{-5}$ kg/ m · s
Gas relative permeability	$K_{rg} = S_g^3$
Temperature	T = 20°C
Vapor pressure	
Carbon tetrachloride	P^o = 12,120 Pa
Toluene	P^o = 2,900 Pa
Molecular weight	
Carbon tetrachloride	M = 154 g/mole
Toluene	M = 92 g/mole
Liquid density	
Carbon tetrachloride	ρ_L = 1,584 kg/m^3
Toluene	ρ_L = 862 kg/m^3
Organic carbon partition coefficient	
Carbon tetrachloride	K_{oc} = 0.11 m^3/kg
Toluene	K_{oc} = 0.14 m^3/kg
Henry's constant	
Carbon tetrachloride	H = 0.958
Toluene	H = 0.260
Air density at 1 atm, 20°C	ρ_{air} = 1.19 kg/m^3

carbon tetrachloride and toluene vapor pressures listed in Table 1 are for a temperature of 20°C. These vapor pressures correspond to saturated carbon tetrachloride and toluene gas concentrations of 0.7664 kg/m^3 and 0.1095 kg/m^3, respectively. The gas-phase retardation coefficients of carbon tetrachloride and toluene for the conditions specified in the simulations are 1.9 and 5.0, respectively.

The results of our simulations of carbon tetrachloride evaporation show that for situations in which the soil permeability is low, $k = 1 \times 10^{-13}$ m^2 or less, the contribution of buoyancy-driven advection to the overall gas transport is minimal, and the concentration distributions with and without the buoyancy flow are nearly identical. In this case, the use of a standard diffusion model to describe the gas-phase transport would be appropriate.

Figure 3 compares the carbon tetrachloride distributions without and with density-driven flow for a permeability of 6×10^{-11} m^2. Although this is a high permeability for natural systems, it is not uncommon for sand and gravel sediments. This comparison illustrates the dramatic effect that buoyancy-driven flow has on the gas-phase transport of dense vapors in systems having high permeabilities. The assumption that diffusion alone determines the gas-phase transport in this case would result in a misleading prediction of the contaminant transport.

From the preceding example, it might appear that the use of a diffusive model to describe the gas transport of VOCs in high-permeability systems is inappropriate. This is not necessarily true, because the magnitude of the buoyancy-flow effects depends on the chemical's saturated vapor density and on the degree to which the chemical is partitioned from the gas phase into the water and solid phases. Simulations of toluene evaporation in high-permeability systems demonstrated that the effect of density-driven flow on the toluene vapor distribution is fairly small. There are two reasons for this. Firstly, the saturated vapor density of toluene is fairly low, 0.1095 kg/m^3, resulting in a relatively small driving force for buoyancy-driven flow. Secondly, because of the relatively low Henry's constant for toluene, there is a strong partitioning of toluene from the gas

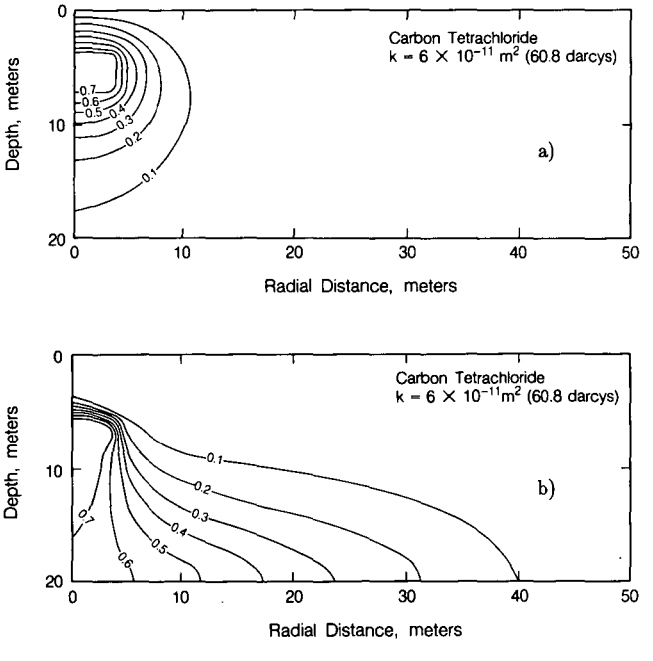

Figure 3. Carbon tetrachloride gas concentration distributions (kg/m^3) after 1 year as a result of (**a**) evaporation and diffusion and (**b**) evaporation, diffusion, and buoyancy flow. [Part a, XBL 8811-10550; part b, XBL 8811-10554]

phase into the water phase, resulting in a reduction of the driving force for buoyancy-driven flow.

The rate at which a liquid VOC evaporates from the unsaturated zone strongly depends on the magnitude of the density-driven gas-flow velocity. A tabulation of the amount of liquid VOC removed from the unsaturated zone after 1 year of evaporation is given in Table 2. In cases where the buoyancy-driven flow is considered and the permeability is large, the amount of carbon tetrachloride that evaporates after 1 year is much larger than in the cases where the buoyancy flow is neglected. In particular, when the permeability is 6×10^{-11} m^2, the amount of carbon tetrachloride that evaporates when density driven flow and diffusion are considered is almost 4 times larger than the amount that evaporates when only diffusion is considered. For a given compound, this difference decreases with decreasing permeability. The effect of buoyancy flow on the rate of toluene evaporation is small, even in the case of large soil permeabilities.

Table 2. Fraction of initial liquid VOC mass removed after 1 year.

		Percent removed	
Chemical	Soil permeability	Diffusion only	Diffusion and buoyancy flow
Carbon tetrachloride	6×10^{-11} m^2	15.1	59.2
	3×10^{-11} m^2	15.1	35.3
	1×10^{-11} m^2	15.1	19.2
	1×10^{-12} m^2	15.1	15.2
	1×10^{-13} m^2	15.1	15.1
Touluene	3×10^{-11} m^2	4.0	4.2

CONCLUSIONS

The results of this study indicate that under certain conditions density-driven gas flows in the unsaturated zone will occur during the evaporation of volatile organic liquids. The magnitude of these flows is mainly a function of the organic liquid vapor pressure and molecular weight, the gas-phase permeability, and the gas-phase retardation coefficient. Some common contaminants that are likely to be affected by buoyancy flow include trichloroethylene, chloroform, 1,1,1-trichloroethane, methylene chloride, 1,2-dichloroethylene, 1,2-dichloroethane, 1-1-dichloroethane, carbon tetrachloride, Freon 113, and possibly benzene. Some common contaminants that are not likely to be affected by buoyancy flow include toluene, ethylbenzene, xylenes, chlorobenzene, napthalene, and phenols. In order for this flow to be significant, the gas-phase permeability (in a homogeneous porous medium) should be at least on the order of 1×10^{-11} m^2 ($\approx$ 10 darcies). The general direction of buoyancy flow is downward from the evaporating source toward the water table and radially outward along the water table.

REFERENCES

Falta, R.W., Javandel, I., Pruess, K., and Witherspoon, P.A., 1989. Density-driven flow of gas in the unsaturated zone due to the evaporation of volatile organic compounds. Water Resour. Res., in press.

Pruess, K., 1987. TOUGH user's guide. U.S. Nuclear Regulatory Commission Report NUREG/CR-4645, Washington, D.C.

Deviation From Fick's Second Law of Diffusion during the Evaporation of Organic Liquids

R.W. Falta, I. Javandel, and K. Pruess

Experience has shown that in many locations, hazardous organic liquids have been released into the subsurface, resulting in the presence of separate-phase organic liquids in the unsaturated zone. As these liquids evaporate, gas-phase transport of the organic compounds to the water table may result in groundwater pollution. Recently, several analytical and numerical models have been developed to simulate the evaporation of organic liquids in the unsaturated zone (Abriola and Pinder, 1985; Corapcioglu and Baehr, 1987; Baehr, 1987). In each of these models, it is assumed that the evaporation and diffusion process is accurately described by Fick's second law of diffusion. For many problems, this assump-

tion is appropriate, but in certain situations, use of this assumption may lead to some error.

In an evaporating system, a significant deviation from Fick's second law of diffusion may occur, depending on the vapor pressure of the evaporating liquid (Bird et al., 1960). The reason for this deviation is that the assumption of equimolar counterdiffusion required for Fick's second law is not satisfied in an evaporating system. This may be illustrated by examining the steady-state evaporation of a liquid in an open column.

Referring to Fig. 1, consider a column containing a liquid layer of species A. Above the liquid, the column contains a binary gas mixture consisting of species A and the gas into which A is evaporating, species B. At the top of the column, the mole fraction of A in the gas phase, χ_A, is maintained at zero. Assuming that vapors A and B behave as ideal gases, at the liquid interface, the mole fraction of A, χ_{A0}, is equal to the vapor pressure of A divided by the total pressure, P_A°/P_T. It is assumed that the system is at constant temperature and pressure and that gas B is insoluble in liquid A.

The governing equation for this system is Fick's first law of diffusion relative to stationary coordinates (Bird et al., 1960):

$$N_A = \chi_A(N_A + N_B) - cD_{AB}\frac{d\chi_A}{dz}, \qquad (1)$$

where N_A and N_B are the molar fluxes of A and B, respectively, c is the total molar density, and D_{AB} is the binary diffusion coefficient for mixtures of A and B in the gas phase. The molar flux, N_A, consists of two components: the quantity $\chi_A(N_A + N_B)$, which is the molar flux due to bulk motion, and $-cD_{AB}\,d\chi_A/dz$, which is the flux due to diffusion.

As the evaporating system reaches steady state, there is a net movement of A away from the liquid surface. Since B is insoluble in liquid A, there is no net motion of B toward the liquid interface. Therefore, $N_B = 0$, and (1) becomes

$$N_A = \frac{-cD_{AB}}{1 - \chi_A}\frac{d\chi_A}{dz}. \qquad (2)$$

Since the system is at steady state, N_A is constant throughout the column. Thus

$$\frac{dN_A}{dz} = 0. \qquad (3)$$

Substituting (2) into (3) and taking c and D_{AB} outside of the derivative gives

$$\frac{d}{dz}\left(\frac{1}{1 - \chi_A}\frac{d\chi_A}{dz}\right) = 0. \qquad (4)$$

Integrating twice and applying the boundary conditions,

$$z = 0, \quad \chi_A = \chi_{A0} = \frac{P_A^\circ}{P_T},$$

$$z = L, \quad \chi_A = 0,$$

the concentration profile is (Bird et al., 1960; Incropera and DeWitt, 1981)

$$\frac{1 - \chi_A}{1 - \chi_{A0}} = \left(\frac{1}{1 - \chi_{A0}}\right)^{z/L}. \qquad (5)$$

Using (5) to calculate $d\chi_A/dz$ and substituting into (2) yields the molar flux of A during evaporation:

$$N_A^E = \frac{-cD_{AB}}{L}\ln(1 - \chi_{A0}). \qquad (6)$$

If the vapor pressure of A is very small, $\chi_A << 1$ and $\chi_A N_A << N_A$. Fick's first law may then be written as

$$N_A = -cD_{AB}\frac{d\chi_A}{dz}. \qquad (7)$$

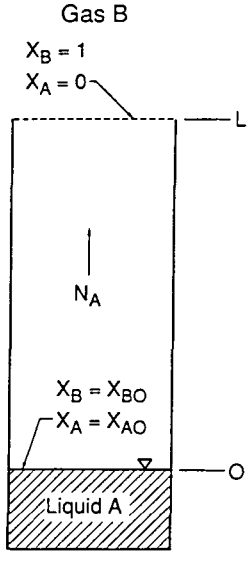

Figure 1. Evaporation of liquid A into a binary mixture of A and B in an open column. [XBL 8811-10561]

Substituting (7) into (3) results in Fick's second law of diffusion at steady state,

$$\frac{d^2\chi_A}{dz^2} = 0. \tag{8}$$

The resulting molar flux, N_A^D, is

$$N_A^D = \frac{cD_{AB}}{L}\chi_{A0}. \tag{9}$$

The ratio of the molar flux due to evaporation to the molar flux calculated from Fick's second law is

$$\frac{N_A^E}{N_A^D} = \frac{-ln(1-\chi_{A0})}{\chi_{A0}}. \tag{10}$$

or

$$\frac{N_A^E}{N_A^D} = \frac{-P_T ln(1-P_A^\circ/P_T)}{P_A^\circ}. \tag{11}$$

From (11), it is evident that the deviation from Fick's second law of diffusion during evaporation is a nonlinear function of the vapor pressure of the evaporating liquid. As the vapor pressure increases, the deviation from Fick's second law increases. A plot of N_A^E/N_A^D as a function of the vapor pressure of liquid A is given by the solid line in Fig. 2.

Evaporation in a porous medium is somewhat more complex than the preceding example indicates, because the relative contribution of the bulk motion of the gas to the total flux is a function of the porous-medium permeability and because the system pressure is not uniform. The numerical simulator TOUGH-VOC (Falta et al., 1989) was used to simulate the steady-state evaporation of a liquid in a column filled with porous material. The results for several permeabilities are shown as the dashed lines in Fig. 2. As the permeability is increased, the computed molar flux ratio approaches the curve calculated using (11), in which there is no porous medium. For permeabilities of 1×10^{-12} m^2 or larger, the numerical simulation results for the porous media agree very closely with the analytical expression for the open column. For very small permeabilities, on the order of 1×10^{-15} m^2, there is not much of a deviation from Fick's second law, but for larger permeabilities, the difference may be significant, depending on the evaporating liquid's vapor pressure.

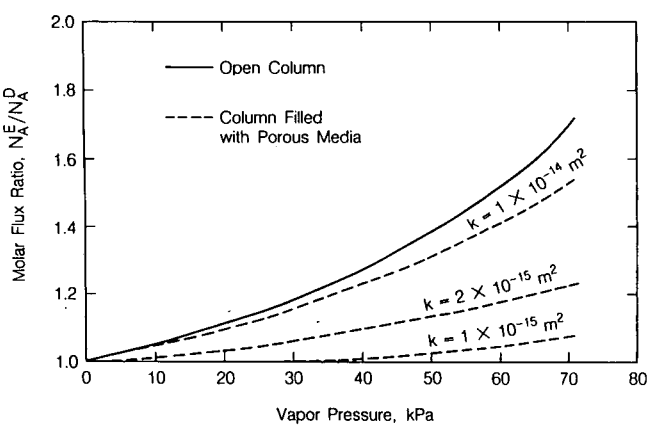

Figure 2. Deviation from Fick's second law of diffusion during steady-state evaporation. P_T = 101.3 kPa. [XBL 8811-10562]

From Fig. 2 it is apparent that the use of Fick's second law to describe evaporation is a good approximation for volatile organic compounds (VOCs) with vapor pressures less than about 10 kPa. However, several commonly encountered VOCs such as methylene chloride, 1,2-dichloroethylene, 1,1-dichloroethane, chloroform, 1,1,1-trichloroethane, and carbon tetrachloride have vapor pressures greater than 10 kPa.

REFERENCES

Abriola, L.M., and Pinder, G.F., 1985. A multiphase approach to the modelling of porous media contamination by organic compounds 1. Equation development. Water Resour. Res., v. 21, no. 1, p. 11–18.

Baehr, A.L., 1987. Selective transport of hydrocarbons in the unsaturated zone due to aqueous and vapor phase partitioning. Water Resour. Res., v. 23, no. 10, p. 201–213.

Bird, R.B., Stewart, W.E., and Lightfoot, E.N., 1960. Transport Phenomena. Wiley, New York, p. 522–598.

Corapcioglu, M.Y., and Baehr, A. L., 1987. A compositional multiphase model for groundwater contamination by petroleum products 1. Theoretical considerations. Water Resour. Res., v. 23, no. 1, p. 191–200.

Falta, R.W., Javandel, I., Pruess, K., and Witherspoon, P.A., 1989. Density-driven flow of gas in the unsaturated zone due to the evaporation of volatile organic compounds, in press.

Incropera, F.P., and DeWitt, D.P., 1981. Fundamentals of Heat Transfer Wiley, New York, p. 745–747.

Borehole Data from Three Wells on Yucca Mountain, Nevada: Analysis of the Fractures

K. Grossenbacher, K. Karasaki, and M. Landsfeld

The planned high-level nuclear waste repository at Yucca Mountain, Nevada, will be situated in a fractured welded tuff within the unsaturated zone. One possible pathway for contaminants into the biosphere is transport by groundwater flow down to and then laterally through the saturated zone. As a way of investigating this process, three wells, UE25c-1, 2, and 3 (hereafter called the C holes), were drilled to study hydraulic properties of rock formations underlying the planned waste repository. The location of the holes is ideal in that the formations in the unsaturated zone occur at the same depths and in the same thicknesses as at the repository site.

The C holes penetrate to a depth of 3000 feet and form a triangle, with separation among the wells of 100 to 300 feet. Borehole data available include geophysical logs, degree of welding, and formation stratigraphy. Geologic data available include a geologic map of the area (Scott and Bonk, 1984). Because the C holes penetrate relatively impermeable rocks, it is believed that the groundwater flow takes place mainly in fractures. Thus understanding the fractures should promote understanding of groundwater flow.

Lawrence Berkeley Laboratory is attempting to develop a fracture-network model in the vicinity of the C holes. The goal is to use hydraulic well tests and other borehole data to characterize fractures near the C holes. This investigation of the geology and fracture pattern near the C holes is still under way, so this article focuses on progress rather than final conclusions.

GEOLOGY

As a first approximation, the geology near the C holes consists of a simple layer-cake stratigraphy, with repeated layers of Miocene rhyolite tuffs, each a few hundred feet thick. The bedding strikes approximately N12°W and dips roughly 18°E. Folding is virtually absent. Most faults trend north-south, dip steeply westward, and are extensional. The geophysical logs correlate from hole to hole in the upper 2700 feet of the well, but below 2700–2800 feet they abruptly stop correlating in one of the wells. Presumably, this break occurs within the bottommost formation in the wells, so formation boundaries are useless in figuring out the reason for this break.

Also at 2700–2800 feet, the well diameters increase by a factor of 2 for vertical distances of 5–10 feet. Taken together, the break in correlation and the hole enlargements suggest a departure from the simple layer-cake stratigraphy. A fault may pass through the bottom of the wells (when the plane containing the hole enlargements is projected up to the surface, it aligns with the mapped trace of a major fault), or certain formation properties, such as fracture density and primary lithology, may vary laterally. Either possibility could account for the lack of correlation.

A fault, if present, could drastically affect groundwater flow and therefore change the interpretation of the hydraulic tests. It could act as either a hydrologic barrier or as a conduit and thereby either increase or decrease the apparent transmissivity over what it would be for fractures alone.

C-HOLE FRACTURES AND HYDRAULIC PROPERTIES

Hydraulic tests conducted by the USGS in 1984 include a series of falling-head injection tests in C-1, involving 27 separate packed-off intervals. Relative decay times for the pressure in each of the tests yield the relative transmissivity and permeability for each interval. These interval results combine to form a graph of permeability as a function of depth. Data from the seisviewer, a sonic device that shows the depth, strike, and dip of fractures, allows comparison of transmissivity with fracture location. Each fracture is assigned a maximum possible transmissivity and a theoretical average transmissivity.

The angle that a fracture makes with the bedding can be significant in deciding the origin of the fracture, so two new parameters are introduced: restored strike and dip. To find these parameters, all fractures are rotated about a horizontal axis (the line of strike) so that they appear as they would if the bedding plane were horizontal.

In analyzing the fractures, there are nine parameters for each one: depth, strike and dip, restored strike and dip, stratigraphic unit, degree of welding, and transmissivity, both average and maximum.

The computer statistics package "S" (Becker and Chambers, 1984) was used to produce histograms of each parameter, scatter plots of transmissivity versus each of the other parameters, and perspective plots of transmissivity as a function of strike and dip.

In analyzing the histograms, several patterns appear: depths of fractures tend to cluster around the central, more welded portions of each tuff. Restored dips tend to cluster logarithmically around 90°; histograms for both restored and unrestored dips are shown in Fig. 1. The strikes of unrestored fractures tend to cluster around 200°. A single high-transmissivity fracture shows up as a clear outlier on both the maximum-transmissivity and the average-transmissivity histograms. This fracture apparently accounts for 60% of all water production in C-1. Scatter plots of average and maximum transmissivity versus each of the other parameters show that average and maximum transmissivities correlate well with one another. Average fracture transmissivity varies among the stratigraphic units, and fractures that dip steeply have the highest transmissivity.

To investigate the correlation between transmissivity and orientation, strike and dip are plotted horizontally and transmissivity is plotted vertically. Four such three-dimensional graphs can be plotted, showing average and maximum transmissivities as functions of strike and dip and restored strike and dip. Figure 2 shows an example of such plots. These plots all show humps in the transmissivity of fractures that strike 150 to 200° and which dip either 60 to 90° for rotated strike and dip or 30 to 70° for the nonrotated strike and dip.

One problem in interpreting these graphs of transmissivity as a true function of strike and dip is that the frequency of fractures with respect to strike and dip space will affect the transmissivity plotted. A 3-D smoothed histogram of frequency with respect to strike and dip closely resembles the corresponding

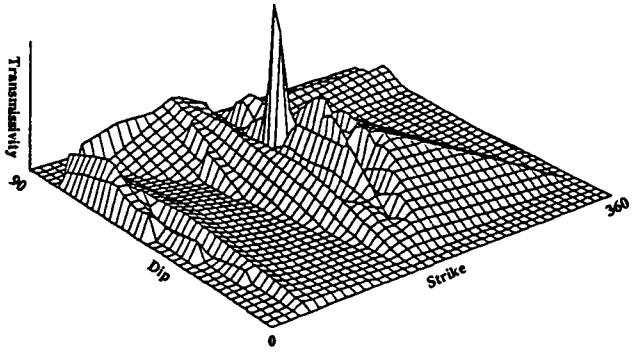

Figure 2. Perspective plot of transmissivity as a function of strike and dip. [XBL 894-1547]

graphs of transmissivity (see Fig. 3). The apparent correlation between transmissivity and orientation seen earlier may actually be an artifact due merely to the large number of fractures with similar orientation.

FRACTURE DEVELOPMENT THEORY

Cooling cracks are produced by thermal contraction as the tuff cools after emplacement. If the tuff had cooled purely as a result of conduction through the rock, the isotherms would be horizontal, and so would the maximum tensile stress. Therefore, the cooling fractures should be vertical. If meteoric waters had entered the initial cracks, however, they would cause the isotherms to form a depression around the crack (De Graff and Aydin, 1987). Subsequent cooling cracks would then be perpendicular to these new isotherms and would tend to radiate away from the tip of the original fracture. In a cooling basalt flow, water infiltration through initial cooling cracks can cause the crack tip to propagate into the liquid portion of the flow (Long and Wood,

```
UE25C#1 Fracture Dips                UE25C#1 Rotated Fracture Dips
---------------------                -----------------------------

 2 : 59
 3 :
 3 :                                      3 : 6
 4 : 344                                  4 : 013
 4 : 7899                                 4 : 59
 5 : 02224                                5 : 0024
 5 : 56666677888999                       5 : 7899
 6 : 01111111222222223334                 6 : 001123
 6 : 55677888889                          6 : 5556789
 7 : 0000001111234444                     7 : 112233334444
 7 : 5555667778888999                     7 : 5555666667788888999
 8 : 000111122233                         8 : 00001222233333334
 8 : 67                                   8 : 555555566666666777777888899
                                          9 : 00

   N = 105   Median = 67                    N = 105   Median = 78.1
   Quartiles = 58.3, 75.2                   Quartiles = 67.4, 84.7

        Decimal point is 1 place to the right of the colon
```

Figure 1. Dip histograms of restored and unrestored fractures. [XBL 894-1546]

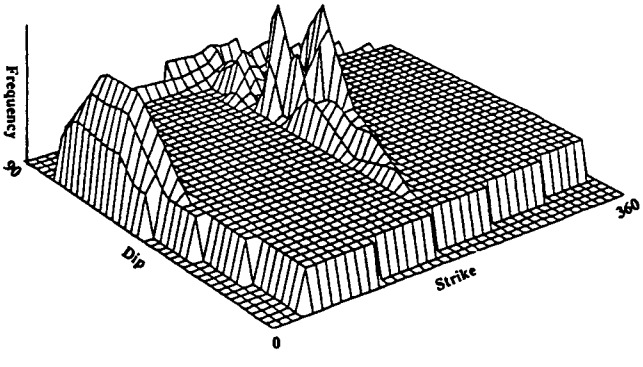

Figure 3. Perspective plot of frequency as a function of strike and dip. [XBL 894-1548]

1987). If an analogous process happens in a tuff, the bulk rheology of the fracturing rock could approach that of the high-temperature newly deposited tuff, affecting the way cooling cracks develop. Computer programs developed for predicting the formation of dikes (Pollard and Holzhausen, 1978) could be modified to analyze formation of these cooling cracks in tuffs (Steve Martel, personal communication, 1988).

3-D RENDERING OF STRIKE, DIP, AND DEPTH

In interpreting well data and understanding fracture patterns, one problem is the difficulty in visualizing both strike and dip simultaneously as they vary with depth. One way of resolving this problem is to plot level surfaces of the density of fracture orientation as a function of strike, dip, and depth. Depth would plot vertically, then strike and dip horizontally on a stereonet projection. This would plot as a vertical cylinder representing the borehole. A computer could then plot a series of cutaway level surfaces of the fracture frequency as a function of both orientation and depth. This approach could include the use of shading to indicate the degree of transmissivity. The final plot would simultaneously illustrate depth, strike, dip, orientation, and fracture transmissivity.

As a first approach to producing these level surfaces, stereoscope plots of fracture orientation versus depth have been produced (see Fig. 4). This yields a 3-D image of a cylinder, as described above. The distinctive cluster of fractures around the vertical (much more so than for the unrestored dips) implies that some sort of mechanism must be responsible. One such mechanism is the formation of cooling cracks perpendicular to the bedding plane. Another is that the cracks may be tectonically induced by tensile stresses created along the outer radius of a fold, thus causing the fractures to be perpendicular to the bedding plane.

One problem with trying to separate cooling cracks from tectonically induced cracks on the basis of orientation is the lack of calibration. This problem could be resolved by using a database for fracture orientation from pavement studies, where particular fractures are known to have formed during cooling (Chris Barton, personal communication, 1988). The orientation density of fractures from the pavements could be plotted, the cooling cracks flagged, and the results compared with fracture plots for the C holes.

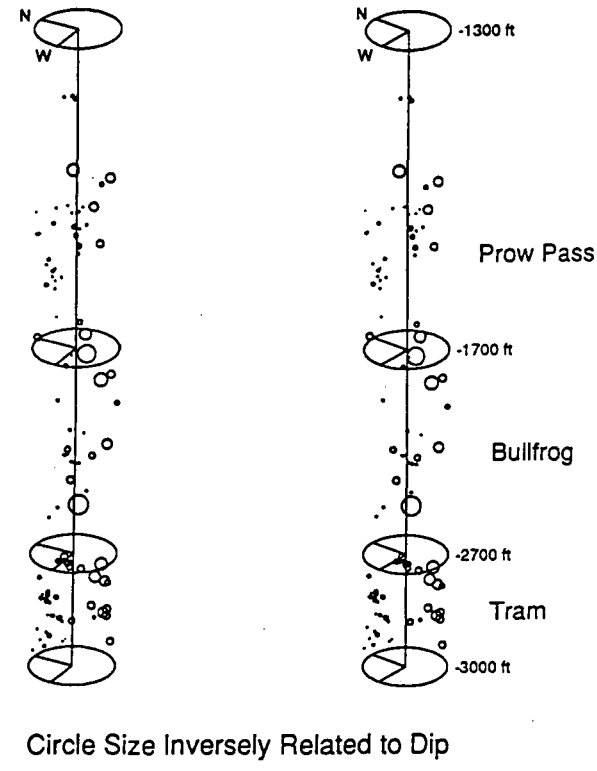

Figure 4. Stereoscopic plot of fracture orientation versus depth. [XBL 894-1549]

SUMMARY

Unresolved evidence indicates that a fault may intersect the C holes. If so, it could act hydraulically as either a barrier or conduit and overwhelm the effect of fracture permeability on the well-test data. Therefore, successful interpretation of the well data depends on accurate location of the fault. Toward this end, cross-hole seismic tests are planned that will locate any such fault.

Significant clusters of fractures in the C holes are perpendicular to the bedding and may be cooling cracks. Further analysis of those clusters could help form a basis for building a model of the fracture network. Other clusters of fractures appear to be associated with zones of high permeability. Further analysis of those fractures could help yield a basis for relating fracture orientation to permeability.

REFERENCES

Becker, R., and Chambers, J., 1984. S, An Interactive Environment for Data Analysis and Graphics. Wadsworth Publishing, Inc., Belmont, California.

DeGraff, J., and Aydin, A., 1987. Surface morphology of columnar joints and its significance to mechanics and direction of joint growth. Geol. Soc. Am. Bull., v. 99, p. 605–617.

Long, P., and Wood, B., 1987. Structures, textures, and cooling histories of Columbia River basalt flows. Geol. Soc. Am. Bull., v. 97, no. 6, p. 1144–1155.

Pollard, D., and Holzhausen, G., 1978. On the mechanical interaction between a fluid-filled fracture and the earth's surface. Tectonophysics, v. 53, p. 27–57.

Scott, R., and Bonk, J., 1984. Preliminary Geologic map of Yucca Mountain, Nye County, Nevada with geologic sections. USGS Open-File Report 84-494, Denver, Colorado.

Hydrologic Characterization of Faults and Other Potentially Conductive Features

I. Javandel and C. Shan

The capability of locating and characterizing near-vertical faults and other potentially highly conductive geologic features in the vicinity of a high-level-waste repository site is of great importance in the site characterization for underground waste-isolation projects. The existence of such features near a repository site could provide a flow path with short travel time from the disturbed zone to the accessible environment (or the water table in the case of the Nevada site). Faults may cut through various geologic formations, in both the saturated and the unsaturated zones. Depending on the properties of local geologic materials, the amount of relative displacement of layers, and the state of stress, a fault can provide a conductive pathway or be practically sealed. In terms of their hydrologic response on field pumping tests, faults may be classified as (1) tight faults, (2) constant-head faults, and (3) nonconstant-head leaky faults (Witherspoon et al., 1967). Tight faults are those that cut through an aquifer and, for all practical purposes, hydraulically disconnect one part of the aquifer from the rest of it and from other water-bearing formations above and below. Constant-head faults are those that connect the aquifer to a large constant-head water body; the path along the fault between the aquifer and the water body has practically infinite permeability. Mathematically tight and constant head faults may be represented by no-flow and constant-head boundary conditions, respectively. Several other types of geologic configurations may also be responsible for such no-flow or constant-head boundaries in a pumping aquifer, as discussed by Ferris (1949).

Adapting a method of images used in 19th-century heat and electricity studies, Ferris (1949) and Jacob (1950) proposed a method for calculating values of drawdown in a pumping aquifer that is intersected by tight or constant-head faults. Furthermore, Ferris (1949) presented a method for finding the location of such boundaries by monitoring, in at least two observation wells, the drawdowns due to a well with constant discharge. In real life, however, there are some discontinuities in rock masses that have finite but higher conductivities than the surrounding rock matrix. Unlike tight or constant-head faults, which represent the two ends of the permeability scale (i.e., zero and infinity), these discontinuities may present potential flow paths with relatively large but finite transmissivity. The goal of this work is to develop hydrologic tests and analysis methods to locate and characterize faults and potentially conductive features close to a candidate repository site. This article summarizes an analytic solution for calculating drawdowns in a pumping aquifer that has been intersected by a finite-transmissivity fault or other similar permeable geologic features. Based on this solution, a method is presented that enables one to locate such linear features and estimate their hydraulic properties.

THEORY

Let us consider an extensive 2-D homogeneous isotropic aquifer that has been intersected by a fault of finite conductivity (Fig. 1). A fully penetrating well located at a distance a from the fault is being pumped at a constant rate Q. The fault divides the aquifer into two regions. The part of the aquifer on the pumping side is designated as region I and the part on the other side as region II. If drawdown at

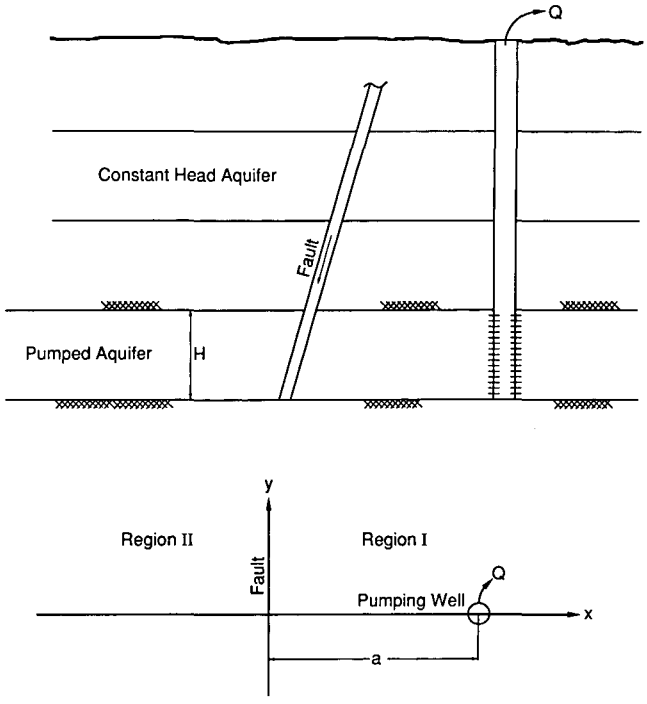

Figure 1. A schematic section and plan of the aquifer intersected by a leaky fault. [XBL 8811-10519]

the point (x,y) in the aquifer and time t is represented by $s_i(x,y,t)$, i = 1,2, then mathematically the problem can be formulated by the following governing differential equations and boundary conditions:

$$\frac{\partial s_1}{\partial t} = \alpha \left\{ \frac{\partial^2 s_1}{\partial x^2} + \frac{\partial^2 s_1}{\partial y^2} \right\} + \frac{\alpha Q}{KH} \delta(x - a), \quad (1)$$

$$\frac{\partial s_2}{\partial t} = \alpha \left\{ \frac{\partial^2 s_2}{\partial x^2} + \frac{\partial^2 s_2}{\partial y^2} \right\}, \quad (2)$$

$$s_1(x,y,0) = s_2(x,y,0) = 0, \quad (3)$$

$$s_1(\infty,y,t) = 0, \quad (4)$$

$$s_2(-\infty,y,t) = 0, \quad (5)$$

$$s_1(x,\pm\infty,t) = s_2(x,\pm\infty,t) = 0, \quad (6)$$

$$s_1(0,y,t) = s_2(0,y,t), \quad (7)$$

$$KH \frac{\partial s_1}{\partial x} = KH \frac{\partial s_2}{\partial x} + K' s_2 \qquad at \ \ x = 0, \quad (8)$$

where $\delta(x)$ is the Dirac delta function, α and K are diffusivity and hydraulic conductivity of the aquifer, respectively, and K' is a measure of the fault's conductivity. Note that the condition at the fault, expressed by (8), indicates that influx into region I is the sum of the the flux from region II and the flux from the fault, which is proportional to the drawdown in the aquifer along the fault. It is important to note that drawdown in the aquifer along the fault is a function of both time and position. Equation (8) implies that (1) storativity of the fault is negligible and (2) the fault is connected to a constant source above or below the aquifer.

Using the Laplace and Fourier transform, consecutively, a solution to the above mathematical model has been derived:

$$s_1 = -\frac{Q}{4\pi KH} Ei \left\{ -\frac{(x-a)^2 + y^2}{4\alpha t} \right\} - \frac{Qc\sqrt{\alpha}\exp[c(x+a)]}{4\sqrt{\pi}KH} \int_0^t g_1(\tau) d\tau, \quad (9)$$

$$s_2 = -\frac{Q}{4\pi KH} Ei \left\{ -\frac{(x-a)^2 + y^2}{4\alpha t} \right\} - \frac{Qc\sqrt{\alpha}\exp[c(a-x)]}{4\sqrt{\pi}KH} \int_0^t g_2(\tau) d\tau, \quad (10)$$

where

$$g_1(\tau) = \frac{\exp[c^2\alpha\tau - \frac{y^2}{4\alpha\tau}]}{\sqrt{\tau}} \operatorname{erfc}\left\{ \frac{x+a}{2\sqrt{\alpha\tau}} + c\sqrt{\alpha\tau} \right\}, \quad (11)$$

$$g_2(\tau) = \frac{\exp[c^2\alpha\tau - \frac{y^2}{4\alpha\tau}]}{\sqrt{\tau}} \operatorname{erfc}\left\{ \frac{a-x}{2\sqrt{\alpha\tau}} + c\sqrt{\alpha\tau} \right\}, \quad (12)$$

and

$$c = \frac{K'}{2KH}. \tag{13}$$

Recalling that s_1 and s_2 refer to drawdowns in region I and II, where values of x are positive and negative, respectively, a unified solution for the whole aquifer is given by

$$s = -\frac{Q}{4\pi KH} Ei\left\{-\frac{(x-a)^2+y^2}{4\alpha t}\right\}$$

$$-\frac{Qc\sqrt{\alpha}\exp[c(a+|x|)}{4\sqrt{\pi}KH}\int_0^t g(\tau)d\tau, \tag{14}$$

where

$$g(\tau) = \frac{\exp[c^2\alpha\tau - \frac{y^2}{4\alpha\tau}]}{\sqrt{\tau}}\operatorname{erfc}\left\{\frac{a+|x|}{2\sqrt{\alpha\tau}} + c\sqrt{\alpha\tau}\right\}. \tag{15}$$

The right-hand side of (14) consists of two parts. Part one, the exponential integral, stands for the drawdown due to a pumping well in an infinite aquifer (Theis solution); part two represents the buildup due to the leakage from the fault. Note that part two vanishes when conductivity of the fault, K', goes to zero.

FAULT RECHARGE RATE

The overall recharge rate from the fault into the aquifer may be obtained by integrating the flux along the y axis from $-\infty$ to $+\infty$. The result of the above integration gives the following expression for the total recharge rate from the fault:

$$Q_f(t) = Q\left\{\operatorname{erfc}[\frac{a}{2\sqrt{\alpha t}}] - \right.$$

$$\left.\exp[ca + c^2\alpha t]\operatorname{erfc}[\frac{a}{2\sqrt{\alpha t}} + c\sqrt{\alpha t}]\right\}. \tag{16}$$

It can be shown that (1) Q_f vanishes when conductivity of the fault, K', and as a result c goes to zero, and (2) when $c \neq 0$, recharge rate from the fault, Q_f, approaches the pumping rate at large times.

DISCUSSION AND RESULTS

Introducing the dimensionless parameters

$$s_D = \frac{4\pi KHs}{Q}, \qquad t_D = \frac{\alpha t}{r^2},$$

$$a_D = \frac{a}{r}, \qquad c_D = c \cdot r,$$

where r is the distance between the pumping and the observation wells, one can prepare families of type curves presenting dimensionless drawdowns versus dimensionless time for various running parameters. Figure 2 shows a sample of these type curves on a log-log plot; Fig. 3 shows the results on a semilog plot.

Note that these curves are very similar in shape to the type curves for the leaky aquifers (r/B solutions). This raises the question whether these two effects can be differentiated from the results of the pumping tests.

The drawdown pattern observed in two monitoring wells located at the same distance from the pumping well in a leaky aquifer are identical. This is because the value of r/B for both wells is the same. However, drawdowns in the same two monitoring wells under the influence of a leaky fault are easily differentiable, because monitoring wells are located at different distances from the fault. Therefore, a proper design of the pumping test is the key for the correct interpretation of the data.

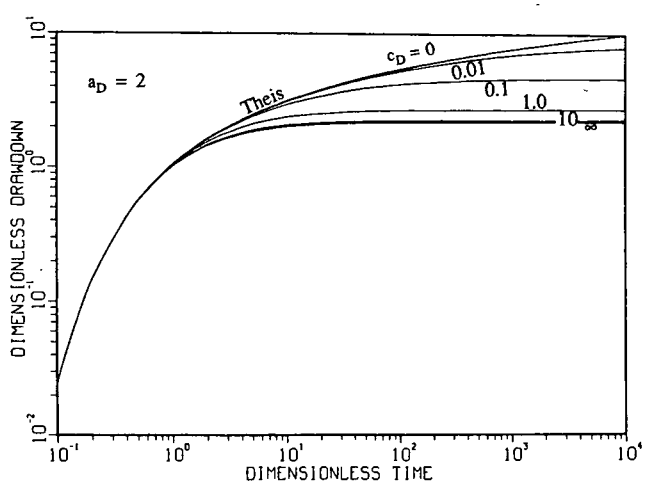

Figure 2. Log-log plots of dimensionless drawdown versus dimensionless time for $a_D = 2$ and c_D ranging from 0 to ∞. [XBL 893-1031]

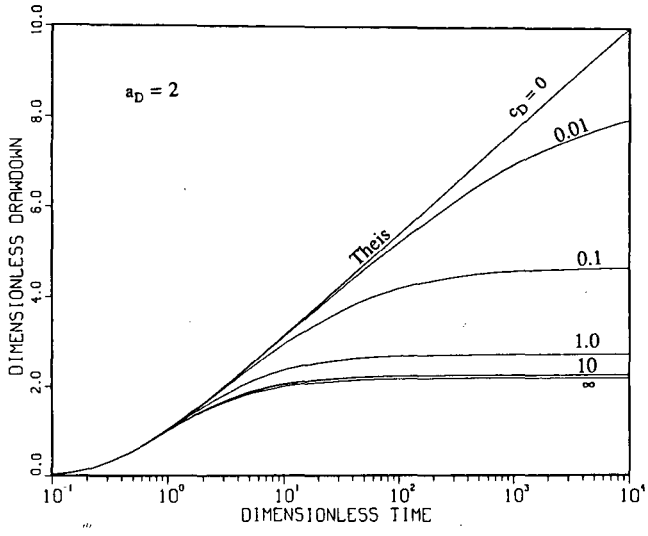

Figure 3. Semilog plots of dimensionless drawdown versus dimensionless time for $a_D = 2$ and c_D ranging from 0 to ∞. [XBL 893-1032]

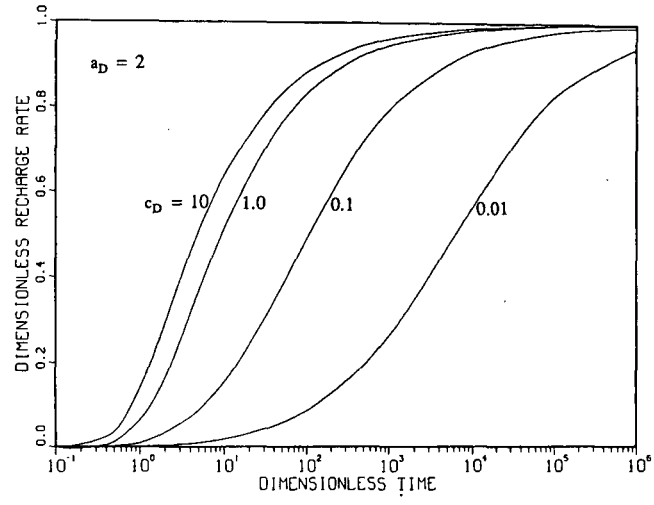

Figure 4. Semilog plots of dimensionless recharge rate versus dimensionless time for $a_D = 2$ and c_D ranging from 0.01 to 10. [XBL 893-1033]

Figure 4 illustrates the variation of the fault recharge rate with time. It shows the change of dimensionless recharge rate, Q_f/Q, as a function of dimensionless time for four values of c_D. As discussed above, one may note that the fault recharge rate tends to increase with time, and if the pumping continues for relatively large periods of time, most of the water extracted from the aquifer is essentially supplied by the fault. Obviously at any given time the percentage of the extracted water coming from the fault is a function of c_D, which, in turn, is a function of the fault's conductivity and its distance from the pumping and observation wells.

Based on the above results, a method has been developed to estimate the conductivity of the leaky fault. Studies have been carried out to identify the sensitivity of the results to different parameters and the limitation of the proposed technique. Details of these studies will appear in a more comprehensive report.

REFERENCES

Ferris, J.G., 1949. Ground water. *In* C.O. Wisler and E.F. Brater (eds.), Hydrology. Wiley, New York, p. 198–272.

Jacob, C.E., 1950. Flow of groundwater. *In* H. Rouse (ed.), Engineering Hydraulics. Wiley, New York, p. 321–386,

Witherspoon, P.A., Javandel, I., Neuman, S.P., and Freeze, R.A., 1967. Interpretation of Aquifer Gas Storage Conditions from Water Pumping Tests. American Gas Assoc., 273 p.

Dynamic Stability of Foam Lamellae Flowing through a Periodically Constricted Pore

A.I. Jiménez and C.J. Radke

Foam is a useful fluid for achieving mobility control in enhanced oil-recovery processes. However, it must remain stable and of fine texture (i.e., small bubble size) in order to maintain a low flow mobility. The primary factor determining foam lifetime is the stability of the lamellae that separate the individual gas bubbles. As lamellae rupture, the bubble size or texture increases. Indeed, if bubble coalescence is very rapid, then most of the gas phase will be continuous and the effectiveness of foam as a

mobility-control fluid will be lost. We address the fundamental mechanisms underlying foam stability in porous media.

Lamellae longevity in porous media is dominated by the mean-capillary-pressure difference between the nonwetting foam phase and the continuous-wetting aqueous foamate phase. Low liquid saturation in the medium can exert high enough capillary-pressure suction forces on the lamellae to drain them to breakage. The capillary pressure at which coalescence occurs is denoted the critical capillary pressure, or P_c^*.

Recently Khatib, et al. (1988) directly measured the critical capillary pressure of foam coalescence for bead packs of permeabilities ranging from 72 to 8970 μm^2 and for various surfactant formulations. These authors found that with all other variables held constant, P_c^* decreases with increasing flow velocity (see Fig. 8 of Khatib et al., 1988). That is, for a porous medium with a given permeability and wetting-phase saturation (and corresponding capillary pressure), there is a critical gas velocity above which lamellae rupture. Similarly, if the capillary pressure is increased at a given velocity of flow, the foam will break. These findings suggest that for high velocities the wetting-liquid content of the medium must increase proportionately in order to reduce P_c^* enough for foam to remain stable.

Our purpose is to explain quantitatively the origin of a critical capillary pressure for foam existence in porous media. A hydrodynamic theory is introduced to rationalize how P_c^* depends on velocity by analyzing the stability of foam lamellae moving through a periodically constricted sinusoidal pore.

STABILITY OF STATIC FOAM IN POROUS MEDIA

To understand the role of the medium capillary pressure upon foam coalescence, consider a flat, cylindrical, stationary foam lamella of thickness $2h$ (circa 1000 Å) and radius R (i.e., 50 to 100 μm) subject to a capillary pressure, P_c, at the film meniscus or Plateau border, as shown in Fig. 1. The liquid pressure at the film meniscus is $(P_g - P_c)$, where P_g is the gas pressure.

Inside the lamella, there is an excess force or conjoining/disjoining pressure, Π, as introduced and tested experimentally by Derjaguin (1939) and Derjaguin and Titievskaja (1957). The conjoining/disjoining pressure is a function of the film thickness, $2h$. A typical isotherm for Π(h) is shown in dimensionless form in Fig. 2. In this case the very short range molecular contributions (Exerova et al., 1987), thought to be of structural origin, are not

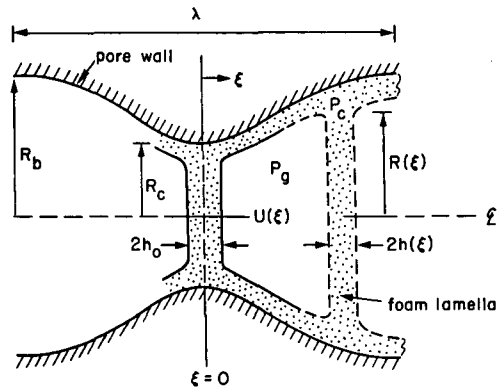

Figure 1. Schematic of flowing lamellae in a periodic constricted pore. The porous medium imposes a capillary pressure, P_c, at each Plateau border. [XBL 894-1550]

shown because such ultrathin films seem unlikely for foam application in porous media. The particular form of $\hat{\Pi}(\hat{h})$ in Fig. 2 is calculated from the constant-potential and weak-overlap subcase of the DLVO theory (Verwey and Overbeek, 1948):

$$\hat{\Pi} = -\frac{1}{\theta \hat{h}^3} + \exp(-\hat{h}), \qquad (1)$$

where $\hat{\Pi} = \Pi/B$, $\hat{h} = 2\kappa h$, and $\theta = B/\kappa^3 A_H$. The first term on the right side of this expression reflects attractive dispersion forces, and the second term corresponds to repulsive electrostatic double-layer

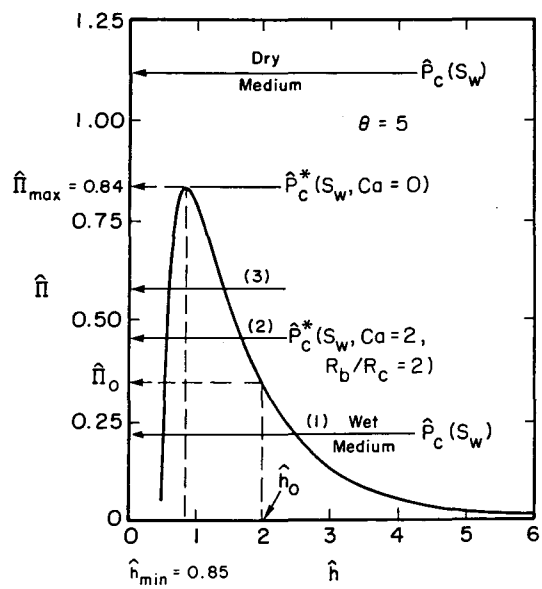

Figure 2. A conjoining/disjoining-pressure isotherm for the constant-potential and weak-overlap electrostatic model. [XBL 894-1551]

forces. B is a known function of the surface potential, ionic strength, surfactant concentration, and temperature (Verwey and Overbeek, 1948), A_H is a Hamaker constant, and $1/\kappa$ is the Debye length. θ is a measure of the ratio of repulsive to attractive forces whose value in Fig. 2 is set at 5.

The driving force for exchange of fluid into and out of the film is $(P_c - \Pi)$. When P_c is greater than Π the pressure difference $(P_c - \Pi)$ drives liquid out of the lamella and vice versa. If it happens that $P_c = \Pi$, then an equilibrium metastable film is possible. Whether a particular intersection of P_c and Π yields a metastable or an unstable foam film depends on the specific shape of the conjoining/disjoining curve (Vrij, 1966; Scheludko, 1967; Ivanov et al., 1970).

Whenever $\partial\Pi/\partial h$ is greater than zero the film is unstable. Thus, in Fig. 2 the critical thickness limit for metastable films, $\hat{h}_{\min}$, is given by the maximum of the conjoining/disjoining curve, or equivalently when $\partial\Pi/\partial h = 0$ for any value of θ. Unbounded films thinner than $\hat{h}_{\min}$ are unstable to infinitesimal perturbations; films thicker than $\hat{h}_{\min}$ are stable to such perturbations.

It is now possible to explain the origin of a critical capillary pressure for the existence of foam in a porous medium. For strongly water-wet permeable media, the aqueous phase is everywhere contiguous via liquid films and channels. Hence the local capillary pressure exerted at the Plateau borders of the foam lamellae is approximately equal to the mean capillary pressure of the medium. Consider now a relatively dry medium for which the corresponding capillary pressure in a dimensionless sense is greater than $\hat{\Pi}_{\max}$, as shown in Fig. 2. Given sufficient time any foam lamella present in such a medium will thin down to a thickness less than $\hat{h}_{\min}$ and rupture, hence the entire foam breaks. Conversely, for a relatively wet medium with $\hat{P}_c < \hat{\Pi}_{\max}$, the lamellae will establish a metastable equilibrium state with $\hat{\Pi} = \hat{P}_c$ and $\hat{h} > \hat{h}_{\min}$. In this case, unless subjected to large disturbances (i.e., those with amplitude of order h), the foam lamellae remain intact and the foam is metastable. Clearly, for a static foam, a critical capillary pressure at $\hat{P}_c^* = \hat{\Pi}_{\max}$ demarks the boundary between metastable and unstable foam lamellae. For dynamic or flowing lamellae additional considerations arise, as discussed below.

STABILITY OF DYNAMIC FOAM IN POROUS MEDIA

To explain coalescence of dynamic foam in porous media consider a single lamella flowing through a periodically constricted sinusoidal pore, as shown in Fig. 1. As noted above, the capillary pressure of the medium imposed on the lamella at the pore wall is assumed constant and is set by the local wetting-liquid saturation. Assuming constant volumetric flow, Q, the lamella moves from pore constriction of radius R_c to pore body of radius R_b with a local interstitial velocity $U(\xi)$, which varies according to the square of the pore radius, given by the periodic function $\hat{R} \equiv R(\xi)/R_c$:

$$\hat{R}(\xi) = (1 + a) + a \cos[\pi(1 + 2\xi/\lambda)], \qquad (2)$$

where ξ is the axial distance measured from the pore constriction and λ is the wavelength of the periodic pore; a characterizes the pore structure and is given by $(1/2)\ (R_b/R_c - 1)$. Thus, for a perfectly straight pore, a is equal to zero.

Upon moving from the pore constriction ($\xi = 0$) to the pore body ($\xi = \lambda/2$), the lamella is stretched as it conforms to the wall. To achieve the requisite volume rearrangement, a radial pressure differential is induced that thins the film but results in no net fluid efflux into the Plateau borders. The converse occurs when the film is squeezed upon moving from a pore body to a pore constriction. If R_b/R_c, or equivalently a, is large enough to thin the lamella at the pore body to about $h_{\min}$ in Fig. 2, then rupture is imminent. Since eventual encounter with a large pore body is virtually assured, this reasoning predicts the collapse of all foam lamellae independent of the flow velocity.

Conversely, whenever the stretched lamella of local thickness h exerts a conjoining/disjoining pressure $\Pi(h)$, which lies above the value of P_c, then fluid moves out of the pendular wetting liquid surrounding the sand grains and into the thin lamellae to prevent the thickness from falling below $h_{\min}$. Unfortunately, the thin lamella resists instantaneous fluid exchange. According to the simple Reynolds parallel-film model (Rao et al., 1982; Reynolds, 1886) adopted below, this hydrodynamic resistance is inversely proportional to h^3 (we ignore any resistance to liquid flow along the channels lining the pore walls and in the Plateau borders (Malhotra and Wasan, 1986)). When the foam flow rate Q is low, there is sufficient time for healing of the thinned lamella at the pore body. When Q is raised sufficiently, however, healing cannot occur quickly enough and the film thickness drops below $h_{\min}$, initiating breakage. Accordingly, for a given capillary pressure in a porous medium, there will be a specific foam flow rate at which the lamellae rupture. This is the proposed origin of the flow-rate dependence of P_c^* measured by Khatib et al. (1988).

Based on the picture above, we combine the expressions for the rate of change of the film thickness due to wall conformity and capillary-pressure-driven influx or efflux into a dimensionless evolution equation (Jiménez, 1989):

$$\frac{\partial \hat{h}}{\partial \hat{\xi}} = \frac{2\pi a \hat{h} \sin\left[\pi(1+\hat{\xi})\right]}{1 + a + a\cos\left[\pi(1+\hat{\xi})\right]} - \frac{\theta \hat{h}^3}{Ca}\left(\hat{P}_c - \hat{\Pi}\right), \quad (3)$$

where

$$\hat{P}_c = P_c/B, \quad (4a)$$

$$Ca = \frac{3\mu Q}{4\pi\lambda\kappa A_H}, \quad (4b)$$

with $\hat{\xi} = 2\xi/\lambda$. $\hat{\Pi}$ follows from Eq. (1), and $\hat{R}$ varies with ξ according to Eq. (2).

The first term on the right side of Eq. (3) corresponds to the rate of stretching/squeezing and is sensitive to pore geometry. The sharper the constriction (i.e., high R_b/R_c), the larger the contribution of this term to the total rate of thinning of the lamella. The second term represents the rate of film drainage/filling caused by the difference between the capillary pressure and the instantaneous conjoining/disjoining pressure. Note that if $\hat{P}_c$ is always less than $\hat{\Pi}(\xi)$ this term causes film thickening and vice versa.

The scaling factor appearing in the denominator of the draining/filling term is a modified capillary number, defined by Eq. (4b), which parameterizes how fast the lamella moves through the constriction. In the limit of Ca $\rightarrow \infty$ the second term is negligible compared to the first term, indicating that the time of flow through the constriction is too short to allow liquid to move into or out of the lamella under the influence of the porous-medium capillary pressure. In the limit of Ca $\rightarrow$ 0 the lamella is at rest, and, regardless of the shape of the constriction, the capillary pressure will drive liquid into or out of the lamella until a metastable equilibrium or an unstable state is reached. In this case, as stated earlier, the limiting capillary pressure above which lamellae cannot exist, P_c^*, is identical to Π_{max}.

Numerical solution of Eq. (3) predicts how the lamella thickness changes during transport along the periodically constricted pore. If at any point during the journey, the lamella thickness just reaches h_{min}, then breakage occurs. This state defines the dynamic critical capillary pressure, $\hat{P}_c^*$. Thus upon changing the pertinent parameters, the mathematical solution to Eq. (3) traces a locus of critical capillary pressures, $\hat{P}_c^*$, as a function of Ca, $\hat{h}_o$, a, and θ.

Figure 3 shows the effect of the pore-body to pore-throat radius ratio, R_b/R_c, on the critical capillary pressure for various values of the capillary number. Given a constant value of Ca and a wetting-phase saturation (i.e., given $\hat{P}_c$), Fig. 3 illustrates that large pore-body to pore-throat radii ratios lead to a more unstable foam. The effect is more dramatic for higher capillary numbers.

In a given porous medium there is a distribution of pore-body and pore-throat sizes. If a lamella exits from a constriction into a pore body whose ratio, R_b/R_c, is less than that set by the appropriate curve in Fig. 3, the lamella survives. Conversely, if it exits into a pore body whose value of R_b/R_c is greater than that in Fig. 3, that lamella must break. Thus particular combinations of pore throats and pore bodies (i.e., those with R_b/R_c greater than critical) can be classified as termination sites, in analogy with the germination sites for foam generation (Ransohoff and Radke, 1988). The overall rate of foam coalescence in a porous medium then depends directly on the number density of termination sites. This number density in turn is a function, among other variables, of the wetting-phase saturation. Given the pore-throat and pore-body size distribution and their probability of interconnection, the termination-site density appears calculable. Hence our periodic-pore theory in Fig. 3 permits calculation of foam coalescence rates in porous media.

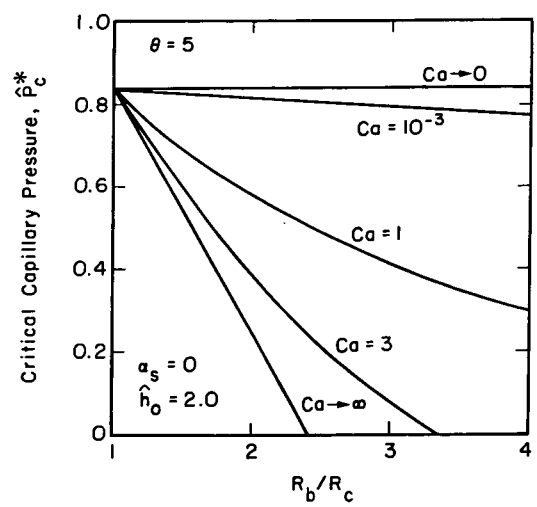

Figure 3. The effect of pore-body to pore-throat radius ratio on the critical capillary pressure. [XBL 849-1552]

CONCLUSIONS

The stability of flowing lamellae controls the longevity of foam in porous media. By analyzing a single lamella as it percolates through a periodically constricted tube, we have developed a hydrodynamic stability theory that explains the physical phenomena governing foam coalescence in porous media. The conjoining/disjoining-pressure isotherm proves to be the crucial physical property of the surfactant system. It determines the maximum capillary pressure that foam can sustain at rest in a porous medium.

For transporting foam, the critical capillary pressure is reduced as lamellae thin under the influence of both capillary suction and stretching by the pore walls. For a given gas superficial velocity, foam cannot exist if the capillary pressure and the pore-body to pore-throat radii ratio exceed a critical value.

REFERENCES

Derjaguin, B.V., 1939. Anomalous properties of thin polymolecular films. Acta Physicochim., v. 10, no. 1, p. 25–44.

Derjaguin, B.V., and Titievskaja, A.S., 1957. Static and kinematic stability of free films and froths. *In* Proc. 2nd Int. Congr. Surface Activity (Vol. 1). Butterworths, London, p. 211–219.

Exerowa, D., Kolarov, T., and Khristov, K. H. R., 1987. Direct measurement of disjoining pressure in black foam films. Colloids Surf., v. 22, p. 171–185.

Ivanov, I.B., Radoev, B., Manev, E.D., and Scheludko, A., 1970. Theory of the critical thickness of rupture of thin liquid films. Trans. Faraday Sci., v. 66, p. 1262–1273.

Jiménez, A.I., 1989. (Ph.D. Thesis). University of California, Berkeley, in preparation, 1989.

Khatib, Z.I., Hirasaki, G.J., and Falls, A.H., 1988. Effect of capillary pressure on coalescence and phase mobilities in foams flowing through porous media. PE Res. Eng., v. 3, no. 3, p. 919–926.

Malhotra, A.K., and Wasan, D.T., 1986. The stability of foam and emulsion films. Chem. Eng. Commun., v. 48, p. 35–56.

Ransohoff, T.C., and Radke, C.J., 1988. Mechanisms of foam generation in glass-bead packs. SPE Res. Eng., v. 3, no. 2, p. 573–585.

Rao, A.A., Wasan, D.T., and Manev, E.D., 1982. Foam stability. Chem. Eng. Commun., v. 15, p. 63–81.

Reynolds, O., 1886. On the theory of lubrication and its application. Phil. Trans. Roy. Soc. (London) v. A177, p. 157–234

Scheludko, A., 1967. Thin liquid films. Adv. Colloid Interface Sci., v. 1, p. 391–464.

Verwey, E.J.W., and Overbeek, J.T.G., 1948. The Theory of Lyophobic Colloids. Elsevier, Amsterdam.

Vrij, A., 1966. Possible mechanism for the spontaneous rupture of thin free liquid films. Disc. Faraday Soc., v. 42, p. 23–33.

Prematurely Terminated Slug Tests

K. Karasaki

Slug tests are relatively easy and inexpensive to perform. For this reason, they are widely used for estimating aquifer parameters. However, when a skin is present, it is very difficult to distinguish the permeability of the formation from that of the skin. Because of the transient nature of the induced boundary condition at the wellbore under slug tests, results obtained by type-curve matching are unknown averages of the two permeabilities.

For infinitesimally thin skin, the shapes of the curves of head versus time are identical to those without skin (Ramey et al., 1975). Therefore, either the skin factor or the formation storativity must be known a priori to estimate the transmissivity. For skin of finite radius, certain combinations of flow parameters give curves of characteristic shape (Moench and Hsieh, 1985). However, in most cases the curves are again indistinguishable from those without skin. The results obtained by type-curve matching, therefore, must be treated with caution when a skin is suspected to be present.

As opposed to the flow-period data, buildup data are in general less obscured by skin effects. Horner analysis is one method used to analyze buildup data. Pressure is plotted as a function of $(t_p + \Delta t)/\Delta t$, where t_p is the flow duration and Δt is the time after shut-in. Transmissivity can be estimated from the slope of the straight-line section of the curve.

Falloff/buildup data of a prematurely terminated slug test (PTST) or drillstem test (DST) are commonly analyzed by using this method. Horner analysis assumes that the formation is produced (or injected) at a constant rate prior to shut-in and utilizes the principle of superposition. However, this assumption is not entirely correct in the case of a PTST or DST. The flow rate actually declines as a function of time. Therefore, the longer the production (or injection) period is, the less accurate the assumption becomes. At the same time, for a constant-flow-rate case, Horner analysis is actually more accurate for longer flow and shut-in periods, because it assumes that the transient pressures can be approximated by a logarithmic function. In the next section, a rigorous solution of the falloff/buildup of a PTST or DST problem will be presented.

THEORY

The boundary condition for premature termination of a slug test at $t_D = \tau$ can be expressed in a dimensionless form as

$$\frac{1}{\omega(t_D)} \cdot \frac{dh_{wD}}{dt_D} = \frac{\partial h_D}{\partial r_D} \quad , \tag{1}$$

and

$$\omega(t_D) = \begin{cases} \omega_1 = \dfrac{2\pi r_w^2 S}{C_{w1}} & (0<t_D<\tau) , \\ \omega_2 = \dfrac{2\pi r_w^2 S}{C_{w2}} & (t_D>\tau) , \end{cases} \tag{2}$$

where h_{wD} is the normalized fluid level in the well, h_D is the normalized head in the system, t_D is the dimensionless time, Tt/Sr_w^2, and r_D is the dimensionless radius, r/r_w. The wellbore storage, C_w, changes from that of the open well to that of the closed interval at the termination of a slug test. It is this time-dependent coefficient that causes a straightforward Laplace transform solution method to fail. Thus, in the work summarized here, a different approach is sought. First the flow rate at the well is solved as a function of time for the usual slug-test boundary conditions. Then this transient flow rate is used as the inner boundary condition of a controlled variable-rate injection/pumping test. Duhamel's theorem is employed to solve for the pressure at the well with time-dependent flow rate. This is done through time-convolution of the flow rate with the solution for a unit injection rate. Premature termination of the test can be formulated by dividing the time integration into parts: before and after the shut-in. In the following section the above procedure is more closely examined.

Duhamel's theorem as described in Carslaw and Jaeger (1946) states that if $F(r,t)$ represents the head distribution in response to a constant unit injection, the solution $h(r,t)$, where the injection rate is a function of time, $\phi(t)$, is given by

$$h(r,t) = \int_0^t \phi(\lambda) \frac{\partial}{\partial t} F(r,t-\lambda) d\lambda \quad . \tag{3}$$

For a homogeneous confined aquifer $F(r,t)$ is the solution given by van Everdingen and Hurst (1949), which can be written in a dimensionless form as

$$F(r_D,t_D) = \frac{2}{\pi} \int_0^\infty \frac{[1-\exp(-\mu^2 t_D)]}{\mu^2[J_1^2(\mu)+Y_1^2(\mu)]} \times [J_1(\mu)Y_0(\mu r_D) - Y_1(\mu)J_0(\mu r_D)] d\mu. \tag{4}$$

The flow rate at the sandface, $\phi(t_D)$, can be obtained by taking a time derivative of the solution in Cooper et al. (1967):

$$\phi(t_D) = \frac{1}{\omega} \frac{dh_{wD}}{dt_D}$$

$$= -\frac{4}{\pi^2} \int_0^\infty \exp(-\mu^2 t_D) \cdot \frac{\mu d\mu}{[\Phi^2(\mu)+\Psi^2(\mu)]} \quad , \tag{5}$$

where

$$\Phi(\mu) = \mu J_o(\mu) - \omega J_1(\mu), \tag{6}$$

$$\Psi(\mu) = \mu Y_o(\mu) - \omega Y_1(\mu). \tag{7}$$

It must be noted that ω is used here in place of α in the paper by Cooper et al.

Evaluating (4) at $r_D = 1$, using the identity

$$J_1(\mu)Y_0(\mu) - Y_1(\mu)J_0(\mu) = \frac{2}{\pi\mu} \quad , \tag{8}$$

and substituting into (3) with (5) yields the solution for fluid level at the well equivalent to that given by Cooper et al. (1967):

$$h_{wD}(t_D) = -\frac{16}{\pi^4}\int_0^{t_D}\left[\int_0^{\infty}\frac{\exp(-\mu^2\lambda)\mu d\mu}{[\Phi^2(\mu)+\Psi^2(\mu)]}\right.$$

$$\left.\times\int_0^{\infty}\frac{\{1-\exp[-\mu^2(t_D-\lambda)]\}d\mu}{\mu^3[J_1^2(\mu)+Y_1^2(\mu)]}\right]d\lambda. \quad (9)$$

As it is, the solution is of little use because it is much more complex than that of Cooper et al. However, premature termination of injection or withdrawal can be easily formulated by breaking up the integration into two time domains. For termination at time τ, the equation can therefore be expressed as

$$h_{wD}(t_D) = -\frac{16}{\pi^4}\int_0^{\tau}\left[\int_0^{\infty}\frac{\exp(-\mu^2\lambda)\mu d\mu}{[\Phi^2(\mu,\omega_1)+\Psi^2(\mu,\omega_1)]}\right.$$

$$\left.\times\int_0^{\infty}\frac{\{1-\exp[-\mu^2(t_D-\lambda)]\}d\mu}{\mu^3[J_1^2(\mu)+Y_1^2(\mu)]}\right]d\lambda.$$

$$-\frac{16}{\pi^4}\int_{\tau}^{t_D}\left[\int_0^{\infty}\frac{\exp(-\mu^2\lambda)\mu d\mu}{[\Phi^2(\mu,\omega_2)+\Psi^2(\mu,\omega_2)]}\right.$$

$$\left.\times\int_0^{\infty}\frac{\{1-\exp[-\mu^2(t_D-\lambda)]\}d\mu}{\mu^3[J_1^2(\mu)+Y_1^2(\mu)]}\right]d\lambda. \quad (10)$$

Because the integration terms in (10) are very slowly converging functions, it is difficult to evaluate the equation numerically. It is much easier to express them in terms of Laplace space solutions and evaluate them by numerical inversion. Hence (10) can be rewritten as

$$h_{wD}(t_D) = \int_0^{\tau} L_{\lambda}^{-1}\left\{\frac{-\sqrt{p}K_1(\sqrt{p})}{pK_0(\sqrt{p})+\omega_1\sqrt{p}K_1(\sqrt{p})}\right\}$$

$$\times L_{t_D-\lambda}^{-1}\left\{\frac{K_0(\sqrt{p})}{\sqrt{p}K_1(\sqrt{p})}\right\}d\lambda$$

$$+\int_{\tau}^{t_D} L_{\lambda}^{-1}\left\{\frac{-\sqrt{p}K_1(\sqrt{p})}{pK_0(\sqrt{p})+\omega_2\sqrt{p}K_1(\sqrt{p})}\right\}$$

$$\times L_{t_D-\lambda}^{-1}\left\{\frac{K_0(\sqrt{p})}{\sqrt{p}K_1(\sqrt{p})}\right\}d\lambda, \quad (11)$$

where p is the Laplace space variable and L^{-1} denotes Laplace inversion. The subscript denotes the real space variable. Here the following property of the transform is used:

$$L\left\{\frac{\partial F(t)}{\partial t}\right\} = pL\{F(t)\} - F(+0) \ . \quad (12)$$

One verification of the solution is to test whether the solution by Cooper et al. can be reproduced when $\omega_1 = \omega_2$, i.e., for the case of no termination. It was found that this is indeed the case.

For premature termination of an open-hole slug test, the wellbore storage typically is reduced by several orders of magnitude before and after shut-in, i.e., $\omega_1 << \omega_2$. Therefore, the second term in (10) can be neglected for most cases of premature termination. Physically, this means that the flow into the interval after shut-in is negligibly small. Figure 1 shows the termination at 50% for various values of ω. It must be noted that the time needed for completion of the test is shortened by as much as one

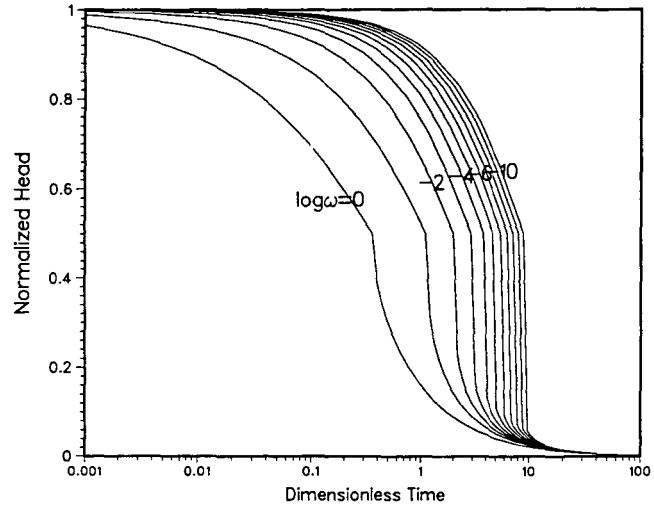

Figure 1. Premature termination of slug test at 50%. [XBL 894-1637]

order of magnitude. This is a significant saving of time and cost in light of the fact that completing the slug test is unlikely to yield more information, for the reason discussed previously. This article summarizes the work by Karasaki (1989).

REFERENCES

Carslaw, H.S., and Jaeger, J.C., 1946. Conduction of Heat in Solids. Clarendon Press, Oxford, p. 30–33.

Cooper, H.H., Jr., Bredehoeft, J.D., and Papadopulos, I.S., 1967. Response of a finite diameter well to an instantaneous charge of water. Water Resour. Res., v. 3, p. 263–269.

Karasaki, K., 1989. Prematurely terminated slug tests. To be submitted to Water Resour. Res.

Moench, A.F., and Hsieh, P.A., 1985. Analysis of slug test data in a well with finite thickness skin. *In* Proceedings, I.A.H. 17th International Congress on Hydrology of Rocks of Low Permeability, Tucson, Arizona, January 7–12, 1985.

Ramey, H.J., Jr., Agarwal, R.G., and Martin, I., 1975. Analysis of "slug test" or DST flow period data. J. Can. Pet. Tech., p. 37–47.

Van Everdingen, A.F., and Hurst, W., 1949. The application of the Laplace transformation to flow problems in reservoirs. Petroleum Trans., AIME, p. 305–323.

Characterization of Fracture Networks for Fluid-Flow Analysis

J.C.S. Long, K. Hestir, A. Davey, E.L. Majer, J.E. Peterson, and K. Karasaki

With the advent of problems such as the storage of nuclear waste and production from fractured oil reservoirs, characterization of fracture networks in rock has been the focus of increasing study. The goal of much of this work is to develop a numerical model that can be used to predict the flow and transport of fluids through rock. Building such models is difficult because fracture networks are complex, three-dimensional systems.

One approach to the problem has been to attempt to build a statistical model of the network based on sampling fracture data in outcrops and boreholes. In building the fracture network up from such small-scale data, we do not get a good statistical sample of unusual features. Consequently, it is very difficult to devise a model that includes the effect of infrequent features; for example, fracture zones. However, it is the fracture zones that often dominate the behavior of the fracture network. We measure many fractures that do not have a large role in fluid flow, and this results in developing a fracture network that is far too dense to be of use in explaining observed noncontinuum behavior. Such models predict millions of fractures in volumes of rock with the dimensions of tens of meters. From the hydrologic point of view, this model is wrong. Hence the "building up" approach fails to give us the dominant behavior of the network.

NEW PERSPECTIVES

We are proposing a new multi-tiered approach to developing fracture network models (Long et al., 1988). In this approach, we first identify the fracture zones using geophysics and geology; we then conceptualize the zones using geomechanics and geology and develop an initial model of the fractured rock. This model becomes the basis for inverse hydrologic analysis.

We present several preliminary examples of ongoing research from two field sites, the Grimsel Rock Laboratory in Switzerland, under investigation by the DOE-NAGRA Cooperative project, and the Stripa mine in Sweden, under investigation by the Stripa Project.

EXAMPLES OF FIELD-DATA ANALYSIS

The first example comes from the Grimsel Rock Laboratory in Switzerland. Here, Lawrence Berkeley Laboratory (LBL) and NAGRA are jointly pursuing an experiment called the FRI experiment. The site of the experiment is shown in Fig. 1 in plan view. At this site, a subvertical shear zone transects the rock between two parallel horizontal drifts. Two holes have been drilled on either side of the zone, between the two drifts. In addition, many small

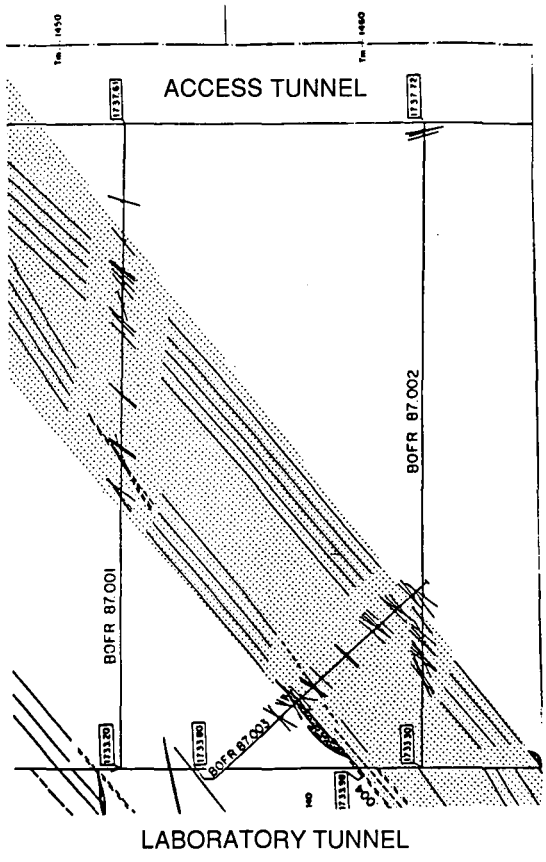

Figure 1. Plan view of the FRI experiment site showing the trace of the subvertical shear zone crossing between two parallel horizontal drifts. [XBL 894-1638]

holes have been drilled along the drift walls between the two larger holes. From these holes LBL has performed four-sided cross-hole seismic measurements resulting in the *P*-wave slowness tomogram shown in Fig. 2. In this tomogram dark zones represent slower velocities than light zones. The tomography shows the shear zone quite clearly.

The next step is to estimate the hydrologic features that control the behavior of well tests performed in the boreholes. Water injected into the shear zone from borehole 87.001 will not be restricted to flowing in the plane of the tomogram. Most likely, water will flow in the plane of the shear zone. So once the zone is identified the hydrologic information must be used to find an equivalent hydrologic network in the plane of the zone. For an example of this, we turn to the Stripa mine in Sweden.

At the Stripa mine, radar tomography has been performed, and several fracture zones have been identified. The zone called RB cuts three parallel boreholes, N2, N3, and N4, and thus is similar to the geometry of the FRI zone.

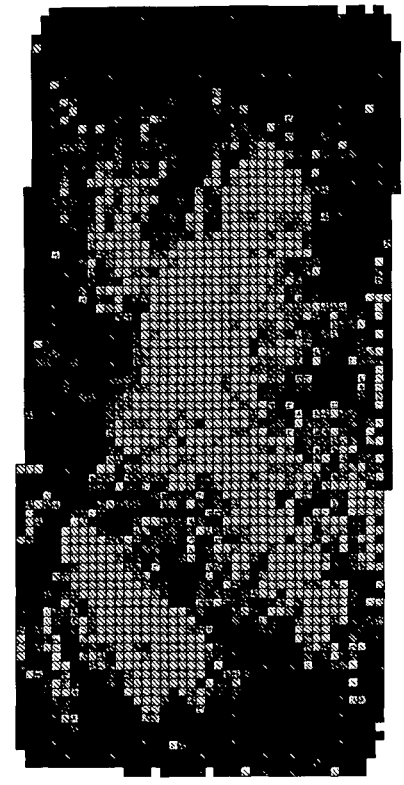

Figure 2. Tomographic results for the FRI zone. [XBL 894-1360]

First we propose a base geometry for hydrologic conductors called a template. In this case, we have chosen one of the simplest possible geometries, a square grid of conductors in the plane of the fracture zone, where not all the elements of the grid are present. Figure 3 shows such a grid, with the pumped well, N3, centrally located between N2 and N4. We anticipate that future investigations of shear-zone morphology will provide a more-sophisticated template for conductors. We now simulate a well test in the pattern of hydrologic conductors. The results of the well test show that N4 is more connected to N3 than is N2 because N3 responds before N2. Given real well test-data from N3 we could adjust the pattern shown in Fig. 3 so that it better matches the hydrologic data. In fact such "adjustment" constitutes hydrologic inversion.

Two inversion techniques are envisioned for finding an equivalent fracture network. In the first technique we note that flow to a well through a porous medium or a very well connected fracture network is either two- or three-dimensional. However, in a partially connected fracture network, the flow may not have an integral dimension.

Barker (1988) has developed a solution for the well-test equation, which treats dimension as a vari-

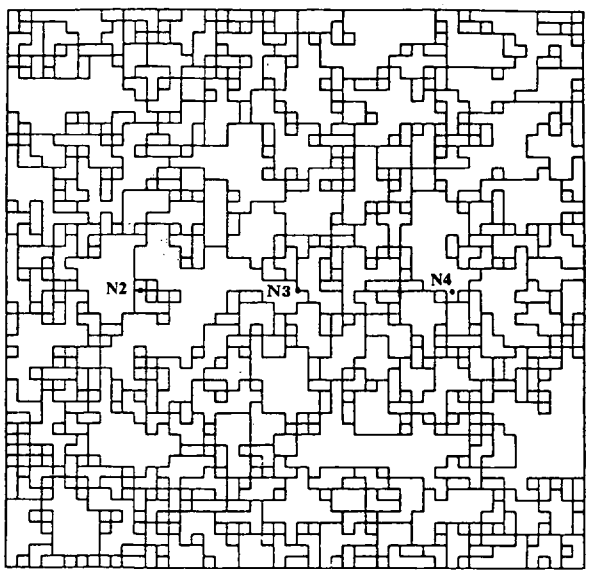

Figure 3. A possible pattern of hydrologic conductors for a shear zone at the Stripa site. [XBL 894-1639]

able. From this solution, he can develop type curves for partial dimension. Physically, such partial dimension is the result of the degree of connectivity in the network, i.e., the percentage of bonds to fill in the lattice template (Long and Witherspoon, 1985).

As an example, we have numerically modeled a well test in a system of theoretical fractal dimension equal to 1.465 (Fig. 4). When the numerical results are fit to Barker's curves they give a partial dimension of 1.40. The difference may be due to the fact that the numerical example is only "fractal" between an upper and lower limit. It remains to relate the connectivity of a random fracture network to its fractal dimension. If this can be done, the Barker solution can be used to find connectivity and, therefore, the percentage of bonds to fill.

A second possible technique is a structured way to make changes in the model of the fracture system such that it behaves more like the real system. In this technique, we model hydraulic tests and compare the results with the field results. Then we change the model by adding or deleting a conductor. We remodel the hydraulic test and see if the results fit the pump-test data better. If so, then we keep the change. If the change makes for a worse fit, we keep the change with a probability equal to

$$P = \exp[(E_1 - E_0)/T],$$

where E is equal to the square of the difference between the prediction and the measurement, 0 refers to the previous iteration, 1 refers to the

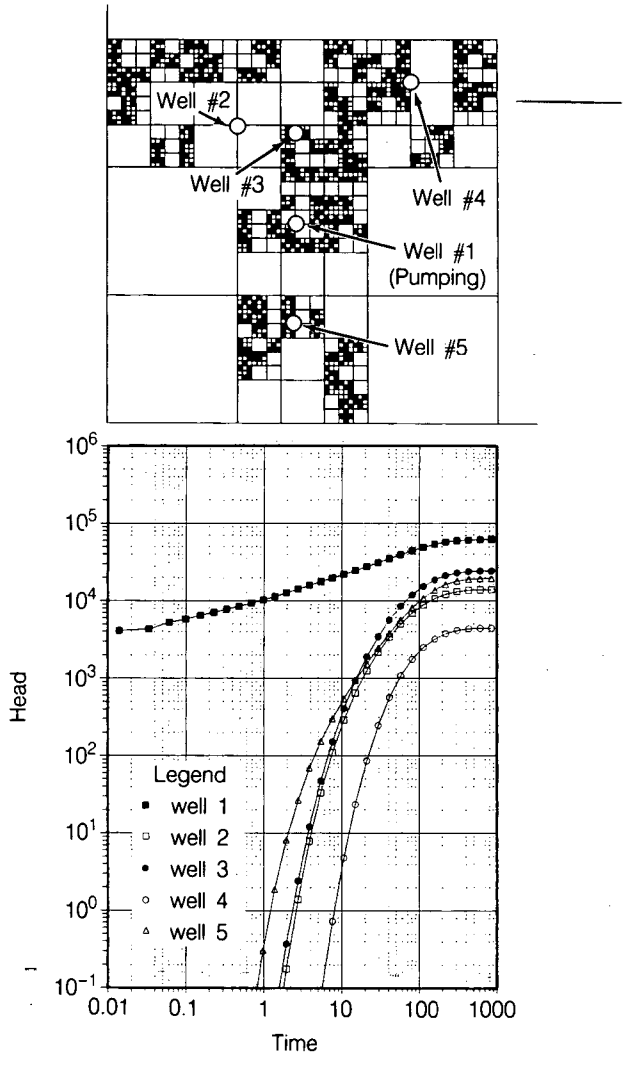

Figure 4. Well-test results in a fractal network. [XBL 891-6132]

present iteration, and T is a factor that decreases geometrically with the number of iterations. This technique allows one to get closer to a global minimum difference between measurements and model results instead of getting caught in a local minimum.

Any hydraulic test that can be modeled can be used to calculate E. Figure 5 shows an artificial example of the change in E, with each iteration based on well tests in a partially filled grid. Tracer-test data probably provide a more ideal type of data to use. However, the technique is computationally intensive, which may be a limitation.

CONCLUSION

The above approaches are still under development. Together, they form the basis of a new

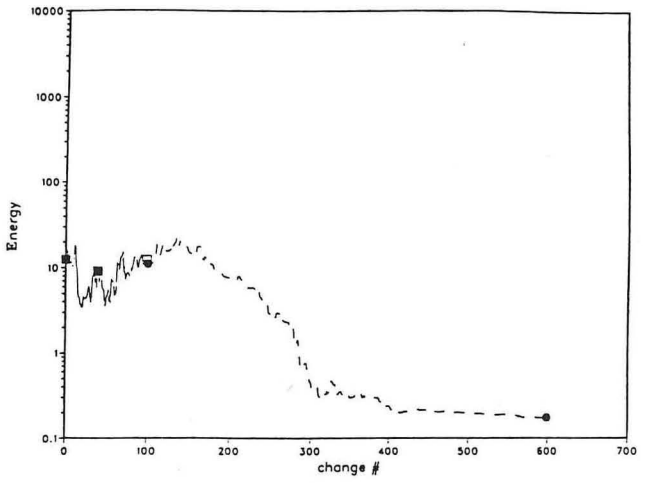

Figure 5. Example of the change in error, E, with iteration toward a model that better matches field data. [XBL 894-1640]

methodology for characterizing fractured rock. In following this methodology, we could produce a variety of systems that would all fit the data. It is unlikely that any of these solutions are unique. Therefore, if we can determine a system that behaves like the real system for our test cases, is that good enough? Of course, the answer to the question depends on the application, but it is clear that this is an area that itself deserves research.

ACKNOWLEDGMENTS

This work was funded through the U.S. Department of Energy's Repository Technology Program. Much of the work is fostered through cooperation with NAGRA, Nationale Genossenschaft für die Lagerung radioaktiver Abfalle and the Stripa Project. We are indebted to Charles McCombie, Piet Zuidema, Peter Blumling, Caroline Wittwer, Gerd Sattel, and many others at NAGRA; John Barker of the British Geological Survey; and Ollie Olsson and Borje Niva of SGUAB and the Stripa Project.

REFERENCES

Barker, John, 1988. A generalized radial-flow model for hydraulic tests in fractured rock. Water Resour. Res., v. 24, no. 10, p. 1796–1804

Long, J.C.S., Billaux, D., Hestir, K., Majer, E.L., Peterson, J., Karasaki, K., Nihei, K., Gentier, S., and Cox L., 1988. Characterization of fracture networks for fluid flow analysis. Presented at the Fourth Canadian/American Conference on Hydrogeology, Banff, Alberta, Canada, June 21–24, 1988 (LBL-26868).

Long, J.C.S., and Witherspoon, P.A., 1985. The relationship of the degree of interconnection to permeability in fracture networks. J. Geophys. Res., v. 90, no. B4, p. 3087–3098.

Fracture-Zone Structure at The US/BK Site, Grimsel Rock Laboratory, Switzerland

S.J. Martel and J.E. Peterson

In low-permeability rocks such as granites and welded tuffs, fluids may flow primarily along fractures. However, at present we know much less about how fluid flows in fractures as compared with porous rock. This is a handicap in predicting the flow behavior in sites being considered for nuclear waste repositories. The Swiss National Cooperative for the Storage of Radioactive Waste (NAGRA) has hosted a variety of experiments in the past few years at its underground Grimsel Rock Laboratory directed toward improving our understanding of fracture flow.

The structure of a fracture system largely controls how fluid flows along it. This article describes how surface and subsurface geologic mapping have been integrated with geophysical remote-sensing techniques to interpret the fracture structure and flow-tracer-test information at the US/BK site at the Grimsel Laboratory.

GEOLOGIC SETTING

The host rocks at Grimsel are slightly foliated granitic rocks. The foliation strikes ~ENE and dips ~70° to the south (Choukroune and Gapais, 1983).

Aplite and quartz veins and lamprophyre dikes intrude the granites. Two sets of steeply dipping fracture zones occur. K-zones strike ~NW and cut the rock grain at nearly right angles. S-zones strike ~NE, approximately parallel to the rock grain. K- and S-zones dip to the south at ~70°.

FINDINGS FROM GEOLOGIC MAPPING

A 100-m-long section of a well-exposed K-zone (Fig. 1) was mapped at the surface to document details of its internal fracture structure and to show how that fine structure is related to the gross structure of the zone. The zone appears to offset a steeply dipping lamprophyre dike by ~20 m left-laterally. The zone contains a series of NW-striking fractures that are linked by smaller fractures that strike ENE. Fractures of both sets dip steeply. Structurally, the zone is remarkably similar to some left-lateral fault zones in the Sierra Nevada of California that developed from fault-parallel joints (Martel et al., 1988; Martel, 1989).

The mapped K-zone clearly is not a uniform planar structure. The zone has a nonlinear trace, with subparallel segments joining at echelon steps. It varies in width from about 1 to 10 m. The relative abundance of ENE-striking fractures varies markedly along strike. They are most abundant, and the zone is widest, at a left-step at the NW end of the map.

In contrast to the K-zones, the S-zones display a braided structure (Fig. 2). Subhorizontal slickenlines within the S-zones indicate that they have slipped in a strike-slip fashion. Several surface exposures at the edges of S-zones contain steeply dipping veins that are plastically sheared in a left-lateral sense, whereas in subsurface exposures veins are sharply offset across S-zones in a right-lateral sense. We infer that the S-zones first slipped left-laterally under elevated pressure-temperature conditions and then right-laterally under lower pressure-temperature conditions.

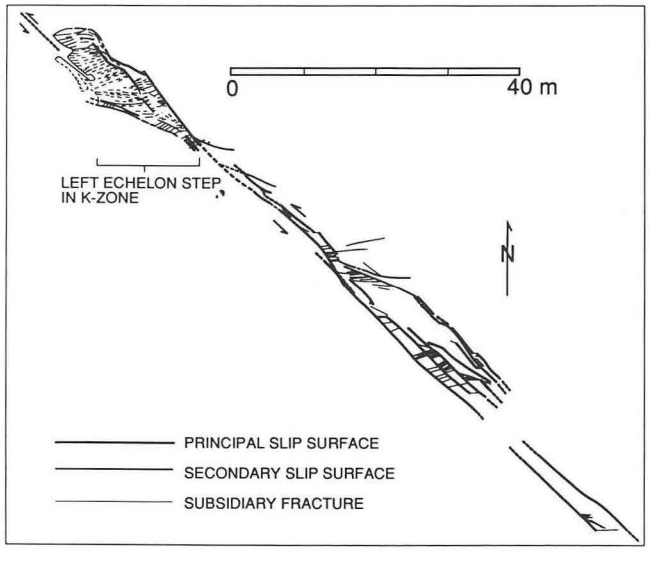

Figure 1. Map of part of a Grimsel K-zone. [XBL 891-5809]

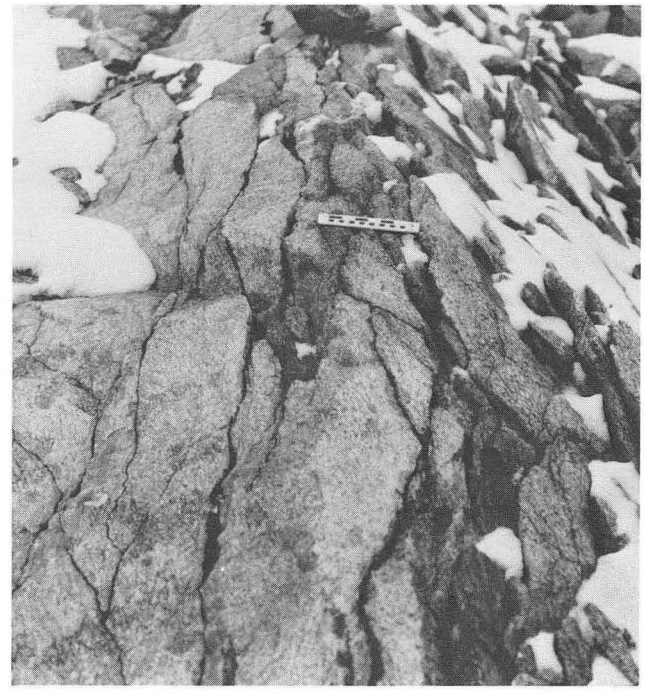

Figure 2. Photograph of the edge of an S-zone (15-cm ruler for scale). Note the braided fracture structure. [XBL 8811-11079]

The distinctly different structures of the K- and S- zones (Fig. 3) appear to reflect differences in the flaws from which the zones developed. The K-zones apparently developed from an irregular distribution of pre-existing NW-striking fractures. The S-zones developed upon the foliation in the rock. Because the rock fabric can be uniform over large areas, we expect that the S-zones would tend to have a more uniform structure than the K-zones.

The differences in their structure suggest that the K- and S-zones would have markedly different fracture-flow characteristics. The K-zones appear structurally more heterogeneous than the S-zones, and we expect that fluid flow would be more heterogeneous along the K-zones than the S-zones. Fluid flow in the K-zones is most likely to be localized at steps, where the fracturing is most extensive. In three dimensions these steps might act as nearly vertical pipes.

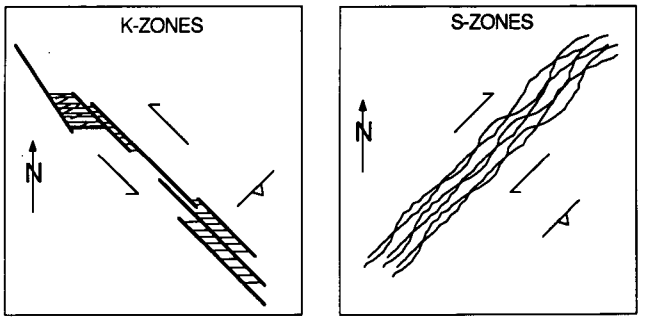

Figure 3. Comparison of K- and S-zones. The rock foliation dips steeply to the southeast. [XBL 891-5806]

The most recent slip on the NW-striking K-zones apparently has been left-lateral, whereas the NE-striking S-zones apparently slipped right-laterally. Both zones may have slipped contemporaneously under a maximum horizontal compressive stress oriented east-west. The zones may offset each other where they intersect. If so, the steeply dipping zone intersections may be sites of extensive fracturing and preferred paths for fluid flow.

GEOPHYSICAL TOMOGRAPHY AT THE US/BK SITE

Geophysical tomography is a nondestructive technique that uses the ways in which signals change as they pass through a body of rock to map properties of the rock. Radar tomography has been used to map the variation of amplitude attenuation and velocity characteristics at the US/BK site (Niva and Olsson, 1987). The rock along fracture zones has different attenuation and velocity properties than unfractured granitic rock, so tomography can be used to map fracture zones that intersect the plane of the tomography. Tomograms have been prepared using radar data gathered before (phase 1) and after (phase 2) the injection of a brine at the US/BK site (Niva and Olsson, 1988). Because dielectric properties of the brine contrast sharply with those of the host rock, phase 1 data can be subtracted from phase 2 data to make difference tomograms showing where the brine flowed. Figure 4 is an attenuation-difference tomogram; two prominent dark areas that represent brine occur near the injection point and the mouth of the US/BK room. Superimposed on Fig. 4 are the locations of two prominent anomalies from a phase 1 attenuation tomogram. Anomaly 1 occurs along the projection of a prominent NE-striking S-zone exposed at the northeast corner of the site. Somewhat surprisingly, this S-zone does not have a prominent trace on the phase 1 or 2 radar

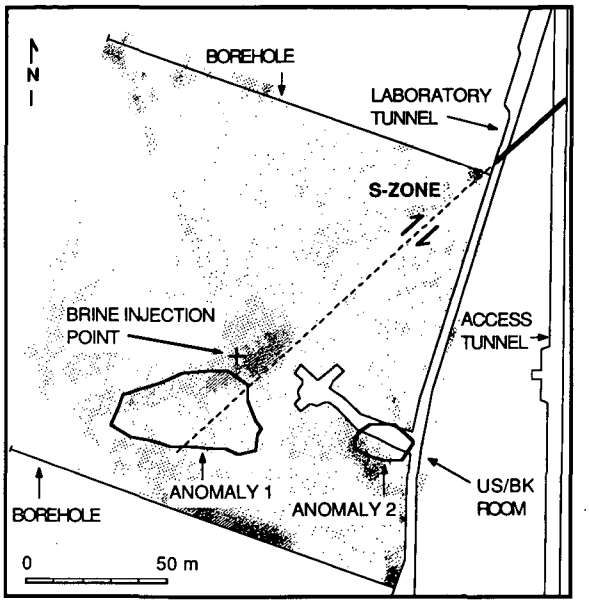

Figure 4. Difference tomogram of radar attenuation at the US/BK site (modified from Niva and Olsson, 1988, Fig. 5.12) showing point of brine injection and areas of brine migration (dark areas). Anomalies 1 and 2 are from phase 1 radar attenuation tomography (Niva and Olsson, 1987, Fig. B3). [XBL 891-5807]

tomograms; it does appear on an acoustic-velocity tomogram, however (Blümling and Sattel, 1988). Anomaly 2 occurs near the mouth of the US/BK room, well away from the S-zone.

MODEL OF FRACTURE ZONES AT THE US/BK SITE

We currently interpret attenuation anomalies 1 and 2 as coinciding with structural anomalies along an S-zone and a K-zone (Fig. 5). The plume of brine that extends southeast of the injection point terminates near the projected intersection (anomaly 1) of the aforementioned S-zone with a K-zone exposed south of the US/BK room. Anomaly 2 coincides with what we interpret as a left step in the K-zone on the basis of an unpublished NAGRA map. Steeply plunging prisms of extensive fracturing would be expected in such areas on the basis of geologic mapping.

Note that the brine "plume" does not extend continuously between the injection point and the mouth of the US/BK room in Fig. 4. Indeed, the mapping of the US/BK room does not indicate that any major fractures would directly link the injection point to the mouth of the room. This suggests that brine flowed out of the plane of the tomography to reach anomaly 2. On the basis of our interpretation

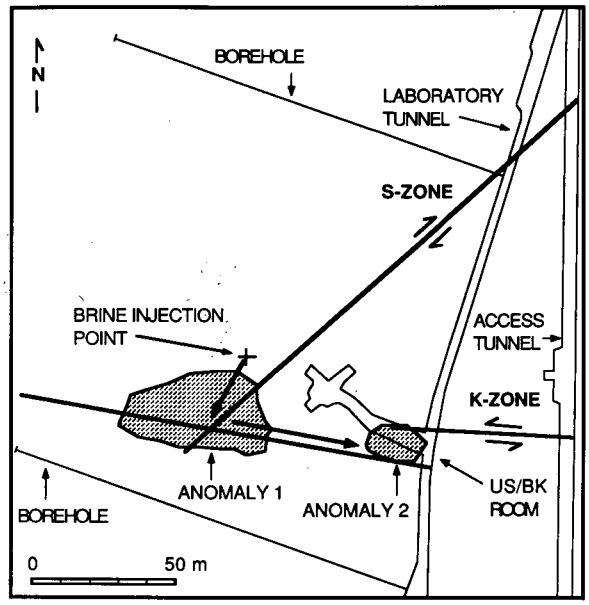

Figure 5. Conceptual model of fracture zone structure at the US/BK site. Anomalies 1 and 2 mark sites of intense fracturing. Heaviest arrows mark possible path of brine flow. [XBL 891-5808]

of the fracture zone structure, we suggest that the brine may have migrated subhorizontally along the S-zone until reaching anomaly 1 and then flowed out of the plane of the tomography. The brine could then have followed the high hydrologic gradient toward the laboratory tunnel and flowed east along the K-zone to anomaly 2, where it re-entered the plane of the tomography. Borehole data are being reviewed to test this hypothesis. A second possibility is that the brine reservoirs, which were located above anomaly 2, leaked. In this case the fractures at anomaly 2 would have acted as a reservoir.

CONCLUSIONS

By combining geologic mapping with geophysical tomography, paths of fluid flow can be considered from a structural standpoint more readily than by using either technique by itself. The resulting models can help guide subsequent research. This integrated approach should also be useful in other settings.

ACKNOWLEDGMENTS

NAGRA provided us the opportunity to work at Grimsel, and we greatly appreciate the gracious help of their research staff. The technical staff at the Grimsel Laboratory kindly assisted in the details of our daily work.

REFERENCES

Blümling, P., and Sattel, G., 1988. Tomographic investigations. *In* M. Guntensperger (ed.), NAGRA Bulletin, Special Edition, p. 35–40.

Choukroune, P., and Gapais, D., 1983, Strain pattern in the Aar Granite (central Alps): Orthogneiss developed by bulk inhomogeneous flattening. J. Struc. Geol., v. 5, p. 411–418.

Martel, S.J., 1989, Formation of segmented strike-slip fault zones, Mount Abbot quadrangle, California. *In* D. Schwartz (ed.), Proceedings, U.S. Geological Survey Workshop on Fault Segmentation and Controls of Rupture Initiation and Termination. U.S. Geological Survey Open-File Report, in press.

Martel, S.J., Pollard, D.D., and Segall, P., 1988. Development of simple strike-slip fault zones in granitic rock, Mount Abbot quadrangle, Sierra Nevada, California. Geol. Soc. Am. Bull., v. 100, p. 1451–1465.

Niva, B., and Olsson, O., 1987. Radar crosshole tomography results from Phase 1. NAGRA Internal Report 88-30.

Niva, B., and Olsson, O., 1988. Radar crosshole tomography results from phase 2. NAGRA Internal Report 88-31.

Numerical Simulation of the Richards Equation: Current Approaches and an Alternate Perspective

T.N. Narasimhan

THE RICHARDS EQUATION

In its essence the Richards equation expresses the evolution in time of some state variable such as pressure head or water saturation in an elemental volume within a variably saturated porous medium. For practical purposes, it is convenient to represent this evolution over a small interval of time Δt. Consider a small elemental volume of index j bounded by a closed surface Γ, as shown in Fig. 1. The temporal evolution of this element from its initial state to its final state can be symbolically represented as follows. At the initial time t_0, the mass of water contained in the element and the average pressure head over the element are, respectively, $M^0_{w,j}$ and ψ^0_j. The state at t_0 is given by

$$M_{w,j}\,(t_0) = M^0_{w,j}, \tag{1a}$$

$$\psi_j\,(t_0) = \psi^0_j, \tag{1b}$$

The change of state from t_0 to $t_0 + \Delta t$ is given by

$$-\left\{\sum_m \rho_w \vec{q}\cdot\vec{n}_{jm}\Delta\Gamma_{jm} + \sum_b \rho_w \vec{q}\cdot\vec{n}_{jb}\Delta\Gamma_{jb} + \rho_w G_j\right\}\Delta t = \Delta M_{w,j} = M_{c,j}\Delta\psi_j. \tag{2}$$

The state at $t_0 + \Delta t$ is given by

$$M_{w,j}(t_0 + \Delta t) = M^0_{w,j} + \Delta M_{w,j}, \tag{3a}$$

$$\psi_j(t_0 + \Delta t) = \psi^0_j + \Delta\psi_j, \tag{3b}$$

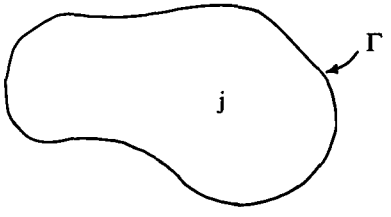

Figure 1. An elemental volume j enclosed by the surface Γ. [XBL 895-1678]

where $M_{w,j}$ and ψ_j denote the mass of water and the fluid pressure head; ρ_w is the mass density of water; $\vec{q}$ is the flux density or Darcy velocity; $\vec{n}_{jm}$ is the unit outer normal to the surface segment of volume element j, which is interior to the flow domain; $\vec{n}_{jb}$ is the outer normal to the bth surface segment of volume element j, which coincides with the external surface of the flow domain; $\Delta\Gamma_{jm}$ and $\Delta\Gamma_{jb}$ are surface segments that enclose volume element j; G_j is the volumetric rate of fluid generation (positive when fluid is injected or negative when fluid is withdrawn) from elemental volume j; $\Delta M_{w,j}$ is the change in mass of water over j during the time interval Δt; $M_{c,j}$ is the *capacitance* of element j (synonymous with *fluid mass capacity* (Narasimhan and Witherspoon, 1977); and $\Delta\psi_j$ is the change in average pressure head over j during Δt. Defined by the relation $M_{c,j} = \partial M_w/\partial\psi$, the *capacitance* is the change in the mass of water stored in the elemental volume j associated with a unit change in the average pressure head ψ over the element, with the external stresses held constant. The superscript zero in (1) through (3) denotes the initial condition.

THE NUMERICAL APPROACH

Two commonly used numerical techniques for solving (2) are the integral-finite-difference method (IFDM) and the finite-element method (FEM). These numerical schemes are founded on the notion that the dependent variable ψ_j and other intensive variables are known at discrete locations within the flow domain of interest. These locations are commonly called nodes or nodal points. The intensive quantities are physically taken to be volume averages over the elemental volume of interest. Upon discretization and algebraic manipulations, both methods lead to a matrix of equations of the form

$$\Delta t\left\{\sum_m U_{jm}[(z_m - z_j) + (\bar{\psi}_m - \bar{\psi}_j)] + \sum_b U_{jb}[(z_b - z_j) + (\bar{\psi}_b - \bar{\psi}_j)] + \rho_w G_j\right\} = M_{c,j}\Delta\psi_j, \tag{4}$$

where the U's denote *conductance*, defined as mass flux per unit difference in potential; the z's denote elevation; and the subscripts j and m denote adjoining elemental volumes.

Examination of (4) makes it clear that the goal is to solve for $\Delta\psi_j$, using the known quantities U and M_c and the known forcing functions on the boundaries as well as the source terms. It follows, therefore, that whatever difficulties arise in numerical simulations must be related to a large degree to errors inherent in estimating the conductances, the capacitances, and the time-averaged values of ψ. Therefore, the following three questions are critical to numerical modeling.

1. How best to calculate the conductances U_{jm} and U_{jb}?
2. How best to define the time-averages $\bar{\psi}$?
3. How best to calculate the capacitances M_c?

In partially saturated systems, both the conductances and the capacitances continually vary in time.

CURRENT APPROACHES

Evaluation of the Conductance

By definition, *conductance* is the time rate of transfer of the mass of water between two adjoining elemental volumes per unit difference in potentiometric head. As shown by Narasimhan (1985), the magnitude of conductance in the context of saturated/unsaturated flow is a function of several factors, including relative hydraulic conductivity (a material property) and local flow geometry. Thus, for a flow tube whose cross-sectional area A is a function x along a curvilinear flow path,

$$\vec{Q}_{jm} = \frac{[(z_m + \psi_m) - (z_j + \psi_j)]}{\frac{1}{K_s}\int_{x_j}^{x_m} \frac{dy}{k_r(\psi(y))A(y)}}. \qquad (5a)$$

In the context of (5a), the conductance is

$$U_{jm} = \frac{1}{\frac{1}{K_s}\int_{x_j}^{x_m} \frac{dy}{k_r(\psi(y))A(y)}}, \qquad (5b)$$

where K_s is the saturated hydraulic conductivity and k_r is the relative permeability to water. Note that in (5a) and (5b) both k_r and the spatially dependent A occur within the integral sign. Since ψ is known only at the end points x_j and x_m but not within the interval $x_j < x < x_m$, (5a) is in general an implicit statement when z_m is not equal to z_j (that is, when gravity is present) or when A or K_s is a function of space. This implicit nature of the flux law has to be duly recognized in setting up the numerical equations. Nevertheless, in current numerical practices the flux law is invariably treated as an *explicit* statement, using ad hoc assumptions. In the IFDM, conductance is usually evaluated as

$$U_{jm} = \frac{K_s \bar{k}_{r,jm} A_{jm}}{d_{jm} + d_{mj}}, \qquad (6)$$

where $\bar{k}_{r,jm}$ is a spatial average of the relative hydraulic conductivity for the region between j and m and A_{jm}, d_{jm}, and d_{mj} are as shown in Fig. 2. Commonly a variety of *predetermined* mean-value options are used for $\bar{k}_{r,jm}$ (e.g., harmonic mean, geometric mean, upstream weighting). These mean values, all chosen a priori, have errors inherent in them because they neither take into account the local flow geometry nor recognize the implicit nature of the flux law.

In the FEM, also, weighting functions chosen a priori are used to compute the conductances by a process of integration over piecewise continuous subdomains. Yet even these conductances have inherent errors in them, as they fail to take into account the implicit nature of the flux law and the nature of the local flow geometry.

The Time Average

It is widely known that if Δt is large, then, to assure stability as well as accuracy of solution, one has to use time-averaged values of ψ in evaluating the fluxes included within the summations in (4). If we assume that we have the ability to evaluate U_{jm} and U_{jb} accurately, it is easy to see that the mass of water transferred from m to j during Δt is given by

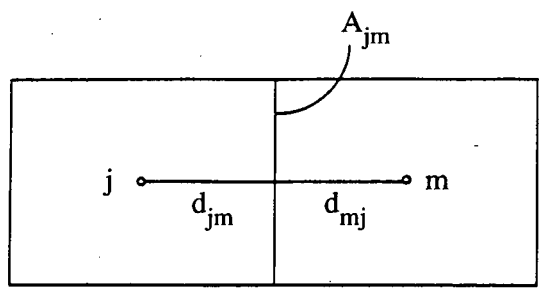

Figure 2. Two interacting volume elements, j and m, in the IFDM. [XBL 895-1679]

$$\text{Mass transferred} = \int_{t_0}^{t_0+\Delta t} U_{jm}[(z_m - z_j) + (\psi_m - \psi_j)]dt. \quad (7)$$

For purposes of setting up the linear equations in the numerical model, we wish to replace (7) by

$$\int_{t_0}^{t_0+\Delta t} U_{jm}[(z_m - z_j) + (\psi_m - \psi_j)]dt = U_{jm}(t_0 + \lambda_{jm}\Delta t)$$

$$\times \left\{(z_m - z_j) + (\psi_m(t_0 + \lambda_{jm}\Delta t) - \psi_j(t_0 + \lambda_{jm}\Delta t)\right\}$$

$$= \bar{U}_{jm}\left[(z_m - z_j) + (\bar{\psi}_m - \bar{\psi}_j)\right], \quad (8)$$

where $\bar{U}_{jm}$, $\bar{\psi}_m$ and $\bar{\psi}_j$ are time-averaged values evaluated at $\lambda_{jm}\Delta t$, where $0 < \lambda_{jm} < 1.0$. To assure maximum accuracy in evaluating the fluxes, therefore, we must choose the time-weighting factor λ_{jm} in such a way that (8) is satisfied as accurately as possible. Because of the dependence of conductance on k_r as well as the local flow geometry, it is to be expected that λ_{jm} will in general be a function of space and time. In other words, to assure maximum accuracy in evaluating fluxes in the numerical model, λ_{jm} must be allowed to vary from elemental interface to elemental interface and from one time step to the next. Nevertheless, it is the general custom in numerical modeling practices (either the IFDM or the FEM) to use a single global value of λ for the entire flow domain. Thus choosing a single time-weighting factor, as is commonly done, introduces a source of error.

The Capacitance

The classical notion of capacitance can be conveniently illustrated with the help of the heat-conduction analogy. The *heat capacity* of a mass of material is defined by

$$C = \frac{\Delta H}{\Delta T}, \quad (9)$$

where C is the heat capacity of the material, ΔH is the change in heat content, and ΔT is the change in temperature. Note that C is uniquely defined only if ΔT is a constant over the mass of material. In an elemental volume within a transient system, the change in potential is a function of space, hence the denominator ΔT in (9) is not unique. In principle, therefore, C is poorly defined, unless one specifies the particular location at which ΔT is measured. So C is defined only in an operational sense and it is a function of the property of the material that occupies the elemental volume and also the *location of measurement.* In a general nonlinear system, the capacitance associated with a given location will vary with time, depending on changes in local flow geometry as well as on the nature of the material property.

In both the IFDM and the FEM, neither the influence of flow geometry nor the operational significance of the capacitance parameter is given consideration, thereby leading to inherent inaccuracies.

ALTERNATE APPROACH

The conventional approach for minimizing these errors is to use finer and finer discretization in space and in time. The suggestion offered here, however, is that in accord with the reasoning presented above, accuracy could be improved through the following procedures (see Narasimhan (1988) for details).

Conductance

In view of (5b), one may first estimate, from prior system behavior, the flux between each pair of interacting elemental volumes in the system using estimated time-averaged potentials and flow geometry. From this estimated flux one may then compute the *conductance* to be used in the matrix used for obtaining the solution. This implementation is fairly straightforward for flow tubes with known geometry. Extension to multidimensions is feasible by discretizing the system into flow tubes and optimizing the flow-tube geometries to minimize an appropriate variational functional.

Time Average

As suggested in (6), the time-averaging parameter may be defined and estimated independently for each pair of interacting elements in the system, depending on the time rates of changes of the conductance as well as the potentials at each pair of elemental volumes concerned.

Capacitance

Finally, errors in estimating the capacitance could be minimized by estimating the change in mass of fluid over the time interval of interest and dividing it by the change in potential at the location of interest. This is in accordance with the reasoning that for an elemental volume in a dynamic state,

capacitance is not exclusively a function of the material property but is also a function of the flow geometry and the location of observation. As shown in Narasimhan (1988), this manner of computing capacitance can be implemented fairly easily by discretizing the system into flow tubes and isopotentials.

CONCLUSION

The discussions presented above suggest that it is feasible to formulate the Richards equation directly in a discrete integral form and solve it in a self-consistent fashion. Such a process may help avoid difficulties that are encountered in integrating the highly nonlinear partial differential equation.

REFERENCES

Narasimhan, T.N., and Witherspoon, P.A., 1977. Numerical model for saturated-unsaturated flow in deformable porous media, Part I: Theory. Water Resour. Res., v. 13, no. 13, p. 657–664.

Narasimhan, T.N., 1985. Geometry imbedded Darcy's law and transient subsurface flow. Water Resour. Res., v. 21, no. 8, p. 1285–1292.

Narasimhan, T.N., 1988. Numerical simulation of richards equation: Current approaches and an alternate Perspective. *In* H.J. Morel-Seytoux (ed.), Unsaturated Flow in Hdyrologic Modeling. Proceedings of the NATO Advanced Research Institute on Unsaturated Flow in Hydrologic Modeling, Arles, France, June 12–17, 1988. Kluwer Academic Publishers, Dordrecht, Netherlands, in press (LBL-26897).

Path Integration and Minimum Work as a Basis for Solving Laplace's Equation

T.N. Narasimhan and J.S.Y. Wang

At the present time the finite-differences method (FDM) and the finite-element method (FEM) are widely used to solve Laplace's equation over heterogeneous domains with complex geometries. Both methods use fixed grids and approximate spatial derivatives of potential using trial functions chosen a priori to characterize spatial variations of potential. Using these derivatives in conjunction with the principle of mass conservation, these methods solve for the spatial distribution of fluid potentials at discrete locations within the flow domain.

In this article, we explore an alternate approach for solving Laplace's equation in which we seek to implement the principle of least action, rather than implementing mass conservation. In this approach one seeks to use resistances integrated over nonuniform flow paths in conjunction with potential drops over finite flow distances rather than computing spatial derivatives of potential. This approach emphasizes the point that in heterogeneous media the essence of solving Laplace's equation is to solve for both fluid potentials and flow geometry, leading to the suggestion that to solve the Laplace equation in a credible fashion over heterogeneous domains, one has to iterate between flow geometry and potentials to obtain an acceptable solution. This article is a summary of the basic concepts involved; a more-detailed account can be found in Wang and Narasimhan (1989).

APPROACH

Path integration, as conceived here, is the procedure by which one integrates resistances along a flow tube using available information on flow geometry and material heterogeneities and relates the integrated resistances to the steady flux through the flow tube. Although the concept is generally valid for three dimensions, for clarity we will restrict our discussions to two-dimensional systems.

Consider a flow region such as the one shown in Fig. 1, through which water is flowing under steady-state conditions due to spatial variations in the fluid potential. The *Maximum Principle* states that in steady-flow systems the maximum potential and the minimum potential will occur only on the boundary of the flow domain. Thus water enters the flow region across boundary segments with high fluid potentials and leaves the flow region across boundary segments with low fluid potentials. The mass of water that enters the flow domain at an appropriate time rate brings energy into the system, because

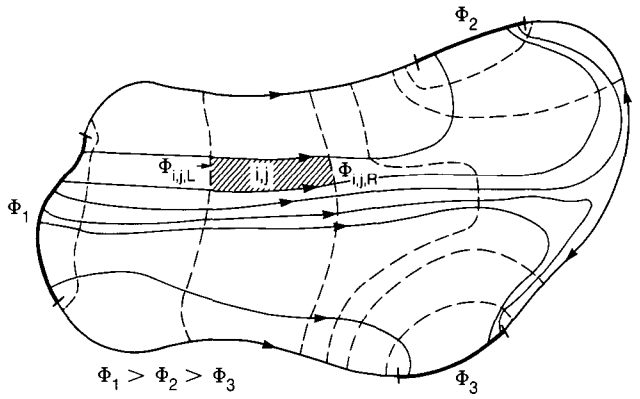

Figure 1. Schematic representation of flow pattern in a steady-state flow domain. Solid segments represent constant-potential boundaries. Lines with arrows are streamlines. Broken lines are isopotential lines. [XBL 881-10002]

fluid potential, by definition, is energy per unit mass. As water moves through the system, it progressively loses energy as it loses fluid potential in the direction of flow. The energy so lost is in part irretrievably expended as frictional heat and is in part expended in performing other work, such as keeping the pores open against external compressive forces.

To facilitate the movement of water within the system, the fluid potentials will have to distribute themselves suitably in space, dictated by maximum and minimum values on the boundary. If we restrict ourselves to macroscopic laminar flow in a domain occupied by isotropic materials, we are aware from empirical knowledge that the lines of flow *(flow lines)* will be perpendicular to surfaces of equal potential *(isopotential surfaces).*

Owing to the inherent tendency of a natural physical system to conform to certain well-established physical laws (e.g., law of least action), the steady-state flow system under consideration must adjust itself in some predictable manner to conditions existing on the boundary of the flow domain. As a consequence, the isopotential surfaces and the associated flow lines must form a unique pattern. The mathematical problem *of steady-state fluid flow, then, is to quantify how the fluid flow system will adjust itself to a unique spatial configuration (a) in response to boundary conditions and (b) in response to natural physical laws.*

We now attempt to formulate the appropriate physical-mathematical expressions on the basis of such physical postulates as minimum work and mass conservation.

Principle of Minimum Work

In Fig. 1, which depicts a system of flow lines and associated streamlines, the region identified by the indices i,j (denoting the jth segment of potential drop in the ith flow tube) is bounded by two isopotential surfaces $\Phi_{i,j,L}$ and $\Phi_{i,j,R}$ $(\Phi_{i,j,L} > \Phi_{i,j,R})$ and by two flow lines. According to the equation of motion,

$$Q_{i,j} = \frac{1}{R_{i,j}}(\Phi_{i,j,L} - \Phi_{i,j,R}), \tag{1}$$

where $Q_{i,j}$ is the steady flux within the tube and $R_{i,j}$ is the resistance offered to fluid flow by the shaded region. Within this region, the rate at which energy is lost by the water consequent to the drop in fluid potential is

$$\text{Energy lost} = \frac{(\Delta\Phi)_{ij}^2}{R_{ij}}, \tag{2}$$

where $(\Delta\Phi)_{i,j}$ is the drop in potential over the shaded region. We now introduce the following postulate regarding the expected tendency of response of the flow system.

Postulate: *In response to the boundary conditions, the flow system will adjust in such a way that the rate at which energy is dissipated over the entire flow domain as a consequence of the drop in potential of the moving mass of fluid will be a minimum.*

Thus the function Ω is a minimum, where

$$\Omega = \sum_i \sum_j \rho\, Q_{i,j}. \tag{3}$$

The physical meaning of the above postulate may be described as follows. Suppose we arbitrarily choose a set of isopotential surfaces distributed over the flow domain and construct flow lines perpendicular to these surfaces. Further suppose that we compute Ω for this arbitrarily chosen configuration of flow as prescribed in (3). Then the postulate asserts that Ω will be larger than that value of Ω which corresponds to the flow configuration that represents the true steady-state behavior of the system.

Comparison with the Variational Principle

It is of interest to compare this minimization postulate with the classical Variational Functional of the steady-state flow problem. The classical varia-

tional expression is sometimes known as Euler's equation. As shown by Narasimhan (1985), for a flow tube of nonuniform cross-sectional area such as the shaded area in Fig. 1, the fluid flux can be expressed by (see Fig. 2)

$$Q_{i,j} = \frac{(\Delta\Phi)_{i,j}}{\frac{\mu}{\rho}\int_{x_{i,j,L}}^{x_{i,j,R}} \frac{dy}{k(y)A(y)}}, \tag{4}$$

where, $x_{i,j,L}$ and $x_{i,j,R}$ are the coordinates of intersection of $\Phi_{i,j,L}$ and Φ_i,j,R, with an appropriately chosen curvilinear x axis such that

$$V_{i,j} = \int_{x_{i,j,L}}^{x_{i,j,R}} A(x)dx, \tag{5}$$

in which $V_{i,j}$ is the volume of the shaded region i,j. Furthermore, in (4), μ is the dynamic coefficient of viscosity of water, ρ is the density of the fluid, k is the absolute permeability, and $A(x)$ is the area of the isopotential surface that intersects the x axis at x. In general, (5) is valid for a flow tube with variable material properties. For the sake of simplicity, we ignore heterogeneities and consider a homogeneous flow domain. Therefore, in view of (4),

$$\Omega = \sum_i \sum_j \rho\frac{k\rho}{\mu}\frac{(\Delta\Phi)_{i,j}\ (\Delta\Phi)_{i,j}}{\int_{x_{i,j,L}}^{x_{i,j,R}} \frac{dx}{A(x)}}. \tag{6}$$

If we make the spatial discretization arbitrarily fine, then the Δ's and the integral in (6) can be dispensed with and we have

$$\Omega = \sum_i \int_{x_{i,j,L}}^{x_{i,j,R}} \rho\frac{k\rho}{\mu}\left(\frac{d\Phi}{dx}\right)^2. \tag{7}$$

But, noting that $A(x)\,dx = dV$, we get

$$\Omega = \sum_i \int_{V_i} \rho\frac{k\rho}{\mu}\left(\frac{d\Phi}{dx}\right)^2 dV. \tag{8}$$

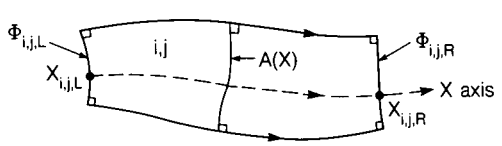

Figure 2. Schematic representation of a segment (i,j) of a flow tube. [XBL 881-10003]

Finally, since $\sum_i V_i = V$,

$$\Omega = \int_V \rho\frac{k\rho}{\mu}, \tag{9}$$

which indeed is Euler's equation representing the variational functional for the steady-state fluid flow problem.

The minimization postulate, in conjunction with Fig. 1, suggests an approach for solving the steady-state fluid-flow problem that is different from the conventional analytical or numerical approaches for solving Laplace's equation. The new approach consists of initially guessing a set of isopotential surfaces. This guessed configuration is then progressively refined through a systematic process of minimizing Ω until the correct configuration (solution) is obtained. At this juncture we do not address the issue as to whether this approach is computationally efficient or advantageous. We merely explore whether an alternate solution strategy is possible.

Two features of this strategy are of interest. First, the task of verifying a solution generated this way consists in asserting that the minimization process indeed yields a global minimum for Ω. Second, the accuracy of the solution depends on how accurately the resistances, $R_{i,j}$, can be evaluated with the available information on flow geometry and heterogeneity, using the integral,

$$\int \frac{dx}{k(x)A(x)}.$$

Note that the entire process of solution and verification is mathematically self-consistent and that the process exists independently of the notion of a partial differential equation.

Relation to Mass Conservation

Suppose the particular configuration of isopotential surfaces and flow lines chosen does not correspond to a minimum for Ω. Then it stands to reason that along a given flow tube i in Fig. 1, the fluxes will not be equal. That is, the $Q_{i,j}$'s will not be the same. This is because the flow geometry is incorrect and the resistances $R_{i,j}$, which depend on the flow geometry, will not assure the equality of fluxes along the flow tube.

Note that the observation that fluxes are variable along a flow tube is exactly equivalent to stating that mass of water is not conserved along the flow tube. Because we know from simple empirical considera-

tions that a steady-state fluid flow system cannot violate the principle of mass conservation, it follows that the flow configuration that corresponds to a global minimum for Ω must also assure mass conservation. In other words, the formulations of the problem of steady-state fluid flow using either the minimization principle or the conservation principle are exactly equivalent. Indeed another way to assert this equivalence is to recognize that by perturbing the variational functional (9) with reference to Φ and minimizing it, one can obtain Laplace's equation, which is merely an expression of mass conservation. This minimization logic is often used as a basis for deriving the finite-element equations.

REFERENCES

Narasimhan, T.N., 1985. Geometry imbedded Darcy's law and transient subsurface flow. Water Resour. Res., v. 21 no. 8, p. 1285–1292.

Wang, J.S.Y., and Narasimhan, T.N., 1989. Processes, mechanisms, parameters and modeling approaches for partially saturated flow in soil and rock media. Lawrence Berkeley Laboratory Report LBL-26224.

A Laboratory Investigation of Foam Flow in Sandstone at Elevated Pressure

P. Persoff, C.J. Radke, K. Pruess, S.M. Benson, and P.A. Witherspoon

Aqueous foam is a promising fluid for achieving mobility control in a variety of underground processes, including enhanced oil recovery by steam, CO_2, or enriched hydrocarbon flooding and aquifer storage of natural gas or air. In contrast to ordinary two-phase flow, in which both gas and liquid exist as continuous phases, the gas phase in foam exists mostly or entirely as bubbles separated by lamellae, and only the liquid phase is continuous. Because of this, foam exhibits low flow mobilities that may possibly overcome gravity override and viscous fingering through the permeable streaks always present in underground porous media. To obtain data on foam mobility and its variation with velocities of injected gas and liquid, we conducted foam-flow experiments with direct measurement of liquid saturation in situ, examining possible separate effects of gas and liquid flow rates and hysteresis on foam flow behavior. A full report of this work is available in Persoff et al. (1989).

EXPERIMENT

The experimental flow apparatus is shown in Fig. 1. A core of 1.3-darcy Boise sandstone, 5.1 cm in diameter and 60 cm long, was epoxy-mounted into a type 316 stainless steel annular cylinder. Pressure was measured using a single Paroscientific 43KT piezoelectric quartz-crystal pressure transducer and a Scanivalve 12L7 multiplexing valve set to visit

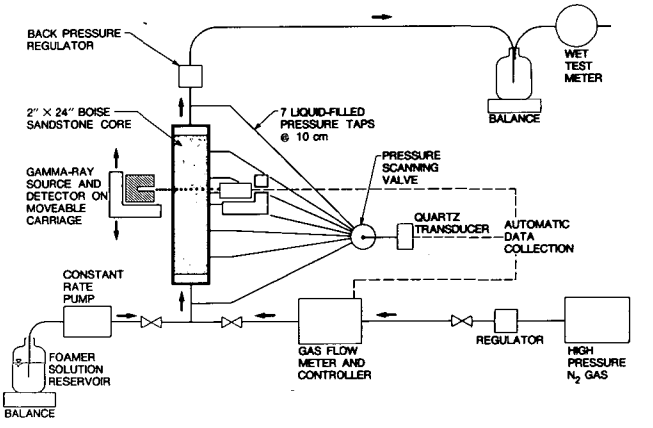

Figure 1. Apparatus for foam-flow experiments. [XBL 882-10046]

all the taps sequentially. Back pressure was maintained by a dome-loaded back-pressure regulator. Liquid saturation was measured by gamma-ray densitometry (Reda et al., 1981). The gamma-ray source and detector were mounted on a carriage that could be moved by a stepper motor for measuring saturation profiles in the core. The foamer solution was a brine with 1% by weight active alkylethoxysulfate surfactant. The viscosity was 1.2 mPa·s; in some runs, 0.2 wt% of long-chain alcohol was added, which increased the liquid viscosity to 1.7 mPa·s.

The core was initially vacuum-saturated with brine and displaced by at least 10 pore volumes (PV) of foamer solution. In all runs, liquid was injected at constant volumetric flow rate and gas was injected at constant mass flow rate. Pressure and liquid-saturation measurements were used to monitor the progress of gas and foam through the core. After foam had propagated through the length of the core and steady state was reached, the gas and liquid flow rates were varied independently to reach a series of steady states.

RESULTS

Figure 2 shows typical liquid-saturation and pressure profiles during displacement of liquid by foam. After the 65% liquid-saturation front passed, desaturation occurred progressively from the inlet end of the core to the outlet end, and gas breakthrough was observed near 1.0 PV. Sometime after 13 PV steady state was attained. The final liquid saturation in the core was about 30%, which is about 5 saturation units above connate saturation. Figure 2 shows that the transient pressure profiles exactly tracked the liquid-saturation history in that high pressure gradients (i.e., large foam-flow resistances) occurred where liquid saturations were lowest.

In all runs, transient foam displacement was characterized by a relatively rapid desaturation front at 65% liquid saturation, followed by a gradual displacement to about 35% commencing from the core inlet. During the transient displacement foam mobility was low where liquid saturation was low and high where liquid saturation was high. Finally, at steady state, the pressure gradient and liquid saturation were practically uniform along the core. The final low foam mobilities and low liquid saturations indicate clearly that the minimum critical velocity necessary to generate a fine-textured, strong foam (Ransohoff and Radke, 1988) was exceeded in all our experiments.

Figures 3 and 4 show the steady-state relationships between the pressure gradient and the gas and liquid flow rates, respectively. For a fixed liquid velocity, the pressure gradient was essentially independent of gas flow rate over a change of almost two orders of magnitude (Fig. 3), and, except at the lowest velocities, the pressure gradient increased almost linearly with increasing liquid velocity (Fig. 4). Note that in Fig. 4 the two data points for the

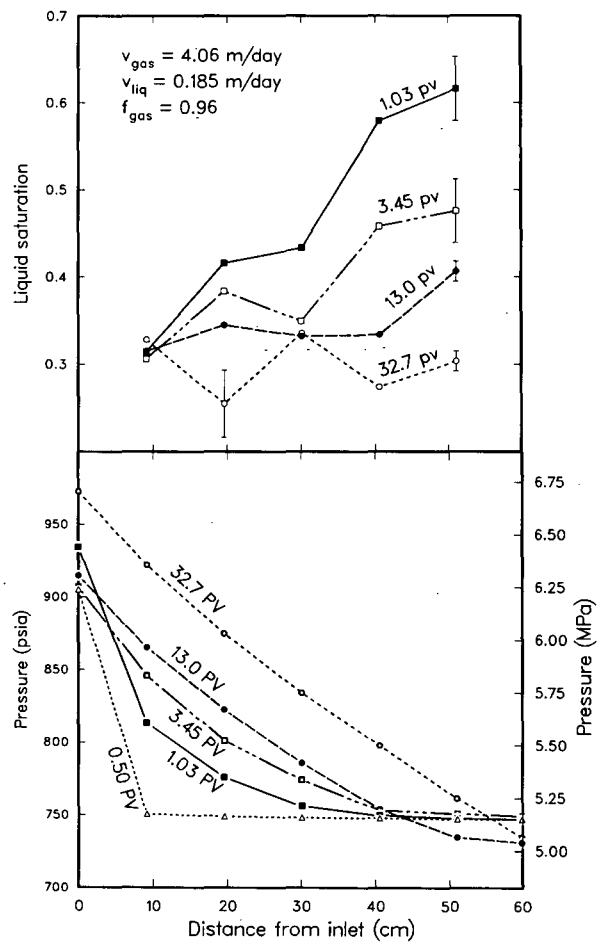

Figure 2. Liquid-saturation and pressure profiles measured during transient displacement of liquid by foam. Error bars shown at 51 cm for saturation measurements are typical. Liquid viscosity = 1.7 mPa·s. [XBL-891-337]

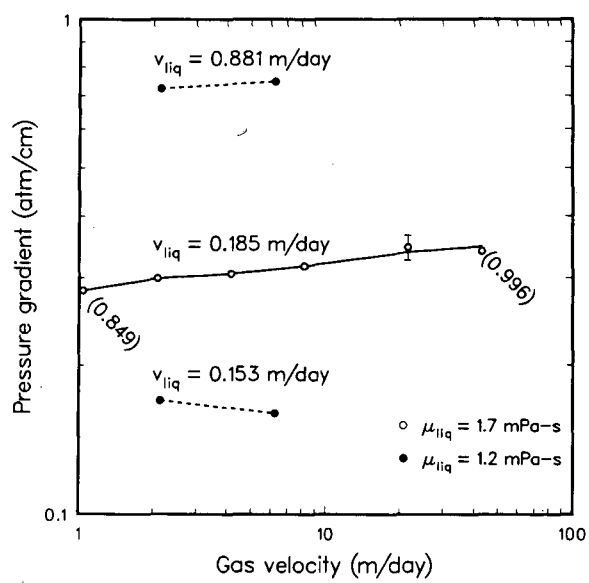

Figure 3. Steady-state pressure gradient versus gas velocity for three constant liquid velocities. Numbers in parentheses correspond to fractional gas flow. A typical error bar is shown. [XBL-891-181]

lower gas velocity fall on the same line as those for the higher gas velocity, confirming the result of Fig. 3.

The letters that label the points in Fig. 4 indicate, in alphabetical order, consecutive steady states. Either raising or lowering gas or liquid flow to the same final state produced identical flow behavior. We did not observe hysteresis in steady-state foam mobilities. Measurements of liquid saturation made in situ during these experiments showed that, for the range of steady-state conditions shown in Figs. 3 and 4, the liquid saturation in the core was uniform and constant at 30–35%.

DISCUSSION

To rationalize the transient displacement results of Fig. 2, we tentatively argue as follows. Initially, unfoamed gas fingers into the larger pore channels because of extremely adverse mobility contrast. Foam bubbles and lamellae are created by leave-behind and by snap-off. This rather coarse-textured, weak foam exhibits some increased flow resistance compared with the free gas (Ransohoff and Radke, 1988); accordingly, the local pressure gradients increase (for constant imposed flow rates) enough to overcome the entrance capillary pressure of nearby liquid-filled pores. More liquid is now displaced, allowing the gas to encounter additional germination and leave-behind sites. Bubble and lamellae density

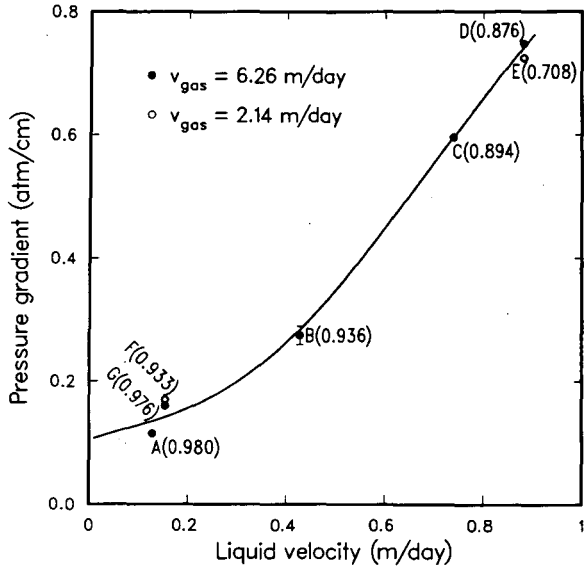

Figure 4. Steady-state pressure gradient versus liquid flow rate. Points labeled A through G represent consecutive steady states. Numbers in parentheses correspond to fractional gas flow. Liquid viscosity = 1.2 mPa·s. A typical error bar is shown. [XBL-891-183]

further increase, which again raises local pressure gradients, and so on in a cascading fashion. This explains why the high pressure gradients correspond directly to the low liquid saturations in Fig. 2. Finally, at steady state, a strong foam (Ransohoff and Radke, 1988) of constant and fine texture (i.e., high flow resistance) develops throughout the core, forcing the liquid saturation down to a low and uniform value and establishing a uniform pressure gradient (i.e., a linear pressure profile).

We interpret our steady-state results in terms of a nondimensional foam-flow resistance, FFR, defined by

$$\mathrm{FFR} \equiv \frac{k}{\mu_{liq} v_{gas}} \left(\frac{-dp_{gas}}{dx} \right), \qquad (1)$$

where k is the absolute permeability, p_{gas} is the gas pressure, v is the superficial velocity, x is the axial distance along the core, and μ_{liq} is the wetting-liquid viscosity. FFR may be considered either as a foam-flow resistance or as an inverse foam mobility, both made nondimensional by the absolute permeability and the liquid-phase viscosity. Because $-dp_{gas}/dx$ is essentially independent of v_{gas} and approximately proportional to v_{liq} (deviations are seen in the slight upward trend of Fig. 3 and at low velocities in Fig. 4), FFR is directly proportional to v_{liq} and inversely proportional to v_{gas}. Therefore, the quantity $\mathrm{FFR}(v_{gas}/v_{liq})$ is approximately constant, independent of fractional flow and total velocity. The data of Figs. 3 and 4 are replotted in Fig. 5, showing that, for all steady-state experimental conditions, the value of $\mathrm{FFR}(v_{gas}/v_{liq})$ is approximately 10^3. If proven general, the constancy of $\mathrm{FFR}(v_{gas}/v_{liq})$ should be extremely useful for practical estimates of foam flow behavior. With only one or two measurements of foam pressure drops and flow rates in a given porous medium and with a given surfactant system, the entire steady-state flow behavior of foam could be predicted. We caution that a wider range of foam qualities and different core permeabilities and surfactant types and concentrations must be studied before such a correlation can be demonstrated.

Finally, note that from the definition (Eq. 1), $\mathrm{FFR}(v_{gas}/v_{liq})$ is identical to the inverse relative permeability to the liquid phase. The observed value is very close to that measured independently in two-phase flow of continuous gas and surfactant-free brine at the wetting-liquid saturation of 30–35%. Hence increasing (or decreasing) liquid flow rates during steady flow of strong foam simply forces more (or less) liquid through the same liquid-filled

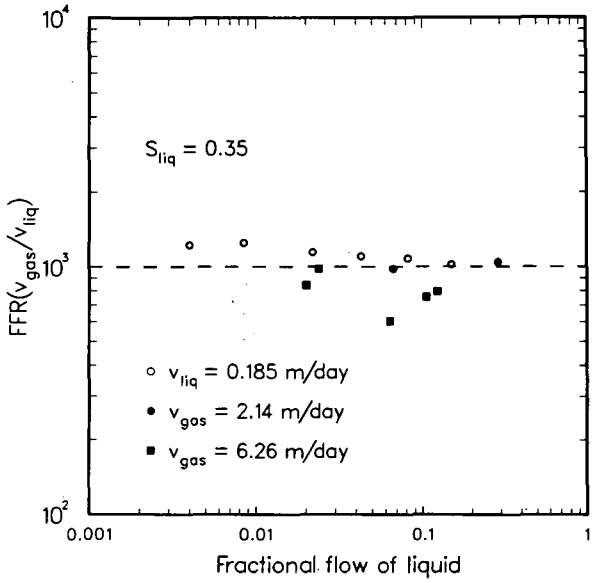

Figure 5. FFR(v_{gas}/v_{liq}) versus fractional flow of liquid. The broken line is eye fit. [XBL-891-186]

channels. The number of liquid flow paths is not materially changed.

In summary, foam flowing in porous media is a rheopectic fluid that at steady state is pseudoplastic with respect to gas flow and Newtonian with respect to liquid flow. Apparently, the foam texture adjusts to set a flow resistance that is compatible with a constant and low liquid saturation in the core.

CONCLUSIONS

We performed foam-flow experiments in a 1.3-darcy sandstone core at about 5 MPa (700 psia) back pressure. Measurements carried out for total superficial velocities between 1 and 45 m/d and foam qualities between 0.7 and 0.995 permit the following conclusions:

1. During transient foam flooding of a surfactant-solution-saturated core, the foam-flow resistance builds in time and continuously varies from that characteristic of free gas to that of a strong, fine-textured foam.
2. Steady-state foam-flow resistance increases with increasing liquid velocity but decreases with increasing gas velocity. No hysteresis is observed in the steady state.
3. Although foam-flow resistance varies with flow rate, liquid saturations at steady state do not. They are constant at 0.3 to 0.35 independent of flow rates and foam quality. Therefore, foam-flow resistance is not a unique function of liquid saturation.
4. Liquid-flow resistance during foam flow obeys Darcy's law and exhibits the standard relative permeability pertinent to the core liquid saturation, independent of liquid and gas flow rates.
5. A unique flow-resistance correlation is suggested that collapses all our data into a single value. This value is determined only by the nature of the porous medium and the stabilizing surfactant package and is independent of foam quality and total velocity.

REFERENCES

Persoff, P., Radke, C.J., Pruess, K., Benson, S.M., and Witherspoon, P.A., 1989. A laboratory investigation of foam flow in sandstone at elevated pressure. Paper SPE-18781 presented at the 1989 California Regional SPE Meeting, Bakersfield, California, April 5–7, 1989.

Ransohoff, T.C., and Radke, C.J., 1988. Mechanisms of foam generation in glass-bead packs. SPE Res. Eng., v. 3, no. 2, p. 573–585.

Reda, D.C., Hadley, G.R., and Turner, J.R., 1981. Application of the gamma-beam attenuation technique to the measurement of liquid saturation for two-phase flows in porous media. *In* Proceedings, 27th International Instrumentation Symposium, Indianapolis, Indiana, April 27–30, 1981. Instrument Society of America, Research Triangle Park, North Carolina, p. 553–568.

A New Semianalytical Method for Numerical Simulation of Fluid and Heat Flow in Fractured Reservoirs

K. Pruess and Y.S. Wu

Permeability and flow in many petroleum, gas, and geothermal reservoirs are dominated by fractures. Despite major advances in recent years, mathematical modeling of fluid and heat flow in fractured reservoirs remains a difficult problem. Porous-medium approximations have been shown to be inadequate for many flow processes in fractured systems.

We have developed a "multiple-interacting-continua" technique (MINC, Pruess and Narasimhan, 1985) that extends the classical double-porosity method by considering not just one but several interacting matrix continua (Fig. 1). The subgridding of matrix blocks as shown in Fig. 1 permits a fully transient description of interporosity flow between matrix blocks and fractures. This provides a great deal of flexibility for treating nonisothermal multiphase flows. A drawback of this method is that computational work is increased by typically a factor of 5 compared with single-porous-medium models.

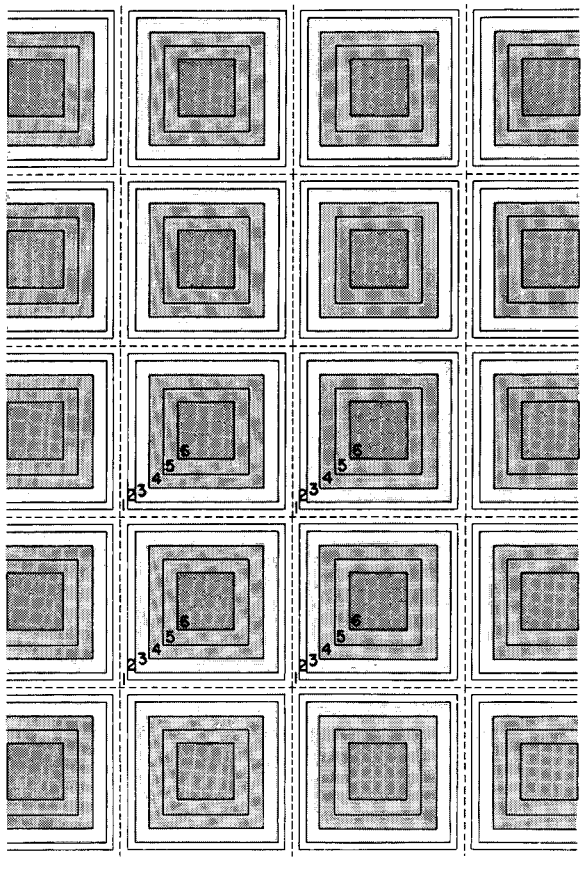

Figure 1. The concept of multiple interacting continua (MINC) for an idealized fracture system. [XBL 813-2753]

Our new semianalytical approach is conceptually similar to the MINC method, but it avoids subgridding of the matrix blocks (see Fig. 2). Therefore, the calculational effort in a fractured-porous flow problem is reduced to that of a single-porous-medium calculation.

The new method for modeling fluid and heat flow in fractured reservoirs is an extension of a technique developed by Vinsome and Westerveld (1980) for calculating heat exchange between permeable layers and impermeable semi-infinite confining beds during thermally enhanced oil recovery. Our method combines a finite-difference description of global flow in the fractures with an analytical representation of interporosity flow by means of trial functions for fluid pressures and temperatures in the matrix blocks (hence we term it "semi-analytical"). The trial functions contain adjustable parameters that are calculated for each time step in a fully coupled way based on matrix-block shapes and dimensions, utilizing simple principles of mass and energy conservation.

MATHEMATICAL APPROACH

The basic trial function for temperature in the matrix blocks is written as a function of distance x

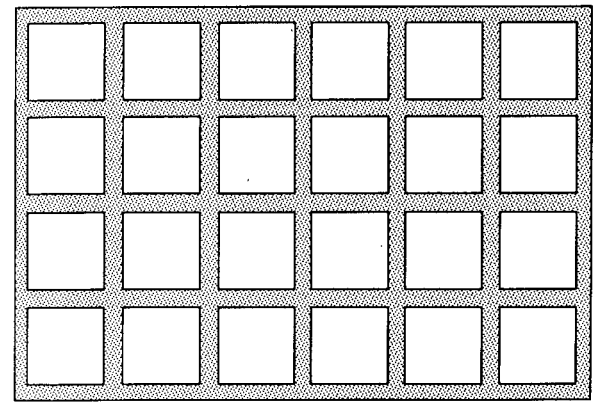

Figure 2. Conceptual diagram of a fractured medium, with blocks of low permeability embedded in a porous medium. [XBL 881-10006]

from the matrix block surface and time t as follows:

$$T(x,t) - T_i = (T_f - T_i + px + qx^2)e^{-x/d}. \quad (1)$$

Here x is the distance from the boundary, T_i is initial temperature in the matrix block (assumed uniform), T_f is the time-varying temperature at the matrix block surface, p and q are time-varying fit-parameters, and d is the penetration depth for heat conduction, defined by

$$d = \frac{\sqrt{\kappa t}}{2}, \quad (2)$$

where $\kappa = K/\rho c$ is the thermal diffusivity, K the thermal conductivity, ρ the density of the medium, and c the specific heat. In connection with a finite-difference simulation of nonisothermal flow, each grid block will have an associated temperature profile in the adjacent impermeable rock as given by Eq. (1). The coefficients p and q will be different for each grid block; they are determined concurrently with the flow simulation from simple physical principles, namely: (1) temperature at the conductive boundary obeys the heat conduction equation in the matrix blocks, and (2) the rate of change in total matrix-block heat content is equal to the heat flux at the boundary.

A formulation analogous to Eq. (1), with different fit parameters p', q', d', is adopted for pressures in the matrix blocks.

IMPLEMENTATION

We have incorporated the semianalytical technique into our general-purpose multiphase simulator MULKOM. The method was verified by comparison with exact analytical solutions for fluid and heat exchange with individual matrix blocks. Applications were made to geothermal well-test and production-injection problems with interporosity fluid and heat flow. The calculations show excellent agreement with numerical simulations using the method of "multiple interacting continua" (MINC), with no noticeable increase in computing work compared with porous-medium calculations.

As an example, Fig. 3 shows temperature profiles along a line connecting production and injection wells in a typical five-spot geothermal production/injection problem. Figure 4 shows simulated pressure buildups for nonisothermal injection into a fractured reservoir.

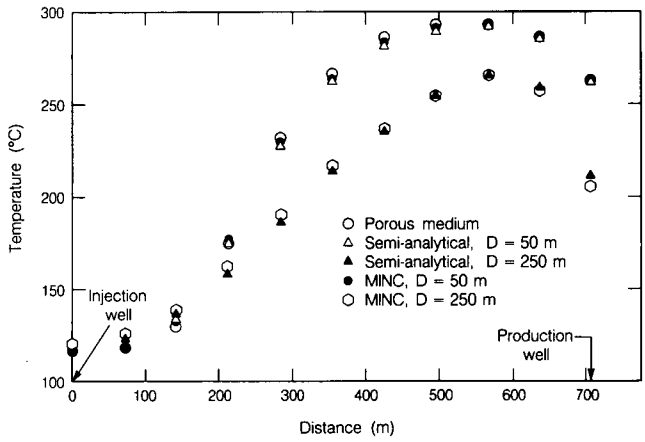

Figure 3. Temperature profiles in the fractures of a five-spot along a line connecting production and injection wells after 36.5 years of production and injection. [XBL 8712-8201]

CONCLUSIONS

Test calculations have shown the method of seminalytical interporosity flow to be capable of producing accurate results for fractured-porous flow problems, with no noticeable increase in computational work compared with single-porous-medium calculations.

The semianalytical treatment of interporosity flow as presented in Pruess and Wu (1989) is applicable to multiphase-fluid and heat-flow problems with impermeable matrix blocks (heat exchange

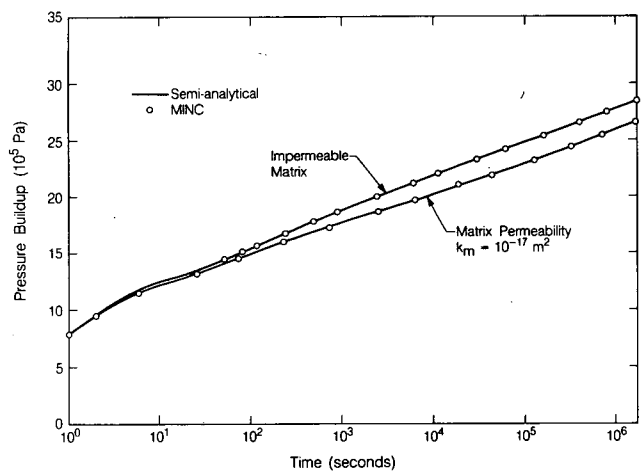

Figure 4. Simulated pressure buildups for nonisothermal injection into a fractured reservoir ($10 \times 10 \times 10$ m^3 matrix blocks). [XBL 888-10389]

only), and to single-phase-fluid and heat-flow problems with permeable matrix blocks (coupled fluid and heat exchange). The method can also be applied to problems of chemical transport in fractured media, because chemical transport in low-permeability blocks of rock can be described in analogy to heat conduction.

REFERENCES

Pruess, K., and Narasimhan, T.N, 1985. A practical method for modeling fluid and heat flow in fractured porous media. Soc. Pet. Eng. J., v. 25, no. 1, p. 14–26.

Pruess, K., and Wu, Y.S., 1989. A semi-analytical method for numerical simulation of fluid and heat flow in fractured reservoirs. Paper SPE-18426, presented at the Tenth Symposium on Reservoir Simulation, Houston, Texas, February 6–9, 1989.

Vinsome, P.K.W., and Westerveld, J., 1980. A simple method for predicting cap and base rock heat losses in thermal reservoir simulators. J. Can. Pet. Tech., p. 87–90.

Analysis of Internal Wellbore Flow

M. Ripperda and G.S. Bodvarsson

Internal wellbore flow occurs in many systems with multiple feedzones. In geothermal wells, relatively small pressure differences may cause substantial flows within a wellbore. Measurements of internal flow rates for wells in the Ngawha and Wairakei fields in New Zealand have ranged from several to 80 kg/s (Grant et al., 1983). This has significant effects on the interpretation of pressure-transient tests and wellbore pressure and temperature profiles. The characteristics of internal flow on static pressure and temperature surveys have been well documented by several authors, including Haukwa and O'Sullivan (1982) and Grant et al. (1983). Bixley and Grant (1981) discussed a method for calculating internal flow rates during injection tests and using the results to estimate pressures and productivities of the individual feedzones.

This article summarizes an alternative method for calculating internal flow rates between the feedzones, using shut-in pressure profiles (Ripperda and Bodvarsson, 1988). Under certain conditions, this method may also be used to calculate transmissivities.

CAUSES OF INTERNAL FLOW

A shut-in wellbore will obviously transmit fluids between feedzones that have different pressure potentials. However, internal wellbore flow often occurs even when the reservoir is initially in vertical pressure equilibrium. This happens after either drilling or production, when the density of the fluid in the wellbore does not match the reservoir fluid density at both feedzones. After drilling, the wellbore is filled with cold fluid, which has a much higher pressure gradient than the reservoir fluid. When circulation is stopped, the fluid level will fall so that pressures are in equilibrium at the pivot point (Fig. 1). If the pivot point is located somewhere between the two feedzones, then the reservoir pressure is higher than the wellbore pressure at the top feedzone and lower at the bottom feedzone. This causes the downflow, as shown in Fig. 1. If the fluids in the top

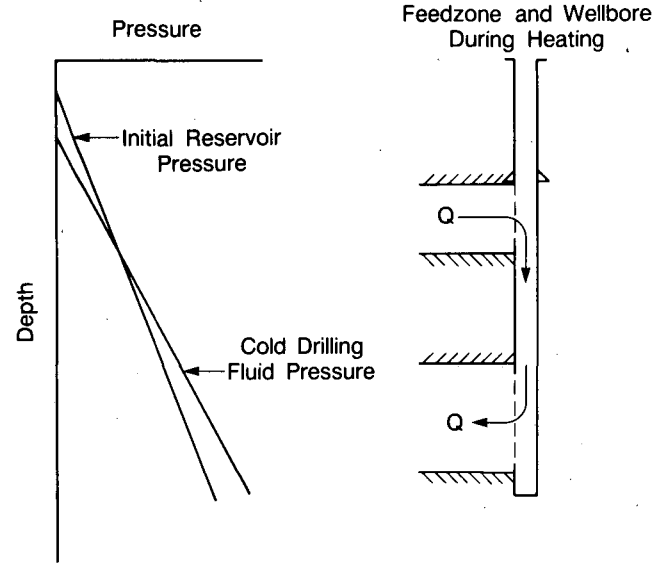

Figure 1. Wellbore pressure and flow conditions during the warmup period after drilling. [XBL 881-10023]

feedzone are cooler and denser than the fluids in the bottom feedzone, then these flow conditions may last for a long period of time.

Upflow will occur when the conditions are similar to those shown in Fig. 2. During production, the pressure in the wellbore is lower than the reservoir pressure at both feedzones. After the well is shut in, the pressure gradient in the wellbore will be smaller than the reservoir-pressure gradient if the fluids in the bottom layer are hotter and less dense than the fluids in the top layer. A continued influx of hotter fluids from the bottom feedzone causes large apparent pressure drawdowns. Thus the measured pressure conditions within the wellbore provide little or no information about in situ pressures when crossflow occurs. However, the rate of crossflow and the relative strengths of the two aquifers can be estimated from the wellbore-pressure measurements.

CALCULATION OF INTERNAL FLOW RATES

Figure 3 shows an idealized system with internal upflow. Because there is generally very little heat loss within the wellbore, the fluid entering the top feedzone has a temperature T_2. The rock and fluid properties are as shown. The radial transient pressure equations can be written for each layer as

$$\frac{\delta^2 P_i}{\delta r^i} + \frac{1}{r}\frac{\delta P_i}{\delta r} = \left(\frac{\phi_i \mu_i c_i}{k_i}\right)\frac{\delta P_i}{\delta t}. \qquad (1)$$

The initial conditions and outer boundary conditions for both layers are shown in Fig. 3.

The inner boundary conditions are slightly more complicated because the pressures will be changing with time. But we do know that flow out of one

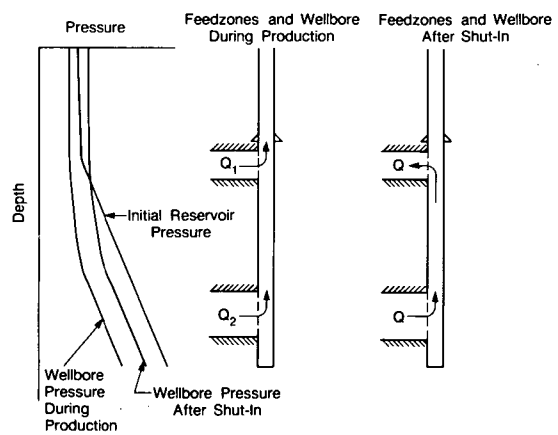

Figure 2. Wellbore pressure and flow conditions during and after production. [XBL 881-10024]

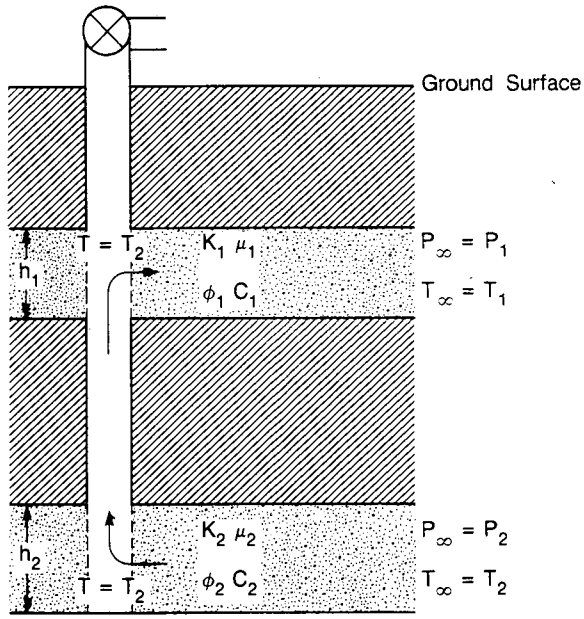

Figure 3. Idealized reservoir with two feedzones used in analytic model. [XBL 881-10025]

layer must equal flow into the second layer if wellbore storage is negligible. Thus

$$\frac{k_1 h_1}{\mu_1}\frac{\delta P_1(r_w,t)}{\delta r} = -\frac{k_2 h_2}{\mu_2}\frac{\delta P_2(r_w,t)}{\delta r}. \qquad (2)$$

Also, the relationship between wellbore pressures for layers one and two, $P_1(r_w)$ and $P_2(r_w)$, can be written as

$$P_2(r_w,t) - P_1(r_w,t) = P^*, \qquad (3)$$

where $P_2(r_w,t)$ and $P_1(r_w,t)$ are taken directly from the wellbore-pressure surveys. Although the wellbore pressures change with time, P^* is usually fairly constant.

The above set of equations may be solved in Laplace space and then numerically inverted to yield pressure distributions in the two layers and the internal flow rate. The result for the flow rate is

$$q = 2\pi\rho\frac{k_1 h_1}{\mu_1}(P_{1_i} - P_1(r_w))\, q_D, \qquad (4)$$

where q_D represents the numerical Laplace inversion.

RESULTS

The factors that strongly affect the internal flow rate are the transmissivities and storage properties of

the two zones. Increasing the transmissivity of both layers has a direct effect on the flow rate, as expected. When both layers have single-phase liquid, the initial flow rate ranges from approximately 10 to 200 kg/s for transmissivities ranging from 1 to 30 darcy-m (Fig. 4). After 3 years, the flow rates are still significant and vary between about 2 and 50 kg/s, respectively. The effects of changing the compressibility (phase composition) and transmissivity ratio of the two aquifers are shown in Figs. 5 and 6. For the results shown in these figures, the transmissivity of layer 1 was held constant at 1 darcy-m, and the transmissivity of layer 2 was varied. Both figures show that the internal flow rate is strongly controlled by the feedzone with the lowest transmissivity. In Fig. 5, for example, increasing the transmissivity of layer 2 by an order of magnitude (from $(kh)_1/(kh)_2 = 0.1$ to $(kh)_1/(kh)_2 = 0.01$) has almost no effect. However, when the transmissivity of layer 2 is less than that of layer 1, increasing its value from $(kh)_1/(kh)_2 = 100$ to $(kh)_1/(kh)_2 = 10$ increases the flow rate by a factor of 3. When both layers have high compressibility (two-phase fluids; see Fig. 6), the initial flow rate is increased by a factor of 3 compared with that for single-phase conditions (Fig. 5). But the decline is much steeper for the case with high compressibilities, and after 3 years the flow rates are almost equal to those of the case with single-phase fluid.

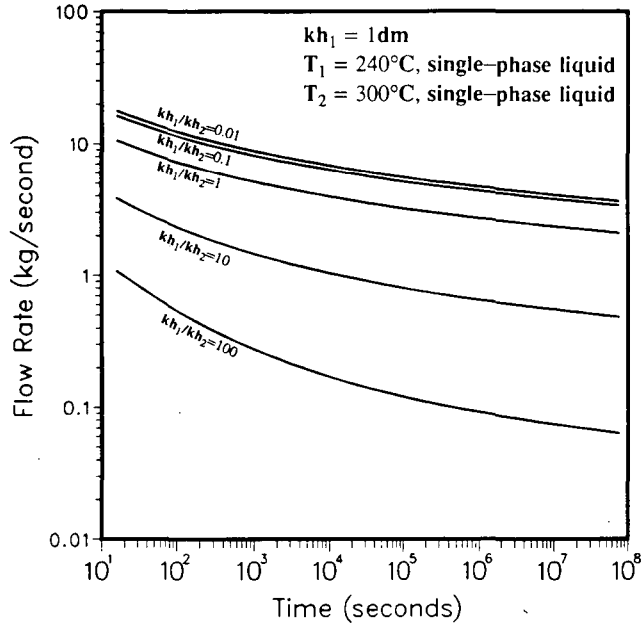

Figure 5. Flow rates versus time for various ratios of the transmissities between the two feedzones. The reservoir fluid is single phase liquid in both layers. [XBL 881-198]

CONCLUSIONS

An analytical model of internal flow between two feedzones has been developed. The equations can be used to calculate the pressure distributions in the two aquifers and the internal flow rates. The flow rates

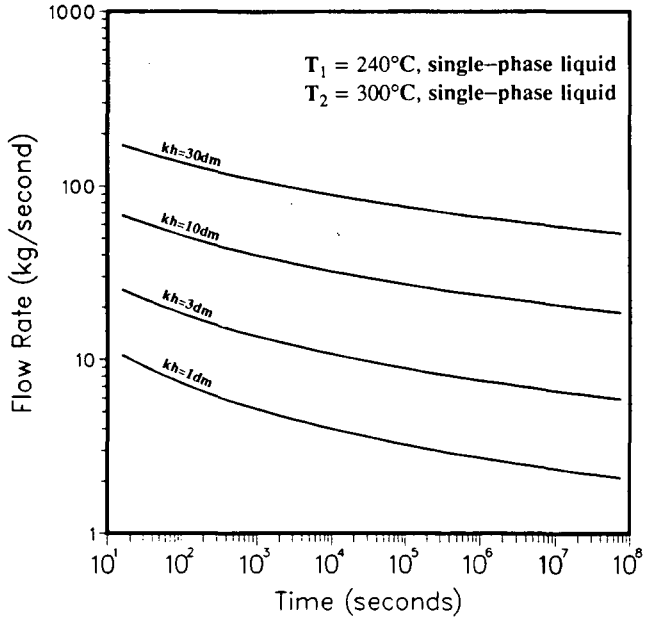

Figure 4. Flow rate versus time for various reservoir transmissivities. The transmissivity of the two feedzones are equal. [XBL 881-197]

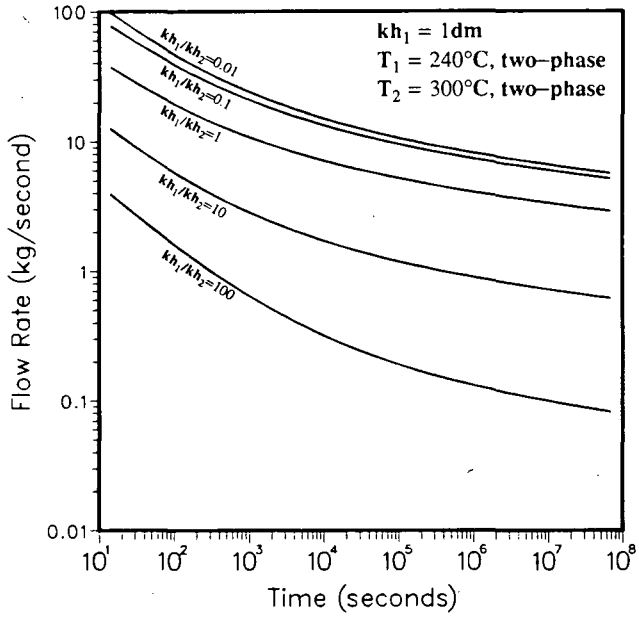

Figure 6. Flow rates versus time for various ratios of the transmissities between the two feedzones. The reservoir fluid is two phase in both layers. [XBL 881-199]

will be higher if the reservoir fluids have high compressibility (two-phase conditions). The properties of the aquifer with the lowest transmissivity control the internal flow rate. The predicted flow rates range from about 1 to over 100 kg/s for reasonable reservoir characteristics. This range is similar to flow rates measured in several geothermal fields in New Zealand. The flow rates are predicted to decline by a factor of between 2 and 10 after 3 years, depending primarily on the phase compositions.

REFERENCES

Bixley, P.F., and Grant, M.A., 1981. Evaluation of pressure-temperature profiles in wells with multiple feed points. *In* Proceedings, The New Zealand Geothermal Workshop, Auckland, p. 121–124.

Grant, M.A., Bixley, P.F., and Donaldson, I.G., 1983. Internal flows in geothermal wells: Their identification and effect on the wellbore temperature and pressure profiles. Soc. Pet. Eng. J., v. 23, no. 1, p. 168–176.

Haukwa, C.B., and O'Sullivan, M.J., 1982. A study of cycling in geothermal wells. *In* Proceedings, The New Zealand Geothermal Workshop, Auckland, p. 425–431.

Ripperda, M.A., and Bodvarsson, G.S., 1988. Analysis of internal wellbore flow. *In* Proceedings, Thirteenth Workshop on Geothermal Reservoir Engineering, Stanford, California. Report SGP-TR-113, p. 269–272.

A Direct Integral Method for the Analysis of Borehole-Fluid-Conductivity Logs to Determine Fracture Inflow Parameters

C.F. Tsang and F.V. Hale

A new approach for obtaining inflow parameters from fractures intercepted by a wellbore (flow rate and salinity of fracture fluid) was proposed by Tsang (1987) and Tsang and Hufschmied (1988). The approach involves flushing the wellbore with deionized water and producing at a low wellhead flow rate while logging the values of fluid electric conductivity within the borehole as a function of depth for a series of time values. The temporal changes of fluid conductivity logs can be used to obtain fracture inflow parameters. A code called BORE has been used to compute borehole-fluid-conductivity profiles given these parameters (Hale and Tsang, 1988). This report describes a new direct-integral method for analyzing a short time series of electric-conductivity logs. This method gives results that are not sensitive to wellbore-radius variations and wellbore-solute dispersion effects. This method was successfully applied to a set of synthetic log data, and then to field data obtained in 1987 in a 1700-m borehole in northern Switzerland.

The combination of the direct solution, implemented in a new code (PRE), along with the numerical modeling code BORE, forms a more-complete system for estimating fracture-inflow parameters based on conductivity logs than was presented in previous work. The steps of the analysis process include correcting the conductivity log's temperature variations, applying PRE to the logs to produce a first guess of the fracture-inflow parameters, applying BORE to the results from PRE to produce conductivity logs from the parameters, and comparing the modeling results of BORE with the temperature-corrected conductivity logs to provide an immediate indication of the suitability of the parameter estimation by PRE. In general, this will not be an ideal estimate, and minor modification of the parameters will be needed.

ANALYSIS METHOD

The parameters to be determined for each inflow are the flow rate, q_i, the concentration, C_i, and the time, t_{0i}, at which the fracture begins to flow. Figure 1 shows a schematic diagram of a wellbore with several inflow points, each with a flow rate q_i, concentration C_i, and position x_i. The total flow rate out of the well is Q, the initial salinity in the well is C_0, and the inflow at the bottom of the well is w. Positions indicated in the figure are depths below the surface.

Let L_0 be a reference point near the bottom of the well, upstream (down the borehole) from the first fracture-inflow point, and let L be a point up the

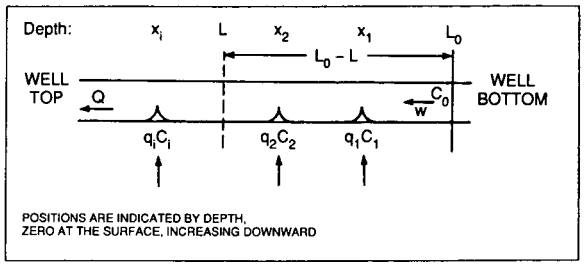

Figure 1. Schematic diagram of wellbore. [XBL 895-1680]

well from L_0. At L_0, the conductivity is assumed constant and equal to the initial conductivity k_0. The problem then is to obtain the flow rate, Q_L, at the point L in the wellbore in terms of the electric conductivity log at different times; Q_L is the sum of all of the q_i's between L_0 and L, plus the inflow, w, from the bottom of the well at L_0. In the analysis that follows, w is assumed to be zero. Note that taking the difference of two values of Q_L, one below an inflow point and one above will yield a value for q_i at that point.

If we assume that all inflows initiate at the same time ($t = 0$), then the mean concentration, $\bar{C}_L$, in the wellbore over the section between L_0 and L is given by the incoming salinity from the inflow points minus the salinity that leaves the section at L with flow rate Q_L:

$$((L_0 - L)\pi r^2)\bar{C}_L(t) = ((L_0 - L)\pi r^2)C_0 + t \sum_{L<x_i<L_0} q_i C_i - Q_L \int_0^t C(L,t)\, dt, \quad (1)$$

where $(L_0 - L)\pi r^2$ is the wellbore volume in the section between L_0 and L, and $C(L,t)$ is the time-varying salinity at the location L. The first term on the right-hand side represents the background mean salinity in the wellbore.

If the electric conductivity k is linearly related to salinity, $k = \alpha C$, we can arrive at the following result by simple algebraic manipulations:

$$Q_L = \frac{\alpha t \sum_{L<x_i<L_0} q_i C_i - [(L_0 - L)\pi r^2][\bar{k}_L(t) - k_0]}{\int_0^t (k(L,t) - k_0)\, dt}, \quad (2)$$

where $\bar{k}_L(t) = \alpha\bar{C}_L(t)$ and $k(L,t) = \alpha C(L,t)$. This equation gives the value of Q_L at any location L in the borehole directly without trial-and-error procedure and is valid for any time t.

The first term in the numerator of Eq. (2) is determined as follows. At time $t = 0$, the well is flushed with water at constant salinity with electric conductivity k_0. Then the well is pumped at a constant small flow rate at the wellhead. An electric conductivity profile will develop at each inflow point. By integrating the areas of the profile at two successive times near each of these inflow points we can obtain

$$\alpha q_i C_i = \frac{\int_{x_i-\delta_1}^{x_i+\delta_2} \pi r^2 (k(x,t_2) - k(x,t_1))\, dx}{t_2 - t_1}, \quad (3)$$

where x_i is the inflow point location and δ_1 and δ_2 are appropriate distances to bracket the local inflow profile. All of the other quantities in the right-hand side of Eq. (2) can be obtained from the measured electric conductivity profile.

Note that $(L_0 - L)\pi r^2$ is an integral quantity representing the total borehole volume over the section L. Thus Eq. (2) is not sensitive to local borehole radius variation, a major advantage over the spinner method of measuring flow rates. Because of the integral forms of the terms in Eqs. (2) and (3), the effects of solute dispersion around the peaks within the interval L_0 to L do not affect the results. However, dispersion effects at or near L introduce an error in the value of $C(L,t)$ or $k(L,t)$. This, we believe, is a source of uncertainty in our parameter estimation. Examining the values of Q_L determined from Eq. (2) at a series of locations between two successive peaks illustrates this uncertainty. At these locations, we know that Q_L should be constant. The variation in Q_L is a measure of solute dispersion in the borehole and can probably be studied to cancel its effect and obtain the proper values of the flow rate.

Equation (2) assumes that all solute flux is up the wellbore and thus does not apply to locations in the wellbore where the solute flux is mainly down the borehole by diffusion. This is not a major restriction because avoiding these locations does not prevent us from obtaining the flow profile in the wellbore. In principle, all we need is to apply the equation to one point at the downstream side (up the borehole) of each inflow point.

VERIFICATION

A synthetic data set composed of a time-series of conductivity logs with times ranging from 0.5 to 600

hours was generated by the code BORE. Four inflow points were used. The data set is designed so that it is similar to the real field data obtained from the Leuggern hole in Switzerland.

PRE was used to estimate the inflow parameters from various subsets of the time-series of logs, with successively larger final times (i.e., using the first five logs, the first eight, the first ten, etc.). The resulting estimates of the parameters indicate that the values stabilize at relatively short times (less than 100 hours) and that the use of additional logs provides little additional information. This may mean that the test need only be carried out for 100 hours, the reason being that the values of $q_i C_i$ are based on early times, so that the data at later times enter into the integral only in the denominator of the equation for Q_L.

The predicted profile of conductivity logs based on parameters obtained by applying PRE to the 96-hour data is shown in Fig. 2. The agreement with the synthetic data is already very good, with the exception of the inflow at 915 m. Minor adjustments result in a good fit to the synthetic data, as shown in Fig. 3.

SUMMARY AND CONCLUSIONS

A direct method has been developed to analyze borehole-electric-conductivity profiles in order to obtain fracture-inflow parameters. Without any trial-and-error matching procedure, the method yields a good set of parameters simply and directly. In general, this set of parameters should be further adjusted (refined), using the BORE code to arrive at a close match between calculations and field data.

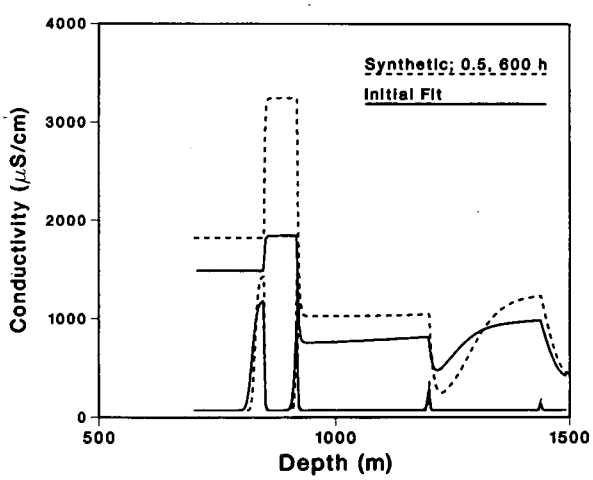

Figure 2. Initial estimate of inflow parameters for synthetic data. [XBL 895-1681]

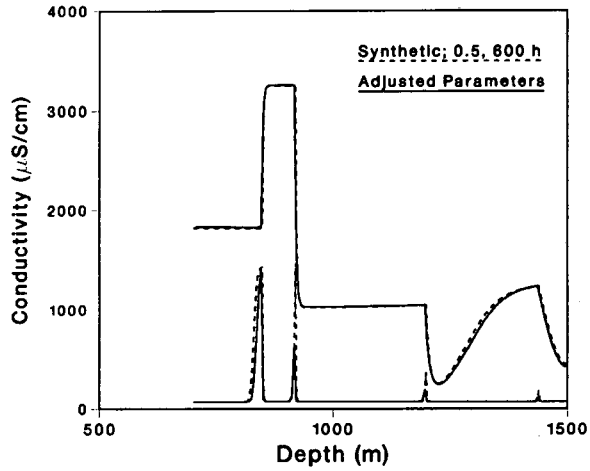

Figure 3. Fit to synthetic data after adjusting inflow parameters. [XBL 895-1682]

The direct-integral method can be used to analyze the fluid-conductivity logs to obtain fracture-inflow parameters. The method gives results that are not very sensitive to wellbore-radius variations and solute-dispersion effects. This method was first applied to a set of synthetic log data and was shown to be rather successful for obtaining a good set of parameters simply and directly.

ACKNOWLEDGMENTS

Discussions and cooperation with NAGRA personnel (Nationale Genossenschaft für die Lagerung radioactiver Abfälle, Switzerland), especially Peter Hufschmied, Marc Thury, Piet Zuidema, and Stratis Vomvoris are much appreciated. We also wish to thank S. Löw of Motor Columbus, Switzerland, and Chris Doughty and Pascal Bidaux of LBL for their comments.

REFERENCES

Hale, F.V., and Tsang, C.F., 1988. A code to compute borehole fluid conductivity profiles with multiple feed points. Lawrence Berkeley Laboratory Report LBL-24928.

Tsang, C.F., 1987. A borehole fluid conductivity logging method for the determination of fracture inflow parameters. Lawrence Berkeley Laboratory Report LBL-23096.

Tsang, C.F., and Hufschmied, P., 1988. A borehole fluid conductivity logging method for the determination of fracture inflow parameters. Lawrence Berkeley Laboratory Report LBL-24752.

Fluid-Flow Parameters in a Single Fracture from Mercury Porosimetry

Y.W. Tsang and F.V. Hale

Mercury porosimetry, the measurement of capillary pressure as a function of the volume of intruded mercury, has long been used to characterize the void spaces of porous materials (e.g., Purcell, 1949; Wardlaw and Taylor, 1976). We have applied this concept to a rock fracture by simulation of mercury intrusion and withdrawal in a single fracture with variable apertures. Increasing experimental evidence of flow channeling in fractures justifies the representation of a single fracture as a two-dimensional heterogeneous medium, characterized mathematically by an aperture-density distribution and a spatial correlation length (Moreno et al., 1988). Our theoretical studies of mercury porosimetry in a single fracture show that capillary-pressure measurements yield relevant information on the parameters that control fluid flow and tracer transport (Tsang and Hale, 1988).

RATE-CONTROLLED VERSUS PRESSURE-CONTROLLED MERCURY POROSIMETRY

For a fracture with spatially varying aperture, the local capillary pressure is given by

$$P_c \approx \frac{-2\sigma \cos\theta}{b}, \qquad (1)$$

where σ is the interfacial tension, θ is the contact angle, and b is the local aperture. Because mercury is a nonwetting fluid, an applied pressure is needed to overcome the capillary pressure, P_c. As P_c is inversely proportional to the local aperture, it is clear that the large apertures will be filled first, with progressively smaller apertures being filled as the injection pressure is increased. Mercury-porosimetry experiments are usually carried out by increasing the injection pressure in small increments and monitoring the volume of intruded mercury as the system is allowed to come into equilibrium. A typical plot from this kind of pressure-controlled measurement is shown schematically in Fig. 1a.

Yuan and Swanson (1986) proposed an experimental technique in which the volumetric rate of mercury injection is kept constant and the mercury pressure is monitored. This kind of rate-controlled experiment is illustrated schematically in Fig. 1b. From a to b, the pressure increases, indicating that

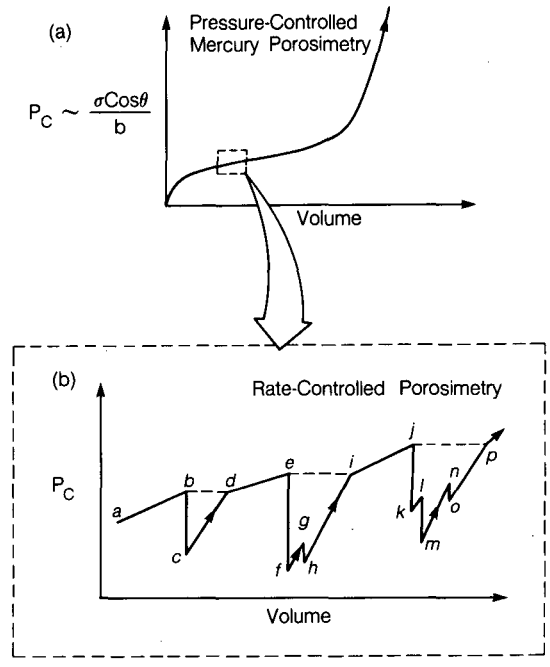

Figure 1. Schematic diagrams of capillary pressure curves from mercury-porosimetry measurements. [XBL 886-10267]

progressively smaller apertures are being filled. The capillary pressure at b corresponds to an aperture constriction that has just been filled and which acts as a barrier in the intrusion experiment. Unfilled fracture apertures that are connected to and larger than the just-filled aperture become accessible as the constriction is being intruded. The rate of mercury injection is kept constant, and mercury moves out of the filled smaller apertures into the unfilled larger apertures; hence the pressure drops rapidly from b to c with negligible change in intruded mercury volume. Pressure climbs again from c as mercury intrudes progressively smaller apertures until at d the pressure reaches the value attained at b before the sharp decrease. The pressure rises again at d, since all apertures contiguous to the filled ones now have smaller apertures. The portion bcd of the curve will not be seen in the pressure-controlled experiment shown in Fig. 1a; instead, the pressure curve will go from b to d horizontally, as indicated by the broken line in Fig. 1b. Hence the total capil-

lary curve obtained from the conventional pressure-controlled mercury porosimetry will follow *abdeijp* in Fig. 1b, whereas the rate-controlled mercury porosimetry curve will give the additional information on the larger apertures behind small aperture constrictions as contained in portions *bcd*, *efghi*, and *jklmnop* of the curve.

Yuan and Swanson (1986) defined those portions of the curve that give new information about the large pore systems behind pore throats (terminology specific to porous rocks) as the subison pore systems. The part of the curve with the subison volumes removed is defined as the rison curve. The rison curve therefore is a composite of the segments *ab*, *de*, *ij*, and so on, with the segment *de* translated in the x direction until d coincides with b and with the segment *ij* translated until i coincides with e. The rison curve is distinct from the total-capillary curve shown in Fig. 1a in that the asymptotic mercury volume reached here is only a fraction of that in the total-capillary curve. This is because the rison curve encompasses only a subset of apertures within the two-dimensional fracture; this subset includes all the aperture constrictions and excludes the larger apertures behind the small-aperture barriers.

SIMULATION OF MERCURY INTRUSION AND WITHDRAWAL EXPERIMENTS

Both the pressure-controlled and the rate-controlled mercury porosimetry may be simulated for a rock fracture with spatially varying apertures. We first generate variable apertures in a single fracture using geostatistical methods. The fracture is characterized by an aperture-density distribution and a spatial correlation length. Mercury intrudes from the fracture edge, and at each pressure P_c we calculate the volume of mercury needed to fill those apertures contacting the mercury and larger than the aperture associated with the prevailing capillary pressure according to Eq. (1). A constant contact angle of $\theta = 180°$ is assumed. We can identify (1) those small-aperture constrictions that define the entry pressure to a subison system of larger apertures (i.e., the pressures b, e, j in Fig. 1b), and (2) the volume of the subison system of large apertures behind each aperture barrier. The above information allows us to simulate both the total-capillary and the rison curves. Figure 2 shows simulated curves for a particular realization of a fracture with lognormally distributed aperture values and a spatial correlation length of one-tenth of the fracture dimension. The x axis is the filled volume of mercury, V_f, normalized to the total available volume of apertures in the fracture, V_t. The y axis is the pressure expressed in

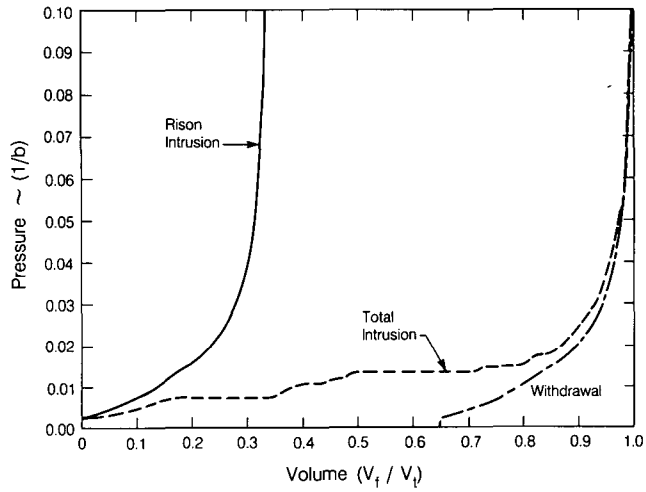

Figure 2. Simulated capillary-pressure curves for pressure-controlled and rate-controlled porosimetry measurements. [XBL 886-10265]

units of $1/b$ (μ^{-1}) on the implicit assumption that the interfacial tension σ and the contact angle θ remain constant throughout the experiment.

The asymptotic volume reached in the rison curve is only a fraction of that reached in the total-capillary curve. The volume is directly proportional to the fracture aperture b, and the limiting volumes reached in the capillary curves are essentially measures of some mean aperture. For the rison curve, this is a mean aperture of the subset of constrictive apertures that form the connected backbone of continuous flow paths in the fracture. This subset of apertures would play the dominant role in flow-permeability measurements. On the other hand, the limiting volume reached in the total-capillary curve corresponds to the arithmetic mean of all the apertures in the fracture, which is used to determine the mean tracer residence time. Then the limiting volumes in mercury porosimetry measurements can give information on the parameters that control fluid flow and tracer transport as follows:

$$\frac{(V_f / V_t)_{rison}}{(V_f / V_t)_{total}} \approx \frac{(\bar{b})_{permeability}}{(\bar{b})_{tracer}}. \qquad (2)$$

In our simulated example, the ratio is approximately one-third. That the equivalent aperture derived from a permeability test is smaller than that derived from data on tracer residence time has been observed in the field for granitic single fractures of 5 to 10 m in extent (Abelin et al., 1985). On the laboratory scale, Gale (1987) has found that the mean fracture aperture derived from flow-

permeability tests is a factor of 3 to 10 times smaller than the arithmetic mean of all the apertures in the fracture derived from the resin-impregnation technique.

In Fig. 2 we also include a curve for the simulated withdrawal of mercury from the fracture. As the mercury-injection pressure is reduced, the nonwetting mercury in apertures that are smaller than $|-2\sigma\cos\theta/P_c|$ will spontaneously flow out of the fracture if there exists a continuous path of mercury to the edge. Since the mercury would stay in place where the apertures are larger than $|-2\sigma\cos\theta/P_c|$, breakage of the continuous mercury phase may occur during mercury withdrawal, and mercury in large apertures may become isolated and trapped. For the example shown in Fig. 2, about 65% of the total volume of mercury is trapped in the fracture when the external pressure is reduced to zero. Since it is the mercury in the small apertures that will be expelled in the withdrawal experiment (i.e., the mercury that formed a continuous path), one may expect the withdrawal curve to have a shape very similar to that of the rison curve for the rate-controlled test. This is indeed the case. If the withdrawal curve is translated to the origin, it may also be labeled the second-intrusion curve, since a simulated second-intrusion curve will be identical to the translated withdrawal curve (on the assumption that the hysteresis due to the difference in contact angles during intrusion and withdrawal is negligible). Therefore, the second-intrusion curve in a pressure-controlled experiment may be a good approximation of the rison part of the intrusion curve in a rate-controlled experiment.

Since the residual trapped mercury is in the large apertures that are isolated by the continuous backbone of small apertures, one may expect that a smaller spatial correlation length of the variable apertures will increase the occurrence of these isolated patches of larger apertures. Results of a systematic study confirm this, as shown in Fig. 3, where residual mercury is plotted against correlation length λ expressed in terms of the linear dimension of the fracture L. Each data point corresponds to a simulated result from a different statistical realization of the same fracture aperture distribution. It is apparent from the figure that the amount of trapped mercury decreases as the spatial correlation length increases. Figure 3 demonstrates that measurements of residual mercury volume in a mercury-withdrawal experiment may give useful information on the spatial correlation length of the aperture variation, and hence on the flow-channeling pattern (Moreno et al., 1988).

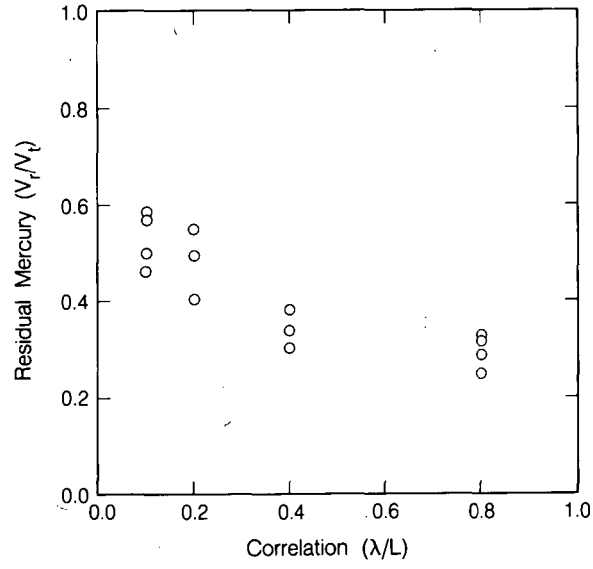

Figure 3. Fraction of trapped residual mercury as a function of spatial correlation length of the aperture spatial variation. [XBL 886-10266]

SUMMARY

Simulations of mercury intrusion and withdrawal in a single fracture with variable apertures show that the first-intrusion curve in a pressure-controlled test gives information on the apertures that control the tracer transport times through the fracture. The second-intrusion curve in a pressure-controlled experiment resembles the rison part of a rate-controlled experiment and gives information on the small apertures that control the flow permeability of the fracture. The ratio of the limiting mercury volumes of the second- and first-intrusion curves can provide estimates of equivalent mean apertures derived from permeability and tracer-transport measurements. Lastly, the fraction of trapped mercury may be related to the spatial correlation of the aperture variation, being larger for fractures with smaller spatial correlation length.

REFERENCES

Abelin, H., Neretnieks, I., Tunbrant, S., Moreno, L., 1985. Final report of the migration in a single fracture, experimental results and evaluations. Stripa Project, Sven Kärbränslefösorjning Tech. Rep. 85–03, Nucl. Fuel Safety Proj., Stockholm, Sweden.

Gale, J.E., 1987. Comparison of coupled fracture deformation and fluid flow models with direct measurements of fracture pore structure and stress-flow properties. *In* Proceedings, 28th U.S.

Symp. on Rock Mechanics, Tucson, Arizona, June 29–July 1, p. 1213–1222.

Moreno, L., Tsang, Y.W., Tsang, C.F., Hale, F.V., and Neretnieks, I., 1988. Flow and tracer transport in a single fracture—A stochastic model and its relation to some field observations. Water Resour. Res., v. 24, no. 12, p. 2033–2048.

Purcell, W.R., 1949. Capillary pressures—Their measurement using mercury and the calculation of permeability therefrom. Trans. AIME, v. 186, p. 39–48.

Tsang, Y.W., and Hale, F.V., 1988. A study of the application of mercury porosimetry method to a single fracture. Presented at the International Conference on Fluid Flow in Fractured Rocks, Atlanta, Georgia, May 15–17, 1988 (LBL-25489).

Wardlaw, N.C., and Taylor, R.P., 1976. Mercury capillary pressure curves and the interpretation of pore structure and capillary behavior in reservoir rocks. Bull. Can. Pet. Geol., v. 24, no. 2, p. 225–262.

Yuan, H.H., and Swanson, B.F., 1986. Resolving pore space characteristics by rate-controlled porosimetry. Paper 14892 presented at the SPE/DOE Fifth Symposium on Enhanced Oil Recovery, Tulsa, Oklahoma, April 20–23.

Gas-Phase Flow Effects on Moisture Migration in the Unsaturated Zone at Yucca Mountain

Y.W. Tsang, K. Pruess, and F.V. Hale

The U.S. Department of Energy is carrying out investigations at the Yucca Mountain site to evaluate its suitability as host to a geological repository for high-level nuclear wastes. Interest in the gas-phase flow in the unsaturated formation arises from concern that radionuclides may be released to the accessible environment. Certain radionuclides such as C^{14} may travel directly by the gaseous pathway; and through vaporization and condensation processes coupled with vapor transport, gas-phase flow effects may also indirectly influence the distribution of moisture and liquid-phase flow.

Of importance for an analysis of these coupled gas- and liquid-flow effects are the boundary conditions at the land surface. The effects of topography and seasonal temperature variation on gas flow have been studied by Weeks (1987) and Kipp (1987). We focus here on two other factors: (1) a condition of lowered relative humidity at the land surface, where soil gas contacts atmospheric air, and (2) atmospheric pressure variations with time, which we denote by "barometric pumping." Both boundary conditions induce a net upward movement of moisture, predominantly as gas-phase vapor fluxes. The study of the factors that affect the fluid movements, and the relative importance of various competing processes, is an essential prerequisite for constructing a credible model in subsequent full-scale simulations of Yucca Mountain for repository-performance assessment.

EFFECTS OF A RELATIVE-HUMIDITY BOUNDARY CONDITION

At the land surface humid formation gas contacts much drier atmospheric air. Near this contact the humidity of the soil gas may be considerably lower than at greater depth, where we expect equilibrium with the liquid phase and a humidity close to 100%. If capillary effects provide for the presence of soil moisture all the way up to the ground surface, a reduced humidity level can come about because of vapor-pressure lowering. In the presence of capillary suction vapor pressure is reduced from its saturated value according to Kelvin's equation (Edlefsen and Anderson, 1943):

$$P_v(T,S_l) = P_{sat}(T)\exp\left[\frac{P_{cap}(S_l)}{\rho_l R T}\right], \qquad (1)$$

where ρ_l is the molar density of the water and R is the universal gas constant, 8.314 J/mol-K. The relative humidity is defined as $h = P_v/P_{sat}$, so that

$$h = \frac{P_v}{P_{sat}(T)} = \exp\left[\frac{P_{cap}(S_l)}{\rho_l R T}\right]. \qquad (2)$$

The lowered-humidity boundary condition implies a composition gradient in the gas phase, giving rise to a downward flux of air and an equal

upward flux of vapor by means of binary diffusion. If one assumes that the reduced vapor pressure is caused by vapor-pressure lowering due to capillary suction, then the equivalent capillary suction, as a result of the lowered-humidity boundary condition (Eq. 2), also provides a driving force for an upward movement of liquid water toward the low-humidity boundary. Hence the lowered humidity boundary condition provides a driving force for an upward flux of water in both phases. To estimate the magnitude of these fluxes, calculations were carried out by means of the numerical simulator TOUGH (Pruess, 1987). To focus on the vertical movement of water, the simulation was carried out in one dimension in a vertical tuff column of height 600 m, which is the approximate distance of the land surface to the water table (see Fig. 1). We employ a highly simplified stratigraphic description, assuming constant hydrological parameters representative of the potential repository host formation (the Topopah Spring welded unit) throughout.

The numerical computation is first carried out for the reference case, where no lowered-humidity boundary condition is imposed. The ground surface and the water table serve as constant-temperature boundaries maintained at 286 K and 304 K, respectively. The water table, which is fully saturated with zero capillary suction serves also as a constant-pressure boundary, and a "no-flow" boundary is imposed at the top. Thus we obtain as a function of elevation the equilibrium profiles of temperature, gas pressure, vapor pressure, and liquid and gas saturations before the lowered-humidity boundary condition at the land surface is engaged. We then implement the lowered-humidity boundary condition by imposing, at the land surface, an additional liquid suction pressure corresponding to Eq. (2). Calculations were carried out for two values of humidity: (1) $h = 0.8$, (2) $h = 0.5$.

Simulated results are shown in Figs. 2 through 4, where those prior to imposition of the lowered-humidity boundary condition are labeled "reference case"; and those with imposed-humidity boundary conditions are labeled "80% humidity" and "50% humidity." Figure 2 shows the equilibrium vapor pressure of the soil gas within the tuff formation. Note that the vapor-pressure profile deviates from the reference case only in the upper 150 m of the column. Figure 3 shows the profiles of equilibrium liquid saturation. Note that because of the very strong capillary pressures the capillary fringe extends all the way to the ground surface, and as a result of the upward movement of moisture and its subsequent loss at the land surface, the liquid-saturation profiles shift quite dramatically to lower values for the lowered-humidity boundary conditions. Figure 4 displays the fluxes, as a function of elevation with positive values for upward fluxes and negative values for downward fluxes. Figure 4a shows that for the reference case, the upward vapor flux is

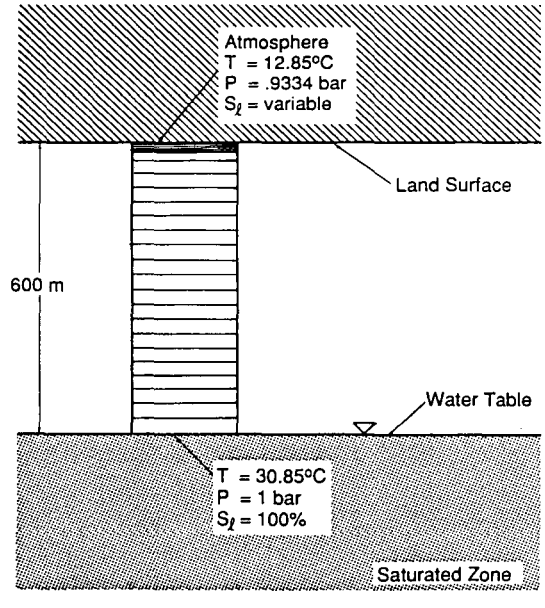

Figure 1. One-dimensional vertical column for simulation studies of humidity effects at the land surface. [XBL 882-10033]

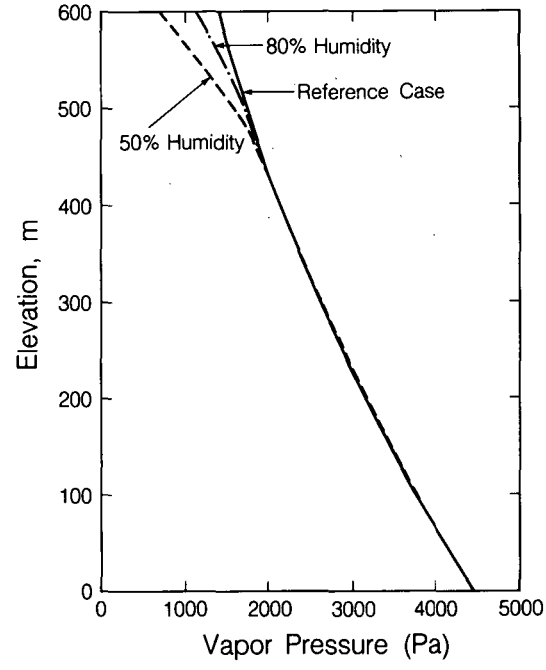

Figure 2. Vapor-pressure profiles for reference case and different humidity boundary conditions. [XBL 891-7441]

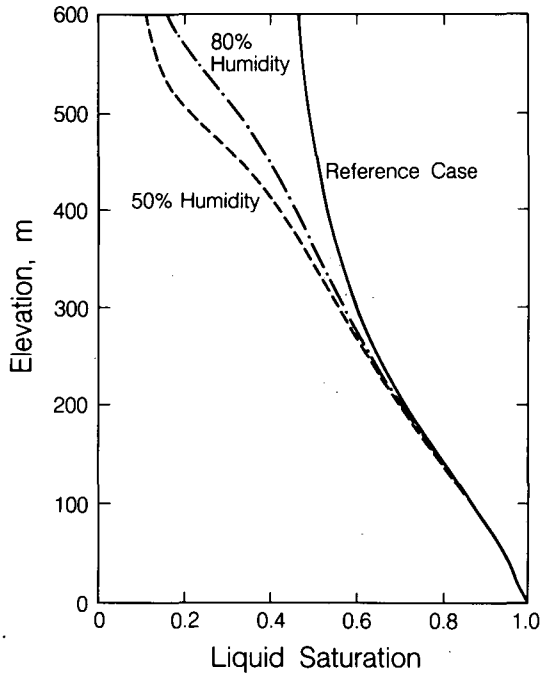

Figure 3. Liquid-saturation profiles for reference case and different humidity boundary conditions. [XBL 891-7442]

exactly balanced by the downward flow of the condensed liquid flux, resulting in zero net water migration. The larger magnitude of the vapor fluxes at depth arises from the geothermal gradient. Figure 4b shows that for the case with 50% humidity boundary condition, both the vapor and liquid fluxes have the same sign, giving rise to a net upward moisture flux on the order of 0.04 mm/yr.

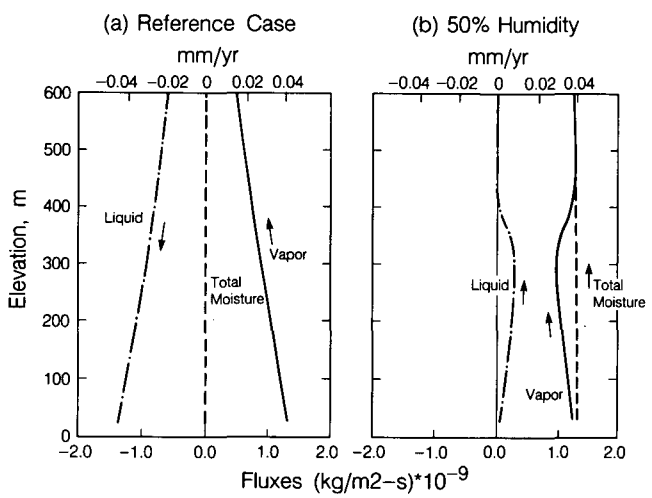

Figure 4. Flux profiles for **(a)** reference case and **(b)** 50%-relative-humidity boundary condition. [XBL 891-7440]

EFFECTS OF ATMOSPHERIC PRESSURE VARIATION—BAROMETRIC PUMPING

Moisture from the formation may be removed as a result of atmospheric pressure variations at the land surface. To examine this effect, we assume that the pressure of the gas phase in the formation immediately beneath the land surface is initially at equilibrium with the atmospheric pressure. As the barometric pressure increases, atmospheric air with rather low relative humidity is forced into the soil. Its humidity then increases from mixing with soil gas and from evaporation of soil moisture. When atmospheric pressure decreases at a later time, this more humid soil gas is discharged back to the atmosphere. Since the incoming gas has a lower relative humidity than the outgoing gas, this "pumping" process provides a mechanism for loss of formation moisture. The net mass of water removed as vapor from the formation per unit area during one pumping cycle (P to $P + \Delta P$ and back to P) is

$$M = H(\Delta P/P)\phi S_g \rho_g \chi_{sat}(h_{out} - h_{in}), \qquad (3)$$

where H is the height of the gas column (approximately 600 m), ϕ is the porosity of the formation, S_g is the gas saturation, ρ_g is the gas density, χ_{sat} is the saturated vapor mass fraction, and h_{in} and h_{out} are, respectively, the relative humidity of the atmospheric air and the discharged soil gas.

The magnitude of ΔP/P and the relative humidity h_{in} were deduced from the meteorological data obtained at two sites near Yucca Mountain site YA (Yucca Alluvial) in the valley to the east of Yucca Mountain and site YR (Yucca Ridge) near the ridge top of Yucca mountain. Data were collected from July 1982 through October 1984. The hourly data recorded on magnetic tape were made available to us by Hugh Church of Sandia National Laboratories; the data are summarized in the reports of Church et al. 1983–1986). Since the idea of moisture removal by barometric pumping hinges on some kind of cyclical variation of the pressure, we performed a spectral analysis on the hourly pressure data. The power spectrum in Fig. 5 shows a predominant peak corresponding to a period of 24 hours. Higher harmonics are also evident.

Processing all the pressure data from 1982 through 1984, we find that the average ΔP in the 24-hour cycle is 0.5 kPa for the Ridge site and 0.8 kPa for the Alluvial site. The mean pressure over the same period is 85.2 kPa. A statistical analysis of the atmospheric relative-humidity data over the period of 2–3 years gives the mean value of

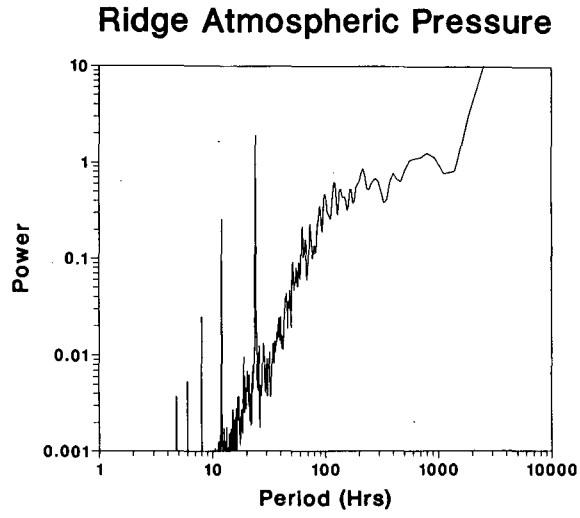

Figure 5. Smoothed Fourier power spectrum of atmospheric-pressure data. [XBL 891-311]

h_{in} = 0.28 for the Ridge site and 0.33 for the Alluvial site. We make the conservative assumption that the soil gas in the formation is very nearly saturated and therefore has a relative humidity of 1.0. This will give a maximum estimate for the amount of water that can be removed from the formation by barometric pumping. Incorporating the formation parameters of the tuff formation in Eq. (3), we estimate the moisture removal rate to be about 0.32 mm/yr.

SUMMARY

We have examined and reviewed some effects of atmospheric boundary conditions at the land surface on the ambient gas and moisture movements at Yucca Mountain. The moisture fluxes for the two processes are found to be small, on the order of 0.1 mm/yr, which is orders of magnitude smaller than the overall precipitation (150 mm/yr), not to mention the potential evapotranspiration. Although the gas-phase flow effects considered are small, they are on the same order of magnitude as the current estimates of the net liquid infiltration at Yucca Mountain. Since all those estimates are indirect with large uncertainty, our results raise the question as to the possibility of an overall drying, suggesting that further measurements should be made to accurately monitor status and migration of moisture at Yucca Mountain.

REFERENCES

Church, H.W., Freeman, D.L., Boro, K., and Egami R.T., 1983–1986. Meteorological tower data for the Nevada Nuclear Waste Storage Investigations. Sandia National Laboratories Reports SAND83-1912, 1983; SAND84-1327, 1984; SAND85-1053, 1985; SAND86-2533, 1986.

Edlefsen, N.E., and Anderson, A.B.C., 1943. Thermodynamics of soil moisture. Hilgardia, v. 15, no. 2, p. 31–298.

Kipp, K.L., Jr., 1987. Effect of topography on gas flow in unsaturated fractured rock–Numerical simulation. *In* D. Evans and J. Nicholson (eds.), Flow and Transport through Unsaturated Fractured Rock (Geophysical Monograph 42). American Geophysical Union, Washington, D.C., p. 171–176.

Pruess, K., 1987. TOUGH user's guide. Lawrence Berkeley Laboratory Report LBL-20700.

Weeks, E.P., 1987. Effect of topography on gas flow in unsaturated rock—Concepts and observations. *In* D. Evans and J. Nicholson (eds.), Flow and Transport through Unsaturated Fractured Rock (Geophysical Monograph 42). American Geophysical Union, Washington, D.C., p. 165–170.

Flow Channeling through Strongly Heterogeneous Permeable Media

Y.W. Tsang and C.F. Tsang

Field evidence that flow in fractures tends to concentrate in some preferred paths has motivated us to study the flow-channeling phenomenon theoretically (Moreno et al., 1988; Tsang et al., 1988) by conceptualizing the void space of a rock fracture as a two-dimensional (2-D) heterogeneous system with variable apertures as a function of position in the fracture plane. Simulated results show that the majority of fluid flow tends to coalesce into certain preferred flow paths (channels) that offer the least resistance. These studies of flow channeling as a result of variable fracture apertures lead to several

interesting observations that are not restricted only to flow in a fracture but are applicable in general to flow and transport in a strongly heterogeneous porous medium.

CHANNELING IN TWO-DIMENSIONAL SINGLE FRACTURES WITH SPATIALLY VARYING APERTURES

Measurements of aperture values in laboratory core samples of fractures (e.g., Gale, 1987) show that they are lognormally distributed. Given the aperture distribution and a spatial covariance, variable apertures in a fracture may be generated by geostatistical methods. Figure 1 shows three schematic representations of the fractures so generated; the various aperture values are shown by five shadings, with the darkest representing the smallest values. The three realizations in Fig. 1 are based on the lognormal distribution, with identical parameters for the mean and variance of the log aperture. All have the same correlation length $\lambda = 0.2L$, where L is the dimension of the single fracture, but have different correlation-anisotropy ratios of $\lambda_x/\lambda_y = 1$, 3, and 5,

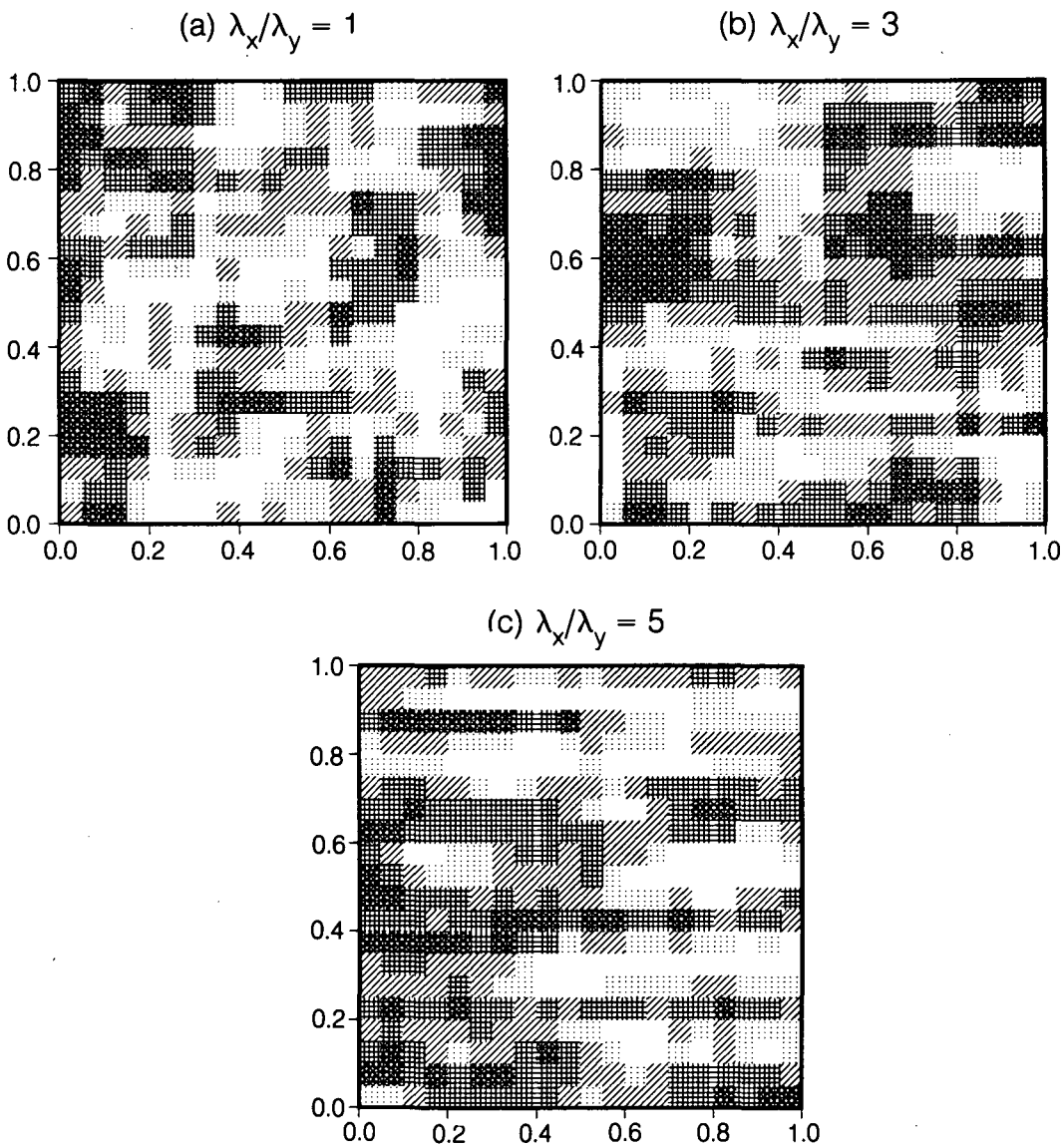

Figure 1. Statistically generated apertures with spatial correlation length of $0.2L$ in the plane of a single fracture of linear dimension L. The aperture values are partitioned into five classes with the smallest apertures corresponding to the darkest shading. The three realizations have different anisotropy ratio for the spatial correlation length: **(a)** $\lambda_x/\lambda_y = 1$, **(b)** $\lambda_x/\lambda_y = 3$, and **(c)** $\lambda_x/\lambda_y = 5$. [XBL 8811-10568]

respectively, in Fig. 1a, b, and c. The increase of the correlation anisotropy ratio from 1 to 5 in Fig. 1 is visually evident.

Following our earlier formulation (Moreno et al., 1988), we assume that Darcy's law holds locally for each grid block where the permeability varies as the square of the local aperture. Then the fluid pressure at each node may be computed by imposing constant-pressure boundary conditions on two opposite fracture boundaries and no-flow conditions on the two remaining boundaries. The fluid-flow rate between each pair of nodes within the fracture may be computed from the calculated fluid potential at each node. As an example, Fig. 2 shows the flow rates so calculated for the fracture with aperture variations as shown in Fig. 1b. Figure 2a shows the fluid flow when the constant-pressure conditions are applied on the left and right boundaries of the fracture; Fig. 2b shows the fluid flow when the pressure difference is applied on the top and bottom boundaries of the same fracture. The calculated flow rates between nodes cover a range of values over four orders of magnitude as a result of the lognormal aperture distribution of the fracture. Five levels of shading (empty space; broken line; and light, medium, and heavy solid lines) are used to represent the ascending values of the flow rates.

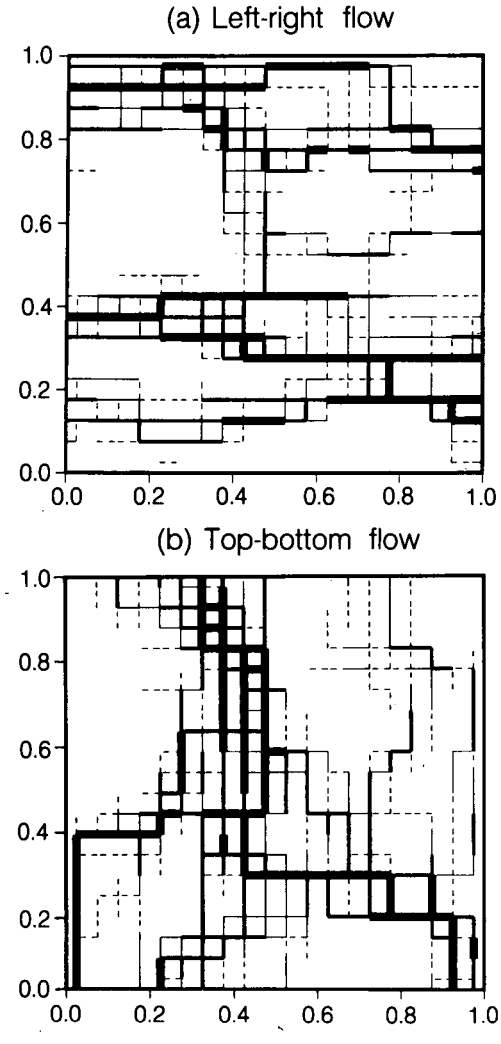

Figure 2. Fluid-flow rates for the fracture with aperture variations as shown in Figure 1b. The thickness of the lines is proportional to the flow rates. Pressure difference is applied from **(a)** left to right, and **(b)** top to bottom. [XBL 8811-10569]

It is apparent from Fig. 2 that even though flow occurs in the entire plane of the fracture, most flow takes place in a few selected pathways, or channels, along which the apertures are variable. These channels are preferred paths, in the sense of stream-tubes in the hydraulic-potential theory, because of the strong variation of the aperture and hence permeability value. The pattern of large-flow-rate channels (Fig. 2a) observed for the constant-pressure boundary conditions applied to the left and right boundaries is quite different from that (Fig. 2b) observed for the constant-pressure boundary conditions applied to the top and bottom boundaries of the same fracture. Similar results are obtained for the fractures in Fig. 1a and c (Tsang and Tsang, 1989).

Tracer transport through the fracture is calculated using the particle-tracking method. As each of the particles travels through the fracture, the aperture values along its flow path are recorded to generate the statistics of the aperture values of the flow channels. Figure 3 gives three probability density distributions: the solid line for the apertures over the entire 2-D plane of the fracture and the dot-dash line and the broken line for the apertures along the actual flow paths of the particles for the boundary conditions of overall left-right flow and top-bottom flow, respectively. All three curves are normalized to unit total integrated probability. Figure 3 shows that the tracer particles tend to favor large apertures and avoid small apertures of the 2-D fracture. A lognormal distribution may be fitted to the apertures along the particle paths; the fitted parameters are found to take on a larger mean and a smaller spread than the original distribution for the apertures of the entire 2-D fracture. They are also found to be almost identical for the two orthogonal flow geometries (left-right and top-bottom flows). The similarity between the aperture-density-distribution functions for the two orthogonal flow geometries is apparent in Fig. 3. This is not obvious a priori, since the channel patterns are quite different in the two cases (Fig. 2a and b). The result is even less obvious when one considers that the anisotropy ratio of the correlation length

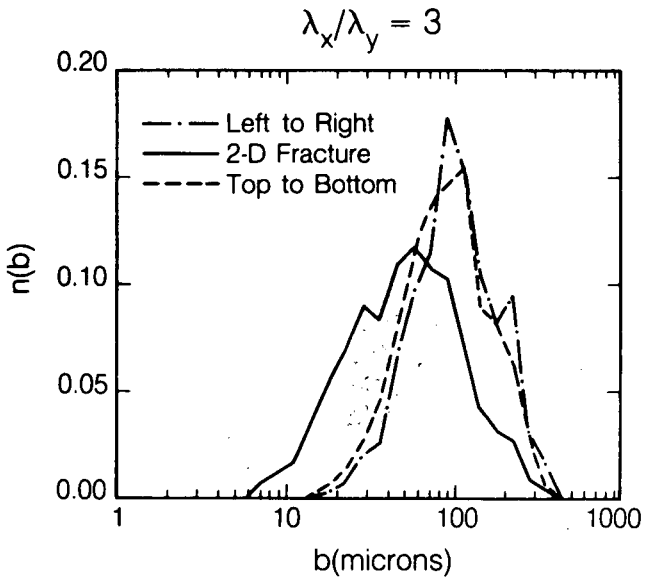

Figure 3. The aperture probability-density distributions for apertures over the 2-D fracture, along flow paths with left-right pressure difference and along flow paths with top-bottom pressure difference for the fractures shown in Figure 1b. [XBL 895-1812]

is a factor of 5 for the case in Fig. 1c, for which similar results are obtained. We believe the insensitivity of the aperture values of the flow paths in the two orthogonal directions of overall flow arises from the fact that the correlation length chosen here is $0.2L$. That is, the scale of heterogeneity is on the order of one-fifth of the region of measurement. Hence the correlation length is small enough for the particles flowing under different boundary conditions to sample statistically similar values of aperture along the flow paths. When the scale of heterogeneity is increased to the size of the flow region, the large anisotropy ratio in the aperture correlation length would give rise to a highly stratified medium through which the flow should consist of major conduits of very large apertures in the direction parallel to the large correlation length, but many smaller apertures are sampled in the orthogonal direction. When this happens, the aperture-density distribution of the particle flow paths will be dependent on the geometric configuration of the boundary conditions. But as long as the spatial correlation length is reasonably small (1/5 of the flow region in the cases studied), we have shown that even over a range of anisotropy ratios of the correlation, flow characteristics in terms of aperture distributions are the same in the two directions.

DISCUSSIONS AND APPLICATIONS TO A HETEROGENEOUS POROUS MEDIUM

The properties observed for the above calculations for a single fracture with variable aperture is applicable to a highly heterogeneous 2-D porous medium. The heterogeneity of a porous medium is typically expressed in terms of a permeability probability distribution $n(k)$, where the scale of heterogeneity is expressed in terms of a correlation length in the spatial variation of k. In their survey of 31 regional aquifers, Hoeksema and Kitanidis (1985) show that the hydraulic conductivity and transmissivity are in general well approximated by the lognormal distribution. In our single-fracture calculations, the stochastic variable is the lognormally distributed fracture aperture b, which relates to the local permeability by the relation $k = b^2/12$. Since we have shown that flow channeling results from the spatial variation of the fracture aperture, one would anticipate that the spatial variation of permeability in a 2-D porous medium can also give rise to flow channeling. Then the above results obtained for the fluid-flow behavior in a single fracture treated as a 2-D heterogeneous system is directly applicable to a highly heterogeneous porous medium (one with a large variance in the permeability density distribution). We may then make the following remarks regarding fluid flow in a strongly heterogeneous porous medium. The heterogeneous medium would give rise to flow channeling, and provided that the largest scale of heterogeneity is less than a few tenths of the scale of measurement, the least-resistive channels for tracer transport are characterized by a permeability distribution that differs from the permeability distribution of the entire medium. The distribution along the channels typically takes on a larger mean and a smaller variance than that which describes the whole region. The deviation of the permeability distribution along the flow channels from that of the whole region increases with the variance of the original permeability distribution. Flow channeling is expected to occur only in a strongly heterogeneous medium, which by definition will have a large variance in the permeability distribution. Calculations have been carried out for "weakly" heterogeneous systems with smaller variances in the permeability distribution, in which cases the discrepancy between the distributions of the entire region and that along the flow paths of tracer particles decreases and tends to zero. This is consistent with the result of the first-order perturbation approximation in the stochastic theory (e.g., Dagan, 1982;

Gelhar and Axness, 1983), which shows that the dispersion of tracer transport is proportional to the variance of the permeability of the entire 2-D region.

SUMMARY

We have presented here a number of observations made in our investigation of transport through strongly heterogeneous systems:

1. Heterogeneity due to permeability variability in a porous medium or aperture variability in a single fracture gives rise to flow channeling. One possible consequence is that since tracers traversing through such a medium will predominantly take a number of main paths, the effective rock area for interaction with tracers is much less than in the case when channeling is absent.
2. These channels for tracer transport are characterized by a probability distribution function for permeability (or fracture aperture) values. This distribution function is different from the permeability distribution function for the entire medium; specifically, it has a larger mean and a smaller variance. It is this distribution function, rather than the permeability distribution function of the entire medium, that is related to the dispersivity of tracer transport. The above conclusions are valid for a range of correlation-length anisotropy, provided that the correlation length is significantly less than the transport distance L; say for λ_x/L or $\lambda_y/L < 0.2$.

REFERENCES

Dagan, G., 1982. Stochastic modeling of groundwater flow by unconditional and conditional probabilities. 2. The solute transport. Water Resour. Res., v. 18, p. 835–848.

Gale, J.E., 1987. Comparison of coupled fracture deformation and fluid flow models with direct measurements of fracture pore structure and stress-flow properties. *In* Proceedings, 28th U.S. Symposium on Rock Mechanics, Tucson, Arizona, June 29–July 1, p. 1213–1222.

Gelhar, L.W., and Axness, C.L., 1983. Three-dimensional stochastic analysis of macrodispersion in aquifers. Water Resour. Res., v. 19, no. 1, p. 161–180.

Hoeksema, R.J., and Kitanidis, P.K., 1985. Analysis of the spatial structure of properties of selected aquifers. Water Resour. Res., v. 21, no. 4, p. 563–572.

Moreno, L., Tsang, Y.W., Tsang, C.F., Hale, F.V., and Neretnieks, I., 1988. Flow and tracer transport in a single fracture: A Stochastic model and its relation to some field observation. Water Resour. Res., v. 24, no. 12, p. 2033–2048.

Tsang, Y.W., and Tsang, C.F., 1989. Flow channeling through strongly heterogeneous permeable media. Lawrence Berkeley Laboratory Report 26596.

Tsang, Y.W., Tsang, C.F., Neretnieks, I., and Moreno, L., 1988. Flow and tracer transport in fractured media—A variable aperture channel model and its properties. Water Resour. Res., v. 24, no. 12, 2049–2060.

Correlation of Saturated and Unsaturated Flow Parameters in Soil and Tuff

J.S.Y. Wang and T.N. Narasimhan

To quantify uncertainties in modeling hydrological processes, we need to analyze the distributions and correlations of model parameters. Since many hydrological parameters are determined from microscopic pore structures, together with fluid properties and rock textures, correlations among different parameters may manifest themselves in the measured values. In this study, we compile and compare saturated and unsaturated parameters of watershed soils with tuff-matrix data. Tuff formations in the unsaturated zone at Yucca Mountain, Nevada, are being evaluated as potential host rocks for a nuclear waste repository. Since many unsaturated-flow models were developed in soil studies, it is important to analyze the similarity and difference between the characteristics of the soil and tuff.

Specifically, the watershed data are from the USDA study by Holtan et al. (1968), fitted by Panian (1987) of Desert Research Institute with the van Genuchten (1980) model. The tuff-matrix data are

from the Sandia National Laboratories study by Peters et al. (1984) and Klavetter and Peters (1987), also fitted with the van Genuchten model. In the van Genuchten model, the dependence of effective saturation S_e on suction pressure head h is described by the equation

$$S_e(h) = [1 + (|\alpha h|)^n]^{-(1-(1/n))}. \quad (1)$$

Figure 1 compares the van Genuchten curves with the popular Brooks and Corey (1966) model:

$$S_e(h) = \begin{cases} 1 & \text{if } |\alpha h| < 1, \\ |\alpha h|^{-\lambda} & \text{if } |\alpha h| \geq 1. \end{cases} \quad (2)$$

In the range of large suction, (1) is asymptotically equivalent to (2) with the pore-size-distribution index $\lambda = n - 1$. The inverse of the parameter α, $|h_{ae}| = \alpha^{-1}$ is frequently referred to as the air-entry value or bubbling pressure in the soil literature. This is one interpretation for the parameter α or h_{ae}. When suction pressure head h overcomes the air-entry pressure h_{ae} ($|h| \geq |h_{ae}|$), air enters the pores and water flows out of the medium to initiate desaturation. This interpretation is based on the cut-off separating the $S_e = 1$ saturated region from the $S_e = |\alpha h|^{-\lambda}$ desaturated region in the Brooks and Corey model. Another interpretation for α is to treat it as a scaling parameter. The saturation depends on αh together and not on α and h separately. Characteristic curves of soils with different α but same λ can be scaled into one curve. Therefore, we refer to α as the *air-entry scaling factor.* If flow channels are represented by capillary tubes, we can define the air-entry radius by the capillary equation

$$r_{ae} = -\frac{2\sigma}{\rho g h_{ae}} = \frac{2\sigma}{\rho g}\alpha. \quad (3)$$

With surface tension σ, water density ρ, and gravitational acceleration g as constants, r_{ae} is proportional to α. We can treat the air-entry radius r_{ae} as a parameter equivalent to the air-entry scaling factor α.

We have analyzed the pore-size-distribution index and the air-entry scaling factor, together with saturated permeability, porosity, and residual saturation. Detailed analyses of the distributions and the correlations of soil and tuff parameters are in the report by Wang and Narasimhan (1988). In the following discussion, we focus on two parameters: the saturated permeability and the unsaturated air-entry scaling factor. Figure 2 compares the distributions of log air-entry scaling factor of watershed soils with tuff matrix. The important observation is that the average air-entry scaling factor for watershed soils is two to three orders of magnitude larger than both the welded tuff and the nonwelded tuff. Since the air-entry radius is proportional to the air-entry scaling factor, the order-of-magnitude differences merely indicate that the soils have much larger pores that can be easily desaturated and that the tuff matrix has smaller pores that are more difficult to desaturate. Figure 3 shows that the average saturated permeability for watershed soils is five to seven orders of magnitude larger than those for welded/zeolitized tuffs.

Figure 4 shows the correlation between saturated permeability and air-entry radius based on mean values of these parameters for different soil-texture categories and different tuff stratigraphic units. This correlation was observed earlier in tuff data in Wang and Narasimhan (1987). If a porous medium is represented by uniform circular tubes with radius r_{ae}, the maximum permeability of this idealized air-entry tube model is

$$k_{ae} = \frac{r_{ae}^2}{8}. \quad (4)$$

Figure 4 shows that the correlation between saturated permeability and air-entry radius follows approximately the functional dependence of Eq. (4) when soil data are compared with welded/zeolitized tuff-matrix data. The soil data alone over smaller ranges do not support this correlation. Between very different media, it may be important to account for such a correlation.

In the literature, the correlation between permeability and porosity has been extensively studied. If

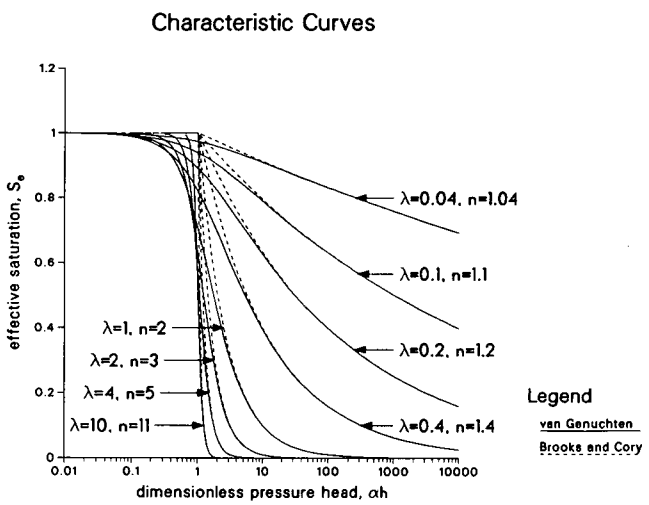

Figure 1. Scaled characteristic curves of the van Genuchten model and the Brooks and Cory model. [XBL 895-1683]

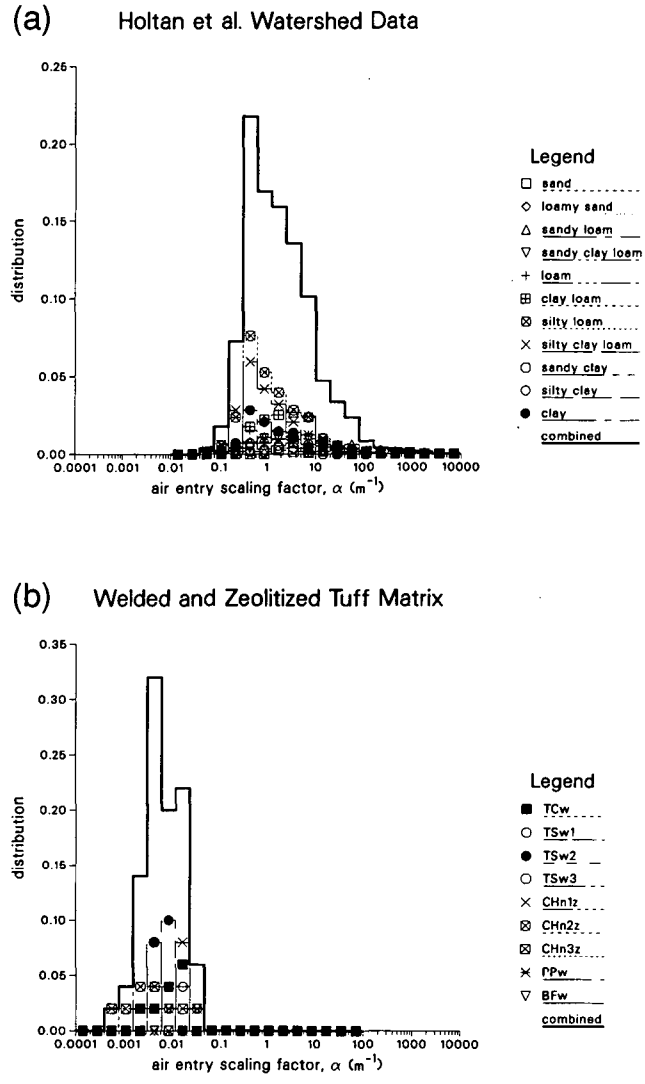

Figure 2. Comparison of distributions of log air-entry sealing factor for watershed soils and tuff matrix. [XBL 895-1684]

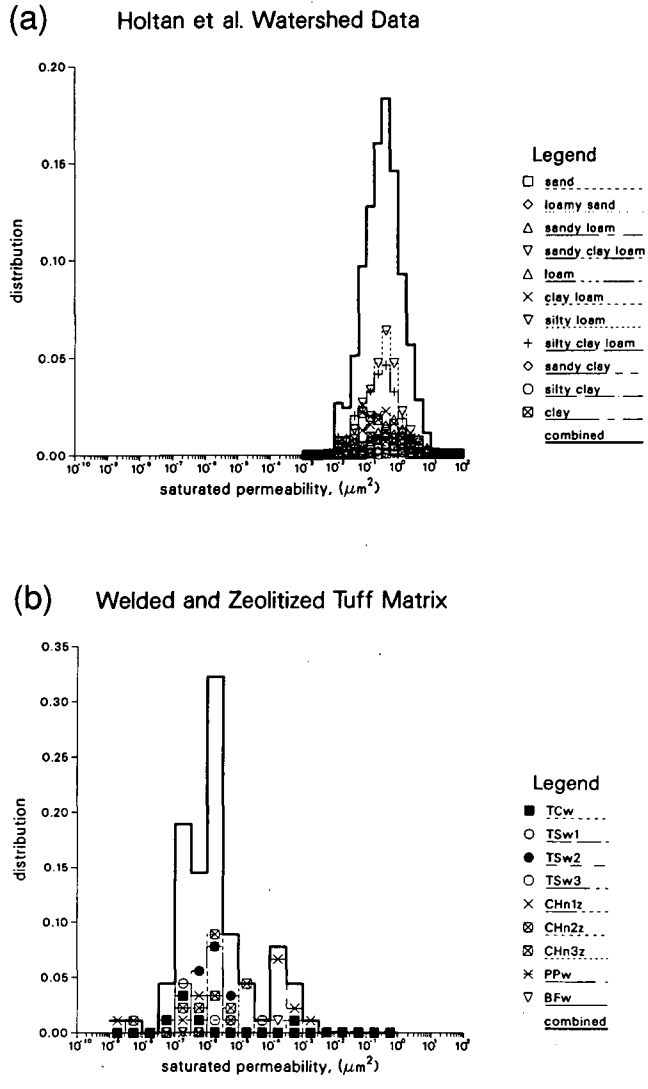

Figure 3. Comparison of distributions of log saturated permeability for watershed soils and tuff matrix. [XBL 895-1685]

the saturated permeability does correlate with other hydrological parameters, it probably correlates better with air-entry radius than with porosity and other parameters. Physically, this correlation makes more sense with air-entry radius than with porosity. The saturated permeability measures the flow through connected channels in a medium. The air-entry radius measures the desaturation of fluid from the interior of the medium through connected channels to the outside. Neither parameter depends on dead-end pores with stagnant fluid isolated from the connected channels. The porosity measures the volume of both connected channels and dead-end pores. There exists considerable interest in the literature on the permeability-porosity relationship. The correlation between permeability and air-entry radius, observed in soil and tuff-matrix data, also deserves attention in studies of natural geological media. Practically, this correlation of saturated permeability can be more easily demonstrated with air-entry radius than with porosity. The air-entry radius, or equivalently the air-entry scaling factor, varies over several orders of magnitude among different geological media. The porosity varies over a much narrower range among different geological media. With wider variations, the air-entry radius may correlate better with saturated permeability, which has the widest range of variation among all hydrological parameters.

If correlation between saturated permeability and air-entry radius is important, we need to take this

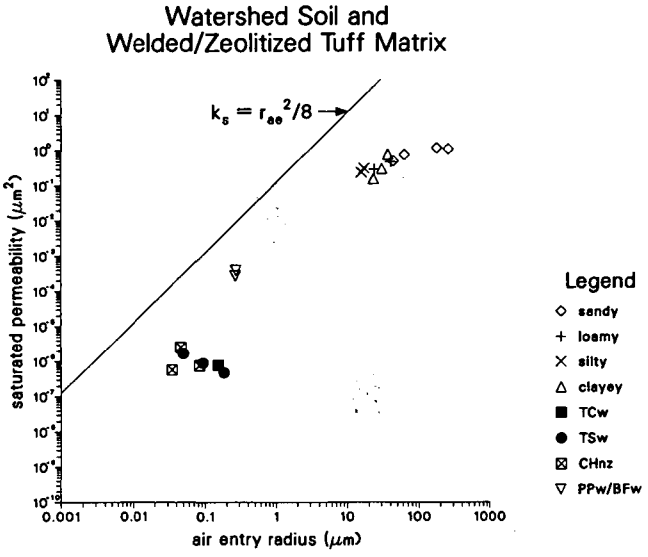

Figure 4. Correlation between saturated permeability and air-entry radius for watershed soils and tuff matrix. [XBL 895-1686]

correlation into account. For stochastic modelings of alternating units of welded and nonwelded tuff or formation blocks bounded by fault zones, we propose to impose correlations and constraints on average values of saturated permeability and air-entry scaling factor between highly different units to avoid unlikely combinations of parameters and predictions. Within a given stratigraphic unit, this physically meaningful correlation is likely masked by data variability, hence uncorrelated parameters with wide distributions may be acceptable.

REFERENCES

Brooks, R.H., and Corey, A.T., 1966. Properties of porous media affecting fluid flow. J. Irrig. Drainage Div., Proc. Am. Soc. Civ. Eng., 92, IR2, p. 61–88.

Holtan, H.N., England, C.B., Lawless, G.P., and Schumaker, G.A., 1968. Moisture-tension data for selected soils on experimental watersheds. Agricultural Research Service, ARS 41-144, U.S. Department of Agriculture, Beltsville, Maryland, 609 p.

Klavetter, E.A., and Peters, R.R., 1987. An evaluation of the use of mercury porosimetry in calculating hydrologic properties of tuffs from Yucca Mountain, Nevada. Sandia National Laboratories, SAND86-0286, Albuquerque, New Mexico.

Panian, T.F., 1987. Unsaturated flow properties data catalog (Vol. II). DOE/NV/10384-20, Desert Research Institute, Reno, Nevada, 493 p.

Peters, R.R., Klavetter, E.A., Hall, I.J., Blair, S.C., Heller, P.R., and Gee, G.W., 1984. Fracture and matrix hydrologic characteristics of tuffaceous materials from Yucca Mountain, Nye County, Nevada. Sandia National Laboratories, SAND84-1471, Albuquerque, New Mexico, 188 p.

van Genuchten, M.Th., 1980. A closed-form equation for predicting hydraulic conductivity of unsaturated soils. Soil Sci. Soc. Am. J., v. 44, p. 892–898.

Wang, J.S.Y., and Narasimhan, T.N., 1987. Hydrologic modeling of vertical and lateral movement of partially saturated fluid flow near a fault zone at Yucca Mountain. Sandia National Laboratories, SAND87-7070, Albuquerque, New Mexico; LBL-23510, Lawrence Berkeley Laboratory, Berkeley, California, 122 p.

Wang, J.S.Y., and Narasimhan, T.N., 1988. Processes, mechanisms, parameters and modeling approaches for partially saturated flow in soil and rock media. Sandia National Laboratories, SAND88-7054, Albuquerque, New Mexico; LBL-26224, Lawrence Berkeley Laboratory, Berkeley, California.

An Analytical Solution for Wellbore Heat Transmission in Layered Formations

Y.S. Wu and K. Pruess

Heat is transferred to or from the wellbore when there is a difference in temperature between the surrounding formation and the injected or produced fluid (Fig. 1). The surrounding formation is generally inhomogeneous and may be approximated as layered formations with different physical properties and arbitrary initial temperature distributions in the vertical direction. To evaluate the feasibility of a

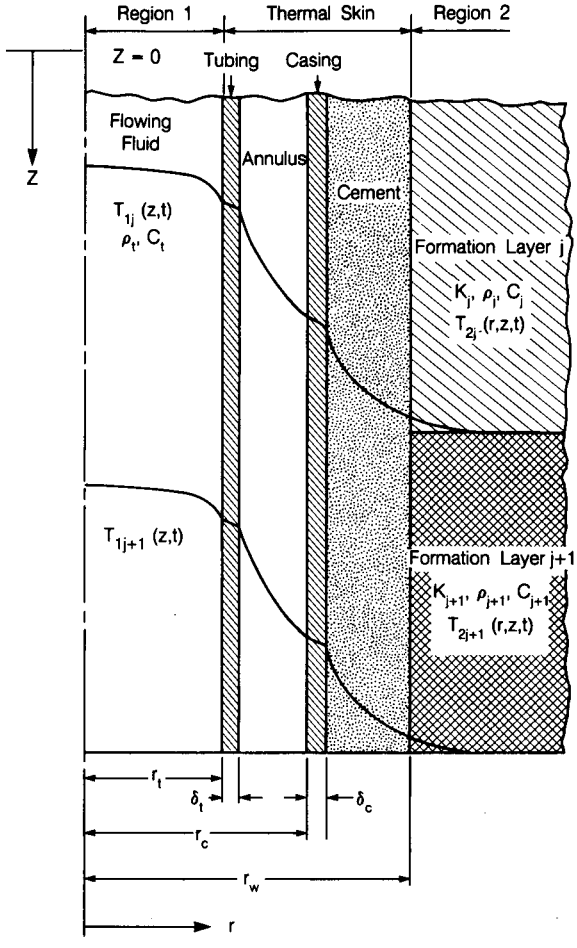

Figure 1. Schematic of wellbore and formation system. [XBL 882-10052]

thermal recovery project, such as in thermal oil recovery or in geothermal reservoir development, it is necessary to estimate the heat lost or gained by the fluid flowing in the wellbore. A quantitative description of heat exchange between a wellbore and the surrounding formation is also often required when one attempts to estimate formation temperature or to interpret temperature-log data.

MATHEMATICAL MODEL

Several authors have studied the problem of wellbore heat transmission using analytical or numerical methods (Lessem et al., 1957; Moss and White, 1959; Squier et al., 1962; Ramey, 1962; Farouq Ali, 1981). Our mathematical approach (Wu and Pruess, 1988) is similar to that of Lessem et al. (1957) and Ramey (1962), with the following extensions and improvements.

1. The partial differential equations of fully transient heat transfer between well fluid and formation are solved simultaneously by incorporating an overall heat-transfer coefficient. Heat transfer in the wellbore is treated as fully transient.
2. The inhomogeneous formation is approximated as multiple layers with different physical properties. The initial temperature distribution in the vertical direction can be arbitrary.
3. Exact solutions for wellbore temperature and heat-transfer rate are obtained in both real space and in Laplace space. The solutions are valid for the entire time range, from early to late.
4. A more-accurate formula is given for the widely used transient heat-conduction function $f(t_D)$ of thermal resistance; $f(t_D)$ is found to be a function not only of time but also of depth.

RESULTS

Figure 2 shows wellbore-temperature profiles during constant-rate injection of $T = 100°C$ (212 F) water. Formation properties are uniform (single layer). The exact and the Laplace-transformed solu-

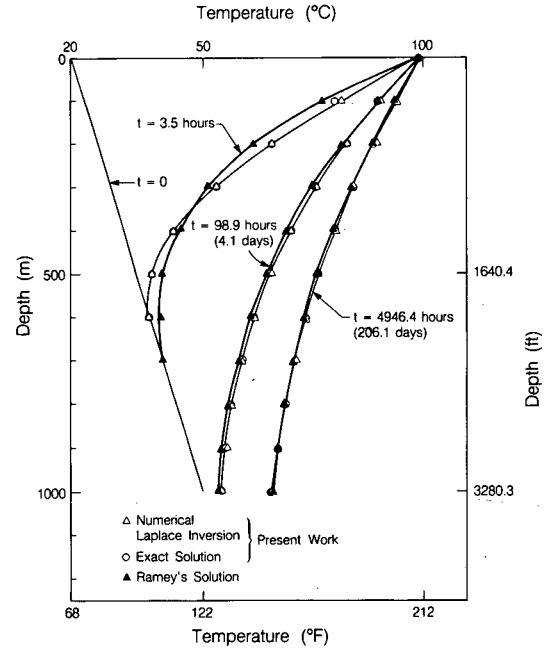

Figure 2. Comparison of numerical inversion of Laplace transformation with exact solution and Ramey's solution. [XBL 882-10050]

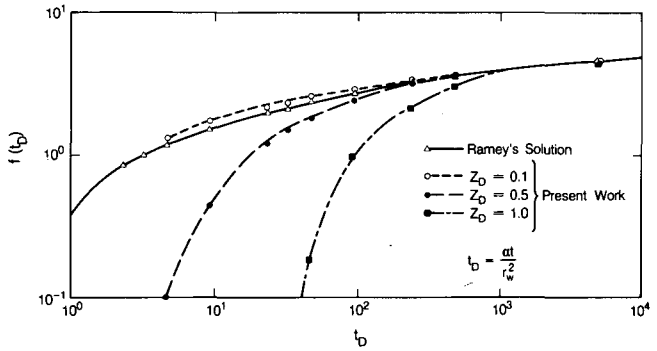

Figure 3. Effect of depth on $f(t_D)$. [XBL 882-10049]

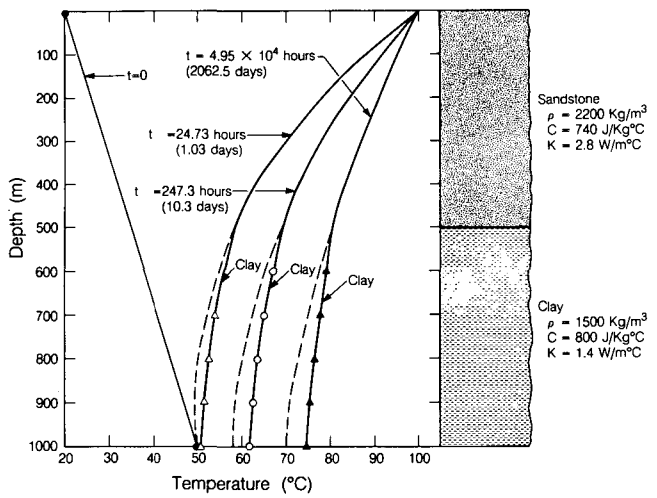

Figure 4. Wellbore temperature distribution of sandstone-clay two-layer formation. [XBL 882-10051]

tions agree well with one another. Significant differences compared with Ramey's approximate solution for a homogeneous formation exist for early times. The numerical inversion of the Laplace-transformed solution was found to give very poor results for $t_D \leq z_D$. The transient heat-conduction function is a function of not only t_D but also of z_D; $f(t_D)$ is given in Fig. 3 for comparison with Ramey's late-time formula. The wellbore-temperature distribution for a two-layered formation is shown in Fig. 4.

REFERENCES

Farouq Ali, S.M., 1981. A comprehensive wellbore steam/water flow model for steam injection and geothermal applications. Soc. Pet. Eng. J., v. 21, no. 4, p. 527–534.

Lessem, L.B., Greytok, F., Marotta, F., and Mcketta, J.J., Jr., 1957. A method of calculating the distribution of temperature in flowing gas wells. Trans., AIME, v. 210, p. 169.

Moss, J.T. and White, P.D., 1959. How to calculate temperature profiles in a water-injection well. Oil and Gas J., v. 57, no. 11, p. 174.

Ramey, H.J., Jr., 1962. Wellbore heat transmission. J. Pet. Tech., v. 14, no. 4, p. 427–435.

Squier, D.P., Smith, D.D., and Dougherty, E.L., 1962. Calculated temperature behavior of hot-water injection wells. J. Pet. Tech. v. 14, no. 4, p. 436–440.

Wu, Y.S., and Pruess, K., 1988. An analytical solution for wellbore heat transmission in layered formations. Presented at the 1988 SPE California Regional Meeting, Long Beach, California, March 23–25, 1988 (LBL-25056).

Boundary-Layer Solution for One-Dimensional Absorption in Unsaturated Porous Media

R.W. Zimmerman and G.S. Bodvarsson

The flow of water through partially saturated rocks or soils poses an interesting and difficult mathematical problem that has applications to various areas of science and technology. The uppermost region of the earth's crust, between the surface and the water table, is typically in a partially saturated state. Historically, the problem of the absorption of water into an unsaturated medium has been of interest to agricultural scientists and groundwater hydrologists. With the proposed use of the upper crust of the earth for the disposal and storage of hazardous wastes, flow in the unsaturated zone has taken on even wider relevance. The nonlinearity of the unsaturated flow equations makes analytical solutions extremely difficult to obtain. We have therefore used the integral (or boundary-layer) approach to derive approximate solutions for absorption into a semi-infinite half-space. Although the

immediate purpose of this work is for modeling flow in the vicinity of the planned nuclear waste repository at Yucca Mountain in Nevada, the results should be of general applicability to flow problems in unsaturated media.

FORMULATION OF PROBLEM

One-dimensional horizontal flow of water through a nondeforming porous medium is governed by Richards' equation (Hillel, 1980):

$$\frac{\partial}{\partial x}\left[\beta k_r(\psi)\frac{\partial \psi}{\partial x}\right] = G(\psi)\frac{\partial \psi}{\partial t} . \qquad (1)$$

The dependent variable $\psi(x,t)$ in Eq. (1) represents the pressure potential of water in the medium; it is positive in regions of full saturation and negative in regions of partial saturation. When the medium is less than fully saturated, the potential is often referred to as the capillary pressure or matric potential. The parameter β equals $k/\mu\phi$, where k is the absolute permeability of the medium, ϕ is the porosity of the medium (assumed constant), and μ is the dynamic viscosity of water. $k_r(\psi)$, which is the relative permeability of the medium to water, is a dimensionless number between zero and one. The storativity function, $G(\psi)$, is defined by $G(\psi) = dS/d\psi$, where S is the fraction of pore space that is filled with liquid water. Equation (1) essentially represents conservation of mass, along with Darcy's law; the left-hand side is the divergence of the volumetric flux of water, and the right-hand side is the change in the water content of the medium. Since Eq. (1) does not include a gravitational-potential term, it can be used to describe horizontal flow, or even vertical flow in situations where the potential gradients are large relative to the gravitational gradient of water.

Each rock or soil has its own "characteristic functions," $k_r(\psi)$ and $S(\psi)$, which relate the saturation, matric potential, and relative permeability. As a general rule, the relative permeability decreases from unity to zero as the saturation varies from some maximum value S_s down to the residual saturation S_r. The matric potential will decrease from zero down to $-\infty$ over this range of saturations. These functions reflect the pore-size distribution, along with other aspects of the pore geometry, and usually must be determined experimentally. Many types of functions have been proposed to represent characteristic curves (Hillel, 1980; Rulon et al., 1986). We have used the equations of van Genuchten (1980), since it has been shown that they can accurately fit the properties of many different rocks and soils. The van Genuchten formulas are

$$S(\psi) = S_r + (S_s - S_r)[1+(\alpha|\psi|)^n]^{-m} , \qquad (2)$$

$$k_r(\psi) = \frac{\{1-(\alpha|\psi|)^{n-1}[1+(\alpha|\psi|)^n]^{-m}\}^2}{[1+(\alpha|\psi|)^n]^{m/2}} , \qquad (3)$$

where n and m are two parameters related by $m = (n-1)/n$ and α is a parameter that has a dimension of 1/pressure. Examples of these characteristic curves are shown in normalized form in Fig. 1, with the normalized saturation defined as $\hat{S} = (S - S_r)/(S_s - S_r)$ and the normalized matric potential as $\hat{\psi} = \alpha\psi$.

A basic problem in the area of fluid flow in the unsaturated zone is that of absorption from a planar surface (such as a fracture) filled with water at some potential ψ_w into a semi-infinite formation that is initially at some uniform saturation S_i. This saturation S_i will correspond (via Eq. 2) to some potential ψ_i, where $\psi_i < 0$. For this problem, the appropriate initial and boundary conditions are

$$\psi(x,0) = \psi_i \quad \text{for all } x > 0 , \qquad (4)$$

$$\psi(0,t) = \psi_w \quad \text{for all } t > 0 , \qquad (5)$$

$$\lim_{x\to\infty} \psi(x,t) = \psi_i \quad \text{for all } t > 0 . \qquad (6)$$

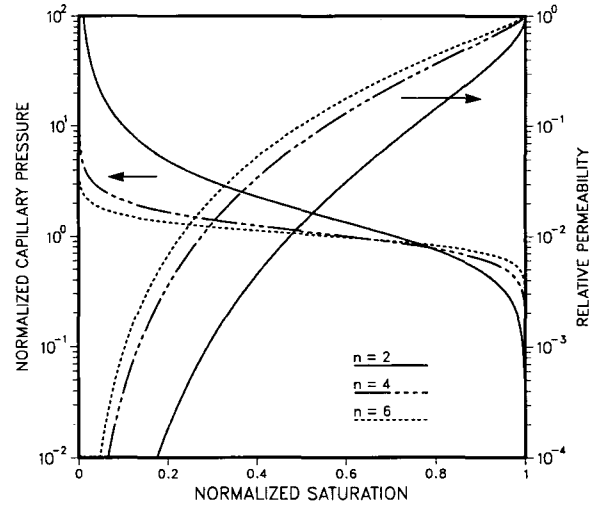

Figure 1. Normalized characteristic curves of the van Genuchten type. [XBL 887-10338]

SOLUTION OF PROBLEM

Because of the variation of k_r and S with ψ, Eqs. (1) to (6) represent a highly nonlinear problem that is not amenable to exact analytical solution. Although many approximate solutions have been found (Parlange, 1971; Philip and Knight, 1974), most require some numerical integration to yield results. We have used the boundary-layer approach to find an explicit, closed-form approximate solution for absorption into a van Genuchten medium.

The boundary-layer method uses an assumed potential profile that satisfies the boundary and initial conditions but only satisfies the governing PDE in an integrated sense. If a reasonable trial function is assumed as the solution to the problem, the method is known to lead to accurate results for many types of diffusion problems. The accuracy of the boundary-layer method for the present problem depends mainly on choosing an appropriate pressure profile; a simple but reasonably accurate profile has been found to be (see Zimmerman and Bodvarsson (1989) for details):

$$\psi = \psi_w [1 - (x/\lambda)] \quad \text{for } 0 < x < \lambda , \tag{7}$$

$$S = S_s - (S_s - S_i)\left(\frac{x-\lambda}{\delta}\right)^n \quad \text{for } \lambda < x < \lambda + \delta , \tag{8}$$

$$S = S_i \quad \text{for } x > \lambda + \delta . \tag{9}$$

Note that it is convenient to use the potential profile in the saturated region and the saturation profile in the unsaturated region. A relationship between the parameters λ and δ is found by requiring the flux (and hence $\partial\psi/\partial x$) to be continuous at $x = \lambda$:

$$\lambda = (\alpha\psi_w)\left[\frac{m(S_s - S_r)}{(S_s - S_i)}\right]^{1/n}\delta . \tag{10}$$

With the pressure and saturation profiles given by Eqs. (7) to (10), Eq. (1) is integrated from $x = 0$ to $x = \infty$. Since $\partial\psi/\partial x = 0$ for all $x > \lambda + \delta$ and $k_r = 1$ at $x = 0$, integrating the left side of Eq. (1) gives

$$\int_0^\infty \frac{\partial}{\partial x}\left[\beta k_r(\psi)\frac{\partial\psi}{\partial x}\right]dx = \frac{\beta}{\alpha\delta}\left[\frac{(S_s - S_i)}{m(S_s - S_r)}\right]^{1/n} . \tag{11}$$

Integrating the right side of Eq. (1) gives

$$\int_0^\infty G(\psi)\frac{\partial\psi}{\partial t}\,dx = (S_s - S_i)\frac{d}{dt}\left(\lambda + \frac{n}{n+1}\delta\right) . \tag{12}$$

Equating Eqs. (11) and (12) and using Eq. (10) to express λ in terms of δ gives

$$\frac{\beta}{\alpha\delta}\left[\frac{(S_s - S_i)}{m(S_s - S_r)}\right]^{1/n} = (S_s - S_i)\left\{\frac{n}{n+1} + (\alpha\psi_w)\left[\frac{m(S_s - S_r)}{(S_s - S_i)}\right]^{1/n}\right\}\frac{d\delta}{dt} . \tag{13}$$

Since none of the parameters appearing in Eq. (13) vary with δ or t, and since $\delta = 0$ when $t = 0$, Eq. (13) can be integrated to yield

$$\delta = \left[\frac{2kt}{\alpha\mu\phi}\frac{(S_s - S_i)^{-1+1/n}}{[m(S_s - S_r)]^{1/n}}\right]^{1/2} \times \left\{\frac{n}{n+1} + (\alpha\psi_w)\left[\frac{m(S_s - S_r)}{(S_s - S_i)}\right]^{1/n}\right\}^{-1/2} . \tag{14}$$

The instantaneous volumetric flux at the wall is found by combining Eqs. (10) and (14) with Darcy's law:

$$q = \left[\frac{k\phi}{2\alpha\mu t}\frac{(S_s - S_i)^{1+1/n}}{[m(S_s - S_r)]^{1/n}}\right]^{1/2} \times \left\{\frac{n}{n+1} + (\alpha\psi_w)\left[\frac{m(S_s - S_r)}{S_s - S_i}\right]^{1/n}\right\}^{1/2} . \tag{15}$$

APPLICATION: TOPOPAH SPRING WELDED TUFF

The unsaturated zone below Yucca Mountain in Nevada is being considered by the U.S. Department of Energy as a site for the construction of an underground repository for high-level radioactive waste. The Topopah Spring unit below Yucca Mountain is

a welded volcanic tuff, with estimated values of porosity and absolute permeability of 0.14 and 3.9×10^{-18} m^2, respectively (Rulon et al., 1986). The van Genuchten parameters that have been found to provide the best fit to capillary pressure and relative permeability data from the Topopah unit are S_s = 0.984, S_r = 0.318, n = 3.04, m = 0.671, and $\alpha = 1.147 \times 10^{-5}$ Pa^{-1} (Rulon et al., 1986).

Consider a vertical fracture that is saturated with water at zero potential, adjacent to a matrix which has an initial saturation of 0.676. Using the parameters listed above for the Topopah Spring welded tuff, a fluid viscosity of 0.001 Pa s (1 cP), and an elapsed time of 1×10^7 s (116 days), the boundary-layer solution represented by Eqs. (7) to (10) and (14) leads to the saturation profile shown in Fig. 2. For comparison, the problem has also been solved using the finite-difference code TOUGH (Pruess, 1987), as well as by numerical integration of the equations that result from subjecting Eq. (1) to a Boltzmann-type similarity transformation. Since the cumulative flux is proportional to the area under the saturation profile, it is clear that the approximate solution is fairly accurate in this case.

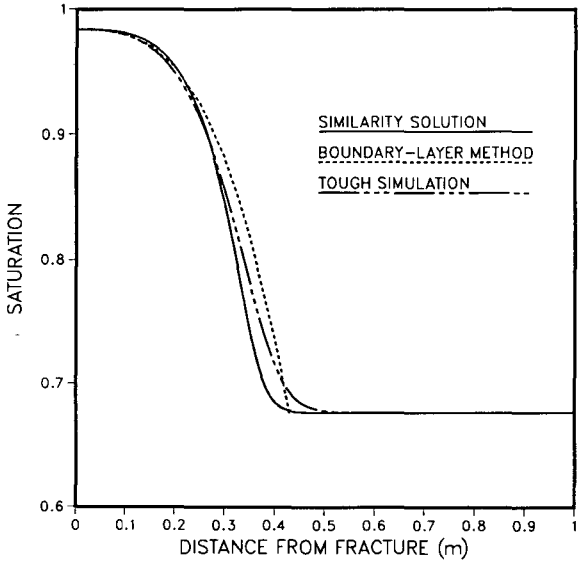

Figure 2. Saturation profile for absorption into Topopah Spring welded tuff. [XBL 887-10332]

A main intended application of the approximate boundary-layer solution is to calculate flow between fractures and matrix in a numerical simulator such as TOUGH with a mesh consisting only of "fracture elements." Equation (15) will be then used as a source/sink term for flow between the fractures and the adjacent matrix blocks. This approach will allow a considerable reduction in the number of elements required for accurate simulation, thereby reducing computational time and expense. The present solution should be useful for times that are small enough so that flow from one fracture is not affected by neighboring fractures. Application of this approach to longer time scales will be made possible by extending the integral-method solution to other geometries, such as spheres, cubes, and slabs.

REFERENCES

Hillel, D., 1980. Fundamentals of Soil Physics. Academic Press, New York, p. 202.

Parlange, J.-Y., 1971. Theory of water movement in soils: I. One-dimensional absorption. Soil Sci., v. 111, p. 134–137.

Philip, J.R., and Knight, J.H., 1974. On solving the unsaturated flow equation: 3. New quasi-analytical technique. Soil Sci., v. 117, p. 1–13.

Pruess, K., 1987. TOUGH user's guide. Lawrence Berkeley Laboratory Report LBL-20700, 78 p.

Rulon, J., Bodvarsson, G.S., and Montazer, P., 1986. Preliminary numerical simulations of groundwater flow in the unsaturated zone, Yucca Mountain, Nevada. Lawrence Berkeley Laboratory Report LBL-20553, 91 p.

van Genuchten, M.Th., 1980. A closed-form equation for predicting the hydraulic conductivity of unsaturated soils. Soil Sci. Soc. Am. J., v. 44, p. 892–898.

Zimmerman, R.W., and Bodvarsson, G.S., 1989. An approximate solution for one-dimensional absorption in unsaturated porous media. Water Resour. Res., v. 25, p. 1422–1428.

Integral-Method Solution for Diffusion into a Spherical Block

R.W. Zimmerman and G.S. Bodvarsson

Fluid flow in fractured reservoirs has received considerable attention for the past two decades, since many petroleum and groundwater reservoirs, as well as nearly all geothermal reservoirs, reside in fractured rocks. Further interest in fractured reservoirs has arisen from research efforts in the subsurface disposal of nuclear waste. Early models of fractured reservoirs include the so-called "double-porosity" model developed by Barenblatt et al. (1960) and Warren and Root (1963). In this model the high-permeability fractures provide paths for the global flow, and the low-permeability matrix blocks provide the fluid storage. Flow between the fractures and the matrix blocks was accounted for by assuming quasi-steady-state conditions. Subsequent studies have extended the model to include transient flow between the matrix blocks and the fractures (Streltsova, 1983) and have evaluated the effects of different matrix-block geometries on the reservoir-pressure response (Barker, 1985). These analytical solutions have been found valuable in the interpretation of pressure-transient tests in naturally fractured reservoirs.

The double-porosity concept has also been utilized in numerical simulation of oil, gas, groundwater, and geothermal reservoirs (Duguid, 1973). However, for field-wide simulations the use of this approach is limited by the large number of grid-blocks, and small time steps, that are often needed for accurate flow simulation. It is therefore of great interest to investigate methods that can analytically estimate the fluid flow between the fractures and the matrix. If flow into or out of the matrix blocks could be represented analytically, the blocks could be treated merely as source/sink terms in numerical simulations, and only the fractures would need to be explicitly discretized. This would lead to considerable reductions in computational time, thereby allowing reservoirs to be simulated more economically. We have used the "integral" approach to derive an extremely simple and relatively accurate expression for the flux into or out of a spherical matrix block that is surrounded by fractures at a given pressure.

FORMULATION OF PROBLEM

The governing equation for spherically symmetric flow of a Newtonian fluid in a homogeneous porous medium, neglecting gravity, is

$$\frac{1}{r^2}\left[\frac{\partial}{\partial r}\left(r^2\frac{\partial p}{\partial r}\right)\right]=\frac{\phi\mu c}{k}\frac{\partial p}{\partial t}\,, \tag{1}$$

where p is the fluid pressure, r is the radial coordinate, t is time, ϕ is the porosity of the medium, k is the permeability of the medium, μ is the viscosity of the fluid, and c is the (formation plus fluid) compressibility. The basic problem to be solved is that of a spherical block of radius a that is initially at equilibrium at some pressure p_i. At some time $t=0$, the pressure at the outer boundary of the sphere is instantaneously changed to some new value p_o, after which it is held constant. The appropriate boundary conditions for this problem are therefore

$$p(r,t=0)=p_i\,, \tag{2}$$

$$p(r=a,t>0)=p_o\,. \tag{3}$$

It is convenient to recast this problem in dimensionless form through the following changes of variables:

$$\hat{p}=\frac{p-p_i}{p_o-p_i}\,, \tag{4}$$

$$\tau=\frac{kt}{\phi\mu ca^2}\,, \tag{5}$$

$$\rho=r/a\,. \tag{6}$$

In terms of these new dimensionless variables, the governing equation and initial boundary conditions are

$$\frac{1}{\rho^2}\left[\frac{\partial}{\partial\rho}\left(\rho^2\frac{\partial\hat{p}}{\partial\rho}\right)\right]=\frac{\partial\hat{p}}{\partial\tau}\,, \tag{7}$$

$$\hat{p}(\rho,\tau=0)=0\,, \tag{8}$$

$$\hat{p}(\rho=1,\tau>0)=1\,. \tag{9}$$

The exact solution to the problem stated in Eqs. (7) to (9) is known (Crank, 1965), but the resulting

expression for the instantaneous flux into the sphere is in the form of a very slowly convergent infinite series, the numerical evaluation of which is computationally expensive. We have therefore used the integral approach to find an approximate solution that is quite accurate but much simpler in form. In the integral method, a trial pressure profile is assumed that satisfies the boundary conditions but only satisfies the governing differential equation in an average sense. If physically sensible trial profiles are used, this method is capable of achieving closed-form solutions of acceptable accuracy.

SOLUTION FOR "SMALL TIMES"

Consider some fixed value of dimensionless time τ, small enough such that the effects of the imposed pressure increment at the outer boundary of the sphere have not yet been felt at the sphere's center. We assume that the pressure decreases to zero over a distance referred to as the penetration depth, which is denoted by $1-\zeta$ (Fig. 1), and that $\hat{p}=0$ for $0<\rho<\zeta$. The simplest continuous pressure profile that satisfies this condition, along with boundary condition (9), is one that varies linearly with ρ over the range $\zeta<\rho<1$:

$$\hat{p} = \frac{\rho-\zeta}{1-\zeta} \quad \text{for } \zeta<\rho<1\,, \tag{10}$$

$$\hat{p} = 0 \quad \text{for } 0<\rho<\zeta\,. \tag{11}$$

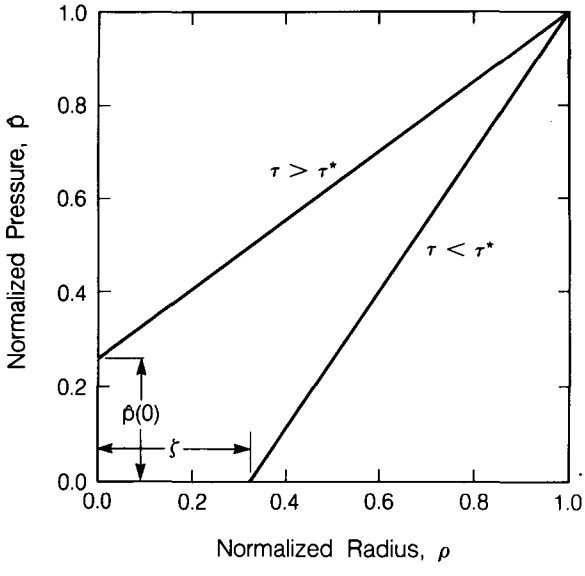

Figure 1. Assumed forms of pressure profile for times before ($\tau<\tau^*$) and after ($\tau>\tau^*$) front has reached center of sphere. [XBL 891-7428]

The penetration parameter ζ depends on τ in some manner that is a priori unknown.

To find an expression for the dependence of ζ on τ, the assumed profile given by Eqs. (10) and (11) is substituted into Eq. (7), which is then integrated over the entire volume of the sphere. This leads to the following differential equation for ζ:

$$\frac{1}{1-\zeta} = \frac{d}{d\tau}\left[\frac{\zeta^4-4\zeta+3}{12(1-\zeta)}\right]. \tag{12}$$

(The details of these and subsequent calculations can be found in Zimmerman and Bodvarsson (1989).) The solutions to Eq. (12), subject to the condition that $\zeta=1$ when $\tau=0$, is

$$12\tau = \frac{3}{4}\zeta^4 - \frac{1}{3}\zeta^3 - \frac{1}{2}\zeta^2 - \zeta + \frac{13}{12}\,. \tag{13}$$

Defining $\epsilon = 1-\zeta$ to be the penetration distance into the sphere, Eq. (13) can also be written as

$$\tau = \frac{1}{4}\epsilon^2 - \frac{2}{9}\epsilon^3 + \frac{9}{144}\epsilon^4\,. \tag{14}$$

The solution expressed by Eq. (14) is valid only for $\zeta>0$, or $\epsilon<1$, which corresponds to $\tau<\tau^*=13/144$.

For application to the double-porosity model, an important quantity is the flux into the sphere. The instantaneous flux can be determined from Darcy's law and the pressure profile given by Eq. (10) as

$$\dot{Q} = A\frac{\partial\hat{p}}{\partial\rho}\bigg|_{\rho=1} = \frac{4\pi}{1-\zeta} = \frac{4\pi}{\epsilon}\,. \tag{15}$$

The total flux from time 0 to time τ is found by integrating the instantaneous flux, using Eq. (14) to express $d\tau$ in terms of ϵ:

$$Q(\tau) = \int_0^\tau \dot{Q}\,d\tau = \frac{\pi}{3}(\epsilon^3 - 4\epsilon^2 + 6\epsilon)\,. \tag{16}$$

Equations (14) and (16) thus describe (implicitly) the cumulative flux as a function of time for $\tau < 13/144$.

SOLUTION FOR "LARGE TIMES"

For $\tau > \tau^*$, the diffusion front has reached the center of the sphere, and Eqs. (10) and (11) can no longer be used to approximate the pressure profile. The simplest profile that can be used for $\tau > \tau^*$ is (Fig. 1):

$$\hat{p} = \hat{p}(0) + [1 - \hat{p}(0)]\rho, \quad (17)$$

where $\hat{p}(0)$ is the pressure at the center of the sphere. Following the same procedure as for the "small-time" solution, the pressure profile from Eq. (17) is substituted into Eq. (7) and integrated, leading to

$$\frac{d\hat{p}(0)}{d\tau} = 12[1 - \hat{p}(0)]. \quad (18)$$

Since the initial condition is that $\hat{p}(0)$ must be 0 when $\tau = \tau^*$, the solution to Eq. (18) is

$$\hat{p}(0) = 1 - \exp[-12(\tau - \tau^*)]. \quad (19)$$

From Darcy's law and Eq. (17), the instantaneous flux per unit area is simply $1 - \hat{p}(0)$, so that the total flux for the entire sphere up until any arbitrary time $\tau > \tau^*$ is

$$Q(\tau) = Q(\tau^*) + 4\pi \int_{\tau^*}^{\tau} \exp[-12(\tau - \tau^*)]d\tau$$

$$= \pi + \frac{\pi}{3}\left(1 - \exp[-12(\tau - \tau^*)]\right). \quad (20)$$

DISCUSSION OF SOLUTION

For very small values of time, Eq. (14) shows that $\epsilon \approx 2\sqrt{\tau}$. The instantaneous flux Q is therefore approximately equal to $2\pi/\sqrt{\tau}$, and the cumulative flux up to time τ is approximately equal to $4\pi\sqrt{\tau}$. This $\sqrt{\tau}$ dependence is characteristic of one-dimensional diffusion problems, since for very small times the curvature of the sphere is not felt. In the limit of very small times, the exact expression for the instantaneous flux can be shown (Crank, 1965) to be asymptotically equal to $4\sqrt{\pi/\tau}$, so that the approximate result is initially about 11% too low. The approximate solution fortuitously compensates for this error as time increases, so that the cumulative flux has a relative accuracy of better than 11% for all subsequent times.

For $\tau > \tau^* = 13/144$, the approximate solution gives the instantaneous flux into the sphere explicitly as $Q = 4\pi\exp[-12(\tau - \tau^*)]$. Note that although the form of the solution is "discontinuous" at $\tau = \tau^*$, the predicted instantaneous flux is nevertheless a continuous function of time for all times. In this sense the approximate solution developed above is superior to the "small-time" and "large-time" approximations that can be found using Laplace transform techniques, since they do not correctly match up for intermediate values of τ. In Fig. 2, the instantaneous flux predicted by the approximate solution is compared with the exact solution (Crank, 1965). Although the approximate flux is lower than the actual flux for some values of τ, and higher for others, in general the two results agree very closely.

The solution derived above can be incorporated into a numerical model that discretizes the fractures and treats the matrix blocks as source/sink terms. Such a model can handle spheres of different sizes in different parts of the field, which would be useful if data were available regarding fracture patterns. Note that this method as described is useful for problems in which the (fracture) pressure at each point in the reservoir changes either monotonically or oscillates with a characteristic time that is larger than about $\Delta\tau \approx 1$, which is roughly the time needed to reach equilibrium throughout the block. Problems with more rapidly oscillating fracture pressures require a somewhat different formulation for the fracture-matrix flow problem (Pruess and Wu, 1988). Finally, note that this solution can be applied to any physical process governed by the diffusion equation, such as heat conduction or chemical transport, both of which are important in reservoir engineering and underground waste-isolation problems.

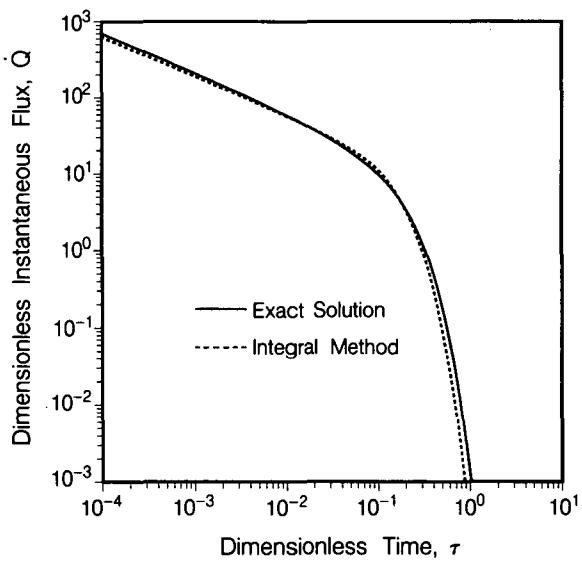

Figure 2. Instantaneous flux into sphere, according to the approximate and exact solutions. [XBL 888-10400]

REFERENCES

Barenblatt, G.E., Zheltov, Y.P., and Kochina, I.N., 1960. Basic concepts in the theory of seepage of homogeneous liquids in fissured rocks. J. Appl. Math. Mech., v. 24, p. 1286–1303.

Barker, J.A., 1985. Block-geometry functions characterizing transport in densely fissured media. J. Hydrol., v. 77, p. 263–279.

Crank, J., 1965. The Mathematics of Diffusion. Clarendon Press, Oxford, p. 91.

Duguid, J.O., 1973. Flow in fractured porous media (Ph.D. thesis). Princeton University.

Pruess, K., and Wu, Y.S., 1988. A semi-analytical method for heat sweep calculations in fractured reservoirs. Presented at the Thirteenth Workshop on Geothermal Reservoir Engineering, Stanford, January 19–21, 1988.

Streltsova, T.D., 1983. Well pressure behavior of a naturally fractured reservoir. Soc. Pet. Eng. J., v. 23, p. 769–780.

Warren, J.E., and Root, P.J., 1963. The behavior of naturally fractured reservoirs. Soc. Pet. Eng. J., v. 3, p. 245–255.

Zimmerman, R.W., and Bodvarsson, G.S., 1989. Integral method solution for diffusion into a spherical block. J. Hydrol., in press (LBL-26020).

GEOLOGY AND GEOCHEMISTRY

Investigators in the Geology and Geochemistry group primarily study phenomena associated with chemical reactions in the earth's crust. These phenomena usually involve interactions between subsurface aqueous fluids and the surrounding geologic media—both the chemical alteration of rock and soil by fluids and the chemical reactions that occur within the fluids. Many of these reactions occur during the movement of fluids; accordingly, our studies have a strong impact on the disposal of radioactive and toxic wastes. The successful containment of waste species is heavily dependent on arresting the movement of dissolved chemical species in groundwaters. As a part of this overall study, separate investigations are conducted in areas of radiochemistry, inorganic chemistry, and surface chemistry in support of geologic transport models and codes that require such data.

Research in the group covers themes related to geochemical reactions and transport. Several programs address field-oriented research, where hydrology is strongly coupled with aqueous analytical chemistry, chemical-species modeling, and hydrochemistry. Other programs emphasize geochemical and chemical modeling of nuclear waste repositories—specifically, how radionuclide species dissolve, react, and migrate under repository conditions.

The group also conducts basic research as it relates to geologic processes that occur in the earth's crust and in the upper mantle. The thermodynamics of liquid silicate minerals are investigated, as are the thermodynamics of high-temperature brines. Thermodynamically coupled processes are being modeled, along with chemical species, as a function of different experimental parameters, such as pH, temperature, and oxidation potentials. Research is also in progress on interfacial geologic chemical reactions that address both solid-liquid and solid-gas reactions on mineral surfaces. The occurrence and movement of radon and its parent radioisotopes in rock and soil are also being investigated.

Transient Diffusion from a Waste Solid into Fractured Porous Rock

J. Ahn, P.L. Chambré, and T.H. Pigford

Previous analytical studies of the advective transport of dissolved contaminants through fractured rock have emphasized the effect of molecular diffusion in the rock matrix on the space-time-dependent concentration of the contaminant as it moves along the fracture (Neretnieks, 1980; Tang et al., 1981; Chambré et al., 1982; Ahn et al., 1985). It was assumed that diffusion through the matrix takes place only in the direction normal to the fracture surface. Contaminant sources were assumed to be constant-concentration surfaces of width equal to the fracture aperture and of finite or infinite extent in the transverse direction, as shown in Fig. 1a. Such studies illustrate the far-field transport features of fractured media. To predict the time-dependent mass transfer from a long waste cylinder surrounded by porous rock and intersected by a fracture, the present study includes diffusion from the waste surface directly into porous rock, as well as the more realistic geometry shown in Fig. 1b. Here we present numerical results from Chambré's analytical solution for the time-dependent mass transfer from the cylinder for the low-flow conditions wherein near-field mass transfer is expected to be controlled by molecular diffusion (Chambré and Pigford, 1984).

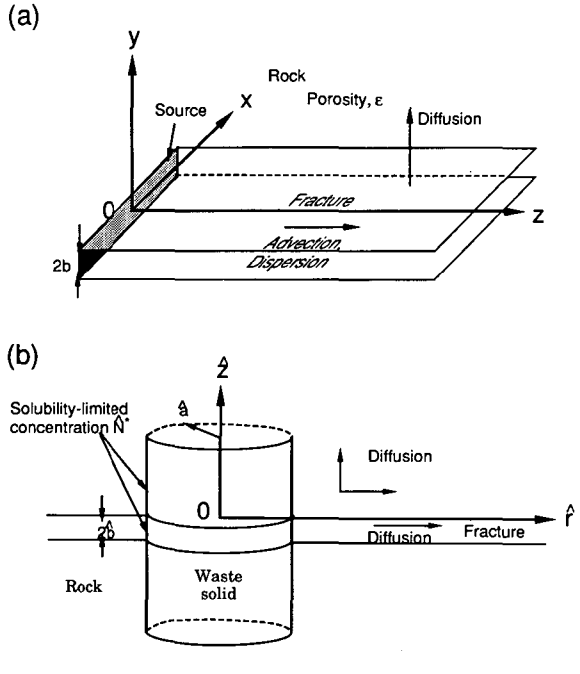

Figure 1. Comparison of **(a)** planar geometry, used in other studies, and **(b)** cylindrical geometry, used in this study. [XBL 895-1962]

The governing equations describe three-dimensional diffusion in the rock matrix and two-dimensional diffusion in the fracture, assuming local sorption equilibrium and uniform concentration across the fracture width. A constant concentration $\hat{N}^*$ of low-solubility dissolved species is prescribed at the waste surface. No waste container is present. The solution applies to an infinitely long cylinder of constant radius and is a good approximation for a long cylinder with negligible end effects. A nonzero steady-state solution exists for species with radioactive decay. The results are illustrated in Fig. 2, which shows instantaneous concentration isopleths, mass flux across the fracture surface, and mass fluxes from the waste into the fracture and into the rock matrix. The diffusion coefficient $\hat{D}$ is conservatively chosen as that for a liquid continuum. Concentrations are normalized by $j_0 = \hat{D}\hat{N}^*/\hat{a}$. The mass flux into the fracture is calculated to be about two orders of magnitude greater than that into the rock matrix, because of the assumed hundredfold greater porosity in the fracture.

Figure 3 presents release rates as a function of time after the beginning of dissolution, calculated by integrating the time-dependent mass flux over the waste surface. The mass-release rates are normalized to the quantity $4\pi\hat{a}\hat{D}\hat{N}^*$, where $\hat{a}$ is the cylinder radius. Even though the mass flux from the waste into the rock matrix is low relative to that into the fracture, the larger waste surface exposed to the matrix and the greater assumed matrix sorption result in a greater release rate to the matrix than to the fracture. This indicates that, for the parameters assumed here, the earlier mass-transfer theories (Chambré et al., 1982) for a waste solid completely surrounded by porous unfractured rock can adequately predict release rates in low-flow conditions in fractured media. If tortuosity significantly reduces the diffusion coefficient in the rock matrix and not in the fracture, mass transfer directly from the waste to the fracture becomes more important.

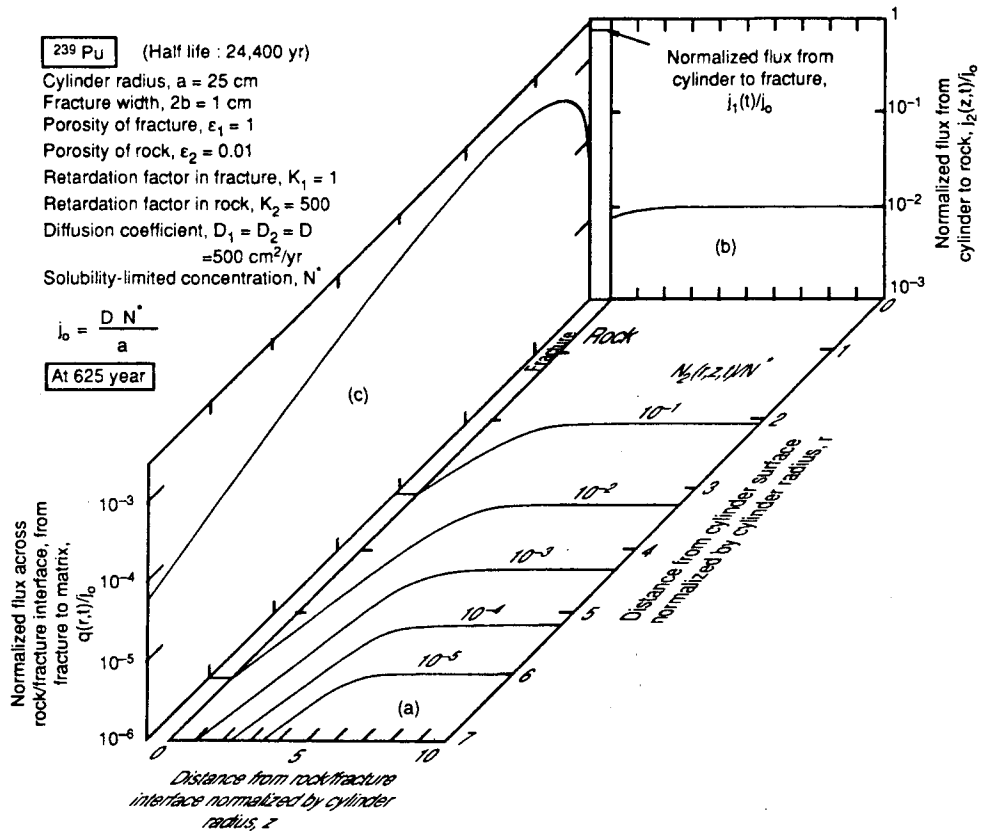

Figure 2. Illustration of nuclide migration at 625 years, or Fourier number 1. **(a)** Isopleths of normalized concentrations in fracture and in rock. **(b)** Normalized flux from waste cylinder to rock. **(c)** Normalized flux from fracture to rock. [XBL 895-1963]

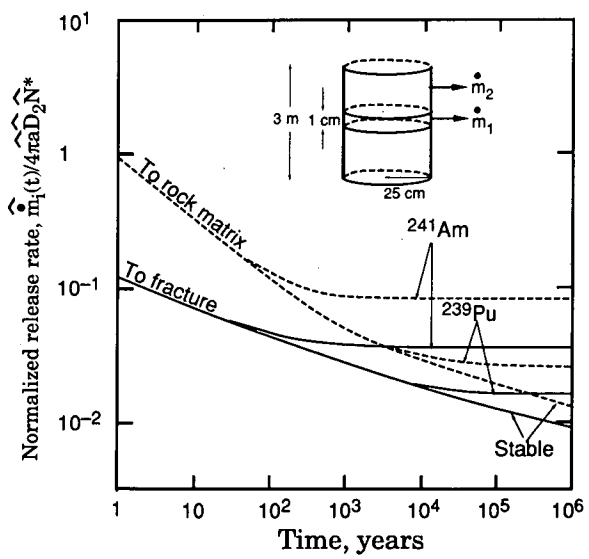

Figure 3. Normalized release rates of nuclides from a 3-m-high waste cylinder. Geologic parameters from Fig. 2 apply. [XBL 895-1964]

REFERENCES

Ahn, J., Chambré, P.L., and Pigford, T.H., 1985. Radionuclide migration through fractured rock: Effect of multiple fractures and two-member decay chains. Lawrence Berkeley Laboratory Report LBL-21121.

Chambré, P.L., and Pigford, T.H., 1984. Predictions of waste performance in a geologic repository. *In* G.L. McVay (ed.), Scientific Basis for Nuclear Waste Management VII. Materials Research Society Symposia Proceedings (Vol. 26). Elsevier, New York, p. 985–1008.

Chambré, P.L., Pigford, T.H., Sato, Y., Fujita, A., Lung, A., Zavoshy, S., and Kobayashi, R., 1982. Analytical performance models for geologic repositories. Lawrence Berkeley Laboratory Report LBL-14842.

Tang, D.H., Frind, E.O., and Sudicky, E.A., 1981. Contaminant transport in fractured porous media: Analytical solution for a single fracture. Water Resour. Res., v. 17, p. 555.

Neretnieks, I., 1980. Diffusion in the rock matrix. An important factor in radionuclide retardation? J. Geophys. Res., v. 85, no. B8, p. 4379–4397.

Thermodynamic Properties of Silicate Materials

I.S.E. Carmichael, D.A. Synder, and V.C. Kress

THEORY OF CRYSTAL DEPOSITION IN MAGMA CHAMBERS

A long-standing problem in igneous petrology is to unravel the processes responsible for the evolution of magmas from only the final preserved products (the rocks). This year we developed a theory that relates the crystal-nucleation rate in a magma chamber to the consequent deposition rate by crystal settling. A unique inverse was derived that permits calculation of nucleation rates from the resulting deposition rate. Calculations using this theory on the nucleation rate of augite as a function of time in the Kiglapait layered intrusion yield results consistent with independent kinetic calculations. This success encourages further application of the theory. The model is immediately useful for evaluating proposed mechanisms for the origin of rhythmic layering in layered intrusions.

A magma chamber can be modeled as a linear tranducer that sends a nucleation-rate function, $g(t)$, to a deposition-rate function, $h(t)$. It can easily be shown from the definition of the Dirac delta functional that

$$g(t) = \int_{-\infty}^{\infty} \delta(t - t')g(t')dt'. \tag{1}$$

From this we can conclude that by knowing the response of the magma chamber to a Dirac delta-like nucleation-rate function, we can predict the response of that system to *any* nucleation-rate function. If we let the response of the chamber to a Dirac delta functional be $k(t)$, it can easily be shown that

$$h(t) = \int_{-\infty}^{\infty} k(t - t')g(t')dt' = \int_{-\infty}^{\infty} k(t')g(t - t')dt'. \tag{2}$$

To derive an expression for $k(t)$, the assumption is made that the rate of crystal depletion in the chamber is proportional to the number of crystals in suspension, $N(t)$. The experiments of Martin and Nokes (1988) indicate the soundness of this assumption. If $g(t) = N_0\delta(t)$, then the crystal-deposition rate is

$$h(t) = N_0\alpha e^{-\alpha t}, \tag{3}$$

where α is the inverse of the crystal-retention time. This parameter can be estimated from Stokes law (Martin and Nokes, 1988; Marsh, 1988). If α is independent of time,

$$\alpha = \frac{4}{9}\frac{gr^2\Delta\rho}{l\eta}. \tag{4}$$

If α is dependent on time because the crystals are growing at a rate G, then

$$\alpha(t) = \frac{4}{9}\frac{g\Delta\rho}{l\eta}\left[\left(\frac{3G}{4\pi}\right)t\right]^{2/3}. \tag{5}$$

Hence

$$k(t) = \alpha e^{-\alpha t}. \tag{6}$$

In general, then, the deposition rate, $h(t)$, is related to the nucleation rate, $g(t)$, by convolution:

$$h(t) = \alpha\int_0^{\infty} e^{-\alpha t'}g(t - t')dt'. \tag{7}$$

This relation is easily inverted using Fourier transform methods. However, an analytic inverse exists that avoids truncation effects that are inherent in Fourier transform methods. Using suitable operator arguments yields

$$g(t) = h(t) + \frac{1}{\alpha}\frac{\partial h(t)}{\partial t} \tag{8}$$

so long as $\alpha \neq \alpha(t)$.

It remains to relate the deposition rate to the modes of the rocks preserved in the cumulate pile. If the concentration of phase i at time t is given by $x_i(t)$, then for n phases,

$$x_i(t) = \frac{h_i(t)}{\sum_{i=1}^{n} h_i(t)}. \tag{9}$$

If $d(t)$ is the depth of the crystal pile as a function of time and we allow each particle to have thickness ϕ_i when lying on the floor, then

$$d(t) = \sum_{i=1}^{n} \phi_i \int_0^t h_i(t')dt'. \quad (10)$$

So long as the deposition rate never drops to zero for any t, the above equations can be combined to calculate the mode of any phase in the cumulate pile as a function of depth from knowledge of the nucleation rates of the phases.

Since nucleation can only occur at finite undercoolings, recent numerical models have suggested that nucleation may occur in pulses of finite duration. If we take these pulses to be approximately Gaussian, then from the above theory we can predict that the consequent deposition rate is of the form

$$h(t) = \sum_{n=1}^{p} \frac{\alpha\sqrt{\pi}}{2}\left[1 + \mathrm{erf}\left(\frac{2t - 2n\theta - \alpha}{2}\right)\right] \times \exp\left(-\alpha t - \lambda n\theta + \alpha n\theta + \frac{\alpha^2}{4}\right), \quad (11)$$

where $\theta > 0$ is the time of maximum nucleation rate, λ is a delay constant between nucleation pulses, and p is the number of individual pulses. Use of this relation to simulate the formation of rhythmic layering by oscillatory nucleation has indicated that the long-proposed hypothesis of oscillatory nucleation is an unlikely mechanism for the generation of rhythmic layers.

REDOX STATE OF IRON IN THE LIME-IRON-SILICA SYSTEM: EXPERIMENTS AND A MODEL FOR PREDICTION

The oxidation reaction in silicate melts can be expressed according to the reaction (Fudali, 1965)

$$FeO^{melt} + \tfrac{1}{4}O_2^{gas} = FeO_{1.5}^{melt}, \quad (12)$$

which is the sum of the heterogeneous reaction $O_2^{gas} = O_2^{melt}$ and the homogeneous reaction $FeO^{melt} + \frac{1}{4}O_2^{melt} = FeO_{1.5}^{melt}$. In calculations involving varying oxidation states of iron, it is preferable to express the ferric component in terms of the $FeO_{1.5}$ component rather than Fe_2O_3 as the total iron content, and thus the mole fractions of other components in the melt become independent of ferric/ferrous ratio. This considerably simplifies the algebra involved in describing mixing properties in iron-bearing systems (Kress and Carmichael, 1988; Lange and Carmichael, 1988). From Eq. (1) we define

$$K \equiv \frac{[a_{FeO_{1.5}}^{melt}]}{[a_{FeO}^{melt}]\cdot[f_{O_2}^{gas}]^{1/4}}, \quad (13)$$

where a represents the activity of the subscripted species in the superscripted phase and K is a function of temperature alone (total pressure is fixed at 1 atmosphere). As a matter of convenience, we adopt the term "bulk composition" to refer to melt composition expressed in terms of silica, lime, and total iron. We will use "ln" to denote the natural logarithm and "log" to represent the base 10 logarithm.

If ferric and ferrous components mix ideally in the melt, then the ferric/ferrous ratio should be independent of bulk composition, and a plot of $FeO_{1.5}/FeO$ against $\ln(f_{O_2})$ at fixed temperature will be linear with a slope of 0.25. Most studies of the iron-oxidation reaction in silicate melts confirm that the ferric/ferrous ratio is not independent of bulk composition. Furthermore, most studies confirm that plots of $\ln(FeO_{1.5}/FeO)$ against $\ln(f_{O_2})$ have slopes that deviate significantly from 0.25 (Hill and Roeder, 1974; O'Horo and Levy, 1978; Sack et al., 1980; Kilinc et al., 1983; Mysen et al., 1984; Dingwell and Virgo, 1987; Kress and Carmichael, 1988). We conclude that the redox behavior of most silicate melts is significantly influenced by nonideal mixing. This nonideality may be described in terms of more-complicated melt components (Kress and Carmichael, 1988), the presence of numerous melt species (Mysen, 1987), or a regular solution with interaction terms between simple oxide components (Lange and Carmichael, 1988).

RESULTS

The broken line in Fig. 1 outlines the range of compositions that we were able to quench completely to a glass. Probe analyses of incompletely quenched samples displayed substantially larger scatter in total iron content than analyses of completely quenched samples. Analyses of samples containing quench crystals also indicated $FeO_{1.5}FeO$ ratios up to an order of magnitude more oxidized than quenched samples equilibrated under similar conditions.

The solid lines in Fig. 2a represent $\ln(FeO_{1.5}FeO)$ contours for completely quenched experiments equilibrated in air at $\sim$ 1360°C. These contours suggest that the iron redox state is approximately independent of total iron content but tends to increase with increasing lime/silica ratio. This behavior contrasts significantly with the compositional trends observed in $Na_2O-FeO_{1.5}-FeO-SiO_2$ liquids (Fig. 2b), where lines of constant

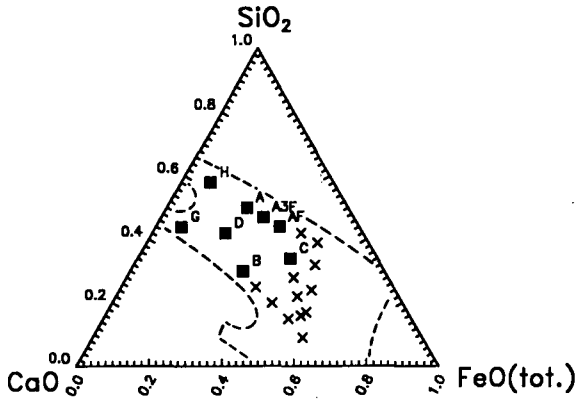

Figure 1. Compositions of starting materials in mol%. The solid line represents the approximate 1500°C liquidus isotherm. The broken line illustrates the boundary of compositions that could be quenched completely to a glass. Solid squares mark quenchable compositions; crosses depict compositions that could not be quenched completely to a glass. [XBL 895-1965]

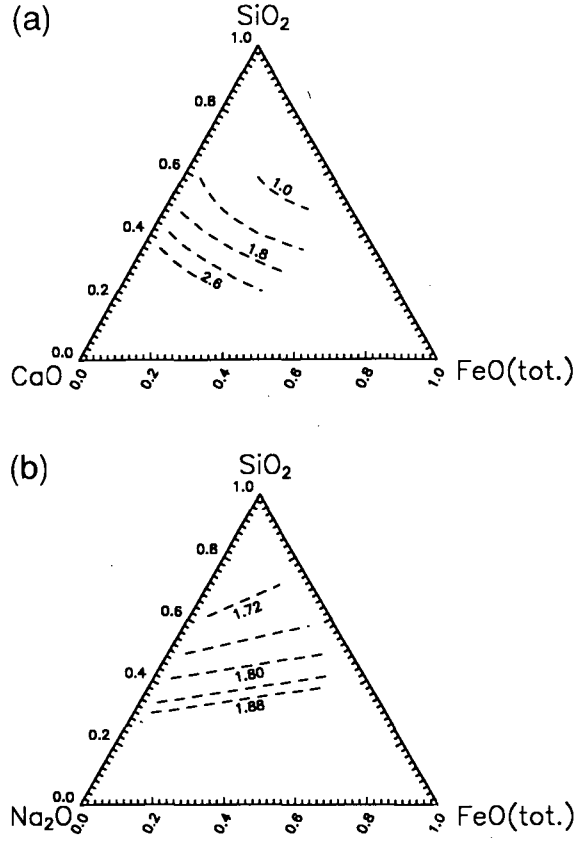

Figure 2. Contours of ln ($FeO_{1.5}$/FeO) equilibrated in air at 1430°C. **(a)** Melts in the $CaO-FeO_{1.5}-FeO-SiO_2$ system from this study. **(b)** Melts in the $Na_2O-FeO_{1.5}-FeO-SiO_2$ system from Lange and Carmichael (1988). [XBL 895-1966]

ln($FeO_{1.5}$/FeO) roughly parallel the soda-silica join (Lange and Carmichael, 1988).

In Fig. 3 ln(FeO/$FeO_{1.5}$) is plotted against ln(f_{O_2}) for one of the compositions studied. A least-squares fit of the data in Fig. 3 yields a slope of 0.21. This is significantly lower than the slope that would be expected if mixing were ideal. These results are consistent with the observations of O'Horo and Levy (1978, recast in terms of $FeO_{1.5}$ component), who also obtained a slope of 0.21 in $SiO_2-FeO_{1.5}-FeO-CaO$ melts. Similar results have been obtained in a wide variety of natural liquid compositions (Hill and Roeder, 1974; Sack et al., 1980; Kilinc et al., 1983; Kress and Carmichael, 1988) where slopes varying between 0.21 and 0.23 have been observed. In contrast, Mysen et al. (1984) measured slopes between 0.24 and 0.35 in $SiO_2-FeO_{1.5}-FeO-CaO$ melts.

DISCUSSION

Equilibrium in Reaction (1) can be expressed as

$$\Delta G = 0 = \Delta H_0 + \int_{Tr}^{T} \Delta Cp dT - T\left[\Delta S_0 + \int_{Tr}^{T} \Delta \frac{Cp}{T} dT\right]$$

$$+ RT\ln(K_D) + RT\ln(K_\gamma), \qquad (14)$$

where ΔG is the Gibbs free energy change of reaction, ΔH_0 and ΔS_0 are the standard-state enthalpy and entropy of reaction, respectively, and ΔCp is the heat capacity of the oxidation reaction. In addition,

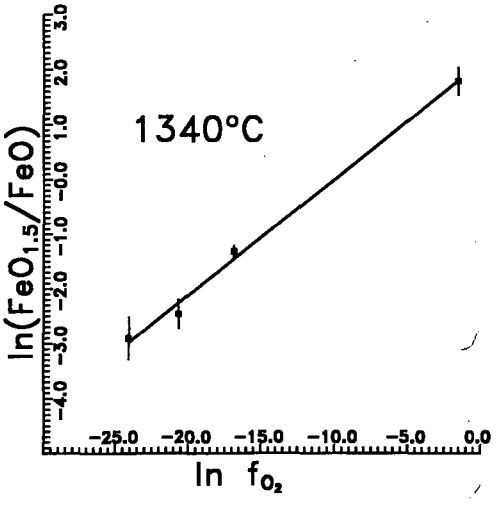

Figure 3. Plot of ln ($FeO_{1.5}$/FeO) against ln(f_{O_2}) for a single bulk composition (composition A) equilibrated at 1340°C. [XBL 895-1967]

we separate the activity of a component i into ideal and excess factors ($a_i \equiv X_i\gamma_i$) and define $K \equiv K_D K_\gamma$, where $K_\gamma = \gamma_{FeO_{1.5}}/\gamma_{FeO}$.

The position and degree of liquid immiscibility in the calcium-ferrisilicate system (Greig, 1927a, 1927b) indicate substantial asymmetric nonideality in the $CaO-FeO_{1.5}-FeO-SiO_2$ system. We choose, therefore, to express the oxidation reaction in lime-iron silicate melts in terms of a simple asymmetric regular-solution model. Using the formalism of Berman and Brown (1984) in a second-order expansion, one can write

$$RT\ln\gamma_m = \sum_{i=1}^{nc-1}\sum_{j=i}^{nc}\sum_{\substack{k=j\\k\neq i}}^{nc} W_{i,j,k}X_iX_jX_k\left[\frac{Q_m}{X_m} - 2\right], \tag{15}$$

where nc represents the number of components in the system and Q_m is a count of the number of i, j, and k indices that are equal to m. To avoid lengthy lists of components, we use the abbreviations si, fc, fs, and ca to denote the components SiO_2, $FeO_{1.5}$, FeO, and CaO, respectively. For the 4-component system considered here, 16 independent parameters must be constrained in order to describe the enthalpy of mixing using this formulation. Thus

$$RT\ln(K_\gamma) = RT\ln(\gamma_{fc}) - RT\ln(\gamma_{fs})$$

$$= \sum_{i=1}^{nc-1}\sum_{j=i}^{nc}\sum_{\substack{k=j\\k\neq i}}^{nc} W_{i,j,k}X_iX_jX_k\left[\frac{Q_{fc}}{X_{fc}} - \frac{Q_{fs}}{X_{fs}}\right]. \tag{16}$$

It can be verified that $RT\ln(K_\gamma)$ is a combination of only 9 parameters that are linearly independent in X. These 9 parameters can be expressed in any of a vast number of combinations of the 16 parameters ($W_{i,j,k}$). It is convenient to combine 14 of the 16 parameters to form the 7 coefficients:

$$\begin{aligned}
\Delta W_{si,si} &= eW_{si,si,fc} - W_{si,si,fs},\\
\Delta W_{si,fc} &\equiv 2W_{si,fc,fc} - W_{si,fc,fs},\\
\Delta W_{si,fs} &\equiv W_{si,fc,fs} - 2W_{si,fs,fs},\\
\Delta W_{si,ca} &\equiv W_{si,fc,ca} - W_{si,fs,ca},\\
\Delta W_{fc,ca} &\equiv 2W_{fc,fc,ca} - W_{fc,fs,ca},\\
\Delta W_{fs,ca} &\equiv W_{fc,fs,ca} - 2W_{fs,fs,ca},\\
\Delta W_{ca,ca} &\equiv W_{fc,ca,ca} - W_{fs,ca,ca},
\end{aligned} \tag{17}$$

which can be combined with Eq. (6), yielding

$$\begin{aligned}
RT\ln(K_\gamma) = {} & \Delta W_{si,si}X_{si}^2 + \Delta W_{si,fc}X_{si}X_{fc}\\
& + \Delta W_{si,fs}X_{si}X_{fs} + \Delta W_{si,ca}X_{si}X_{ca}\\
& + \Delta W_{fc,ca}X_{fc}X_{ca} + \Delta W_{fs,ca}X_{fs}X_{ca}\\
& + \Delta W_{ca,ca}X_{ca}^2 + W_{fc,fc,fs}(2X_{fc}X_{fs} - X_{fc}^2)\\
& + W_{fc,fs,fs}(X_{fs}^2 - 2X_{fc}X_{fs}).
\end{aligned} \tag{18}$$

Ferric/ferrous equilibrium can then be represented by

$$\begin{aligned}
\ln\left(\frac{X_{FeO_{1.5}}}{X_{FeO}}\right) = {} & 0.25\ln(f_{O_2}) - \frac{\Delta H}{RT} + \frac{\Delta S}{R}\\
& - \frac{1}{RT}\Big[\Delta W_{si,si}X_{si}^2 + \Delta W_{si,fc}X_{si}X_{fc}\\
& + \Delta W_{si,fs}X_{si}X_{fs} + \Delta W_{si,ca}X_{si}X_{ca}\\
& + \Delta W_{fc,ca}X_{fc}X_{ca} + \Delta W_{fs,ca}X_{fs}X_{ca}\\
& + \Delta W_{ca,ca}X_{ca}^2 + W_{fc,fc,fs}(2X_{fc}X_{fs} - X_{fc}^2)\\
& + W_{fc,fs,fs}(X_{fs}^2 - 2X_{fc}X_{fs})\Big].
\end{aligned} \tag{19}$$

The terms involving ΔCp are omitted because their contribution is far below the experimental resolution in $\ln(K_D)$ (Kress and Carmichael, 1988; Lange and Carmichael, 1988). Experimental results are used to regress the 11 parameters in Eq. (19) that yield the values presented in Table 1. The final variable values presented in Table 1 reproduce the input values of $\ln(FeO_{1.5}/FeO)$ with a root-mean-squared deviation of 0.06 natural log units. More importantly, the model predicts K values that are all within the estimated 2σ uncertainty in chemical analysis for each of the experiments. Contours of $\ln(FeO_{1.5}/FeO)$ in Fig. 2a are calculated using the parameters in Table 1.

VOLUMES

The derivation of partial molar properties from experimental data requires accurate knowledge of experimental melt composition (Lange and Carmichael, 1988). For this reason, the density determinations of Dingwell and Brearly (1988) were reregressed using a simple ideal-mixing model of the form

$$V = \sum_i\left[\bar{V}_i + \frac{\partial\bar{V}_i}{\partial T}(T-1673K)\right]. \tag{20}$$

Table 1. Parameters for estimation of $FeO_{1.5}/FeO$ equilibrium using Eq. (19).[a]

Variable	Value	Standard error	Units
ΔH	−157.74	0.02	kJ
ΔS	−65.46	0.01	J/K
$\Delta W_{si,si}$	13.17	0.03	kJ
$\Delta W_{si,fc}$	169.01	0.05	kJ
$\Delta W_{si,fs}$	17.29	0.05	kJ
$\Delta W_{si,ca}$	96.46	0.06	kJ
$\Delta W_{fc,ca}$	−18.86	0.04	kJ
$\Delta W_{fs,ca}$	−87.56	0.04	kJ
$\Delta W_{ca,ca}$	−59.66	0.03	kJ
$W_{fc,fc,fs}$	−13.17	0.05	kJ
$W_{fc,fs,fs}$	97.99	0.06	kJ

[a]See text for definition of symbols.

Ferric and ferrous components of the experimental data incorporated in the regression were recalculated using the parameters in Table 1. In order to minimize errors in extrapolation, only compositions with more than 20 wt% silica were considered. Fe_2O_3 rather than $FeO_{1.5}$ was used to represent the ferric component in these regressions in order to facilitate comparison with the results of previous studies. Also included in this regression are the results of 9 density determinations from Mo et al. (1982) in a highly reduced iron-silicate melt. The values obtained from our volume regression are listed in Table 2. The large uncertainty in the individual parameters reflects the fact that the model is significantly underdetermined. The partial molar volume temperature derivatives are particularly poorly constrained by the data. Lange and Carmichael (1987) suggest that $\partial \overline{V}_{SiO_2}/\partial T$ is probably quite small. This value was, therefore, set to zero in the final regression in order to reduce the degree of underdetermination.

The partial molar volumes in Table 2 are all within uncertainty of corresponding values from Lange and Carmichael (1987). This is quite significant in that the values quoted in Lange and Carmichael (1987) are based on a regression of data from a wide variety of silicate liquids including 2- to 9-component compositions. The fact that the values from Dingwell and Brearly (1988) indicate values similar to those regressed by Lange and Carmichael (1987) provides additional evidence that partial molar volumes can be considered independent of composition, within the resolution of the data.

Table 2. Partial molar volumes at 1673 K and their temperature derivatives.

Variable	Value	Standard Error	Units
$\overline{V}_{SiO_2}$	25.68	2.49	cc/mol
$\overline{V}_{Fe_2O_3}$	36.92	5.51	cc/mol
$\overline{V}_{FeO}$	14.71	3.31	cc/mol
$\overline{V}_{CaO}$	18.54	3.24	cc/mol
$\frac{\partial \overline{V}_{SiO_2}}{\partial T}$	0.0	fixed	
$\frac{\partial \overline{V}_{Fe_2O_3}}{\partial T}$	2.28	54.30	10^{-3}cc/(molK)
$\frac{\partial \overline{V}_{FeO}}{\partial T}$	3.40	20.47	10^{-3}cc/(molK)
$\frac{\partial \overline{V}_{CaO}}{\partial T}$	2.23	25.18	10^{-3}cc/(molK)

The linear-volume model presented in Table 2 reproduces the measured volumes from Dingwell and Brearly (1988) and Mo et al. (1982) with a standard error of 0.09 cc/gfw. This value for the standard error of our regression happens to correspond exactly with the experimental uncertainty indicated by Dingwell and Brearly (1988). This result suggests that the large temperature-dependent, volume-mixing terms proposed by Dingwell and Brearly (1988) may merely be an artifact of incorrect partitioning of iron between its ferric and ferrous state in the experimental liquids. If this is the case, then many of the structural interpretations presented by Dingwell and Brearly (1988) concerning coordination changes in the melt must also be regarded with skepticism. The significant enthalpy of mixing in this system hints that excess volume of mixing terms may eventually be justified, but volume measurements are not yet precise enough to resolve such an effect unambiguously.

REFERENCES

Berman, R.G., and Brown, T.H., 1984. A thermodynamic model for multicomponent melts, with application to the system $CaO–Al_2O_3–SiO_2$. Geochim. Cosmochim. Acta, v. 48, p. 661–678.

Dingwell, D.B., and Brearly, M., 1988. Melt densities in the $CaO–FeO–Fe_2O_3–SiO_2$ system and the compositional dependence of the partial molar volume of ferric iron in silicate melts. Geochim. Cosmochim. Acta, v. 52, in press.

Dingwell, D.B., and Virgo, D., 1987. The effect of oxidation state on the viscosity of melts in the system Na_2O–FeO–Fe_2O_3–SiO_2. Geochim. Cosmochim. Acta, v. 51, p. 195–205.

Fudali, R.F., 1965. Oxygen fugacities of basaltic and andesitic magmas. Geochim. Cosmochim. Acta, v. 29, p. 1063–1075.

Greig, J.W., 1927a. Immiscibility in silicate melts: Part I. Am. J. Sci., v. 5, no. 13, p. 1–44.

Greig, J.W., 1927b. Immiscibility in silicate melts: Part II. Am. J. Sci., v. 5, no. 13, p. 133–154.

Hill, R., and Roeder, P., 1974. The crystallization of spinel from basaltic liquids as a function of oxygen fugacity. J. Geol., v. 82, p. 709–729.

Kilinc, A., Carmichael, I.S.E., Rivers, M.L., and Sack, R.O., 1983. The ferric-ferrous ratio of natural silicate liquids equilibrated in air. Contr. Mineral. Petrol., v. 83, p. 136–140.

Kress, V.C., and Carmichael, I.S.E., 1988. Stoichiometry of the iron-oxidation reaction in silicate melts. Am. Mineral., v. 73, p. 1267–1274.

Lange, R., and Carmichael, I.S.E., 1987. Densities of Na_2O–K_2O–CaO–MgO–FeO–Fe_2O_3–Al_2O_3–TiO_2–SiO_2 liquids: New measurements and derived partial molar properties. Geochim. Cosmochim. Acta, v. 51, p. 2931–2946.

Lange, R., and Carmichael, I.S.E., 1988. Ferric-ferrous equilibria in Na_2O–FeO–Fe_2O_3–SiO_2 melts: Effects of analytical techniques on derived partial molar volumes. Submitted to Geochim. Cosmochim. Acta.

Marsh, B.D., 1988. Crystal size distribution (CSD) in rocks and the kinetics and dynamics of crystallization I. Theory. Contrib. Mineral. Petrol., v. 99, p. 277–291.

Martin, D., and Nokes, R., 1988. Crystal settling in a vigorously convecting magma chamber. Nature, v. 332, p. 534–536.

Mo, X., Carmichael, I.S.E., Rivers, M., and Stebbins, J., 1982. The partial molar volume of Fe_2O_3 in multicomponent silicate liquids and the pressure dependence of oxygen fugacity in magmas. Mineral. Mag. v. 45, p. 237–245.

Mysen, B.O., 1987. Magmatic silicate melts: Relations between bulk composition, structure and properties. *In* B.O. Mysen (ed.), Magmatic Processes: Physiochemical Principles. Geochemical Society, University Park, Pennsylvania, p. 375–399.

Mysen, B.O., Virgo, D., and Seifert, F.A., 1984. Redox equilibria of iron in alkaline earth silicate melts: Relationships between melt structure, oxygen fugacity, temperature and properties of iron-bearing silicate liquids. Am. Mineral., v. 69, p. 834–847.

O'Horo, M.P., and Levy, R.A., 1978. Effect of melt atmosphere on the magnetic properties of a $[(SiO_2)_{45}(CaO)_{55}]_{65}[Fe_2O_3]_{35}$ glass. J. Appl. Phys., v. 49, p. 1635–1637.

Sack, R.O., Carmichael, I.S.E., Rivers, M., and Ghiorso, M.S., 1980. Ferric-ferrous equilibria in natural silicate liquids at 1 bar. Contrib. Mineral. Petrol., v. 75, p. 369–376.

Coupling of Precipitation/Dissolution Reactions to Mass Diffusion

C. L. Carnahan

Changes in the sizes of pores or apertures of fractures can alter the effective mass diffusivities and permeabilities of porous or fractured materials (Witherspoon et al., 1980; Coudrain-Ribstein, 1983), and these alterations can affect the subsequent movement of dissolved chemicals. Neglect of these effects not only might produce inaccurate computational results (Pearson, 1985) but might also lead to physically unrealizable consequences, such as the calculated volume of a precipitate exceeding available pore space. The reactive chemical transport simulator THCC (Carnahan, 1987, 1988a; Jacobsen and Carnahan, 1988a,b) has been modified to study effects of precipitation/dissolution reactions on mass diffusion.

MODIFICATION OF THE COMPUTER PROGRAM THCC

The THCC program simulates transport of reactive chemical species by advection and hydrodynamic dispersion or by mass diffusion in one-dimensional or cylindrically symmetric geometry. In THCC, chemical reactions are assumed to be in a state of local equilibrium. The reactions simulated are complexation, oxidation-reduction, ionization of

water in the aqueous phase, reversible precipitation of solid phases, and ion exchange. The THCC program has the capability to simulate systems with temporally and spatially variable fields of temperature and to simulate radioactive decay of selected reactants.

The program was modified by incorporating the variable porosity explicitly in the transport equations solved by the program. The primary unknowns found by the THCC program are the aqueous-phase concentrations of a set of "basis" species and the "concentrations" (mole/dm^3 of porous matrix) of reversibly formed solid phases. This set of unknowns is not increased by the addition of variable porosity. Instead, the porosity (a function of space and time) is treated as a secondary unknown and is calculated from values of the primary unknown set of solid concentrations. A detailed description of the treatment of variable porosity has been given by Carnahan (1988b).

EXAMPLE CALCULATION

This example simulates diffusion of silicic acid into a domain where temperature decreases with increasing distance from the inlet at $x = 0$. The temperature field is steady in time. Quartz precipitates according to the reaction

$$SiO_2(\text{quartz}) + 2H_2O = Si(OH)_4^0(aq),$$

for which the equilibrium constant, K, is given as a function of absolute temperature, T, by (Rimstidt and Barnes, 1980):

$$\log K = 1.881 - \frac{1560.}{T} - 2.028 \times 10^{-3}T.$$

The temperature gradient is -20°C/m, and the temperature at the boundary $x = 0$ is 150°C. The outer boundary is located at $x = 5$ m. Initial porosity in the domain $x \geq 0$ was 0.05, and initial concentrations of silicic acid and quartz were zero. At $x = 0$ the incoming flux of silicic acid is 10^{-4} mole/m^{2}s.

Because quartz exhibits prograde solubility, it precipitates along the decreasing temperature profile within the domain $x \geq 0$. However, significant changes of porosity occur only at the boundary $x = 0$. Figure 1 shows the accumulation of quartz at this boundary at times up to 10^9 s for simulations with variable porosity and constant porosity. In the case of constant porosity the nonphysical result that the volume of precipitated quartz exceeds available pore space is obtained at about 0.45×10^9 s, when the solid concentration exceeds 2.2 moles/dm^3 of

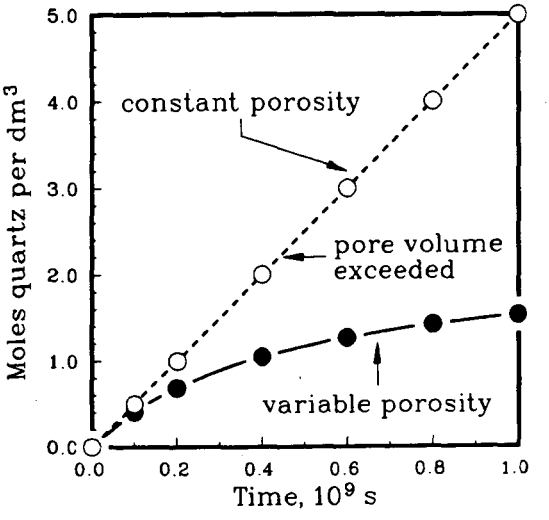

Figure 1. Quartz precipitated at boundary $x = 0$. [XBL 895-1968]

matrix. On the other hand, in the case of variable porosity the concentration of solid increases gradually with time and does not exceed the critical concentration. This is a result of a decreasing influx of silicic acid at the boundary caused by the decreasing porosity there. Moreover, the concentration of precipitated solid at the adjacent node is smaller in the variable-porosity case than in the constant-porosity case for all times, a consequence of reduced effective diffusivity at the boundary. Figure 2 shows the porosity at the boundary $x = 0$ as a function of time for the variable-porosity case. The decline of porosity appears to be exponential in time, approaching the asymptotic value of zero.

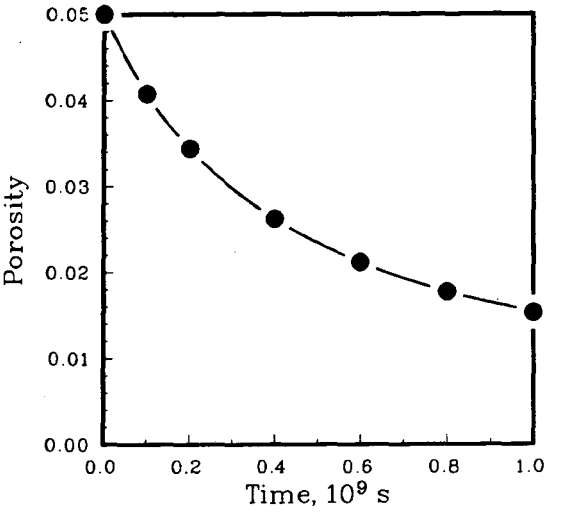

Figure 2. Porosity at boundary $x = 0$ for quartz precipitation. [XBL 895-1969]

DISCUSSION

The ability to account for variations of porosity and mass diffusivity associated with precipitation/dissolution of reactive solids provides a previously absent coupling in the direction from chemical reactions to mass transport. The method used here does not allow precipitated solids to exceed available pore volume.

It is important to note that in systems of the type considered here variations of porosity and mass diffusivity do not affect fluid-phase concentrations of reactants in equilibrium with a reactive solid; only the rate of accumulation of the solid is affected. In the present examples the profiles of fluid-phase concentrations of reactants were identical in the cases with and without porosity variations whenever the reactive solid was present. This is a necessary consequence of the assumption of chemical equilibrium in the precipitation/dissolution process. However, in simulations involving dissolution of a previously precipitated solid and transport of the dissolution products, the limitation imposed by available porosity on quantities of precipitate may have to be considered.

REFERENCES

Carnahan, C.L., 1987. Simulation of uranium transport with variable temperature and oxidation potential: The computer program THCC. *In* J.K. Bates and W.B. Seefeldt (eds.), Scientific Basis for Nuclear Waste Management X. Materials Research Society Symposia Proceedings (Vol. 84). Materials Research Society, Pittsburgh, Pennsylvania, p. 713–721.

Carnahan, C.L., 1988a. Simulation of effects of redox and precipitation on diffusion of uranium solution species in backfill. *In* M.J. Apted and R.E. Westerman (eds.), Scientific Basis for Nuclear Waste Management XI. Materials Research Society Symposia Proceedings (Vol. 112). Materials Research Society, Pittsburgh, Pennsylvania, p. 293–302.

Carnahan, C.L., 1988b. Coupling of precipitation/dissolution reactions to mass diffusion. Presented at the Symposium on Chemical Modeling in Aqueous Systems II, 196th Annual Meeting of American Chemical Society, Division of Geochemistry, Los Angeles, California, September 25–30, 1988. Lawrence Berkeley Laboratory Report LBL-26183.

Coudrain-Ribstein, A., 1983. Docteur-Ingenieur Thesis. L'École Nationale Supérieure de Mines de Paris, 1983.

Jacobsen, J.S., and Carnahan, C.L., 1988a. Numerical simulation of alteration of sodium bentonite by diffusion of ionic groundwater components. *In* M.J. Apted and R.E. Westerman (eds.), Scientific Basis for Nuclear Waste Management XI. Materials Research Society Symposia Proceedings (Vol. 112). Materials Research Society, Pittsburgh, Pennsylvania, p. 415–424.

Jacobsen, J.S., and Carnahan, C.L., 1988b. Numerical simulation of cesium and strontium migration through sodium bentonite altered by cation exchange with groundwater components. Presented at the Twelfth International Symposium on the Scientific Basis for Nuclear Waste Management, Berlin, FRG, October 10–13, 1988.

Pearson, F.J., Jr., 1985. Research needs for coupling geochemical and flow models for nuclear waste isolation. *In* Proceedings, Workshop on Fundamental Geochemistry Needs for Nuclear Waste Isolation, Los Alamos, New Mexico, June 20–22, 1988. US DOE CONF8406134, p. 173–182.

Rimstidt, J.D., and Barnes, H.L., 1980. The kinetics of silica-water reactions. Geochim. Cosmochim. Acta, v. 44, p. 1683–1699.

Witherspoon, P.A., Wang, J.S.Y., Iwai, K., and Gale, J.E., 1980. Validity of cubic law for fluid flow in a deformable rock fracture. Water Resour. Res., v. 16, p. 1016–1024.

Theory and Calculation of Water Distribution in Bentonite in a Thermal Field

C.L. Carnahan

Highly compacted bentonite is under consideration for use as a buffer material in geological repositories for high-level radioactive wastes. To assess the suitability of bentonite for this use, it is necessary to be able to predict the rate and spatial extent of water uptake and water distribution in highly compacted bentonite in the presence of thermal gradients.

The "Buffer Mass Test" (BMT) was conducted by workers in Sweden as part of the Stripa Project (Pusch et al., 1985a,b). The BMT measured uptake and spatial distributions of water infiltrating annuli of compacted MX-80 sodium bentonite heated from within and surrounded by granitic rock; the measurements provided a body of data very valuable for comparison with results of theoretical calculations.

Results of experiments on adsorption of water by highly compacted MX-80 bentonite have been reported by workers in Switzerland (Kahr et al., 1986). The experiments included measurements of an adsorption isotherm and residual heats of immersion. These measurements provide the basis for prediction of water-vapor pressures in equilibrium with bentonite having specified adsorbed-water contents at various temperatures.

To analyze the BMT results, a phenomenological description of the processes influencing movement of water in compacted bentonite in the presence of a variable thermal field was derived. The theory was applied to the bentonite buffer-water system in an assumed steady state of heat and mass transport, using data derived from the experimental work done in Switzerland. Results of the theory were compared with distributions of adsorbed water in buffers observed in the Swedish BMT.

COUPLING BETWEEN HEAT AND MASS FLUXES

The theory relating fluxes of heat and mass to the thermodynamic forces driving the fluxes is based on the thermodynamics of irreversible processes. The complete development has been given by Carnahan (1988). Only the salient features will be given here.

The thermodynamic analysis provides a set of phenomenological equations relating the fluxes of heat, water substance (adsorbed water and water vapor), and air to the forces driving the fluxes. If it is assumed that adsorption of water by bentonite has reached equilibrium, these forces are represented by the gradients of temperature, partial pressure of water vapor, and partial pressure of air. Each flux contains a contribution from each gradient. This implies the possibility that in addition to the usual direct transport processes in which a flux is driven by its conjugate gradient (e.g., heat flux driven by temperature gradient), there exist six coupled processes in which each flux is driven also by seemingly unrelated gradients.

The assumption was made that all gradients are steady in time and that the fluxes of air and water are zero in the steady state. (The heat flux is not zero, but is constant in the steady state.) The BMT results used in the subsequent analysis appear to conform closely to this assumption. Then it is found that in the absence of any coupling among the transport processes, the gradient of the logarithm of partial pressure of water vapor in equilibrium with adsorbed water should be zero at all locations in the bentonite annulus. On the other hand, if coupling is present, the local gradient of the logarithm of the partial pressure of water vapor should be proportional to the local gradient of reciprocal absolute temperature.

MEASUREMENTS OF ADSORPTION OF WATER BY BENTONITE

The Swiss workers have published one adsorption isotherm (at 20°C) for highly compacted MX-80 bentonite, the material used in the BMT. (An adsorption isotherm represents the variation of adsorbed water content as a function of equilibrium partial pressure of water vapor at a constant temperature. Water content is defined as the ratio of mass of adsorbed water to mass of dry bentonite.) They also reported measurements of residual heats of immersion for the same material at 34°C for eight initial values of adsorbed water content.

In the present analysis, the Swiss measurements were used to derive the variation of the isosteric heat of adsorption of water on bentonite as a function of water content at 34°C. Then, assuming the isosteric heat is independent of temperature over the temperature range of interest and using the adsorption isotherm measured at 20°C, an expression was derived

relating the partial pressure of water vapor in equilibrium with adsorbed water to the temperature and water content of bentonite. This relationship, based on experimental data, was vital to the theoretical analysis of the BMT data.

ANALYSIS OF RESULTS OF BUFFER MASS TEST

The Swedish workers have published (Pusch et al., 1985a) graphs of adsorbed water contents, w, and temperatures, T, versus radial distance, r, from the centerline of the heaters measured within two annular bentonite buffers in the BMT: hole 3 after 15 months of heating at 600 W and hole 4 after 10 months of heating at 600 W. For the present analysis, values of w and T were read from the graphs at discrete values of r and the corresponding values of ln $P_v(w,T)$ were calculated. Figure 1 shows graphs of ln P_v against M_w/RT for each experiment, where M_w is the molecular weight of water and R is the universal gas constant. According to the thermodynamic analysis, the slope of such a graph should be zero if no coupling were present. The graphs in Fig. 1 have nonzero slopes (significant at the 95% confidence level) equal to $(-1.45 \pm 0.12) \times 10^6$ kg/J for the experiment in hole 3 and $(-1.78 \pm 0.10) \times 10^6$ kg/J for the experiment in hole 4. These results indicate the possibility of coupling among the processes transporting heat, water, and air in these tests.

The profiles of T and w observed in the two experiments are shown in Fig. 2. Also shown are

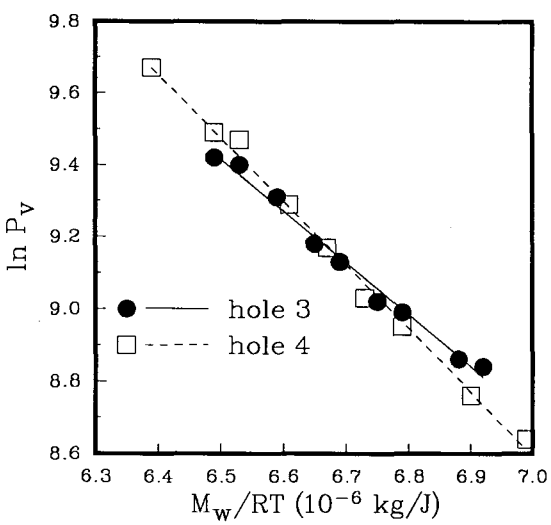

Figure 1. Plot of ln P_v (calculated) versus M_w/RT for BMT experiments in holes 3 and 4. Lines are linear fits to points by least-squares method. [XBL 895-1970]

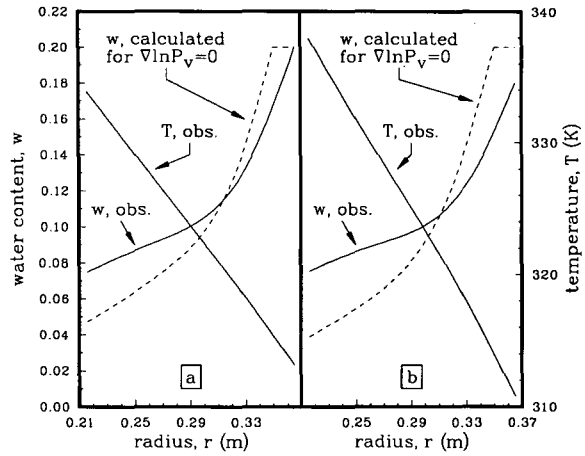

Figure 2. Absolute temperature, T, and water content, w, versus radial distance, r. Solid lines: T, w observed in BMT experiments. Broken lines: w calculated for condition grad(ln P_v) = 0. (a) Hole 3. (b) Hole 4. [XBL 895-1971]

calculated profiles of w for the same T-profiles under the assumption of no coupling (zero gradient of partial pressure of water vapor). The calculated profiles correspond to the same mass of water per unit length of bentonite annulus as the observed profiles. For both cases, the calculated constant value of ln P_v was 9.02, and the calculated adsorbed water content reached the saturation value (w = 0.20) near the outer edges of the bentonite annuli. From these results, it appears that coupling among transport processes may have produced a less-pronounced variation of water content, and hence of swelling pressures, than would be predicted without consideration of coupling.

CONCLUSIONS

The calculations presented here indicate the possibility of coupling among transport processes in the tested bentonite buffers. However, this conclusion must be regarded as tentative, given that the critical experiments were performed by different workers in different laboratories using different samples of the buffer materials. Further experimental work is needed to confirm the existence of coupling in these materials and to determine the dependence on temperature and composition of the phenomenological coefficients for both coupled and direct processes. Measurements of residual heats of immersion at several temperatures would provide data on the temperature variation of the isosteric heat of adsorption and would improve the accuracy of calculated adsorption curves as functions of temperature.

ACKNOWLEDGMENT

Drs. Piet Zuidema and Bernard Knecht of Nagra provided valuable discussions of this problem. This work was supported by the U.S. Department of Energy as part of the DOE/NAGRA Joint Research Project on Flow and Transport in Fractured Media.

REFERENCES

Carnahan, C.L., 1988. Theory and calculation of water distribution in bentonite in a thermal field. Presented at the Twelfth International Symposium on the Scientific Basis for Nuclear Waste Management, Berlin, FRG, October 10–13, 1988. Lawrence Berkeley Laboratory Report LBL-26058.

Kahr, G., Kraehenbuehl, F., Müller-Vonmoos, M., and Stoeckli, H. F., 1986. Wasseraufnahme und Wasserbewegung in hochverdichtetem Bentonit. Nagra Technischer Bericht 86-14, Baden, Switzerland, 40 p.

Pusch, R., Börgesson, L., and Ramqvist, G., 1985a. Final report of the buffer mass test—Volume II: Test results. Stripa Project Technical Report 85-12, Swedish Nuclear Fuel and Waste Management Company (SKB), Stockholm, 195 p.

Pusch R., Nilsson, J., and Ramqvist, G., 1985b. Final report of the buffer mass test—Volume I: Scope, preparative field work, and test arrangement. Stripa Project Technical Report 85-11, Swedish Nuclear Fuel and Waste Management Company (SKB), Stockholm, 190 p.

The Influence of Soluble Surfactants on the Flow of Long Bubbles through a Cylindrical Capillary

G.M. Ginley and C.J. Radke

Foam is a promising fluid for achieving mobility control in underground enhanced oil recovery. Widespread application of this technology to, for example, steam, CO_2, enriched hydrocarbon, or surfactant flooding requires quantitative understanding of foam-flow properties in porous media. Because foam in porous media is a complicated dispersion of gas (or liquid) in an aqueous surfactant phase, the pressure-drop/flow-rate relationship depends critically on the pore-level microstructure or texture (i.e., on the bubble size and/or bubble-size distribution). Foam texture in turn depends on the dynamic interaction of the generation and breakage mechanisms, both of which are strong functions of pore geometry, and surfactant type and concentration.

Numerous visual micromodel studies of foam generated and shaped in oil-free, water-wet porous media with robust stabilizing surfactants show that the bubble size is variable but generally on the order of one to several pore-body volumes. As shown in Fig. 1, the bubbles ride over thin-film cushions of the wetting phase adjacent to the rock surfaces. They are separated from one another by surfactant-stabilized lamellae that terminate in Plateau borders. When flowing, the lamellae move as a contiguous bubble train that snakes through available pores not occupied by the wetting phase.

The foam microstructure depicted in Fig. 1 suggests that important aspects of the hydrodynamic resistance of flowing bubble trains in porous media can be captured in studies of bubbles in capillaries. This work considers the hydrodynamic behavior of a single gas bubble translating in a cylindrical capillary whose radius is smaller than that of the undeformed bubble. The continuous liquid phase contains a surfactant whose concentration is close to or above the critical micelle concentration. Specifically, we extend Bretherton's analysis for a clean gas bubble (Bretherton, 1961) to include the effects of a soluble

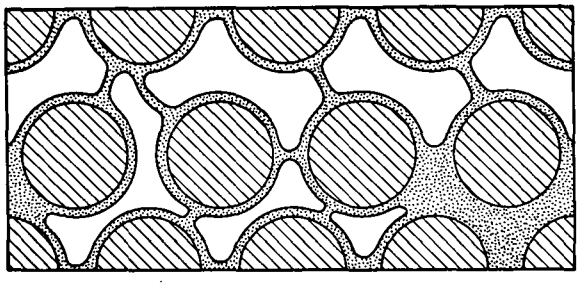

Figure 1. Schematic diagram of the bubble-flow regime in porous media. Open space corresponds to bubbles, dotted space is the aqueous surfactant solution, and cross-hatched areas are sand grains. [XBL 895-1972]

surfactant that is kinetically hindered from attaining local equilibrium at the gas/liquid interface. The shape of the bubble and the resulting pressure drop across the bubble are obtained numerically for small deviations in surfactant adsorption from equilibrium.

PROBLEM STATEMENT

Figure 2 is a schematic diagram of a long bubble flowing in zero gravity through a tube filled with a completely wetting surfactant solution. The reference frame is such that the bubble is stationary, with the walls moving past at a velocity of $-U$. The height of the bubble interface, h, is measured from the tube wall. In this analysis the undistorted bubble radius is always greater than the tube radius, and the bubble is longer than at least twice the tube radius. Consequently, there is a region of constant liquid-film thickness, h_0, in the middle of the bubble, even when surfactants are present. The origin of the axial coordinate, x, is placed near the constant-thickness film, but its exact location is initially unspecified.

The shape of the front and rear menisci change as a result of the resistance to bubble flow. Calculation of this deviation in bubble shape establishes the dynamic pressure drop across the bubble.

The expected surfactant distribution is also portrayed qualitatively in Fig. 2. At low capillary numbers, $Ca = \mu U/\sigma_0$, recirculation eddies in the liquid phase lead to two stagnation rings around the bubble, as shown by the two pairs of heavy black dots on the interface near the tube walls. Near the bubble front, surfactant molecules are swept along the interface and away from the stagnation perimeter. They are not instantaneously replenished from the bulk solution. Accordingly, a surface stress develops along the interface directed from low to high surface tension (i.e., from high to low surfactant adsorption). Surface stresses at the rear stagnation perimeter also occur, but the surfactant now accumulates near the ring, and there is a net flux of surfactant away from the interface. Sufficiently far from the stagnation rings, the surfactant achieves sorption equilibrium, and the surface tension approaches the equilibrium value, σ_0. Thus a stress-free, constant-thickness film underlies the bubble. Equilibrium surface tension in the constant-thickness film portion of the bubble implies that all resistance to flow occurs near the ends. Thus the bubble can be viewed as infinite in length, and the front and back menisci may be treated separately.

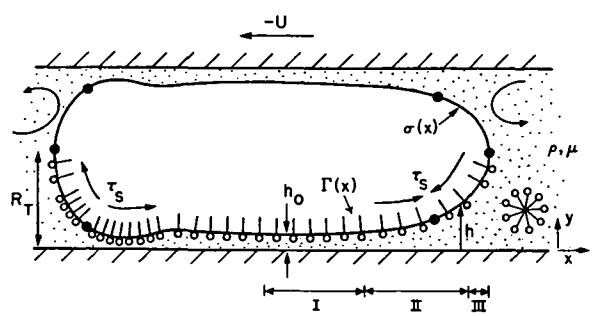

Figure 2. Flow of a single gas bubble through a liquid-filled cylindrical capillary. The liquid contains a soluble surfactant whose distribution along the bubble interface is sketched. [XBL 895-1973]

On examining either end of the bubble, one sees that the interface can be divided into three distinct regions, as shown in Fig. 2. Region I is characterized by a constant film thickness, h_0. In region III, near the tube center, viscous stresses scale by the tube radius and, for small capillary numbers, do not significantly distort the bubble shape from that of a spherical segment. Thus, even though surfactant collects near the front stagnation point (and depletes near the rear stagnation point), the bubble ends are treated as spherical caps at the equilibrium tension, σ_0. Region II provides a transition between the two asymptotic limits. Viscous stresses now scale by the local thickness of the film, h, and the bubble shape varies from the constant-thickness film to the spherical segment. Here the surfactant distribution along the interface may be important. Fortunately, for small capillary numbers, $dh/dx < 1$, and the lubrication approximation may be used throughout. Region II is quantified below.

PROBLEM FORMULATION

The axial velocity profile in region II follows from the lubrication form of the Navier-Stokes equations with the following boundary conditions. The liquid velocity at the tube wall equals $-U$, and the tangential stress at the surfactant-contaminated gas-liquid interface is given by the negative gradient of the surface tension, $-d\sigma/dx$. Pressure in the liquid phase is replaced by a normal stress balance and the Young-Laplace equation, consistent with the lubrication approximation. Finally, macroscopic continuity demands that the average flow rate at any x position along the bubble must equal the flow rate in the constant-thickness thin-film region. Combination of the normal stress balance, the Navier-Stokes equation, and the macroscopic continuity balance results in a third-order differential equation for the position of the bubble interface as a function of x:

$$\frac{h^3}{3\mu}\sigma h_{xxx} + \frac{h^3}{3\mu}\sigma_x h_{xx} + \frac{h^2}{2\mu}\sigma_x - Uh + Uh_0 = 0, \tag{1}$$

where the subscript x denotes differentiation. If $\sigma_x = 0$ (i.e., if $\sigma = \sigma_0$), this relationship reduces to that of Bretherton for a constant-tension bubble. The second term originates from the normal stress balance, and the third term emerges from the shear-stress boundary condition.

A second equation is needed to determine the surface tension as a function of axial position. We adopt the quasistatic assumption that σ is a unique equilibrium function of the surface excess concentration, Γ, even during dynamic events. A surface-species continuity balance dictates how Γ varies along the interface. Upon neglect of surface diffusion and for $h_x < 1$, the steady-state form of this balance is

$$(\Gamma U_s)_x = kc_0\Gamma_{\max}\left[1 - \frac{\Gamma}{\Gamma_0}\right], \tag{2a}$$

where

$$k \equiv k_1/(1 + k_1\Gamma_{\max}/k_m), \tag{2b}$$

and U_s is the bubble surface velocity so that ΓU_s is the convected flux of surfactant along the bubble interface. k_1 is the adsorption rate constant, and k_m is a constant mass-transfer coefficient. At high surfactant concentrations and with slow sorption kinetics, Eq. (2) reduces to the Langmuir kinetic model. For low surfactant concentrations and with slow diffusion rates, Eq. (2) reflects a Nernst constant-diffusion-layer-thickness model.

With the surface-velocity expression known from hydrodynamics, Eq. (2) can be rewritten as

$$\left[\Gamma\left\{\frac{\sigma h^2}{2\mu}h_{xxx} + \frac{h^2}{2\mu}\sigma_x h_{xx} + \frac{h}{\mu}\sigma_x - U\right\}\right]_x = kc_0\Gamma_{\max}\left(1 - \frac{\Gamma}{\Gamma_0}\right). \tag{3}$$

The above expression and the quasistatic adsorption assumption provide the additional information necessary to establish both the bubble profile, $h(x)$ from Eq. (1), and the surfactant distribution, $\Gamma(x)$ from Eq. (3).

To reduce Eqs. (1) and (3) to canonical form we adopt the scaling of Bretherton (1961):

$$\eta \equiv \frac{h}{h_0^{(0)}}, \tag{4a}$$

and

$$\xi \equiv \frac{x}{h_0^{(0)}}\left\{\frac{3\mu U}{\sigma_0}\right\}^{1/3}. \tag{4b}$$

Here, $h_0^{(0)}$ is the constant thin-film thickness obtained by Bretherton for a constant-tension bubble. The value of the surface tension used in the capillary number is the equilibrium value, σ_0. It also proves convenient to express the surface excess concentration as a deviation from equilibrium in the following manner:

$$\theta \equiv \left[\frac{\Gamma}{\Gamma_0} - 1\right](3Ca)^{-2/3}. \tag{5}$$

Finally, the surface tension is expanded about the equilibrium adsorption, Γ_0, and only the first term in the deviation from equilibrium is retained.

These transformations, after elimination of terms that are appropriately higher order in capillary number, yield the following expressions (Ginley, 1987):

$$\eta^3\eta_{\xi\xi\xi} - \frac{3}{2}\alpha\eta^2\theta_\xi - \eta + \eta_0 = 0, \tag{6}$$

and

$$\frac{3}{2}\eta^2\eta_{\xi\xi\xi\xi} + 3\eta\eta_\xi\eta_{\xi\xi\xi} - 3\alpha\eta_\xi\theta_\xi - 3\alpha\eta\theta_{\xi\xi} + \beta\theta = 0, \tag{7}$$

where the subscript ξ refers to differentiation with respect to ξ. Equations (6) and (7) quantify the interface shape and surfactant distribution, respectively, in region II.

Two important parameters, α and β, arise; these depend on the equilibrium and kinetic properties of the surfactant. First, α measures the fractional change in equilibrium surface tension with a fractional change in surfactant adsorption:

$$\alpha \equiv \left[-\frac{d\sigma_0}{d\Gamma_0}\right]\left[\frac{\Gamma_0}{\sigma_0}\right]. \tag{8}$$

It is based on equilibrium properties and is directly related to the Gibbs elasticity. In the present context α gauges how strongly the surface tension depends on the surfactant distribution along the bubble inter-

face. Second, β captures the kinetics of the adsorption process and is defined by

$$\beta \equiv 3P^{(0)} \left[\frac{kc_0\Gamma_{max}}{\Gamma_0} \right] \left[\frac{R_T\mu}{\sigma_0} \right]. \quad (9)$$

Observe that β is a Damköhler number, since it can be interpreted as the ratio of a characteristic contact time for flow in a thin film ($R_T\mu/\sigma_0$), to a characteristic time for adsorption, ($\Gamma_0/[kc_0\Gamma_{max}]$). The constant $P^{(0)} = 0.643$ reflects the curvature of the bubble front for the constant-tension Bretherton analysis.

The ratio of the two parameters, $\alpha/\beta = E$, is also important:

$$E = (-d\sigma_0/d\Gamma_0)\,\Gamma_0^2/(3P^{(0)}\mu R_T kc_0\Gamma_{max}). \quad (10)$$

E is one of several elasticity numbers characterizing the stabilizing effect that adsorbed surfactant molecules have on an interface during mass-transfer processes. Note that E is inversely proportional to the capillary radius, so that the effect of soluble surfactants on the bubble-flow resistance is larger for smaller capillary radii.

To effect an analytical expression for the bubble-flow resistance, we consider fast sorption kinetics or, equivalently, small deviations from equilibrium surfactant coverage, which make β large. Hence a regular perturbation expansion is performed in $1/\beta$ about the constant-tension case. The zero- and first-order differential equations are restated as initial-value problems and solved by a numerical marching technique. Matching to the thin-film region I and the spherical-cap region II provides the necessary boundary conditions. Extensive details on the mathematical and numerical procedures are available elsewhere (Ginley, 1987).

RESULTS

The main results of our first-order regular perturbation analysis are the expressions for the constant thin-film thickness, h_0, and for the total hydrodynamic pressure drop across the entire bubble (front and back), $-\Delta P_B$:

$$h_0/R_T = 1.34\,[1 - 1.56(10^{-2})E]\,Ca^{2/3}, \quad (11)$$

and

$$\frac{(-\Delta P_B)R_T}{\sigma_0} = 9.40\,[1 + 0.469E]\,Ca^{2/3}. \quad (12)$$

The first term in both Eqs. (11) and (12) is the constant surface-tension contribution, and the second term gives the first-order contribution resulting from the presence of a soluble surfactant with finite sorption kinetics. A linear dependence on the surfactant elasticity number arises because only the first-order term in the regular perturbation expansion has been evaluated.

COMPARISON WITH EXPERIMENT

Goldsmith and Mason (1963) have experimentally observed the constant-thickness thin-film region underlying a gas bubble flowing in a tube. They report that its value does not differ significantly upon addition of surfactant to the continuous liquid phase. This is in accord with Eq. (11), demonstrating a very small influence of surfactant on the film thickness.

Figure 3 gives ambient temperature-pressure-drop/flow-rate data for trains of isolated bubbles in precision cylindrical capillaries. A dimensionless pressure drop per bubble is plotted as a function of the capillary number on logarithmic scales. Open triangles are the data of Hirasaki and Lawson (1985) for a 1- wt% aqueous solution of a commercial sodium dodecyl benzene sulfonate (Siponate DS-10) in a 1-mm-diameter tube. Open squares reflect preliminary data of Ginley (1987) for a 1-wt% solution of sodium dodecyl sulfate in a 50-wt% mixture of

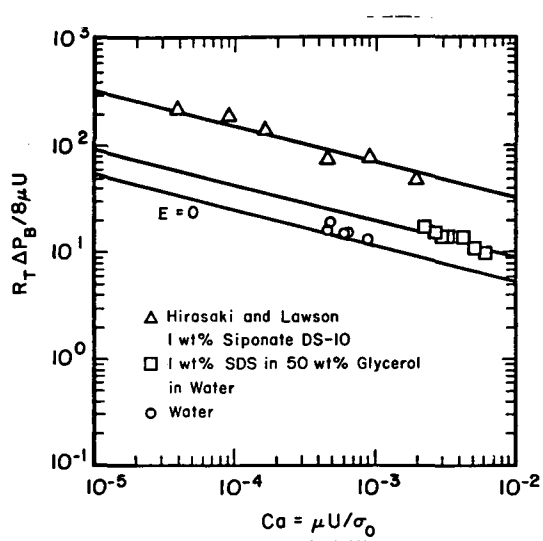

Figure 3. Experimental data of the dimensionless pressure drop per bubble as a function of capillary number for 1- and 2-mm-diameter glass capillaries. The solid line denoted by $E = 0$ gives the theory of Bretherton. [XBL 895-1974]

glycerol and water. The capillary tube diameter is 2 mm, both for these experiments and for those in pure water, shown as open circles. The lowest solid line, labeled $E = 0$, corresponds to the constant-tension theory of Bretherton. The remaining two lines are best fit according to a 2/3 power dependence on the capillary number.

Figure 3 reveals that the few data available for surfactant-laden bubbles do confirm the capillary-number dependence of the proposed theory in Eq. (12). Careful examination of Fig. 3, however, reveals that the regular perturbation analysis carried out to the linear dependence on the elasticity number is not adequate. More significant deviations are evident that cannot be predicted using only the linear term, especially for the SDBS surfactant. Clearly, more data are needed over wide ranges of capillary number and tube radius and for several more surfactant systems. Further, it will be necessary to obtain independent measurements of the surfactant properties that constitute the elasticity number before an adequate test of theory can be made. Finally, it is quite apparent that a more general solution of Eqs. (6) and (7) is needed—one that is not restricted to small deviations of surfactant adsorption from equilibrium.

CONCLUSIONS

The effect of a soluble surfactant on the flow of long bubbles in a cylindrical tube has been quantified for surfactants that exhibit small deviations from equilibrium adsorption. A regular perturbation expansion in large adsorption rates is constructed about the low-capillary-number/singular-perturbation theory of Bretherton. The pressure drop across the bubble increases upon the addition of surfactant, whereas the thin-film thickness decreases slightly. Both the pressure drop and the thin-film thickness retain their 2/3 power dependence on the capillary number found by Bretherton for surfactant-free bubbles. To first order, a linear dependence on the surfactant-elasticity number arises. Comparison of the proposed theory to new and available pressure-drop data for single bubbles immersed in anionic surfactant solutions confirms the $Ca^{2/3}$ prediction but demonstrates that higher-order terms in the elasticity number are required.

ACKNOWLEDGMENT

We thank John Newman for helpful discussions on several mathematical issues.

REFERENCES

Bretherton, F.P., 1961. The motion of long bubbles in tubes. Fluid Mech., v. 10, p. 166–188.

Ginley, G.M., 1987. Flow of surfactant laden bubbles in circular capillaries (M.S. Thesis). University of California, Berkeley.

Goldsmith, H.L., and Mason, S.G., 1963. The flow of suspensions through tubes. II. Single large bubbles. J. Coll. Sci., v. 18, p. 237–261.

Hirasaki, G.J., Lawson, J.B., 1985. Mechanisms of foam flow in porous media: Apparent viscosity in smooth capillaries. Soc. Pet. Eng. J., v. 25, p. 176–190.

Pressure-Induced Brine Migration in Consolidated Salt in a Repository

Y. Hwang, P.L. Chambré, W.W.-L. Lee, and T.H. Pigford

Within a few years after the emplacement of waste packages in a geologic repository for nuclear waste in salt, salt creep is expected to close the air gap between a waste container and the borehole wall (Brandshaug, 1987). In this article we present an analysis of brine migration completely inside consolidated salt, considered here to be a thermoelastic, porous rock.

Salt creep causes consolidation of the crushed salt in the annulus between the waste package and the borehole, resulting in monolithic consolidation of salt around the waste package. Thereafter, except for whatever brine is consumed by container corrosion, the brine in grain boundaries near the waste package can only migrate outward into the surrounding salt under the influence of pressure gradients caused by transient heating of the salt. Hot salt near the waste package expands against the waste package and surrounding salt, resulting in high compressive stresses near the waste package. Grain-boundary brine

expands more than does the salt and further increases the local pressure and pressure gradients that cause brine to flow outward into the cooler salt. Such outward flow of brine relieves the pressure gradient on the fluid, which finally relaxes to near-lithostatic pressure. If the waste containers are corroded, this outward brine movement by pressure difference may become a mechanism for radionuclide transport. To determine the extent to which advection by brine in grain boundaries is an important transport mechanism for released radionuclides, we have estimated the time-dependent migration of brine after salt consolidation.

We consider a spherical-equivalent spent-fuel waste package of 0.72-m radius in an infinite salt medium. The governing equations for brine migration treat salt as a thermoelastic, porous rock, following the equations of McTigue (1986). Chambré has obtained analytic solutions to the governing equations, and numerical illustrations of the solutions are given here. The parameter values used in the calculations are from McTigue and are shown in Table 1. The initial heat flux at the waste-form surface was 928 $W \cdot m^{-2}$. Calculated time-dependent profiles of temperature and brine pressure after consolidation are shown in Figs. 1 and 2.

Table 1. Parameter values used in calculations.

Property	Value	Units
Conductivity (λ)	6.60	$W \cdot m^{-1} \cdot K^{-1}$
Drained bulk modulus (K)	20.7	GPa
Fluid bulk modulus (K_f)	2.0	GPa
Solid bulk moduli (K'_s,K_s'')	23.5	GPa
Shear modulus (G)	12.4	GPa
Porosity (ϕ_o)	0.001	
Permeability (k)	10^{-21}	m^2
Fluid expansivity (α_f)	3.0×10^{-4}	K^{-1}
Solid expansivity (α'_s,α_s'')	1.2×10^{-4}	K^{-1}
Fluid viscosity (μ)	1.0×10^{-3}	$Pa \cdot s$
$\frac{1}{B} = 1 + \phi_o \frac{K(1 - K_f/K_s'')}{K_f(1 - K/K_s')}$	1.075	
Poisson's ratio (ν)	0.25	
Undrained Poisson's ratio (ν_u)	0.27	
b', Eq. (2a)	29.0	$kPa \cdot K^{-1}$
Fluid diffusivity (c)	0.16×10^{-6}	$m^2 \cdot s^{-1}$
Thermal diffusivity (κ)	3.5×10^{-6}	$m^2 \cdot s^{-1}$
$R(\sqrt{c/\kappa})$	0.21	

Source: After McTigue (1986) for the Salado formation, Delaware Basin, New Mexico.

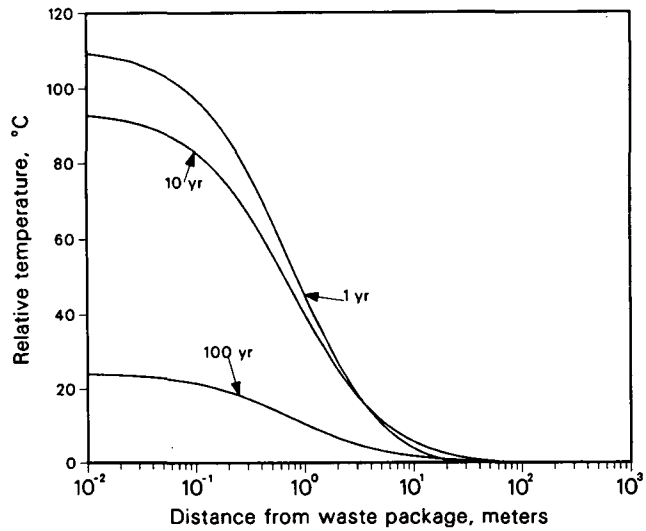

Figure 1. Relative temperature in salt after emplacement. [XBL 895-1975]

Figure 3 shows the Darcy brine velocity near a waste package as a function of time (Hwang et al., 1987). Pressure-induced brine migration within consolidated salt is a transient phenomenon. After about 10 years the velocity is nearly zero. Even the highest velocity is on the order of *millimeters per year* and occurs only within a meter or so of a waste package. At these Darcy velocities molecular diffusion may be the dominant transport process for radionuclides in salt. In a companion paper (Cham-

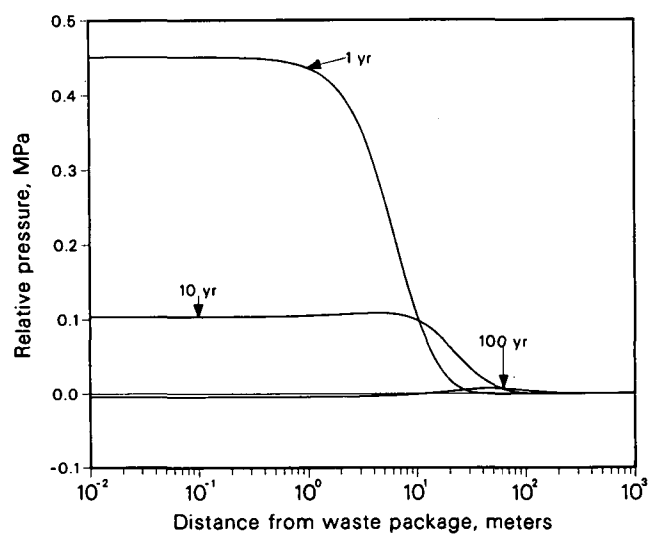

Figure 2. Pressure profile in consolidated salt. [XBL 895-1976]

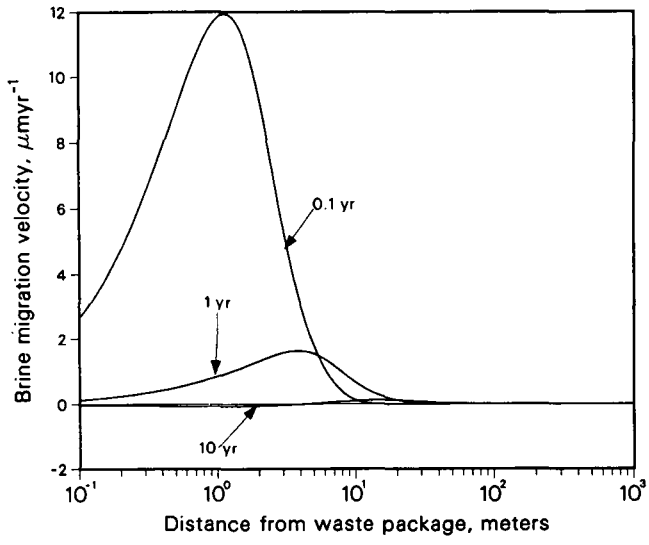

Figure 3. Darcian brine migration velocity in consolidated salt. [XBL 895-1977]

bré et al., 1987) we show the application of diffusional mass transfer to estimating release rates in a salt repository.

REFERENCES

Brandshaug, T., 1987. Estimate of consolidation of crushed salt around a spent fuel waste package. RE/SPEC Report RSI-315.

McTigue, D.F., 1986. Thermoelastic response of fluid-saturated, porous rock. J. Geophys. Res., v. 91, no. B9, p. 9533.

Hwang, Y., Chambré, P.L., Lee W.W.-L., and Pigford, T.H., 1987. Pressure-induced brine migration in consolidated salt in repository. Trans. Am. Nucl. Soc., v. 55, p. 132.

Chambré, P.L., Hwang, Y., Lee, W.W.-L., and Pigford, T.H., 1987. Release rates from waste packages in a salt repository. Trans. Am. Nucl. Soc., v. 55, p. 131.

Numerical Simulation of Cesium and Strontium Migration through Sodium Bentonite Altered by Cation Exchange with Groundwater Components

J.S. Jacobsen and C.L. Carnahan

A mechanism by which fission products present in high-level nuclear waste are sorbed by sodium bentonite is reversible cation exchange. This article describes numerical simulations designed to investigate how spatial and temporal changes in the ion-exchange properties of bentonite affect the migration of $^{135}Cs^{+}$, $^{137}Cs^{+}$, and $^{90}Sr^{2+}$ through compacted, saturated bentonite. Simulations in which fission products compete for exchange sites with ions present in groundwater diffusing into the bentonite are compared with simulations in which the exchange properties of bentonite are constant.

DESCRIPTION OF THE ION-EXCHANGE MODEL USED

Distribution coefficients are commonly used to describe the sorptive character of clay materials such as bentonite. The "K_d approach" suffers from several shortcomings when applied to modeling the migration of cationic fission products. Values of the distribution coefficient depend on the concentration of the species and on the pH and ionic strength of the solution (Apps et al., 1978). In addition, the K_d approach fails to account for the presence of other ions in the solution competing for exchange sites or for the fixed cation-exchange capacity of the bentonite (Cho, 1985).

In this work an ion-exchange model based on the thermodynamic equilibrium constant was used (Jacobsen and Carnahan, 1989). In contrast to the distribution coefficient, the thermodynamic equilibrium constant "is an integral quantity characteristic of the whole isotherm surface and is a true constant depending on temperature only" (Helfferich, 1962).

DESCRIPTION OF THE THCC COMPUTER PROGRAM

The computer program used to perform the simulations is the THCC program developed by Carnahan (1987, 1988). THCC simulates the transport of reactive chemical species in a one-dimensional nonisothermal system and has been used to simulate transport of uranium species under conditions of changing temperature and oxidation potential (Car-

nahan, 1987) and to study the effect of database variations on numerical simulations of uranium migration (Carnahan, 1988).

The chemical reactions included in THCC are aqueous complexation, ionization of water, oxidation-reduction, and precipitation-dissolution. They have been incorporated into the program using the "one-step" method. Before performing the simulations reported in this work, ion-exchange reactions and radioactive decay were added to THCC. Ion-exchange reactions were incorporated in such a way as to avoid increasing the number of unknowns that must be solved for (Jacobsen and Carnahan, 1988, 1989).

INITIAL AND OUTER BOUNDARY CONDITIONS AND CHEMICAL DATA

The initial conditions for the simulations consisted of specifying the composition of the pore water in the bentonite and the concentrations of species sorbed by ion exchange. Using the equilibrium routine in THCC, a solution containing major components of a Swiss reference groundwater was numerically equilibrated with a compacted bentonite having a specified cation-exchange capacity (Jacobsen and Carnahan, 1989).

The formation constants for the complexes and the solubility-product constant for calcite were taken from data tabulated by Benson and Teague (1980). The exchange constants for ion-exchange reactions involving K^+, Ca^{2+}, and Mg^{2+} were derived from exchange constants determined by Wanner (1986) and Jacobsen and Carnahan (1988). Exchange constants for Cs^+ and Sr^{2+} were taken from data compiled by Bruggenwert and Kamphorst (1982).

PROBLEM GEOMETRY AND INNER BOUNDARY CONDITIONS

To simplify the problem geometry, an infinite cylinder was used to approximate a series of waste canisters emplaced horizontally in a circular drift. The cylinder is surrounded by an annulus of compacted, saturated bentonite. At the inner boundary, flux boundary conditions were imposed for all species: zero fluxes for the groundwater species and time-dependent fluxes for the fission products. For each fission product, the time-dependent flux incorporates the initial mass and decay constant of the fission product and the rate of dissolution of the waste form. The rate of dissolution was assumed to be constant (McKinley, 1985).

RESULTS OF NUMERICAL SIMULATIONS

Migration of $^{135}Cs^+$, $^{137}Cs^+$, and $^{90}Sr^{2+}$ through compacted sodium bentonite was simulated under three sets of conditions, denoted below and in the figures by (a), (b), and (c). In case (a), no chemical reactions were included; in case (b), ion-exchange reactions between the fission products and a pure sodium bentonite were included; in case (c), the ion-exchange reactions in (b) were included, as were ion-exchange reactions between the bentonite and constituents, in the inwardly diffusing groundwater, aqueous complexation reactions among the groundwater constituents, and dissolution of calcite present in the bentonite. In all cases, the transport mechanism was diffusion. An additional assumption made was that the waste canister fails immediately upon emplacement.

Figure 1 shows the concentration of $^{137}Cs^+$ in the bentonite at a simulation time of 100 years. The concentration profile for case (a) exceeds that for the other two cases because the migration of $^{137}Cs^+$ has not been retarded by sorption by ion exchange. Whereas the concentrations for case (a) decrease by less than an order of magnitude in 0.7 m, the concentrations for cases (b) and (c) decrease by nearly five orders of magnitude. Curve (b) shows more retardation than curve (c). The concentration profiles for $^{90}Sr^{2+}$ at a simulation time of 100 years are similar to those for $^{137}Cs^+$, shown in Fig. 1. Because the exchange coefficient of Sr^{2+} is smaller than that of Cs^+, the difference between cases (a) and (c) is not as large for $^{90}Sr^{2+}$ as that for $^{137}Cs^+$.

Figure 2 shows the concentration profiles for $^{135}Cs^+$ at a simulation time of 1000 years. Concentration profiles for $^{90}Sr^{2+}$ and $^{137}Cs^+$ (not shown) for

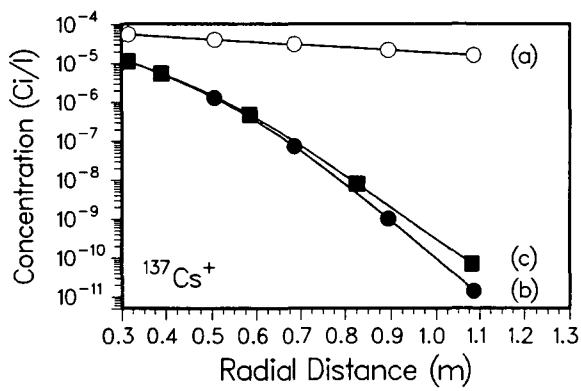

Figure 1. Concentration of $^{137}Cs^+$ at a simulation time of 100 years. See text for explanation of curves shown. [XBL 889-3431]

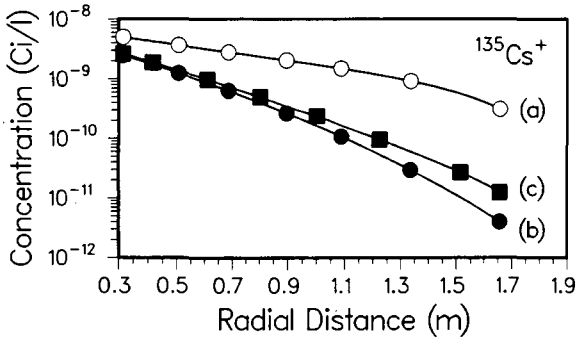

Figure 2. Concentration of $^{135}Cs^+$ at a simulation time of 1000 years. See text for explanation of curves shown. [XBL 889-3428]

the three cases resemble those for $^{135}Cs^+$, but because of radioactive decay, the concentrations of the two short-lived fission products have significantly decreased. The trends in Fig. 2 are similar to those shown in Fig. 1, but the differences between curves (a) and (c), though significant, are not as large.

At a simulation time of 100 years, the ratio of sorbed-phase to fluid-phase concentration for all three fission products is constant for the range of data plotted in Fig. 1. At a simulation time of 1000 years, however, the ratio of sorbed-phase to fluid-phase concentration for case (c) decreases with distance from the inner boundary because of the inward diffusion of the groundwater ions and the resulting increase in competition for ion-exchange sites.

SUMMARY

As groundwater diffuses through sodium bentonite, the ion-exchange properties of the bentonite will change as ion exchange takes place between Na^+ and cations present in the groundwater. The numerical simulations described previously show that neglecting the spatial and temporal variations in the ion-exchange properties of bentonite results in overpredicting the amounts of $^{135}Cs^+$, $^{137}Cs^+$, and $^{90}Sr^{2+}$ sorbed by bentonite. When competition for exchange sites between the groundwater cations and fission products is accounted for, the ratio of the sorbed-phase to fluid-phase concentration of the fission products is not constant but varies spatially and temporally.

ACKNOWLEDGMENTS

The authors would like to thank Piet Zuidema for discussions concerning this work. This work was supported by the U.S. Department of Energy as part of the DOE/NAGRA Joint Research Project on Flow and Transport in Fractured Media.

REFERENCES

Apps, J.A., Cook, N.G.W., and Witherspoon, P.A., 1978. An appraisal of underground radioactive waste-disposal in argillaceous and crystalline rocks—Some geochemical, geomechanical and hydrogeological questions. Lawrence Berkeley Laboratory Report LBL-7047, 50 p.

Benson L.V., and Teague, L.S., 1980. A tabulation of thermodynamic data for chemical reactions involving 58 elements common to radioactive-waste package systems. Lawrence Berkeley Laboratory Report LBL-11448, 97 p.

Bruggenwert, M.G.M., and Kamphorst, A., 1982. Survey of experimental information on cation exchange in soil systems. *In* G.H. Bolt (ed.), Soil Chemistry, B. Physico-chemical Models. Elsevier, Amsterdam, Netherlands, p. 141–203.

Carnahan, C.L., 1987. Simulation of uranium transport with variable temperature and oxidation potential: The computer program THCC. *In* J.K. Bates and W.B. Seefeldt (eds.), Scientific Basis for Nuclear Waste Management X. Materials Research Society Symposia Proceedings (Vol. 84). Materials Research Society, Pittsburgh, Pennsylvania, p. 713–721.

Carnahan, C.L., 1988. Some effects of data base variations on numerical simulations of uranium migration. Radiochimica Acta, v. 44/45, p. 349–354.

Cho, C.M., 1985. Ionic transport in soil with ion-exchange reactions. Soil Sci. Soc. Am. J., v. 49, p. 1379–1386.

Helfferich, F., 1962. Ion Exchange. McGraw-Hill, New York, 624 p.

Jacobsen, J.S., and Carnahan, C.L., 1988. Numerical simulation of alteration of sodium bentonite by diffusion of ionic groundwater components. *In* M.J. Apted and R.E. Westerman (eds.), Scientific Basis for Nuclear Waste Management XI. Materials Research Society Symposia Proceedings (Vol. 112). Materials Research Society, Pittsburgh, Pennsylvania, p. 415–424.

Jacobsen, J.S., and Carnahan C.L., 1989. Numerical simulation of cesium and strontium migration through sodium bentonite altered by cation exchange with groundwater components. *In* W. Lutze and R.C. Ewing (eds.), Scientific Basis for Nuclear Waste Management XII. Materials Research Society Symposia Proceedings (Vol.

127). Materials Research Society, Pittsburgh, Pennsylvania, p. 749–754.
McKinley, I.G., 1985. The geochemistry of the near field. NAGRA Technical Report 84–48, Baden, 94 p.
Wanner, H., 1986. Modelling interaction of deep groundwaters with bentonite and radionuclide speciation. NAGRA Technical Report 86–21, Baden, 103 p.

Release Rates of Soluble Species at Yucca Mountain: A Preliminary Mass-Transfer Analysis

W.W.-L. Lee, T.H. Pigford, and P.L. Chambré

To determine compliance with the release-rate criterion established by the U.S. Nuclear Regulatory Commission (U.S. NRC, 1983) for the engineered barrier system, the Yucca Mountain Project plans to analyze a bounding case that can be summarized as an abundant-water-and-bare-waste case (U.S. DOE, 1988). This article summarizes some preliminary results obtained by using mass-transfer analysis to predict the fractional release rates of soluble species such as ^{135}Cs, ^{129}I, and ^{99}Tc.

ANALYSIS

For species that dissolve readily in water, we assume that a specified amount dissolves instantaneously into a water-filled gap or void space in contact with the porous rock. Linear geometry is used. The dissolved species migrate into the porous material under the influence of a concentration gradient. It is expected that advective transport in the pore liquid will be relatively small, so that the governing equation for this migration is

$$K\frac{\partial N(x,t)}{\partial t} = D\frac{\partial^2 N(x,R)}{\partial x^2} - \lambda K N(x,t), \quad x > a, t > 0, \quad (1)$$

where $N(x,t)$ is the species concentration in the pore liquid, K is the retardation coefficient, and D is the diffusion coefficient. The initial and boundary conditions are

$$N(x,0) = 0, \quad x > a, \quad (2)$$

$$N(x,0) = c(t), \quad t \geq 0, \quad (3)$$

$$N(\infty,t) = 0, \quad t \geq 0, \quad (4)$$

where a is the interface between the void space and rock and $c(t)$ is the time-dependent of the soluble species in the water in the gap or void water. Because this void space is small, we assume that it is well mixed and that $c(t)$ is not position-dependent. To solve for $c(t)$, the mass balance in the void is

$$V\frac{dc(t)}{dt} = \dot{m}_f(t) - \dot{m}(t) - \lambda V c(t), \quad t \geq 0, \quad (5)$$

where $\dot{m}_f(t)$ is the mass rate of dissolution of the species from the waste form into the void water, $\dot{m}$ is the mass rate of diffusion into the rock, and V is the volume of the void water. To solve (5), we use the initial condition

$$c(0) = c^o,$$

where c^o is the initial concentration of the species in the void water. The solution below was obtained by Chambré.

$$c(t) = c^o e^{-\lambda t} F(\beta^2 t) + \frac{1}{V}\int_0^t \dot{m}_f(t-\tau) e^{-\lambda\tau} F(\beta^2\tau) d\tau, \quad t > 0, \quad (6)$$

where $F(\beta^2 t) \equiv e^{\beta^2}\mathrm{erfc}\sqrt{\beta^2 t}$ and $\beta \equiv \sqrt{DK\epsilon^2/a^2}$. The mass rate of diffusion of the dissolved species into the tuff is

$$\dot{m}(t) = -SD\epsilon\frac{\partial N(a,t)}{\partial x}, \quad t > 0, \quad (7)$$

where S is the surface area of the interface between

the void space and the tuff. If the void water extends from $x = 0$ to $x = a$ then $S \equiv V/a$. Using (6) the solution to (7) is

$$\dot{m}(t) = N^o \beta V e^{-\lambda t} \left\{ \frac{1}{\sqrt{\pi t}} - \beta F(\beta^2 t) \right\}$$

$$+ \beta \int_0^t \dot{m}_f(t - \tau) e^{-\lambda \tau} \left\{ \frac{1}{\sqrt{\pi \tau}} - \beta F(\beta^2 \tau) \right\} d\tau,$$

$$t > 0. \quad (8)$$

The fractional release rate of a soluble species whose initial inventory is M_o, denoted f', is

$$f'(t) = \frac{N^o \beta V e^{-\lambda t}}{M_o} \left\{ \frac{1}{\sqrt{\pi t}} - \beta F(\beta^2 t) \right\}$$

$$+ \beta \int_0^t \dot{m}_f(t - \tau) e^{-\lambda \tau} \left\{ \frac{1}{\sqrt{\pi \tau}} - \beta F(\beta^2 \tau) \right\} d\tau,$$

$$t > 0. \quad (9)$$

Equation (9) is used to compute fractional release rates for soluble species. The initial concentration c^o can be calculated by specifying the void-water volume and the amount of the species in the waste that is available for rapid dissolution when water fills the void space.

NUMERICAL ILLUSTRATIONS

We illustrate the above analytic results using conditions typical of a nuclear waste repository at Yucca Mountain. Our reference-waste-package is reference waste package design No. 4 (three spent-fuel assemblies from pressurized water reactor), as shown on p. 7–28 of the SCP-CD (U.S. DOE, 1988). The fuel assemblies are assumed to be Westinghouse 17 by 17 STD, and the dimensions of the fuel assembly are obtained from p. 2A-343 of DOE/RW-0184 (U.S. DOE, 1987). The inventory of various nuclides as a function of time is also taken from the official OCRWM data source, DOE/RW-0184. Table 1 lists dimensions of the waste package. Table 2 lists assumed properties of the tuff. Table 3 lists characteristics of the nuclides used in the calculations. The retardation coefficient for cesium was calculated from the sorption ratios in column tests,

Table 1. Waste package dimensions; spent fuel from pressurized water reactors.

Parameters	Dimensions
Height	4.76 m
Radius	0.33 m
Thickness of gap	0.15 m
Volume of gap	1.5 m^3

Table 2. Tuff properties.

Diffusion coefficient	10^{-6} $cm^2 \cdot s^{-1}$
Porosity	0.14

reported in Chapter 4 of the SCP-CD (U.S. DOE, 1988). The porosity value is taken from the Reference Waste Package Environment report by Glassley (1986).

We assume that 1%, 10%, or 100% of the initial inventories of these soluble species has been released to the fuel-cladding gap, gas plenum, and grain boundaries during reactor operation and dissolve immediately when water fills the voids in the waste package. For these calculations the slower dissolution from the fuel matrix is neglected. Effects of temperature changes on the diffusion coefficient are also neglected.

RESULTS

In Figs. 1 to 4 we show the calculated fractional release rates of ^{135}Cs, ^{129}I, and ^{99}Tc to the surrounding tuff as a function of time since the beginning of dissolution. Here the fractional-release rate of a species is obtained by calculating the mass-release rate and dividing by the 1000-year inventory of that species. Also shown in the figures are the U.S. NRC

Table 3. Characteristics of the nuclides studied.

Characteristics	^{135}Cs	^{129}I	^{99}Tc
Retardation coefficient	9200	1	1
Decay constant (a^{-1})	2.3×10^{-7}	4.1×10^{-8}	3.3×10^{-6}
Calculated USNRC release rate limit (a^{-1})	5.0×10^{-5}	5.5×10^{-4}	1.0×10^{-5}

release rate limit for ^{99}Tc (U.S. NRC, 1983) and the calculated release rate limits for ^{135}Cs and ^{129}I.

The fractional-release-rate curves for ^{135}Cs (Fig. 1) begin at a higher fractional release and greater negative slope than those for ^{99}Tc and ^{129}I because of the greater sorption of cesium in the surrounding tuff. The higher early release rate of cesium depletes the inventory of soluble cesium in the void water and, after a few years, results in a lower fractional release rate for cesium than for technicium and iodine. If the readily soluble fraction of cesium is only a few percent, the calculated release limit for ^{135}Cs is exceeded only for a few years, assuming that all waste packages fail at the same time. A distribution of container failures over several decades can result in a repository-average fractional release rate of cesium below the calculated limit for soluble fractions of a few percent.

For the same readily soluble fractional inventory, the fractional-release-rate curves for ^{99}Tc and ^{129}I (Figs. 2 and 3) are identical for times up to about 100,000 years, because both species are assumed to be nonsorbing. At later times, the fractional release rates for ^{99}Tc become smaller because of its shorter half-life. For soluble fractions of a few percent, the release-rate limit for ^{99}Tc is exceeded for several hundred years if all containers fail simultaneously. Container failures distributed over about a thousand years could result in a repository-average fractional release rate below the regulatory limit. The calculated release-rate limit for ^{129}I is lower than the limit for ^{99}Tc because ^{129}I falls within the regulatory

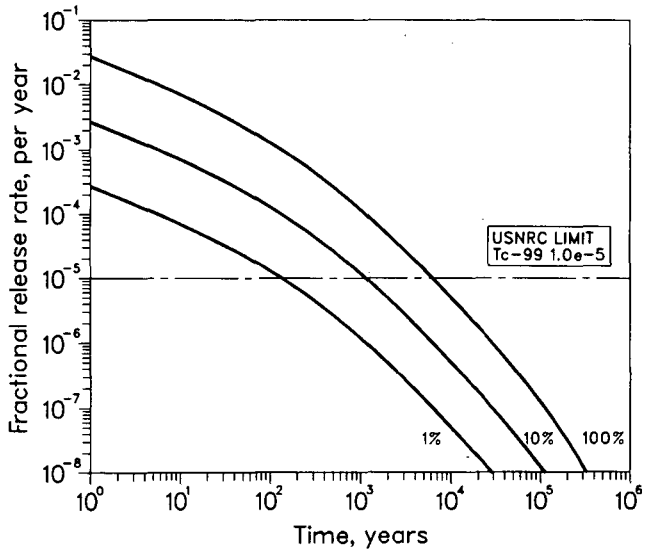

Figure 2. Fractional-release rates of ^{99}. [XBL 895-1979]

category for a "low-inventory" species. If the readily soluble fraction is only a few percent for iodine, the calculated limit is not exceeded, even if all containers fail at initial emplacement.

Figure 4 shows what the fractional release rates of all three soluble species would be if 1% of the inventory of each one was dissolved at t = 0. Even if all the inventory of cesium and iodine were readily soluble, the calculated fractional-release rates would fall below the calculated limits if the container failures were distributed over about a thousand

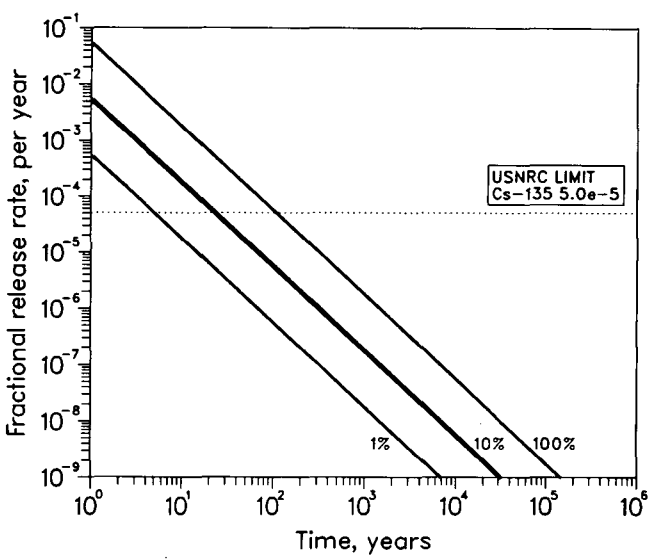

Figure 1. Fractional-release rates of ^{135}Cs. [XBL 895-1978]

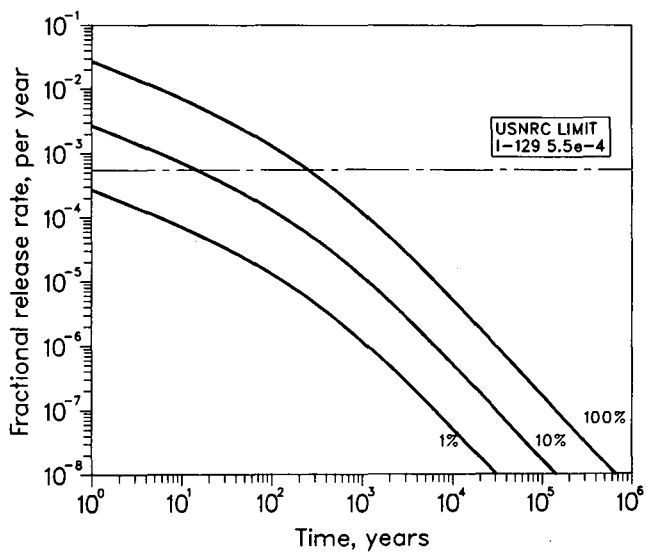

Figure 3. Fractional-release rates of ^{129}I. [XBL 895-1980]

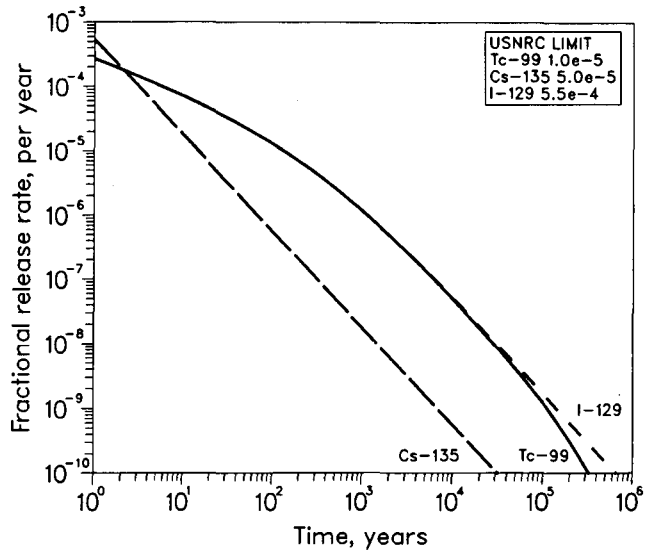

Figure 4. Fractional-release rates of soluble species; 1% of inventory dissolves at $t = 0$. [XBL 895-1981]

years. These calculations are from a bounding analysis that conservatively assumes bare spent fuel, with water in waste-package voids and in contact with saturated porous rock. Because the container, fuel cladding, and corrosion products can still present diffusion barriers after the containers and cladding fail, the more realistic release rates are expected to be less than those calculated here. Calculations of the effects of these additional barriers are in progress.

REFERENCES

Glassley, W.E., 1986. Reference waste package environment report. Lawrence Livermore National Laboratory Report UCRL-53726.

U.S. Department of Energy, 1987. Characteristics of spent fuel, high-level waste, and other radioactive wastes which may require long-term isolation. DOE/RW-0184.

U.S. Department of Energy, 1988. Site characterization plan, Yucca Mountain site. DOE/RW-0160.

U.S. Nuclear Regulatory Commission, 1983. Disposal of high-level radioactive wastes in geologic repositories. Code of Federal Regulations, Title 10, Part 60.113(a)(1)(ii)(B).

The Effect of a Stationary Precipitation Front on Nuclide Dissolution and Transport: Analytic Solutions

W.B. Light, P.L. Chambré, W.W.-L. Lee, and T.H. Pigford

Waste material in a geologic repository will dissolve and migrate away. For many waste components, this process will be limited by the solubility of the waste matrix and species involved. In this article we deal with a single contaminant species and analyze the effect of a precipitation front caused by a discontinuity in the solubility of the contaminant at some distance from the waste package. The precipitation front may be due to local geochemical changes— e.g., changes in temperature, pH, or redox potential—caused by nearby geologic features or the waste itself. In contrast with other work on precipitation fronts (Garisto, 1986; Garisto and Garisto, 1986a,b; Garisto et al., 1986), we provide analytic solutions to the problem of precipitation at a stationary front. Numerical illustrations of these solutions are also presented.

ANALYSIS

A spherical waste solid of radius r_o is embedded in an infinite water-saturated porous medium. There is no contaminant in the porous medium when dissolution begins at time $t = 0$, and direct contact is assumed between the waste and the porous medium (no container or other barriers). The solubility discontinuity, or so-called precipitation front, is assumed to be a concentric spherical shell of radius r_p surrounding the waste package (Fig. 1). The dissolution rate at the waste surface is governed by a solid-liquid reaction-rate law, with the maximum rate occurring when there is no contaminant in the pore water and the minimum rate, zero, approached only as the contaminant concentration in the pore water approaches the solubility at the waste surface.

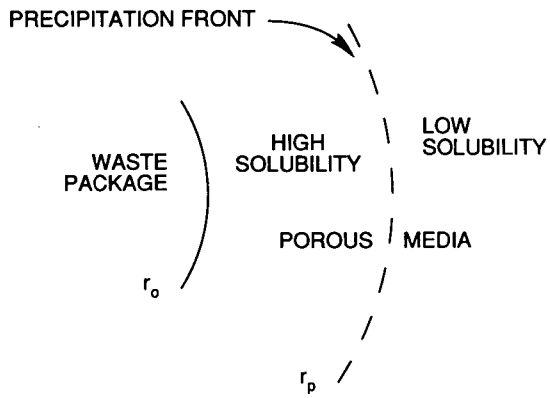

Figure 1. The stationary precipitation front. [XBL 895-1982]

In the limit that the reaction rate goes to infinity, this law reduces to a constant-concentration boundary condition.

Transport in the porous medium is by fluid-phase diffusion only, with no advection. Retardation of the contaminant in the porous medium is treated by equilibrium sorption.

The precipitation front is assumed to be at a known, fixed location. Inside the spherical front and near the waste package, the solubility of the contaminant, C_0, is high. Outside the front and farther away from the waste, the reduced solubility, C_r, is lower. This creates the possibility that some of the contaminant being released from the waste will precipitate at the front and become immobilized. At early times, when the concentration is below the solubility limits at the front location, the front is transparent to the transport process. The domain from the waste surface to infinity is then treated as a single homogeneous region, and we have

$$\frac{\partial C_1}{\partial t} = \frac{D}{K}\nabla^2 C_1, \quad \begin{matrix} r_o < r < \infty, \\ 0 < t < t_p. \end{matrix} \tag{1}$$

where $C_1(r,t)$ is the fluid-phase contaminant concentration for $0 < t < t_p$, D is the contaminant diffusion coefficient in the pore fluid, and t_p is the time at which the solubility limit is reached and precipitation begins. The initial concentration and the concentration at infinity are both assumed to be zero:

$$C_1(r,0) = 0, \quad r_o < r < \infty, \tag{2}$$

$$C_1(\infty,t) = 0, \quad 0 < t < t_p. \tag{3}$$

The reaction-rate-controlled dissolution rate at the waste surface as a function of concentration is

$$-\epsilon D\frac{\partial C_1}{\partial r}\bigg|_{r=r_o} = j_o\left(1 - \frac{C_1}{C_0}\right)\bigg|_{r=r_o},$$

$$0 < t < t_p, \tag{4}$$

where ϵ is the porosity and j_o is the forward dissolution reaction rate (assumed constant). To determine the precipitation time, t_p, we first solve Eqs. (1)–(4). The contaminant concentration predicted by Eqs. (1)–(4) increases steadily with time and monotonically decreases with distance from the waste. The concentration may not reach the solubility limit anywhere, but if it does it will occur first at the front location, r_p, and we can then determine t_p implicitly from

$$C_1(r_p,t_p) = C_r. \tag{5}$$

At time $t = t_p$, when precipitation begins, the governing Eq. (1) is no longer valid at the front so we divide the domain into two regions, one inside the front and the other outside the front. For the inner region,

$$\frac{\partial C_2}{\partial t} = \frac{D}{K}\nabla^2 C_2, \quad \begin{matrix} r_o < r < r_p, \\ t_p < t < \infty. \end{matrix} \tag{6}$$

where $C_2(r,t)$ is the contaminant concentration for $r_o < r < r_p$ and $t_p < t < \infty$. The initial condition for this problem is given by C_1 evaluated at $t = t_p$:

$$C_2(r,t_p) = C_1(r,t_p), \quad r_o < r < r_p. \tag{7}$$

The boundary condition at the waste surface is the reaction-rate law as before, with C_2 replacing C_1:

$$-\epsilon D\frac{\partial C_2}{\partial r}\bigg|_{r=r_o} = j_o\left(1 - \frac{C_2}{C_0}\right)\bigg|_{r=r_o},$$

$$t_p < t < \infty. \tag{8}$$

At the new boundary, $r = r_p$, we fix the concentration at the reduced solubility limit C_r:

$$C_2(r_p,t) = C_r, \quad t_p < t < \infty. \tag{9}$$

This is a result of (a) the physical requirement that the concentration be continuous across the front and (b) the fact that we are (somewhat artificially) fixing the concentration at the C_r limit in the region $r_p < r < \infty$. In reality, the front would extend over

some nonzero transition thickness without well-defined boundaries. We assume instead an abrupt discontinuity and also neglect any effects that the accumulating precipitate might have on the transport process, such as filling the pores or moving as a colloid.

The region outside the precipitation front is treated similarly, with the governing equation given by

$$\frac{\partial C_3}{\partial t} = \frac{D}{K}\nabla^2 C_3, \quad \begin{matrix} r_p < r < \infty, \\ t_p < t < \infty. \end{matrix} \tag{10}$$

with the side conditions

$$C_3(r,t_p) = C_1(r,t_p), \quad r_p < r < \infty, \tag{11}$$

$$C_3(r_p,t) = C_r, \quad t_p < t < \infty, \tag{12}$$

$$C_3(\infty,t) = 0, \quad t_p < t < \infty. \tag{13}$$

The solution to Eqs. (1)–(4) is

$$C_1(\rho,\tau) = \frac{C_0}{\sigma\rho}\operatorname{erfc}\left(\frac{\rho-1}{2\sqrt{\tau}}\right)$$

$$-\frac{C_0}{\sigma\rho}\exp\left(\sigma\alpha(\rho-1)+\sigma^2\alpha^2\tau\right)$$

$$\times \operatorname{erfc}\left(\frac{\rho-1}{2\sqrt{\tau}}+\sigma\alpha\sqrt{\tau}\right), \quad \begin{matrix} 1 < \rho < \infty, \\ 0 < \tau < \tau_p. \end{matrix} \tag{14}$$

with the dimensionless parameters $\sigma = 1 + 1/\alpha$, $\alpha = j_o r_o/\epsilon D C_0$, $\rho = r/r_o$, and $\tau = tD/Kr_o^2$. Using this result, Eq. (5) is solved implicitly to obtain a numerical value for $\tau_p = t_p D/Kr_o^2$. Assuming a known value for τ_p, which is dependent of α and C_0/C_r, Eqs. (6)–(9) are solved by the Fourier method, with the result in infinite series form:

$$C_2(\rho,\tau) = C_0\left\{a + \frac{b}{\rho} + \frac{1}{\rho}\sum_{n=1}^{\infty} A_n\Phi_n(\rho)\right.$$

$$\left.\times \exp[-\lambda_n(\tau-\tau_p)]\right\}, \quad \begin{matrix} 1 < \rho_p\rho_p, \\ \tau_p < \tau < \infty. \end{matrix} \tag{15}$$

where

$$a = \frac{\sigma\rho_p C_r/C_0 - 1}{\sigma\rho_p - 1},$$

$$b = \frac{\rho_p(1 - C_r/C_{0)}}{\sigma\rho_p - 1}.$$

The series coefficients A_n in (15) are given by

$$A_n = \frac{1}{|\Phi_n|^2}$$

$$\times \int_1^{\rho_p}\Phi_n(\rho)\left[\rho C_1(\rho,\tau_p)/C_0 - (a\rho + b)\right]d\rho,$$

where

$$|\Phi_n|^2 = \int_1^{\rho_p}\Phi_n^2(\rho)d\rho.$$

The eigenfunctions Φ_n in (15) are defined by

$$\Phi_n(\rho) = \sin\left[\sqrt{\lambda_n}(\rho_p - \rho)\right], \quad 1 < \rho < \rho_p,$$

and the eigenvalues λ_n are determined implicitly from

$$\tan\left[\sqrt{\lambda_n}(\rho_p - 1)\right] = \frac{-\sqrt{\lambda_n}}{1+\alpha}.$$

Equations (10)–(13) are solved by the Green's Function method to yield the solution

$$C_3(\rho,\tau) = \frac{\rho_p}{\rho}C_r + \frac{1}{\rho}\int_{\rho_p}^{\infty}\left[\eta C_1(\eta,\tau_p) - \rho_p C_r\right]$$

$$\times\left\{\frac{\exp\left[\frac{-(\rho-\eta)^2}{4(\tau-\tau_p)}\right] - \exp\left[\frac{-(\rho+\eta-2\rho_p)^2}{4(\tau-\tau_p)}\right]}{\sqrt{4\pi(\tau-\tau_p)}}\right\}d\eta,$$

$$\begin{matrix} \rho_p < \rho < \infty, \\ \tau_p < \tau < \infty. \end{matrix} \tag{16}$$

The mass-transfer rate $\dot{M}$, representing the flow rate of contaminant species through a concentric sphere of radius r at time t, is proportional to the concentration gradient, in this case

$$\dot{M}(r,t) = -4\pi r^2 \epsilon D \frac{\partial C}{\partial r}, \qquad (17)$$

where $C_1(r,t)$, $C_2(r,t)$, or $C_3(r,t)$ is inserted for $C(r,t)$, depending on the place and time of interest.

NUMERICAL ILLUSTRATION

Figure 2 summarizes the principal results of the numerical illustration. The normalized mass-transfer rates at two locations are plotted against dimensionless time, with the location of the precipitation front as a parameter. The mass-transfer rate $\dot{M}$ [M/T] is normalized by the constant $4\pi\epsilon r_o DC_o$ [M/T]. The dimensionless time τ is obtained by dividing actual time by Kr_o^2/D [T]. As indicated on the caption for Fig. 2, the solubility C_r in the outer region is set at 10^{-3} of the solubility of the inner, higher-solubility region. The calculations have been done for $\alpha = 500$ to ensure that dissolution is controlled primarily by diffusion.

The upper set of curves in Fig. 2 shows the mass-transfer rates at the surface of the waste sphere, r_o, for four locations of the precipitation front r_p. The start of precipitation is indicated by the vertical bars. If the precipitation front is close to the waste surface, precipitation starts soon and steady-state is reached at early times. The mass-transfer rate at steady state is about 100 times higher for the precipitation front at $(r_p - r_o)/r_o = 0.01$ than for the precipitation front at infinity. The precipitation front is essentially an additional sink for dissolving contaminants, and putting it closer to the waste surface magnifies its effect.

The lower set of curves shows the mass-transfer rates at the location of the precipitation front. The contaminant takes some time to arrive at this location. At a certain time, the precipitation concentration is reached and precipitation begins. Once precipitation starts, the mass-transfer rate out of the precipitation front decreases dramatically. The location of the precipitation front affects the time when precipitation begins. It also affects the steady-state mass-transfer rate out of the precipitation front, but only slightly.

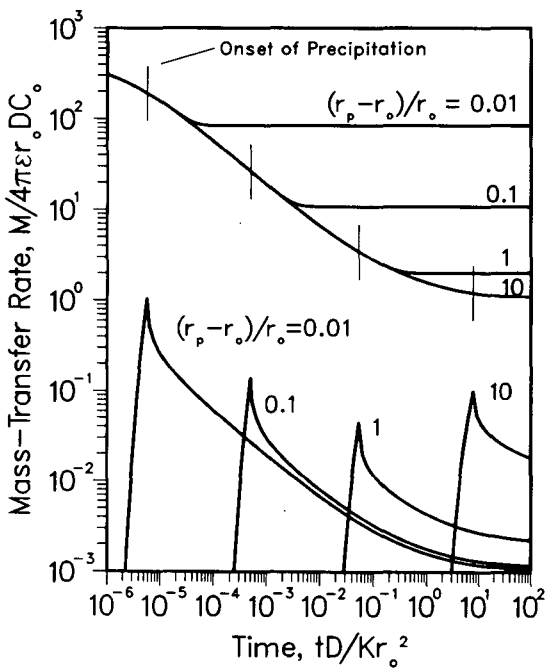

Figure 2. Mass-transfer rate at the waste surface and precipitation front, $\alpha = 500, C_0/C_r = 10^{-3}$. [XBL 895-1983]

CONCLUSION

At early times, the release rate is controlled by the solid-liquid reaction rate represented by the dimensionless quantity α. At later times extending to steady state, the release rate depends on the location of the precipitation front and on the solubility ratio C_0/C_r.

The result of fixing the front concentration at C_r is to steepen the concentration gradient on the waste-package side of the front and to flatten the gradient in the region outside the front. The rate of contaminant transport from the waste to the front location is thereby maintained at higher than normal levels, and the rate of transport away from the front is held to lower levels. The difference in the transport rates at the front determines the rate of precipitation. Nearly all of the species released at C_r from the waste form is immobilized. Whether this scenario is more or less desirable than other predictions without precipitation depends on the goals—whether we care about the waste dissolution rate or far-field transport rates, and whether the assumed uniform solubility is nearer to C_0 or C_r.

If a near-field region of high solubility is viewed as a perturbation to the normal low-solubility case, then we may conclude that the effect of the perturbation is to increase the release rate at the waste surface as well as at the precipitation front. The release rate at the waste surface may be greatly affected if the front is very close to the waste surface and the ratio C_0/C_r is very large. The release rate from the front location will increase with increasing size of the high-solubility region due to the larger radius at which the concentration C_r is maintained.

The effect at the waste surface has the greatest potential for dramatic influence (Garisto, 1986; Gar-

isto and Garisto, 1986a,b; Garisto et al., 1986). If we apply our model to a controlling matrix species, the dissolution of which releases other waste components, we see that if these components are not solubility-limited, their release toward the far-field could be greatly accelerated by a local high-solubility region for the controlling matrix species.

REFERENCES

Garisto, F., 1986. Solid dissolution: Effect of mass transport-precipitation coupling. Chem. Eng. Sci., v. 41, p. 3219.

Garisto, N.C., and Garisto, F., 1986a. The effect of precipitation on the long-term release of radionuclides from used fuel. Ann. Nucl. Energy, v. 13, p. 591.

Garisto, F., and Garisto, N.C., 1986b. The effect of precipitation on radionuclide release from used fuel. *In* Proceedings, 2nd International Conference on Radioactive Waste Management, p. 645.

Garisto, N.C., Harvey, K.B., Garisto, F., and Johnson, L.H., 1986. Source term models for the assessment of nuclear fuel waste disposal in Canada. *In* Waste Management '86 (Vol. 2), p. 397.

Oxidation of Copper(I) and Sulfide in Chalcopyrite

D.L. Perry and K.M. Ogle

Over the last several years, many new techniques have been developed for studying surface reactions that occur on the faces of geologic materials. Such techniques are especially useful for studying chemical processes that are important to the processing of mineral ores and their mixtures in froth flotation effected in aqueous reaction systems. Alternatively, these surface techniques can also be applied to the study of the chemical mechanisms involved in the leaching of metal ions from spent ores for the purpose of recovering additional metal and determining how the pertinent metal-ion complexes involved in the process migrate through soil, rock, and other material in the ground.

One surface technique that has found widespread applications to these studies is x-ray photoelectron spectroscopy (XPS), also sometimes referred to as electron spectroscopy for chemical analysis (ESCA). This technique yields a considerable amount of chemical information about reactions, including the oxidation state of an element, the chemical species of the element involved in the reaction, and the changes that these chemical species undergo during the course of a particular reaction sequence (Perry, 1986). Materials that are particularly amenable to study by this technique are metal sulfide ores, such as galena (Perry et al., 1984a), sphalerite (Perry et al., 1984b), and covellite (Perry and Taylor, 1986); in the case of covellite, for example, one can detect oxidation of the copper(I) ion to copper(II) as well as the possible oxidation of the sulfide (S^{2-}) anion to the sulfate (SO_4^{2-}) during its aqueous reaction chemistry.

This article summarizes the results from our study of the reaction of chalcopyrite (Fig. 1), $CuFeS_2$, with aqueous solutions of H_2SO_4. The reaction was studied in two phases: (1) the simple reaction of the chalcopyrite with a solution of H_2SO_4 at pH = 2.00 and (2) the reaction of the chalcopyrite with the same H_2SO_4 under an electrochemical potential to simulate groundwater-leaching conditions. In Fig. 2,

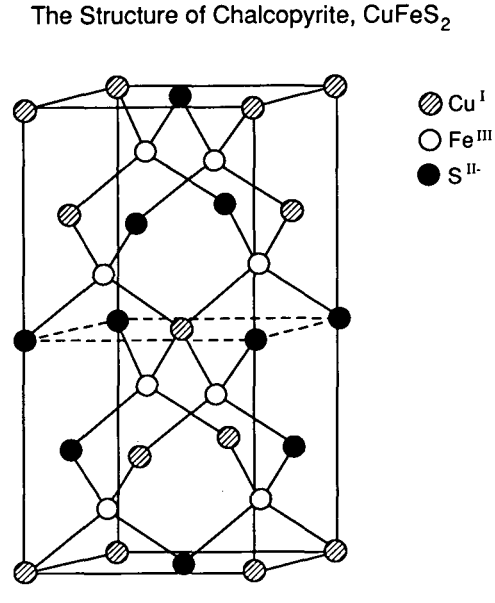

Figure 1. The structure of chalcopyrite, $CuFeS_2$. [XBL 889-10436]

for example, one can see the copper $2p_{3/2,1/2}$ photoelectron spectrum of the sputter-cleaned, unreacted sample (Fig. 2a). After exposure to air for 30 min (Fig. 2b), there is no perceptible change in the spectrum; the intense line on the right side of the spectrum (the $2p_{3/2}$ line) is still quite symmetric and narrow, indicative of the diamagnetic copper(I) species inherent in the mineral. This is confirmed by the lack of any satellite structure to the high-binding-energy side of the $2p_{3/2}$ line. This situation persists in the spectrum (Fig. 2c) of the sample that has been exposed to the H_2SO_4 solution, reflecting the lack of oxidation of the chalcopyrite copper in the solution or, alternatively (possibly), the dissolution of any oxidized copper species that might have formed.

In Fig. 2d, however, a different situation is observed. After reacting the chalcopyrite sample under an applied potential for 12 hours, the copper $2p_{3/2}$ photoelectron line broadens considerably, and a decided amount of satellite structure begins to form to the high-binding-energy side of the main line. This satellite structure results from paramagnetic effects due to the formation of the copper(II) ion upon oxidation of the copper(I) ion. Moreover, this broadening is possibly due to the formation of another copper(I) sulfur phase; the initial sulfide attributable to the $CuFeS_2$ has disappeared in the sulfur $2p_{3/2,1/2}$ spectrum of this sample. All of these data point to a heterogeneous reaction surface with several chemical species present.

The iron $2p_{3/2,1/2}$ spectra exhibited in Fig. 3 represent a series of changes parallel to those found for the copper lines. In Fig. 3a, for example, one sees the familiar contour of both iron oxides and iron sulfides that have been reported previously. This contour consists of a steeply rising background

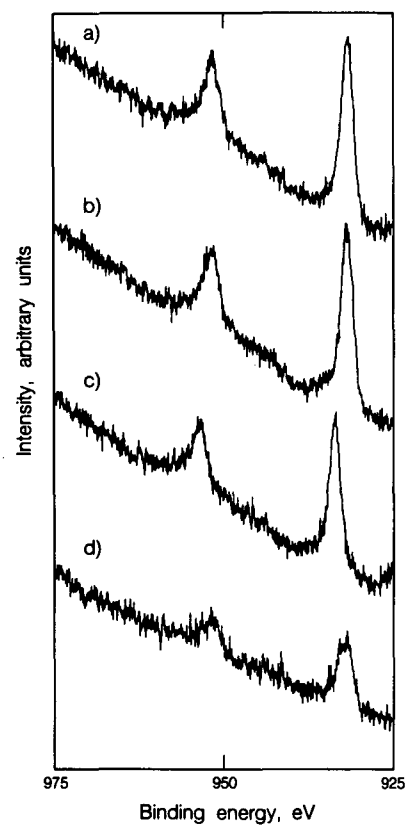

Figure 2. X-ray photoelectron spectra of the copper $2p_{3/2,1/2}$ region of a chalcopyrite sample **(a)** after undergoing argon ion sputtering for 120 s to remove natural contaminants, **(b)** after exposing sample (a) for 30 min to air, **(c)** after exposing sample (b) for 60 s to H_2SO_4 (pH = 2.00), and **((d)** after exposing sample (c) to H_2SO_4 (pH = 2.00) at a potential of E = 0.540 V versus Ag/AgCl for 12 hr. The spectra have not been graphically corrected for charging. [XBL 878-10302]

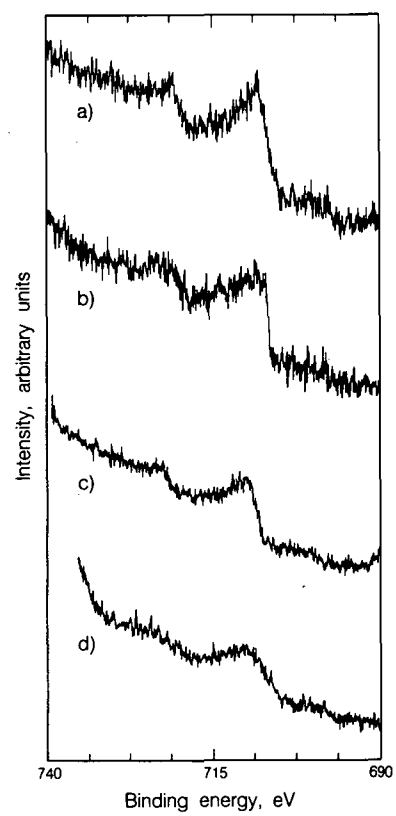

Figure 3. X-ray photoelectron spectra of the iron $2p_{3/2,1/2}$ region of a chalcopyrite sample **(a)** after undergoing argon ion sputtering for 120 s to remove natural contaminants, **(b)** after exposing sample (a) for 30 min exposure to air, **(c)** after exposing sample (b) for 60 s to H_2SO_4 (pH = 2.00), and **(d)** after exposing sample (c) to H_2SO_4 (pH = 2.00) at a potential of E = 0.540 V versus Ag/AgCl for 12 hr. The spectra have not been graphically corrected for charging. [XBL 883-10113]

to the high-binding-energy side of the $2p_{1/2}$ photoelectron line coupled with the broadened $2p_{3/2,1/2}$ lines themselves, this broadening presumably due to multiplet splitting and "shakeup" structures arising from paramagnetic species. In the air-oxidized chalcopyrite spectrum shown in Fig. 3b, the contours of both the $2p_{3/2,1/2}$ lines have changed to include at least two main lines that have fused. Again, however, the predominant peak is the one at 708.8, attributable to the original $CuFeS_2$. The shakeup satellite contributions are also much stronger. In Fig. 3c,d, this same spectral pattern is observed; in Fig. 3c, however, the spectrum has lost some of the complexity of the spectrum in Fig. 3b, along with a concomitant narrowing of the lines. This is undoubtedly due to the interaction of the H_2SO_4 with previous surface-oxidation species effected by the air, with some of the oxidation products shown in Fig. 3b undergoing acid dissolution. Finally, in Fig. 3d, the iron $2p_{3/2,1/2}$ spectrum consists again of an even broader and more featureless main set of peaks. The binding-energy range of this multiplet band encompasses both the iron(II) and iron(III) region. Indeed, oxidation/reduction processes occurring at the $CuFeS_2$/solution interface could produce "high-spin" iron(II) species whose shakeup satellites lie in this region and are too weak to be observed as separate features. The $2p_{3/2}$ line, on the high-binding-energy side, has become more diffuse; this is often observed when there is a group of species on a surface, with some of the chemical species not being well defined crystallographically. This results in poorly shaped (and weak) satellite structure associated with iron spectra of the species.

The changes in the sulfur $2p_{3/2,1/2}$ spectra for the samples are even more dramatic. In Fig. 4a,b, the binding energy for the sulfur $2p_{3/2,1/2}$ lines of the chalcopyrite have the same value, 161.2 eV (the two lines are separated by only 1.2 eV, and, unlike the $2p_{3/2,1/2}$ lines of copper, appear as a broadened singlet, hence only one binding energy is often given—for the more intense $2p_{3/2}$ line). In Fig. 4c, however, the binding energy has remained at 161.2 eV, indicating the presence of the original sulfide; this value is about 0.5 eV lower than that for elemental sulfur but indicates the approach of an oxidation product. Finally, in Fig. 4d, two forms of sulfur are observed. The first one, at a binding energy of 163.4 eV, is indicative of elemental sulfur; the second peak, however, at a binding energy of 168.0 eV, can be unequivocally attributed to the sulfate species. Thus one sees that the sulfur form and the sulfate ion are in equilibrium with one another

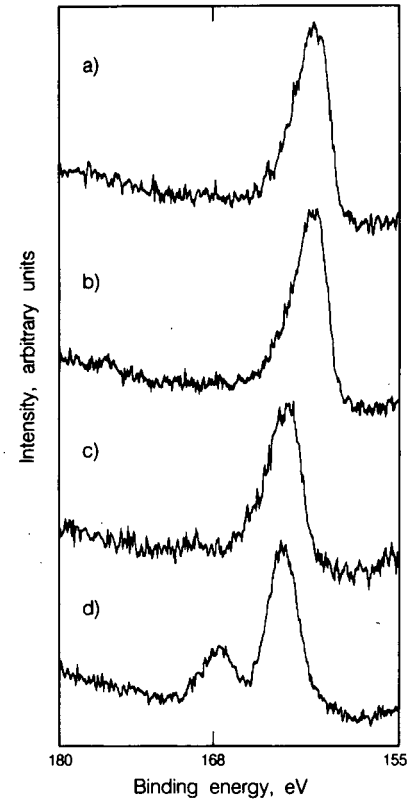

Figure 4. X-ray photoelectron spectra of the sulfur $2p_{3/2,1/2}$ region of a chalcopyrite sample **(a)** after undergoing argon ion sputtering for 120 s to remove natural contaminants, **(b)** after exposing sample (a) for 30 min to air, **(c)** after exposing sample (b) for 60 s to H_2SO_4 (pH = 2.00), and **(d)** after exposing sample (c) to H_2SO_4 (pH = 2.00) at a potential of E = 0.540 V versus Ag/AgCl for 12 hr. The spectra have not been graphically corrected for charging. [XBL 878-10303]

on the electrochemically treated surface. These data are in agreement with the coexistence of the two chemical forms of sulfur on other sulfide minerals, such as galena (Perry et al., 1984a).

REFERENCES

Perry, D.L., 1986. Applications of surface techniques to chemical bonding studies of minerals (Chapter 18). *In* J.A. Davis and K.F. Hayes (eds.), Geochemical Processes at Mineral Surfaces (ACS Symposium Series No. 323). American Chemical Society, Washington, D.C., p. 389–402.

Perry, D.L., and Taylor, J.A., 1986. X-ray photoelectron and Auger studies of Cu_2S and CuS. J. Mater. Sci. Lett., v. 5, p. 384–386.

Perry, D.L., Tsao, L., and Taylor, J.A., 1984a. The galena/dichromate solution interaction and the nature of the resulting chromium(III) species. Inorg. Chim. Acta, v. 85, p. L57–L59.

Perry, D.L., Tsao, L., and Taylor, J.A., 1984b. Surface studies of the interaction of copper ions with metal sulfide minerals. *In* Proceedings, International Symposium on Electrochemistry in Mineral and Metal Processing (Vol. 84–10), p. 169–184.

Magnetic Resonance Imaging of the Reaction between Berea Sandstone and Sodium Fluoride

*D.L. Perry and C. Sotak**

Two of the most important questions that can be asked concerning the migration of chemical fluids in geologic media are (1) *what* chemical reactions occur? and (2) *where* do they occur? Gross chemical measurements using tracers can be made, but these studies basically yield only a knowledge of the final location of the tracer in the field; questions about the paths and regions traversed by the fluid go unanswered. Experimental approaches of this type also give no information concerning chemical reaction products or kinetics in the geologic media bulk.

In this summary, initial results are discussed concerning the application of magnetic resonance imaging (MRI) (Rabenstein and Guo, 1988) to reactions occurring in rock bodies. The specific reaction shown here—between NaF and Berea sandstone—was chosen for several reasons. First, Berea sandstone is quite porous and will allow water to permeate it on a reasonable time scale. Second, the NaF provides a nucleus (fluorine-19) that exists in 100% natural abundance and thus maximizes the possibility that the reaction of the ion can be followed using nuclear magnetic resonance spectroscopy; the water-reaction region can be mapped using proton nuclear magnetic resonance spectroscopy. Finally, previous work (Perry et al., 1983) has shown that the fluoride ion is quite chemically reactive with respect to aluminosilicate materials. The purpose of the experiment was to determine if this approach could yield direct experimental data documenting actual reaction products formed in the Berea sandstone and to determine if the reaction could be followed on a reasonable time scale.

Figure 1 shows the proton magnetic resonance image of the water molecule in a 3″ × 2″ Berea sandstone core (the image is along the lengthwise principal axis) that has been immersed in an aqueous solution of 0.1 M NaF for 3 min at 25°C under atmospheric pressure. The whitened area represents the intrusion area of the NaF solution, this area defining the reaction zone. The reaction involving the sandstone and NaF is thus shown to occur quite heterogeneously within the core. The upper lateral portion of the core is the primary reaction site; the right and left sides exhibit virtually no activity.

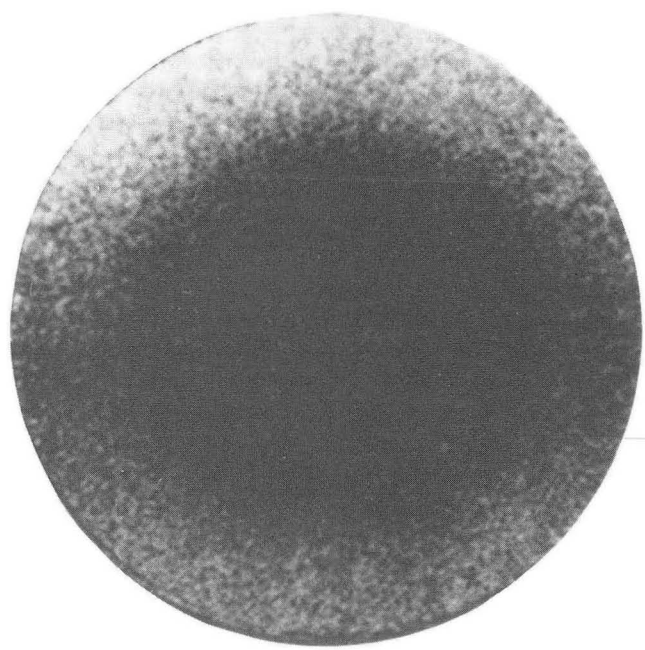

Figure 1. Proton magnetic resonance image (longitudinal) of a Berea sandstone core reacted for 3 min at 25°C with 0.1 M NaF (H_2O) solution. [XBB 870-9035]

*Department of Biomedical Engineering, Worcester Polytechnic Institute, Worcester, MA 01609.

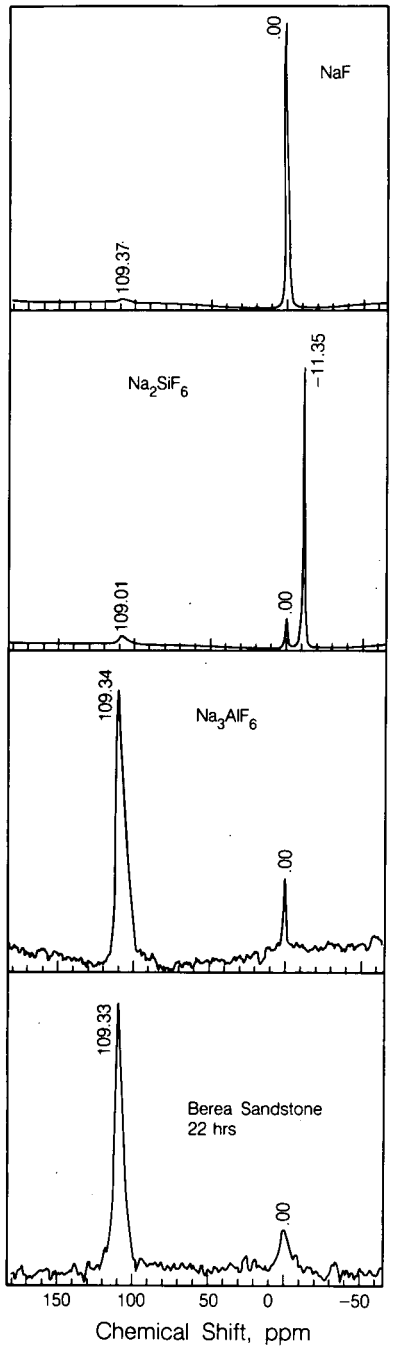

Figure 2. Fluorine-19 nuclear magnetic resonance spectra of NaF-reacted Berea sandstone and model compounds. [XBL 8710-10413]

The fluorine-19 nuclear magnetic resonance spectrum of the Berea sandstone core exhibited in Fig. 2, along with the spectra of the aqueous NaF reactant and other possible reaction products, gives information as to the exact nature of the chemical reaction occurring. In the spectra of both reagent grade NaF and Na_2SiF_6 samples, a small signal resulting from AlF_6^{3-} (a common, documented impurity) can be seen. However, in the Berea sandstone core that has been reacted for 3 min and then allowed to allowed to react several hours outside the NaF solution, the signal resulting from the AlF_6^{3-} increases dramatically.

The following gross reactions can be envisaged:

$$NaF \rightarrow Na^+ + F^- \quad (1)$$

$$Al^{3+} + 6F^- \rightarrow AlF_6^{3-} \quad (2)$$

$$AlF_6^{3-} \rightarrow AlF_4^- + 2F^- \quad (3)$$

Reaction (3) has been reported (Filin et al., 1983) for natural Na_3AlF_6 (cryolite) in aqueous solution.

REFERENCES

Filin, V.N., Rakcheeva, L.V., and Zaitsev, V.A., 1983. Study of physicochemical processes in the liquid phase during cryolite dissolution in water. Zh. Prikl. Khim. (Leningrad), v. 56, p. 2175.

Perry, D.L., Tsao, L., and Gaugler, K.A., 1983. Surface studies of HF- and HF/H_2SO_4-reacted feldspars. Geochim. Cosmochim. Acta, v. 47, p. 1289.

Rabenstein, D.L., and Guo, W., 1988. Nuclear magnetic resonance spectroscopy. Anal. Chem., v. 60, p. 1R.

Thermodynamics of High-Temperature Brines

K.S. Pitzer, R.T. Pabalan, and J.C. Tanger IV

Equilibrium considerations based on various types of experimental measurements interrelated and extended by thermodynamic calculations provide an important basis for understanding and prediction in a variety of geochemical systems. This article includes in its first part a brief summary of a new method for the prediction of standard-state (infinite dilution) properties of various salts under supercritical conditions (Tanger and Pitzer, 1989). The second part is a summary of recent measurements of the heat capacities of aqueous KCl and Na_2SO_4 and of the modeling of these systems for various properties, including mineral solubilities (Pabalan and Pitzer, 1988, 1989).

CALCULATION OF STANDARD-STATE PROPERTIES TO 1000°C AND 5 KBAR

The basis of this calculation is a semicontinuum model in which the innermost shell of water molecules around an ion is treated on a detailed basis and the effect of more-distant water is calculated from the dielectric properties of water as a continuous fluid. For the inner shell, the entropy and enthalpy changes for the successive additions of water molecules have been measured by mass spectrometry (Kebarle, 1977). As had been shown earlier for the self-ionization of water and for NaCl(aq) (Pitzer, 1982, 1983), these parameters allow the calculation of the inner-shell hydration properties as a function of water fugacity (obtained from the pressure) and temperature. The present calculations extend to the other alkali halides and include significant improvements but are essentially the same as reported earlier. The inner shell is limited to six molecules.

Although the previous calculations made some attempt to account for the effect of more-distant water on the Gibbs energy, enthalpy, entropy, heat capacity, or volume change on hydration, the treatment was very simple, and no claim was made for validity where outer-shell effects were substantial. The present calculations are based on a modification of the rather complex methods that Tanger and Helgesen (1988) developed for hydration effects under liquid-like conditions. They used a continuous dielectric model for the entire effect, whereas the present calculations use it only for the outer shell. The most sensitive aspect is the determination of the radius of the spherical cavity in the dielectric, which must now accommodate the inner shell of water molecules as well as the ion. These effective radii were determined empirically for moderate temperatures at which water is liquid-like and experimental data are available for the Gibbs energy of hydration. It was found that these radii could be regarded as independent of pressure while a universal function was developed for their temperature dependence.

Figure 1 shows the calculated values for the standard-state properties of hydration for $Na^+ + Cl^-$. The behavior for any other alkali halide would be similar. Although the Gibbs energy shows rather smooth properties, with appropriate discontinuities in the two-phase region, the derivative functions show sudden and large variations even in the single-phase region near the critical point. Figure 2 shows the mean hydration number for the inner shell for Na^+ and for Cl^-. In the liquid region these numbers range from 5 to the maximum, 6, and in the vapor near the saturation curve they also exceed 5. Thus the principal difference in hydration properties between the saturated vapor and the liquid arises from the outer shell region. It is only at higher temperatures that the inner-shell hydration number decreases gradually below 5. It is also clear that Na^+ is somewhat more strongly hydrated than Cl^-.

In the vapor or the supercritical fluid of moderate density, NaCl or other alkali halides are largely ion-paired. The conductance data of Quist and Marshall (1968) are used to evaluate the difference in standard-state properties between the ions and the ion pair for NaCl up to 400°C, and the model of Pitzer and Pabalan (1986) for NaCl in steam is used for higher temperatures at 321 bars. In a final calculation, all of these data are used to calculate the apparent molal heat capacity of a very dilute solution through the near-critical region (321 bars, 350–450°C) for comparison with experimental measurements of White et al. (1988). The calculated curve shows the same pattern as the experimental one, with very large negative values near 400°C and very large positive values near 430°C, but there are substantial quantitative differences for this very demanding calculation. The primary effects are those of any aqueous solution with a strongly hydrated solute near the critical point of water, but in the same range the NaCl shifts from a state of nearly complete ionization below 360°C to one of nearly complete ion-pairing above 450°C.

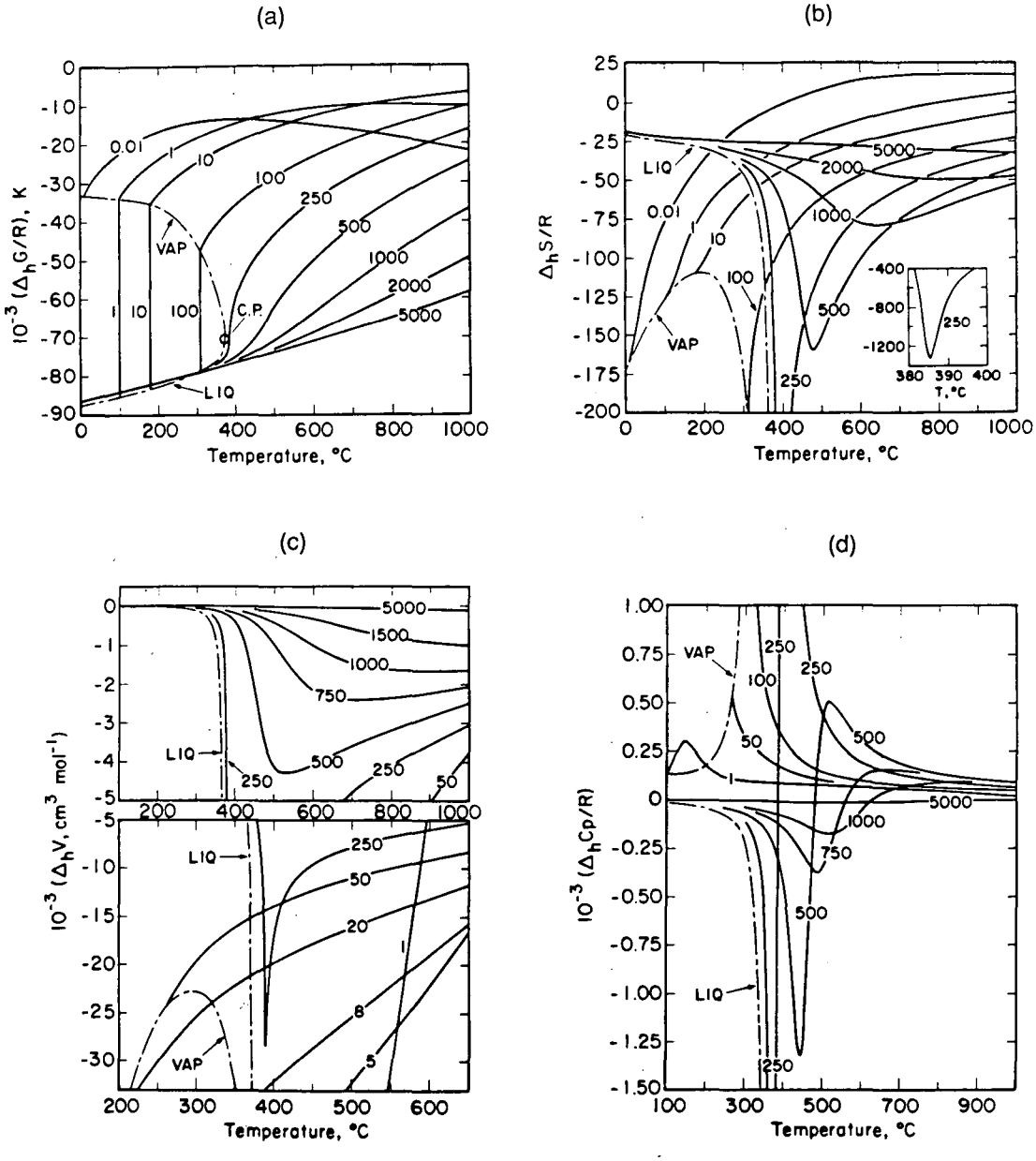

Figure 1. Standard-state properties for the hydration of $Na^+ + Cl^-$ from the semicontinuum model as a function of temperature at selected pressures in bars. Calculated values are shown for Gibbs free energies **(a)**, entropies **(b)**, volumes **(c)**, and heat capacities **(d)**. [XBL 895-1984]

HEAT CAPACITY AND OTHER THERMODYNAMIC PROPERTIES OF KCl(aq) AND Na_2SO_4(aq) to 300°C AND HIGH MOLALITY

In two closely similar projects, measurements were made in the high-pressure, high-temperature flow calorimeter for aqueous KCl at 200 bars from 140 to 300°C and from 0.05 to 3.0 mol · kg^{-1} and for aqueous Na_2SO_4 at 200 bars from 140 to 300°C and from 0.05 to 1.5 mol · kg^{-1}. The resulting apparent molal heat capacities for Na_2SO_4 are shown in Fig. 3 along with earlier measurements (below 200°C) of this project (Rogers and Pitzer, 1981) and literature data (Likke and Bromley, 1973). For each system the new measurements were combined with other data, including enthalpies, densities, and osmotic coefficients, to yield comprehensive equations for all thermodynamic properties over wide ranges of conditions. For Na_2SO_4(aq) the osmotic-

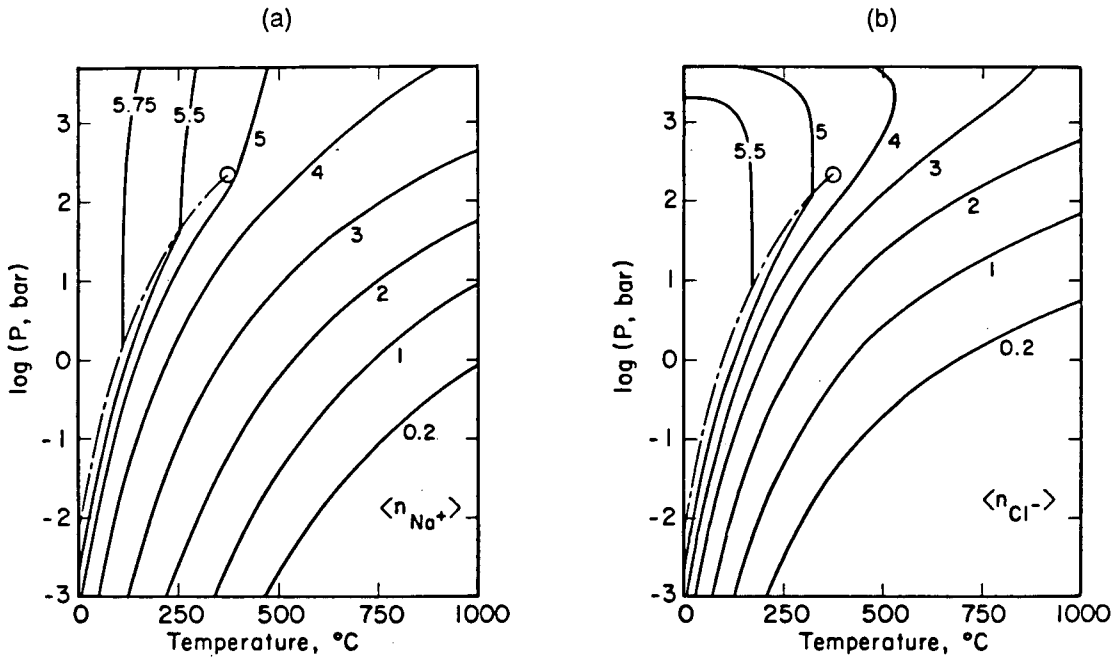

Figure 2. Isopleths of the mean hydration number of the inner-shell region, $\langle n \rangle$, for Na^+ **(a)** and Cl^- **(b)** as functions of pressure and temperature. [XBL 895-1985]

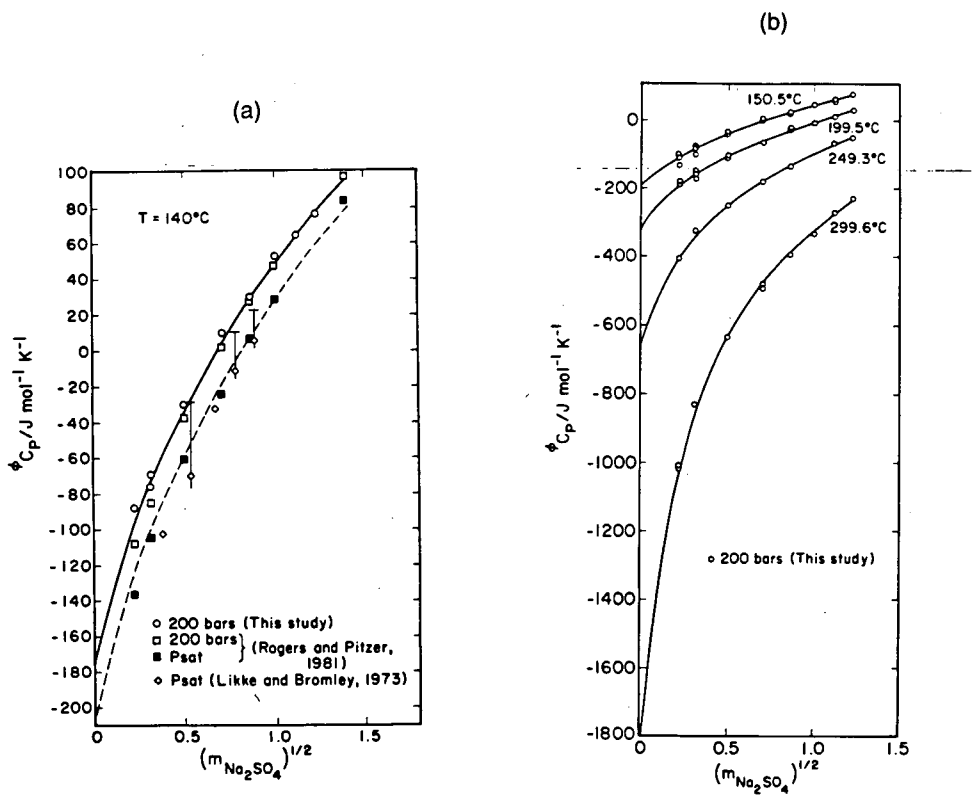

Figure 3. Apparent molar heat capacity, $^{\phi}C_p$, of Na_2SO_4(aq) for 140°C at 200 bars and at saturation pressure **(a)**, and for several higher temperatures at 200 bars **(b)**. The curves are calculated from the comprehensive equation for Na_2SO_4(aq). [XBL 895-1986]

coefficient measurements of Holmes and Mesmer (1986) were of special importance, since they cover a wide range of temperature and extend to a molality of 3.0, whereas most other measurements extend only to 1.5 mol · kg^{-1} or less.

Data concerning the solubility of solid minerals were not used in evaluation of parameters for the KCl(aq) or Na_2SO_4(aq) properties; hence a comparison of calculated with experimental solubilities is an independent check on the equations. Figure 4 shows the comparison for the various forms of solid Na_2SO_4 that are stable in the indicated ranges of temperature. The agreement is excellent to 300°C; indeed, an extrapolation of the equation for aqueous-solution properties above 300°C yields surprisingly good estimates to 340°C. Various details related to these solubility calculations are given by Pabalan and Pitzer (1987, 1989).

In addition to the comparison for the binary system Na_2SO_4–H_2O, calculations were made for the ternary systems Na_2SO_4–NaCl–H_2O and Na_2SO_4–NaOH–H_2O and for the quaternary system Na_2SO_4–NaCl–NaOH–H_2O. For each ternary, two parameters related to the mixing of different anions were evaluated from the solubility data. No further parameters arise for the quaternary system; hence the calculated solubilities are predictions. Figure 5 shows the predicted curves and experimental solubilities at 200 and at 300°C.

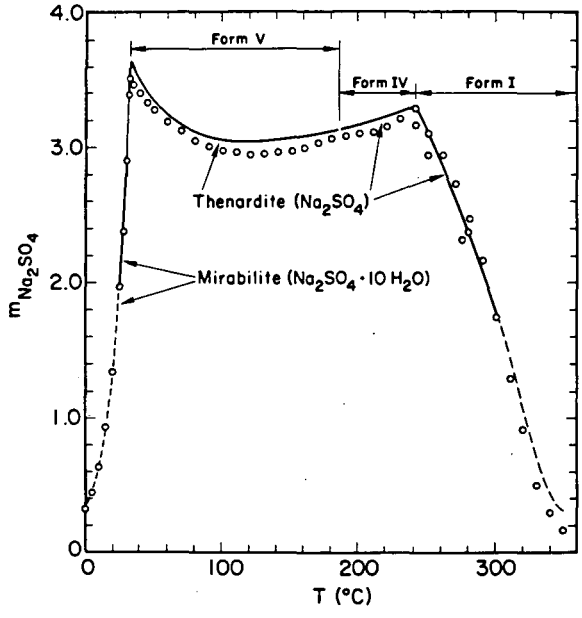

Figure 4. Solubilities of mirabilite ($Na_2SO_4 \cdot 10H_2O$) and thenardite (Na_2SO_4) in water as a function of temperature. The symbols are experimental data tabulated by Linke and Seidell (1965), and the curves are predicted values. The curves are dashed outside the temperature range of our regression Na_2SO_4(aq) properties. [XBL 895-1987]

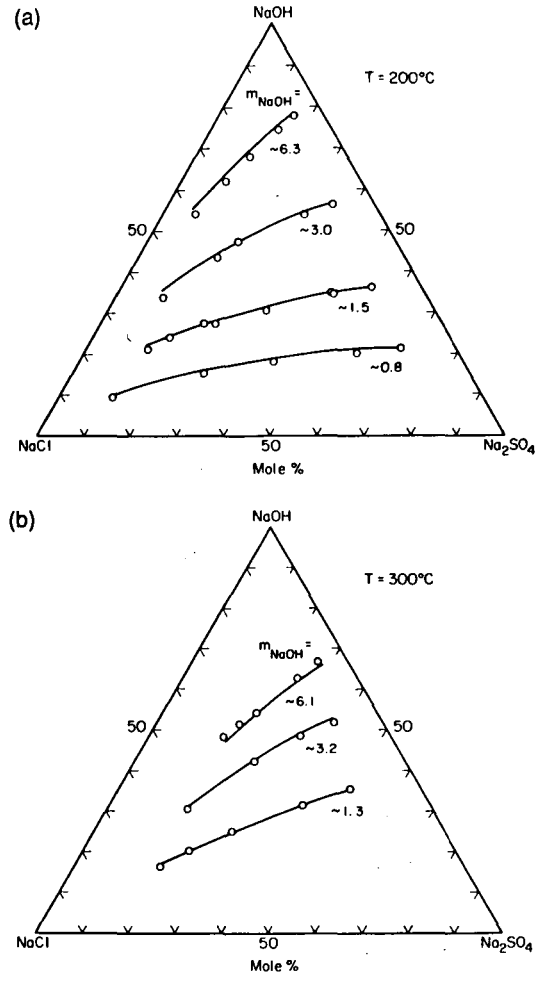

Figure 5. Calculated and experimental solubilities of thenardite (Na_2SO_4), at fixed molalities of NaOH in the quaternary system NaCl–Na_2SO_4–NaOH–H_2O, at P_{sat} and at temperatures of **(a)** 200°C and **(b)** 300°C. The symbols are experimental data from Schroeder et al. (1935). [XBL 895-1988]

REFERENCES

Holmes, H.F., and Mesmer R.E., 1986. Isopiestic studies of aqueous solutions at elevated temperatures. VIII. The alkali-metal sulfates. J. Chem. Thermodyn., v. 18, p. 263–275.

Kebarle, P., 1977. Ion thermochemistry and solvation from gas phase ion equilibria. Ann. Rev. Phys. Chem., v. 28, p. 445–476.

Likke, S., and Bromley, L.A., 1973. Heat capacities of aqueous NaCl, KCl, $MgCl_2$, $MgSO_4$, and Na_2SO_4 solutions between 80° and 200°C. J. Chem. Eng. Data, v. 18, p. 189–195.

Linke, W.F., and Seidell, A., 1965. Solubilities of Inorganic and Metal Organic Compounds (4th ed., Vols. 1 and 2). American Chemical Society, Washington, D.C.

Pabalan, R.T., and Pitzer, K.S., 1987. Thermodynamics of concentrated electrolyte mixtures and the prediction of mineral solubilities to high temperatures for mixtures in the system $Na-K-Mg-Cl-SO_4-OH-H_2O$. Geochim. Cosmochim. Acta, v. 51, p. 2429–2443.

Pabalan, R.T., and Pitzer, K.S., 1988. Apparent molar heat capacity and other thermodynamic properties of aqueous KCl solutions to high temperatures and pressures. J. Chem. Eng. Data, v. 33, p. 354–362.

Pabalan, R.T., and Pitzer, K.S., 1989. Heat capacity and other thermodynamic properties of $Na_2SO_4(aq)$ in hydrothermal solutions and the solubilities of sodium sulfate minerals in the system $Na-Cl-SO_4-OH-H_2O$ to 300°C. Geochim. Cosmochim. Acta, v. 53, p. 2392–2404.

Pitzer, K.S., 1982. Self-ionization of water at high temperature and the thermodynamic properties of the ions. J. Phys. Chem., v. 86, p. 4704–4708.

Pitzer, K. S., 1983. Thermodynamics of sodium chloride solutions in steam. J. Phys. Chem., v. 87, p. 1120–1125.

Pitzer, K.S., and Pabalan, R.T., 1986. Thermodynamics of NaCl in steam. Geochim. Cosmochim. Acta, v. 50, p. 1445–1454.

Quist, A.S., and Marshall, W.L., 1968. Electrical conductances of aqueous sodium chloride solutions from 0 to 800°C and at pressures to 4000 bars. J. Phys. Chem., v. 72, p. 684–703.

Rogers, P.S.Z., and Pitzer, K.S., 1981. High-temperature thermodynamic properties of aqueous sodium sulfate solutions. J. Phys. Chem., v. 85, p. 2886–2895.

Schroeder, W.C., Gabriel, A., and Partridge, E.P., 1935. Solubility equilibria of sodium sulfate at temperatures from 150 to 350°C. I. Effect of sodium hydroxide and sodium chloride. J. Am. Chem. Soc., v. 57, p. 1539–1546.

Tanger, J.C. IV, and Helgeson, H.C., 1988. Calculation of the thermodynamic and transport properties of aqueous species at high pressures and temperatures: Revised equations of state for the standard partial molal properties of ions and electrolytes. Am. J. Sci., v. 288, p. 19–98.

Tanger, J.C. IV, and Pitzer, K.S., 1989. Calculation of the thermodynamic properties of aqueous electrolytes to 1000°C and 5000 bar from a semicontinuum model for ion hydration. J. Phys. Chem., v. 93, p. 4941–4951.

White, D.E., Wood, R.H., and Biggerstaff, D.R., 1988. Heat capacities of 0.0150 mol · kg^{-1} NaCl(aq) from 604 to 718 K at 32 MPa. J. Chem. Thermodyn., v. 20, p. 159–168.

Sulfur Compounds Control the Solubility and Biological Availability of Selenium in Reducing Environments

O. Weres, G. Screechfield, and A.-R. Jaouni

Zero-valent selenium (Se^0) is thermodynamically stable and accounts for a large fraction of the selenium in soil under reducing conditions (Weres et al., 1989a). Se^0 includes not only elemental selenium but also other compounds in which a formally zero-valent selenium atom is bonded to one or more selenium or sulfur atoms; e.g., SeS_2 and amino acid dimers bridged by the group —SSeS—. In practice, Se^0 is operationally defined as selenium that is preferentially extracted by thiophyllic reagents; e.g., Na_2S, NaCN, Na_2SO_3, which also dissolve S_8 (Weres et al., 1989a; Davis, 1968).

Extensive studies of a selenium-contaminated wetland (Kesterson Reservoir, Merced County, California) have demonstrated that in the absence of nitrate and oxygen, selenate and selenite are quickly removed from soil pore water by microbial reactions (Weres et al., 1989b), which explains the absence of selenium from the groundwater beneath Kesterson Reservoir (Weres et al., 1989b). In areas of Kesterson Reservoir with thick organic deposits and strongly reducing conditions, selenium has penetrated up to 75 cm into the soil profile, suggesting that selenium regains limited mobility under strongly reducing conditions (Weres et al., 1989a). Above pH 7 elemental sulfur will react with H_2S to form polysulfide anions, which are present in sulfidic pore water (Boulegue and Michard, 1979). Hydrogen sulfide and polysulfide anions also react with selenium above pH 7, producing selenium-

substituted polysulfide anions (Weres et al., 1989a); e.g.,

$$Se_n + HS^- + OH^- \rightarrow Se_{n-1} + SeS^{2-} + H_2O \quad (1)$$

A variety of thiols, including cysteine, glutathione, mercaptoacetic acid, and both isomers of mercaptopropionic acid have recently been identified in water extracted from mildly sulfidic ocean-bottom sediments (Shea and MacCrehan, 1988). Thiols will react with Se^0, as does H_2S, forming a selenium-containing organic anion; e.g., the 3-mercaptopropionate ion will react thus:

$$HSCH_2CH_2COO^- + Se_n + OH^- \rightarrow$$

$$^-SeSCH_2CH_2COO^- + H_2O + Se_{n-1} \quad (2)$$

The solubility of black Se in solutions of thiols and related compounds is presented in Fig. 1 (experimental details in report by Earth Sciences Division, 1988). The three thiols dramatically increase the solubility of selenium, particularly above pH 7. At pH 9.1, 4–8% of the sulfur compound has reacted

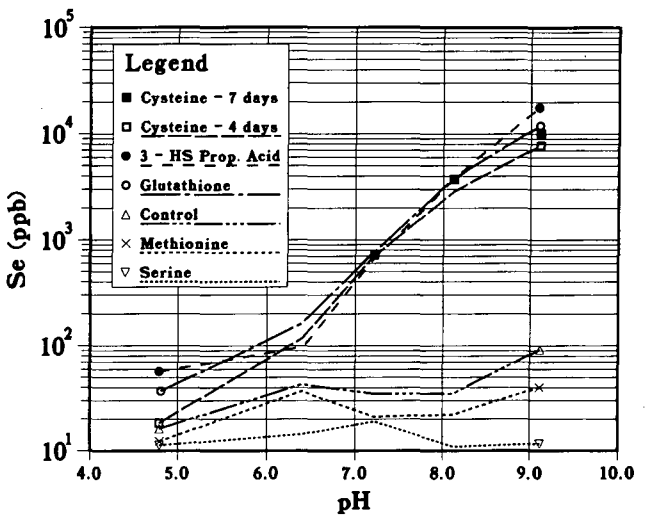

Figure 1. Solubility of selenium in the presence of thiols versus pH. Each solution consisted of deaerated Na_2SO_4/NaCl (0.04 M/0.03 M) brine with 2.5 mM of the given test compound and citrate/phosphate/borate buffer (5 mM each) with pH adjusted to the value desired. Solution deaerated and sealed with small amount of black Se (325+ mesh) under vacuum in glass ampoule and placed on shaker table for 4 to 7 days at room temperature, then filtered and analyzed for total Se using hydride generator AAS after digestion with alkaline H_2O_2 and HCl. Control = buffered brine only. [XBL 8812-4370]

with selenium. Because the reaction requires hydroxide ion, increasing pH favors it. In the case of mercaptopropionic acid, the curve flattens out below pH 6, reflecting protonation of the carboxylate group, which favors formation of the negatively charged —SSe^- group. The effects of the amino acids serine and methionine are practically indistinguishable from those of the control.

Filtered sulfidic pore water has the bright yellow color that is characteristic of polysulfides. Polysulfides are readily decomposed by acid, precipitating colloidal sulfur, which may be filtered, carrying selenium with it (Weres et al., 1989a). This method was extended, allowing three classes of selenium in reducing water to be resolved. The filtered water samples were analyzed three ways:

A. To determine total selenium, add 1 ml of 1 M Na_2S + 1 M NaOH to 3-ml sample to open up polysulfides; digest with 1 ml of 30% H_2O_2 at 100°C until bubbles are gone; digest with 5 ml of 12 N HCl at 100°C for 20 minutes; analyze HG-AAS.

B. Add 2.5 ml of 0.2 M Na_2S_4 to 10-ml sample at room temperature, allow to stand for 2 minutes, add 1 ml of 6 N HCl, purge for 2 minutes with N_2, and filter twice (0.45 μm) to remove colloidal sulfur. Analyze filtrate for total Se as above. Fresh Na_2S_4 was made by reacting S_8 with 0.2 M Na_2S at 100°C.

C. Add 0.5 ml of 6 N HCl to 30-ml sample, let stand for 2 minutes, filter (0.45 μm), and analyze for total Se as above.

Reference solutions of selenium/sulfur compounds were prepared by reacting a deaerated 4 mM solution of the given sulfur compound in water with black Se (325+ mesh) in an ampoule for 3 days (Na_2S_4 at pH 10, all others adjusted to pH 8.1). Immediately before use the solution was filtered and diluted 1:25 in deaerated Na_2SO_4/NaCl brine. Polysulfidic Se produced by reaction of black Se with Na_2S_4 is quantitatively precipitated by acid (Table 1). The difference A−C corresponds to polysulfidic Se. Acid does not precipitate thiol-bound Se, but adding a large excess of Na_2S_4 to the solution quantitatively converts the selenium from thiol-bound to polysulfidic, which is precipitated by acid. The difference C−B corresponds to thiol-bound Se. The Se in a solution that contains both Na_2S_4 and glutathione behaves as thiol-bound Se, indicating that thiols will take Se from polysulfides. The B reading includes a blank and additional selenium compounds in which Se is not bound to sulfur and cannot be extracted by Na_2S_4 or precipitated by acid; e.g.,

Table 1. Precipitation of complexed Se.

Solution	N	A (ppb Se)	A–C	C–B	B
Na_2S_4	2	792 ± 200	99 ± 0	0 ± 0	2 ± 2
HS-Acetic Acid	2	220 ± 63	1 ± 0	96 ± 1	3 ± 1
HS-Prop. Acid	2	159 ± 24	0 ± 0	96 ± 0	4 ± 0
Cysteine	3	38 ± 12	0 ± 0	85 ± 6	15 ± 6
Glutathione	3	56 ± 10	3 ± 4	84 ± 10	14 ± 7
Na_2S_4+Glut.	3	507 ± 136	3 ± 2	95 ± 2	2 ± 0
Pond 5 muck	1	267	67	9	25
Pond 2 mud	2	222 ± 4	52 ± 1	9 ± 2	38 ± 0
Peat slurry	2	176 ± 6	26 ± 6	14 ± 8	61 ± 3
Oxid. P2 peat	2	171 ± 9	2 ± 0	28 ± 4	69 ± 3
Oxid. P5 muck	2	176 ± 0	0 ± 0	62 ± 2	38 ± 2

Notes to Table 1. N = number of repetitions. Tabulated values are $\bar{x} \pm \sigma$. A–C = percent polysulfidic Se. C–B = percent thiol-bound Se; may include SeO_3^{2} and CH_3SeO_2H in the last two, nonsulfidic samples. B = percent Se not precipitated by Na_2S_4 and/or acid; e.g., SeO_4^{2} and selenomethionine.

selenate and selenomethionine. It may include selenium associated with amino acids and peptides, as reported for anoxic ocean water (Cutter, 1982).

Samples were obtained by centrifuging sulfidic materials collected at Kesterson Reservoir and filtering the supernatant through 0.45-μm membrane filters just before use. Five samples of sulfidic sediment were collected at Kesterson Reservoir, and two of them were exposed to air in the laboratory while wet. In the three sulfidic samples, polysulfidic Se was the major dissolved species, followed by non-ppt Se and a much smaller amount of thiol-bound Se. Polysulfidic Se was absent from the two partially oxidized samples. The values reported for thiol-bound Se in the oxidized samples may include selenite or methaneseleninic acid, which are also precipitated by procedure B. (These compounds react with HS^- and cannot coexist with it.)

The microbial conversion of selenium to volatile compounds offers a convenient assay of the biological availability of selenium in soil. Starting material was 0–15 cm saline surface soil collected in May 1987 in a part of Kesterson Reservoir vegetated by salt grass (*Distichlis*). The soil was crushed and sieved at 30 mesh. Twelve tests were run simultaneously in open 250-ml wide-mouth plastic bottles at room temperature (Table 2). In each test, 25 g of soil was wetted with 5 ml of a solution of glucose plus $NaNO_3$ in water (5% plus 0.75%; C/N = 16). In four of the tests penicillin-G and streptomycin were added to glucose/nitrate solution (200 ppm each) to inhibit bacteria. Test compounds were added as 2% solutions in water adjusted to pH 7.5 – 8.0, 1 ml at the start and 1 ml seven times during the experiment plus distilled water as needed to replace water lost by evaporation. Glucose/nitrate solution was used in place of test solution in control experiments. After 5 weeks, soluble selenium was extracted with Na_2SO_4/NaCl brine (0.04 M/0.03 M) and the residue dried to constant weight, crushed, and analyzed for total Se and Se^0. Soluble selenium in the Na_2SO_4/NaCl brine extract was determined after digestion with alkaline H_2O_2.

The effect of the antibiotics was never statistically significant, suggesting that bacteria are not the organisms responsible for volatilization. Results with and without antibiotics were combined in analyzing the data. Results with serine or glutamic acid added were not significantly different from those of the control experiments. All four sulfur compounds dramatically increased the amount of selenium lost to the atmosphere, averaging 29% of the total inventory in just 5 weeks, or roughly four times more than in the control. Although the per-

Table 2. S-Compounds stimulate volatilization of Se.

Experiment	N	Se(tot) (ppm)	% Se gone	Soluble Se(ppm)	Se^0 (ppm)	% Se^0 gone
Start	3	7.30 ± 0.35	–	nd	3.26 ± 0.34	–
Control	4	6.80 ± 0.30	7	0.12 ± 0.01	2.32 ± 0.04	26
Serine	1	6.80 ± 0.35	7	0.20	2.66	18
Glutamic A.	1	6.67 ± 0.42	9	0.17	2.29	30
Average	6	6.76 ± 0.21	7 ± 6	0.16 ± 0.02	2.42 ± 0.12	26 ± 11
Methionine	1	4.99 ± 0.29	32	0.42	1.55	52
3-HSProp. A.	2	5.35 ± 0.35	27	0.30 ± 0.08	1.65	47
Cysteine	2	5.16 ± 0.35	29	0.21 ± 0.03	1.54 ± 0.02	53
Glutathione	1	5.15 ± 0.35	29	0.15	1.66	49
Average	6	5.16 ± 0.17	29 ± 5	0.27 ± 0.06	1.62 ± 0.05	50 ± 10
Difference		1.60 ± 0.27	22 ± 4	−0.11 ± 0.06	0.80 ± 0.13	24 ± 4

Notes to Table 2. nd = not determined. N = number of repetitions of the given experiment. Tabulated values are $\bar{x} \pm \sigma_{\bar{x}}$. Se(tot) determined by x-ray fluorescence analysis. $\sigma_{\bar{x}}$ for Se(tot) assumed to arise entirely from analytical error, which is ± 0.6 ppm for a single analysis, and was decreased by repeat analyses of individual experiments and averaging groups of experiments. Total selenium values corrected for soluble selenium extracted. $\sigma_{\bar{x}}$ for soluble Se and Se^0 calculated from σ values of averaged data. First average includes control, serine, glutamic acid. Second average includes the four sulfur compounds, and the "difference" is between the two averages.

centage lost in control experiments was scarcely greater than the experimental uncertainty, the percentage lost with sulfur compounds added was highly significant, and so was the effect of the sulfur compounds. The amount of Se^0 decreased by 26% in the control experiments and by 50% with sulfur compounds added. Although some of the Se^0 may have been converted to other species rather than volatilized, Se^0 was clearly reactive under these conditions, and adding sulfur compounds increased its reactivity. As expected, adding sulfur compounds increased the amount of soluble selenium in the soil.

The dramatic pH-dependent effect of thiols upon solubility of selenium assures them an important role in soil chemistry of selenium. Although it is not necessarily a unique explanation, the ability of thiols to solubilize selenium does explain the ability of microorganisms to oxidize Se^0 (Sarathchandra and Watkinson, 1981) and to volatilize it. Selenoglutathione was reported as a major species of selenium in pore water extracted from selenium-poor peat soil (van Dorst and Peterson, 1984). Peterson and Butler (1962) made extracts of soil spiked with $Se^{75}O_3^{2-}$ and analyzed them using high-voltage electrophoresis, a technique that they report cannot resolve corresponding sulfur and selenium amino acids. It is likely that the Se-glutathione complex, containing the group —SSe$^-$, was misidentified as selenoglutathione, containing the group —Se$^-$. Since the ability of glutathione to form selenium complexes is central to the intracellular biochemistry of selenium (Garberg and Hogberg, 1986), it is entirely likely that microorganisms also exploit the ability of glutathione and other thiols to solubilize Se^0 in the extracellular environment. The large effect of thiols upon the volatilization of selenium, including Se^0, supports the role of thiols in making selenium biologically available.

Methionine is a thioether rather than a thiol and has no effect upon the solubility of selenium but, like thiols, stimulates selenium volatilization. Volatilization of selenium involves its methylation, and methionine is the major source of methyl groups for biochemical transmethylation reactions and thereby directly stimulates the volatilization process. Demethylation of methionine produces homocys-

teine, a thiol that solubilizes selenium. The increment in total selenium volatilized in the presence of sulfur compounds was twice the increment of additional Se^0 removed. Evidently, thiols increase the bioavailability of other chemical species of selenium in soil as well.

The large effect of pH upon selenium solubility with thiols explains the large decrease of soluble selenium in soil with decreasing pH (van Dorst and Peterson, 1984). An analogous effect has been reported in aquatic ecosystems: decreasing the pH of water in a selenium-contaminated pond decreases the selenium content of invertebrates living in the pond (Cherry et al., 1979). These observations suggest that dissolution of Se^0 by reaction with thiols is a critical step in the geochemical cycling of selenium, one that may be blocked by simply decreasing pH. Professor A.J. Horne has suggested that it may be possible to reduce the recycling and ecosystem toxicity of selenium in water bodies contaminated with selenium (e.g., from fly ash) by reducing the pH of the pond-bottom sediment (A.J. Horne, private communication, 1988). Sedimentary selenium will certainly be less biologically available in the acid sedimentary environment typical of freshwater bodies than it was in the brackish, moderately alkaline environment of Kesterson Reservoir. Conversely, increased pH and addition of thiols will enhance the conversion of selenium to soluble and volatile forms.

REFERENCES

Boulegue, J., and Michard, G., 1979. Sulfur speciation and redox processes in reducing environments. *In* E.A. Jenne (ed), Chemical Modeling in Aqueous Systems, Speciation, Sorption, Solubility, and Kinetics. ACS Society Symposium Series, No. 93, American Chemical Society, Washington, D.C., p. 25–50.

Cherry, D.S., Guthrie, R.K., Larrick, S.R., Sherberger, F.F., 1979. The influence of coal ash and thermal discharges upon the the distribution and bioaccumulation of aquatic invertebrates. Hydrobiologia, v. 362, p. 257–267.

Cutter, G.A., 1982. Selenium in reducing waters. Science, v. 217, p. 829.

Davis, R.E., 1968. Mechanisms of sulphur reactions. *In* G. Nickless (ed.), Inorganic Sulphur Chemistry. Elsevier, Amsterdam, p. 85–136.

Earth Sciences Division, 1988. Hydrological, geochemical and ecological characterization of Kesterson Reservoir (Annual Report to Bureau of Reclamation, October 1, 1987 through September 30, 1988). Lawrence Berkeley Laboratory Report LBL-26438.

Garberg, P., and Hogberg, J., 1986. The role of selenium-oxygen interactions in selenium metabolism. Ambio, v. 315, p. 354.

Peterson, P.J., and Butler, G.W., 1962. Paper chromatographic and electrophoretic systems for the identification of sulphur and selenium amino acids. J. Chromat., v. 38, p. 70.

Sarathchandra, S.U., and Watkinson, J.H., 1981. Oxidation of elemental selenium to selenite by *Bacillus megaterium*. Science, v. 211, p. 600.

Shea, D., and MacCrehan, W.A., 1988. Determination of hydrophilic thiols in sediment porewater using ion-pair liquid chromatography coupled with electrochemical detection. Anal. Chem., v. 360, p. 1449.

van Dorst, S.H., and Peterson, P.J., 1984. Selenium speciation in the soil solution and its relevance to plant uptake. J. Sci. Food-Agric., v. 335, p. 601.

Weres, O., Jaouni, A.-R., and Tsao, L., 1989a. The distribution, speciation, and geochemical cycling in a sedimentary environment. Accepted for publication in Appl. Geochem.

Weres, O., Bowman, H.R., Goldstein, A., Smith, E., Tsao, L., and Harnden, C.W., 1989b. Nitrate and organic matter control the mobility of selenium in groundwater. Accepted for publication in Air, Water, Soil Pollution.

Radium Regionalization in California

H.A. Wollenberg

There has been recent concern about indoor concentrations of radon and the ingress of radon into houses. Radon-222, the isotope of particular concern, is an inert, radioactive gas that occurs everywhere in soil and rock. It is a decay product of radium-226, a member of the uranium-238 decay series that is ubiquitous in the earth's crust. Radon-220 of the thorium-232 decay series is also present but is of less concern than radon-222, mainly because it has a short half-life (56 seconds, compared with 3.8 days for radon-222). Several factors determine the movement of radon from its source location in the rock or soil into a house's basement (Nazaroff et al., 1988). They include the soil's permeability to gases, the pressure difference between the soil and the basement, the soil's emanation capability (the ratio of radon produced to radon actually emanated from the soil), and the concentration in the soil of radon's parent, radium. In this context, it is of interest to examine the large-scale distribution of radium in California. It is assumed in this examination that radium is in radioactive equilibrium with its ultimate parent, uranium. With this assumption, we used the large database provided by airborne gamma-radiometric surveys for uranium (the NARR program (Moed et al., 1984)) and a database covering the concentration and distribution of uranium in California rocks.

COMPILATION AND RESULTS

The geographic distribution of radium in soils in northern and central California is compared with the lithologic setting. The extensive database at Lawrence Berkeley Laboratory on the concentrations of radioelements in rock of northern and central California provided mean radium concentrations of lithologic units. These concentrations were applied to the fractions of total area occupied by specific lithologic units as estimated from the 1:2,500,000-scale geologic map of California (CDMG/USGS, 1966) in a band that is two 1 × 2° quadrangles (4° in longitude) in width and extends from southern Oregon to southern California. The geographic distribution of aeroradiometrically determined and lithologically weighted mean Ra concentrations is shown in Fig. 1. Lack of a sufficient Ra-lithologic database for southern California rocks currently precludes the inclusion of lithologic estimates for rocks south of latitude 35°N.

DISCUSSION

A general north-to-south increase in Ra is evident between 43 and 36°N, then Ra decreases southward. This pattern may be explained primarily by (1) the relatively large abundance of basic to ultrabasic intrusive rocks, generally low in uranium, that contributed substantially to soils of northwestern California and southwestern Oregon, (2) a substantial contribution to central California Coast Range soils by the Franciscan formation, and (3) an increasing contribution to central and south-central California soils from relatively high-uranium rocks of the Sierra Nevada batholith and granitic plutons and intermediate to acidic volcanic rocks of the Coast Ranges. The trend in mean Ra estimated from lithology matches that from the aeroradiometric data, though there are substantial discrepancies between aeroradiometrically and lithologically estimated means for quadrangles in central California. This discrepancy is most evident in Fig. 2, where mean Ra concentrations determined by the two methods are compared. The aeroradiometric mean Ra concentrations are substantially higher than those estimated from lithology in the San Jose, Santa Cruz, San Francisco, and San Luis Obispo quadrangles by factors of 2.2, 1.7, 1.5, and 1.6, respectively. However, despite these discrepancies, the region-wide overall lithologically weighted and aeroradiometric Ra concentrations are similar, 0.7 (± 0.3) and 0.8 (± 0.4) pCi/g, respectively.

The anomalously high Ra in the San Jose quadrangle was considered by Revzan and Nero (1988). The contour plot of Ra distribution in the quadrangle (Fig. 3) shows a strong east–west Ra high near the quadrangle's northern border that is not obviously explainable lithologically, nor is there an obvious lithological explanation for the high-Ra zone in the southern part of the quadrangle. These zones of apparent high Ra are not matched by corresponding highs in the NARR "thorium" channel (^{208}Tl) data, nor is the northern anomaly matched by a similar pattern in the southern portion of the Sacramento quadrangle, immediately to the north.

A ground-borne gamma-spectral measurement and sampling traverse was conducted across the anomalous areas on the west side of the San Joaquin Valley, with sampling sites in open fallow fields spaced 2 to 3 miles apart. This traverse (Fig. 4) shows essentially no concordance of apparent Ra

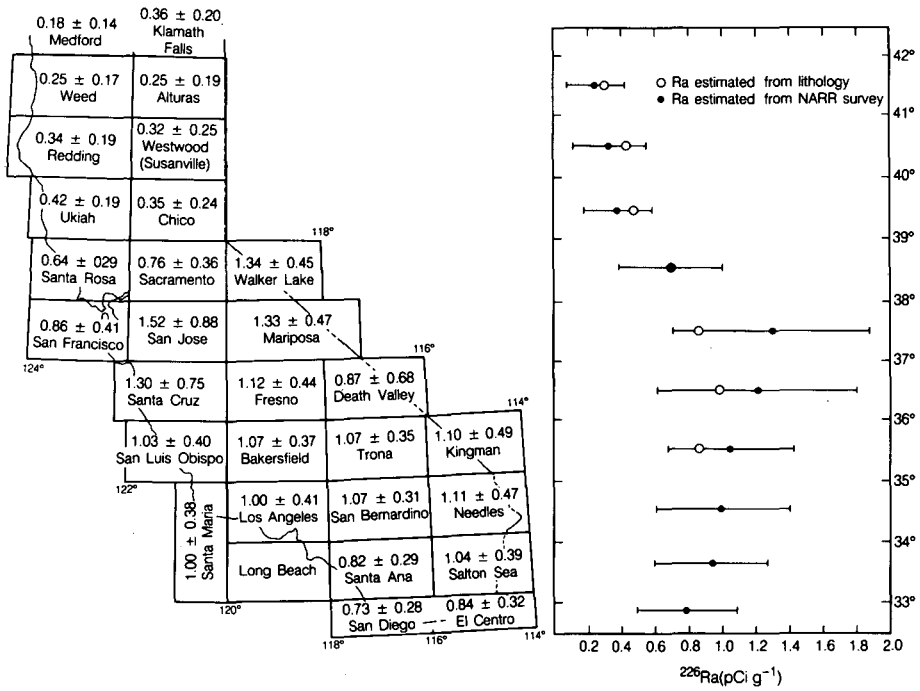

Figure 1. **(Left)** Map of California, showing mean and standard deviations of ^{226}Ra concentrations in 1 × 2° quadrangles, determined from NARR data (Moed at al., 1984). **(Right)** Plots of data from map at left (solid circles and error bars) and of Ra concentrations estimated from lithology (open circles) in a 4°-longitude-wide band along the Pacific coast from 43 to 33°N. [XBL 8811-10565]

concentrations (from ground-borne measurement of ^{214}Bi gamma radioactivity) with aeroradiometrically determined apparent Ra. With the exception of three stations, apparent Ra determined from ground measurements is substantially lower than the Ra determined from the airborne survey. We therefore suspect that the aeroradiometrically determined Ra in the San Jose quadrangle is artificially high, due perhaps to improper operation of the airborne gamma spectrometer system or to conduct of the survey during a period of atmospheric inversion, when airborne ^{222}Rn might have concentrated in the relatively low-altitude zone of aircraft operations. A recent compilation of aeroradiometric Ra, Th, and K data by counties in the U.S. (Revzan, 1988) also supports the supposition that the Ra data are in error. The counties of San Joaquin, Stanislaus, and Merced, which make up a large portion of the San Jose quadrangle, have substantially higher aeroradiometric Ra concentrations, than adjacent counties. These Ra concentrations are also not commensurate with corresponding average Th and K concentrations, which are similar to those of counties to the north and south of this zone in the Central Valley. Similar examinations of the NARR Ra data for the Santa Cruz, San Francisco, and San Luis Obispo quadrangles and accompanying field checks are necessary to determine the causes of their also apparently high, aeroradiometrically determined Ra concentrations.

CONCLUSION

Though standard deviations of mean Ra concentrations are large and outcrop-area percentages are estimated, it appears that, with the exception of some anomalously high aeroradiometrically determined Ra concentrations, the north-to-south regional variation of Ra in northern and central California is attributable to lithology. Care must be taken to verify aeroradiometrically determined data before they are used to help predict areas of relatively high radon production.

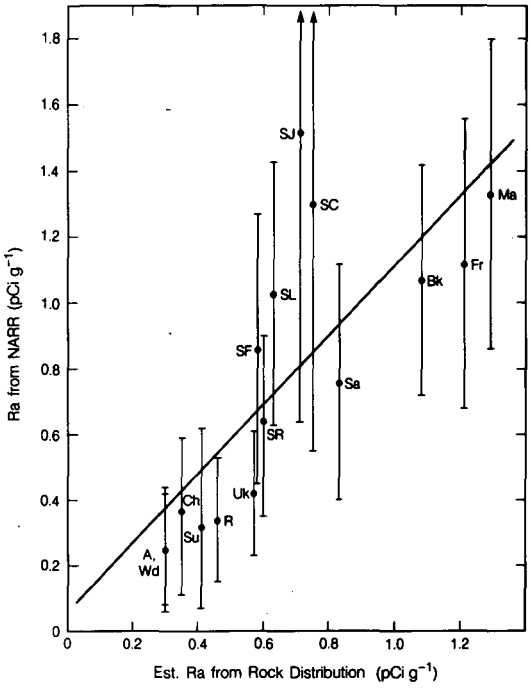

Figure 2. Comparison of ^{226}Ra in 1 × 2° quadrangles, determined from NARR data (Moed et al., 1984) with Ra in quadrangles estimated from lithology. Best-fit (r^2 = 0.60) is indicated. Quadrangle abbreviations: A = Alturas, Bk = Bakersfield, Ch = Chico, Fr = Fresno, Ma = Mariposa, R = Redding, Sa = Sacramento, SF = San Francisco, SJ = San Jose, SL = San Luis Obispo, SC = Santa Cruz, SR = Santa, Rosa, Su = Susanville, Uk = Ukiah, Wd = Weed. [XBL 8811-10566]

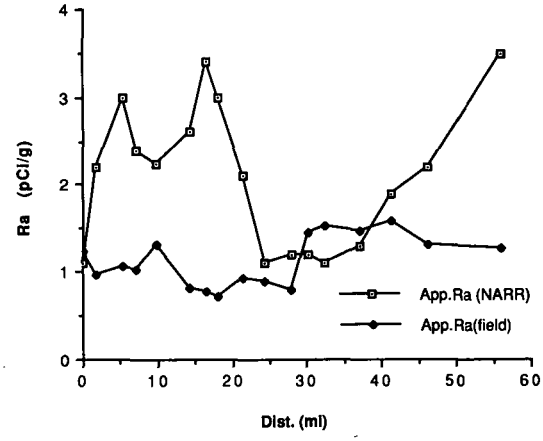

Figure 4. Comparison of aeroradiometric and ground-borne determinations of radium in soil along a north–south transcent on the west side of the San Joaquin Valley, San Jose quadrangle. [XBL 895-1990]

REFERENCES

CDMG/USGS, 1966. Geologic map of California. Compiled by the California Divison of Mines and Geology and the U.S. Geological Survey.

Moed, B.A., Nazaroff, W.W., Nero, A.V., Schwehr, M.B., and Van Heuvelen, A., 1984. Identifying areas with potential for high indoor radon levels: Analysis of the National Airborne Radiometric Reconnaissance data for California and the

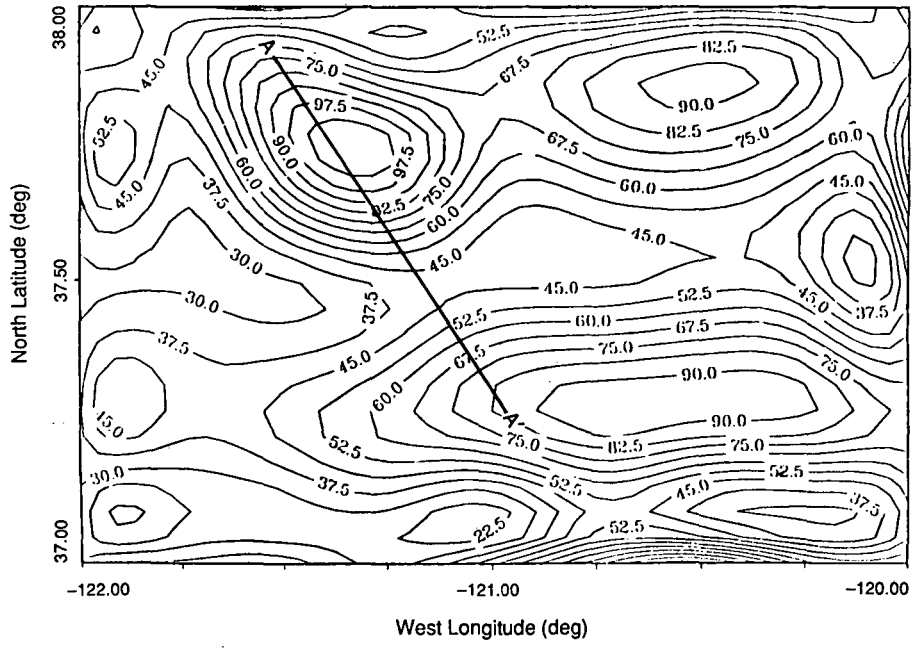

Figure 3. Contour map of Ra in soil (in Bq-kg^{-1} soil; 1 pCi-g^{-1} = 37 Bq-kg^{-1} in the San Jose quadrangle (Revzan and Nero, 1988). The ground-borne traverse is also indicated (A-A'). [XBL 895-1989]

Pacific Northwest. Lawrence Berkeley Laboratory Report LBL-16955.

Nazaroff, W.W., Moed, B.A., and R.G. Sextro, 1988. Soil as a source of indoor radon: Generation, migration, and entry. *In* W.W. Nazaroff and A.V. Nero (eds.), Radon and Its Decay Products in Indoor Air. Wiley Interscience, New York, p. 57–112.

Revzan, K.L., 1988. Supplemental information on the National Aerial Radiometric Reconnaissance (NARR) database. Lawrence Berkeley Laboratory Report LBID-1453.

Revzan, K.L., and A.V. Nero, 1988. Mapping surficial radium content of U.S. Soil as a partial indicator of indoor radon concentrations. *In* Proceedings, Fourth International Symposium on the Natural Radiation Environment, Lisbon, Portugal, December 7–11, 1987. Rad. Prot. Dosim., v. 24, p. 179–184.

APPENDIXES

APPENDIX A: ABSTRACTS OF JOURNAL ARTICLES

Bodvarsson, G.S., 1988. Model predictions of the Svartsengi reservoir, Iceland. Water Resour. Res., v. 24, no. 10, p. 1740–1746 (LBL-21253).

Several models have been developed of the Svartsengi geothermal field and used to predict the future pressure drawdown due to exploitation. These are based upon different reservoir geometries and recharge patterns. All of them neglect the effect of a two-phase zone overlying the main reservoir. A numerical model is developed that includes the effect of the two-phase zone and the reservoir parameters determined and predicted pressure drawdown are compared to previous estimates. It is found that the assumed recharge patterns and two-phase zones have significant impact upon the long-term pressure drawdown predictions

Bodvarsson, G.S., 1988. Reservoir development strategy for hot water reservoirs with emphasis on reservoir modeling. Geoth. Resour. Counc. Bull., v. 17, no. 4, p. 69–90 (LBL-26901).

The physical properties of geothermal systems, the processes that control their behavior, and conceptual models of various fields are briefly reviewed. Different reservoir assessment methods are described, with emphasis on numerical modeling approaches. Finally, short discussions are given on injection, fracture flow, geochemical modeling and power plant sizes.

Bodvarsson, G.S., Pruess, K., and Lippmann, M.J., 1987. Numerical evaluation of geothermal systems. Rev. Brasileira Geofis., v. 5, p. 311–318 (LBL-26971).

In the last few years the geothermal group of the Lawrence Berkeley Laboratory has developed comprehensive expertise in numerical modeling of geothermal systems. We have carried out detailed simulations of various fields in the U.S.A. (Baca, New Mexico; Heber, California); Mexico (Cerro Prieto); Iceland (Krafla); and Kenya (Olkaria). These simulation studies have illustrated the usefulness of numerical models for the overall evaluation of geothermal systems. The methodology for modeling the behavior of geothermal systems, different approaches to geothermal reservoir modeling and how they can be applied in comprehensive evaluation work are discussed.

Carle, S.F., 1988. Three-dimensional gravity modeling of the geological structure of Long Valley caldera. J. Geophys. Res., v. 93, no. B11, p. 13,237–13,250 (LBL-23788).

A 48-mGal gravity low coincides with Long Valley caldera and is mainly attributed to low-density caldera fill. Gravity measurements by Unocal Geothermal have been integrated with U.S. Geological Survey data, vastly improving gravity station coverage throughout the caldera. A strong regional gravity trend is mainly attributed to isotasy. A "best fitting" (based on regional control of basement densities) Airy-Heiskanen isostatic model was used for the regional correction. A three-dimensional, multiple-unit gravity modeling program with iterative capabilities was developed to model the residual gravity. The density structure of Long Valley caldera and vicinity was modeled with 22 discrete density units, most of which were based on geologic units. Information for drill hole lithologies, surface geology, and structural geology interpretations constrain the model. Some important points revealed by the three-dimensional gravity modeling are that (1) the volume of ejected magma associated with the Bishop Tuff eruption is greater than previously thought, (2) the caldera structure is strongly influenced by precaldera topography and the extensions of major, active faults, (3) the main west ring fracture is coincident with the Inyo Domes–Mono Craters fracture system, (4) a relatively low-density region probably underlies the caldera, and (5) a silicic magma chamber may underlie Devils Postpile.

Carnahan, C.L., 1988. Some effects of data base variations on numerical simulations of uranium migration. Radiochim. Acta, v. 44/45, p. 349–354 (LBL-16817).

Numerical simulations of migration of chemicals in the geosphere depend on knowledge of identities of chemical species and on values of chemical equilibrium constants supplied to the simulators. In this work, some effects of variability in assumed speciation and in equilibrium constants were examined, using migration of uranium as an example. Various simulations were done of uranium migration in systems with varying oxidation potential, pH, and major component content. A simulation including formation of aqueous species UO_2^{2+}, $UO_2CO_3^0$, $UO_2(CO_3)_2^{2-}$, $UO_2(CO_3)_3^{4-}$, $(UO_2)_2CO_3(OH)_3^-$, UO_2^+, $U(OH)_4^0$, and $U(OH)_5^-$ is compared to a simulation excluding formation of UO_2^+ and $U(OH)_5^-$. These simulations relied on older data bases, and they are compared to a further simulation using recently published data on formation of $U(OH)_4^0$, $(UO_2)_2CO_3(OH)_3^-$, $UO_2(CO_3)_3^{5-}$, and $U(CO_3)_5^{5-}$. Significant differences in dissolved uranium concentrations are noted among the simulations. Differences are noted also in precipitation of two solids, $USiO_4$(c) (coffinite) and $CaUO_4$(c) (calcium uranate), although the solubility products of the solids were not varied in the simulations.

Cummins, P., and Johnson, L., 1988. Synthetic seismograms for an inner core transition of finite thickness. Geophys. J., v. 94, p. 21–34 (LBL-23716).

We describe calculations for short-period body waves that interact with an inner-outer core transition of finite thickness. This involves development of a hybrid full wave-reflectivity algorithm which is used to calculate synthetic seismograms for earth models with various transition thicknesses. The numerical results indicate that the frequency content of reflected short-period PKiKP waveforms observed at distances less than 40° is very sensitive to the thickness of the transition zone. Comparison with published data in this distance range indicates that the inner core transition must be less than 5 km thick. In the distance range 60–90°, effective decoupling of short-period PKiKP and PKJKP is achieved for transition zones as thin as 3 km, resulting in substantial distortion of the PKiKP waveform. PKIKP + PKiKP waveforms in the distance range 120–130° are not as sensitive to the detailed properties of the transition, but the signal quality is good enough to constrain the transition thickness to be less than 10 km.

Cummins, P., and Johnson, L.R., 1988. Short-period body wave constraints on properties of the earth's inner core boundary. J. Geophys. Res., v. 93, no. B8, p. 9058–9074 (LBL-24719).

In this study we model short-period waveform data in an attempt to constrain the *P* and *S* velocity structure at the Earth's inner core boundary (ICB). The data set consists of recordings from 10 events in the South Pacific, and the data selection criteria as well as methods of analysis were designed to avoid problems with receiver response often associated with short-period waveform data. These data are modeled using a calculation technique that facilitates the consideration of a wide variety of models for the ICB. Results suggest that Q_α in the inner core has the frequency dependence proposed by Doornbos (1983). The data determine the *P* velocities above and below the ICB to within a trade-off that is well constrained by the data. For example, with a *P* velocity structure above the ICB given by

PREM, the P velocity below the ICB is 11.03 ± 0.03 km/s. Similarly, for the data analyzed here the estimate of the S velocity at the top of the inner core trades off with the estimate of Q_α, but we use the Q_α model of Doornbos (1983) to estimate the jump in S velocity to be 3 ± 1 km/s.

Daley, T.M., McEvilly, T.V., and Majer, E.L., 1988. Analysis of *P* and *S* wave vertical seismic profile data from the Salton Sea Scientific Drilling Project. J. Geophys. Res., v. 93, no. B11, p. 13,025–13,036 (LBL-22246).

As part of the Salton Sea Scientific Drilling Project at California State well 2–14, vertical seismic profile (VSP) data were collected from P and S wave sources at two distances from the well. Use of a three-component geophone, along with rotation of the recorded data traces into a wave front-based coordinate system, allows analysis of many aspects of seismic wave propagation properties around the well. Standard VSP analysis techniques were used to measure interval P and S wave velocities and to identify reflection horizons both within and below the survey interval (from 455 to 1735 m). A reflection from below the survey interval, seen with both P and S sources, seems to be associated with a fractured reservoir near 2100 m. Indications of fracturing were observed, including vertical scattering of P waves from a zone near 915 m. Orthogonally polarized shear waves were generated at each offset to study anisotropy by travel time measurement and particle motion analysis of the shear wave arrivals. Three-component particle motion analysis of shear wave arrivals was found to be effective for characterizing the subtleties in the S wave splitting throughout the various zones in the well. The SH_1 source (horizontal and transverse to the well) produced complicated, elliptical particle motion while the SV source (in-line with the well) produced linear particle motion. The difference in linearity of particle motion from orthogonally polarized shear wave sources was unexpected and may be related to regional tectonics. Anomalous zones may be related to transition depths in the Salton Sea geothermal field. Travel time difference between SV and SH waves, while clearly observable, indicates only about 1% average anisotropy.

Daley, T.M., McEvilly, T.V., and Majer, E.L., 1988. Multiply-polarized shear wave VSPs from the Cajon Pass drillhole. Geophys. Res. Lett., v. 15, no. 9, p. 1001–1004 (LBL-25289).

A 3-component VSP data set was acquired in the Cajon Pass Drillhole, with a multiply-polarized shear-wave source and a conventional P-wave source, producing a 9-component data set. The VSP data show effects on the full wavefield from the sediment-granite interface. Mode-converted waves are identified, with significant scattering of S-wave energy from the leading P-wavefront. Hodographs are used to display S-wave particle motions in two dimensions. Shear-wave splitting is observed in the hodographs. The shear-wave particle motion is used to infer anisotropy orientation with respect to the local strike of the San Andreas fault. Stress-induced fracturing is assumed to be a possible cause of the shear-wave splitting. A variation of particle motion orientations with depth is observed, implying a variation in anisotropy orientation as a function of depth.

Doughty, C., and Pruess, K., 1988. A semianalytical solution for heat-pipe effects near high-level nuclear waste packages buried in partially saturated geological media. Int. J. Heat Mass Transfer, v. 31, no. 1, p. 79–90 (LBL-23023).

The emplacement of a strong heat source, such as a high-level nuclear waste package, in a partially saturated permeable medium will give rise to the development of a heat pipe. The present paper analyzes a simplified version of this problem that has a steady state solution, for radial geometry. The solution is obtained in semianalytical form, and is compared to the analogous solution for a linear heat pipe. Various applications are presented for porous as well as for fractured-porous media with different hydrologic properties. The parameters determining heat-pipe length and the question of whether the vicinity of the heat source dries up are discussed. The semianalytical solution is verified by numerical simulations that show the transient evolution from uniform initial conditions to the eventual steady state.

Gauglitz, P.A., and Radke, C.J., 1988. An extended evolution equation for liquid film breakup in cylindrical capillaries. Chem. Eng. Sci., v. 43, no. 7, p. 1457–1465 (LBL-25967).

The dynamics of a viscous liquid film forming lenses or stable collars and the static stability of such collars are investigated in straight cylindrical capillaries for various approximations of the Young-Laplace equation. We find that the leading order approximation of the Young-Laplace equation in a thin-film expansion does not predict the known instability of wetting collars forming lenses. Hence, we propose a simple approximation that does. Numerical solution of the new extended evolution equation for a film in a tube of radius R_T^* gives a critical film thickness of 0.12 R_T^*, which demarks the transition between films that evolve into stable collars and those that break up to form lenses. New experimental measurements of the critical thickness agree well with the theoretical result, confirming the validity of the proposed evolution equation.

Gauglitz, P.A., St. Laurent, C.M., and Radke, C.J., 1987. An experimental investigation of gas-bubble breakup in constricted square capillaries. J. Pet. Technol., v. 39, no. 9, p. 1137–1146 (LBL-25305).

Recent advances in EOR involve generating foam within underground porous media to displace the oil. We investigate the important snap-off mechanism of gas-bubble generation in constricted square capillaries experimentally. The snap-off of smaller bubbles from a larger bubble as it moves through the constriction is recorded on 16-mm movies. The time required for bubbles to snap off once they move past the constriction and the length of the generated bubbles are obtained from viewing the movie frames. The bubble capillary number, $\mu v_T/\sigma$, is varied from 10^{-5} to 5×10^{-3} by adjusting the wetting-fluid viscosity, μ, and the surface tension, σ, by adding aqueous surfactants to mixtures of glycerol and water, and by altering the bubble velocity, v_T.

Results show that a dimensionless time to snap-off depends weakly on the capillary number and that the generated bubble size increases almost linearly with increasing capillary number. Surfactants create dynamically immobile interfaces for surfactant solutions of 1 wt% sodium dodecyl benzene sulfonate (SDBS) and Chevron Chaser SD1000®. Compared with the surfactant-free solutions, the time to breakup with surfactants increases by a factor of about 3; generated bubble length increases by a factor of at most 3.

Gauglitz, P.A., St. Laurent, C.M., and Radke, C.J., 1988. Experimental determination of gas-bubble breakup in a constricted cylindrical capillary. Ind. Eng. Chem. Res., v. 27, p. 1282–1291 (LBL-26741).

To gain insight into the mechanisms of gas-foam generation in porous media, this work quantifies how smaller bubbles snap off from a single, larger bubble as it moves through a smooth, cylindrical constriction. Time to snap off, generated bubble size, and bubble velocity are obtained from viewing 16-mm movies taken of snap-off events. The bubble capillary number, Ca_T is varied from 10^{-5} to 5×10^{-2}. We study two narrowly constricted capillaries of different tube radii (neck radius/tube radius of 0.17 and 0.20) and one widely constricted capillary (neck radius/tube radius = 0.40). In the widely constricted capillary, time to breakup is proportional to Ca_T^{-2}, and the generated bubble length is proportional to Ca_T^{-2}. In the narrow constrictions, the same results apply above $Ca_T = 5 \times 10^{-4}$; below this critical Ca_T, time to breakup is independent of Ca_T but depends on the Ohnesorge number. Snap-off behavior with surfactant solutions is found to be similar to that in surfactant-free solutions.

Goldstein, N.E., 1988. Pre-drilling data review and synthesis for the Long Valley caldera. Eos: Trans. Am. Geophys. Union, v. 69, no. 3, p. 43–45 (LBL-23486).

A 2-day symposium was held at the Lawrence Berkeley Laboratory (LBL) on March 17–18, 1987, to review a large body of scientific investigations for the Long Valley Caldera and to discuss concepts and models for the present-day magmatic-hydrothermal system. Speakers at the symposium also addressed the problem of where to locate future scientific drill holes in the caldera.

Deep scientific drilling projects such as those being contemplated by the U.S. Department of Energy (DOE) Geothermal Technologies Division (GTD), under the Magma Energy Program, and by the DOE Office of Basic Energy Sciences (OBES) along with the U.S. Geological Survey (USGS) and the National Science Foundation (NSF), under the Continental Scientific Drilling Program (CSDP), will be major and expensive national undertakings that will require strong support from geoscientists and engineers and from industry and government-supported laboratories. DOE/OBES is sponsoring a program of relatively shallow core holes (less than 1 km) in the caldera, and DOE/GTD is considering the start of a deep (6-km) hole for geophysical observations and sampling of the near-magmatic environment as early as fiscal year (FY) 1988.

Goldstein, N.E., 1988. Subregional and detailed exploration for geothermal-hydrothermal resources. Geothermal Sci. Technol., v. 1, no. 4, p. 303–432 (LBL-26962).

Geothermal exploration is a relatively new area of applied science that has evolved rapidly over the last 15 years or so in response to the challenge of developing alternative energy sources. Prior to 1965 most exploration was done by the pioneering countries in the field of geothermal development: New Zealand, Iceland, France, and Italy. The techniques applied were derived mainly from those used for studying active volcanos and for mineral exploration. The need for improved techniques gained impetus as the more obvious and accessible areas were drilled and developed, and attention focused on exploring areas where greater exploration risks and uncertainties existed. Aided by the Geothermal Energy Act of 1974, the U.S. Department of Energy (DOE) has been able to foster much needed research and development that, coupled with case studies, has provided improved tools and techniques to the private sector for data acquisition and interpretation. The case-study investigations supported by DOE in Nevada, the Cascade Range, Cerro Prieto, Roosevelt Hot Springs, and the Valles Caldera, among other places, and the detailed scientific investigations by the U.S. Geological Survey at The Geysers, Long Valley caldera, and Yellowstone National Park, to name but a few systems studied, have provided a greater depth of understanding of the thermophysical, thermochemical, and hydrogeologic processes and parameters associated with a variety of hydrothermal-geothermal systems. Together with corroborating subsurface information gained from many wells, the exploration-technology research has provided substantial benefits to the geothermal industry mainly by putting existing tools and techniques on a sounder scientific basis, by providing better interpretative methods, by assembling a vast amount of basic data, and by improving cost-effectiveness of certain methods.

Goldstein, N.E., and Stein, R.S., 1988. What's new at Long Valley. J. Geophys. Res., v. 93, no. B11, p. 13,187–13,190 (LBL-25681).

At few places in the conterminous United States does magma, the raw material of the Earth's crust and mantle, appear as tantalizingly close to the surface as at Long Valley caldera in eastern California. Here the search for a site to drill into a magma chamber for the purpose of geothermal energy development coincides with a separate scientific imperative, the need to monitor the caldera for potential hazards due to earthquakes and volcanic eruptions. The region has a proven potential for these hazards; five $M \geq 6$ earthquakes have struck since 1978, and phreatic, ash and steam, eruptions have occurred as recently as 550–600 years ago. As we assess the results of additional intermediate depth holes and the results from a widening spectrum of divining tools, the magma seems farther from the surface and less abundant than it did just a few years ago. We have also begun to discern the profound imprint of structures which predate the formation of the caldera 0.73 Ma and which now appear to control its eruptive behavior and hydrothermal system.

To help plan future drilling of the caldera, a symposium was held at Lawrence Berkeley Laboratory in California in 1987. Most of the papers which appear in this issue were born at that conference. Special sections of the *Journal of Geophysical Research* devoted in part or in total to the caldera appeared in 1976, 1984, and 1985. The Geothermal Technologies Division of the Department of Energy plans to begin drilling the first phase of a deep hole in 1988, which is hoped to reach conditions close to the solidus temperature of a silicic melt at a depth of 6 km.

Hellstrom, G., Tsang, C.F., and Claesson, J., 1988. Combined forced-convection and buoyancy flow at a two-fluid interface in a porous medium: Analytical studies. Water Resour. Res., v. 24, no. 4, p. 507–515 (LBL-24753).

The motion of a two-fluid interface in an aquifer is a combination of buoyancy flow and forced convection. The buoyancy flow, which is due to density variations of the fluid, and the forced convection, which acts on the viscosity variations, will cause the two-fluid interface to tilt. The basic case of a plane interface between two immiscible fluids of different density and viscosity in an infinite anisotropical aquifer bounded by two horizontal planes is analyzed in detail. The groundwater flow in the aquifer is treated as a superposition of buoyancy flow and forced convection. The buoyancy flow and the forced-convection components are shown by analytical methods to be related to each other. The tilting angle of the two-fluid interface is given by a simple formula containing only two parameters. There exists a certain stationary tilting angle, the stability of which depends on the two viscosities.

Hellstrom, G., Tsang, C.F., and Claesson, J., 1988. Buoyancy flow at a two-fluid interface in a porous medium: Analytical studies. Water Resour. Res., v. 24, no. 4, p. 493–506 (LBL-24754).

Analytical solutions for the pressure distribution and the flow field are derived for several idealized situations involving an injection well and a vertical plane or cylindrical interface between two fluids of different density and viscosity in an infinite anisotropic aquifer bounded by two horizontal planes. The interface, or transition zone, between the two fluids may be either sharp or of finite width. The buoyancy flow induced by the density difference will cause the two-fluid interface to tilt. A characteristic time scale for the buoyancy tilting rate is deduced. The conditions at the well are found to have only a small influence on the buoyancy flow except very close to the well. The buoyancy flow decreases with increasing width of the transition zone.

Javandel, I., Tsang, C.F., and Witherspoon, P.A., 1988. Hydrologic detection of abandoned wells near proposed injection wells for hazardous waste disposal. Water Resour. Res., v. 24, no. 2, p. 261–270 (LBL-21888).

Deep saline aquifers are being used for disposal of hazardous liquid wastes. A thorough knowledge of the competency of such aquifers and their confining geologic beds in permanently isolating the hazardous substances is the key to successful disposal operations. Characterization of such systems, and in particular the detection of any conduit that may permit hydraulic communication between the host aquifer and nearby freshwater aquifers, must be carried out prior to the initiation of disposal projects. In deep, multi-aquifer systems, leaky faults, abandoned wells, highly conductive fractures, or shear zones may all provide leakage paths. If not initially detected, such conduits may show no apparent effect until contaminants in the freshwater aquifer reach detectable levels at the discharge point. By then, of course, detection is generally too late. This paper is an attempt to address the problem of initial detection of improperly plugged or open abandoned wells. A new analytic solution has been derived to calculate the amount of leakage from an abandoned well and the corresponding drawdown at monitoring wells. A method is proposed that can be used to detect such deep abandoned wells in the area of influence of a proposed deep injection well in a multiple-aquifer system

Jensen, D.J., and Radke, C.J., 1988. Caesium and strontium diffusion through sodium montmorillonite at elevated temperature. J. Soil Sci., v. 39, p. 53–64 (LBL-22078).

Counter ionic migration rates of dilute Cs^+ and Sr^{2+} against sodium in a Na-montmorillonite gel are measured using a radially perfused diffusion cell. Enhanced or surface diffusion for caesium is observered both at ambient and elevated temperature. To quantify these surface diffusivities the ion-exchange properties of the diffusing species are required. Thus, exchange isotherms for caesium against sodium on montmorillonite at 22 and 90°C are given for 10^{-1}, 10^{-2}, and 10^{-3} M background NaCl concen-

trations. Caesium counterion surface diffusivities at 22 and 90°C are 2.2×10^{-6} and 8.0×10^{-6} cm^2s^{-1}, respectively. These values are found to be essentially independent of background ionic strength over the range 10^{-3} to 10^{-1} M NaCl. Experimental evidence of enhanced transport Na-montmorillonite for the divalent cation Sr^{2+} is also confirmed with a surface diffusivity of 2×0^{-6} cm^2s^{-1} at 22°C and in 10^{-1} M NaCl.

Jensen, D.J., and Radke, C.J., 1988. Chromatographic transport of alkaline buffers through reservoir rock. SPE Res. Eng., v. 3, no. 3, p. 849–856 (LBL-26738).

Use of relatively low-pH alkaline buffers, such as sodium carbonate or sodium silicate, is explored as a means for overcoming sodium/hydrogen ion-exchange delay in alkaline waterflooding. A local equilibrum chromatographic model is outlined to describe the concentration velocities for injection of alkaline buffers into a linear porous medium that exhibits reversible sodium/hydrogen exchange. The theory predicts a buffer ion-exchange wave that is substantially faster than that for equivalent-pH sodium/hydrogen solutions, H^3-tagged water, and ^{14}C-tagged carbonate. The experiments confirm that Na_2CO_3 propagates through the Berea sand at a higher rate than NaOH. For example, at pH = 11.4, Na_2CO_3 migrates with a velocity that is 3.5 times faster than NaOH.

New experimental displacement data are presented for NaOH over a pH range from 11 to 13 and for 0.1, 0.5, and 1.0 wt% Na_2CO_3 flowing through a 1 wt% NaCl brine saturated Berea sandstone core at 50°C [122°F]. To permit a complete description of the system, column effluent concentrations are measured for sodium ions, hydroxide ions, H_3-tagged water, and ^{14}C-tagged carbonate. The experiments confirm that Na_2CO_3 propagates through the Berea sand at a higher rate than NaOH. For example, at pH = 11.4, Na_2CO_3 migrates with a velocity that is 3.5 times faster than NaOH.

Comparison of experiment with the ion-exchange chromatography theory shows good agreement. We successfully model the concentration histories of tritium-labeled water, total carbon, sodium, and hydroxide, all with no adjustable parameters.

This work establishes with both theory and experiment that buffered alkali significantly increases the propagation speed of hydroxide in reservoir sands in comparison with unbuffered alkali at equivalent sodium and hydroxide concentrations. Because lower-pH buffered alkali can also protect against rock dissolution loss, the validated reduction of buffer ion-exchange lag considerably improves the promise of the alkaline flooding process for field application.

Karasaki, K., Long, J.C.S., and Witherspoon, P.A., 1988. Analytical models of slug tests. Water Resour. Res., v. 24, no. 1, p. 115–126 (LBL-23948).

In the present paper, attempts are made to develop solutions to various models of slug tests that may be applicable in analyzing the results of such tests where existing solutions are inadequate. Various geometries that may be encountered in heterogeneous systems such as fractured rocks are considered. Solutions are presented for linear flow, radial flow with boundaries, two layer, and concentric composite models with different flow geometries between the inner and outer region. Solutions are obtained in Laplace space and inverted back to real space numerically. Type curves are presented for each solution. Analyses of the type curves and derivative response curves reveal that many curves have unique shapes only for certain combinations of the flow parameters and the distance. Other sets of type curves are similar in shape, although log-log plots and derivative plots may emphasize some features that may not be apparent in semilog plots. These results show that slug tests suffer problems of nonuniqueness to a greater extent than other well tests.

Karasaki, K., Long, J.C.S., and Witherspoon, P.A., 1988. Analytic model for fracture-dominated reservoirs. SPE Form. Eval., v. 3, no. 1, p. 242–250 (LBL-23441).

A new analytic model for analyzing well test data from fracture-dominated reservoirs is presented. It is a concentric composite model with a finite-radius well located in the center. In the inner region the flow is assumed to be linear, and in the outer region the flow is assumed to be radial. Solutions are obtained analytically and type curves for ranges of dimensionless parameters are presented. The model can be used to find the extent and the flow parameters of the fractures near the well and the average values for the entire system provided that wellbore-storage effects do not mask the early-time data.

Khorrami, P., and Radke, C.J., 1988. A random-scission model for chemical degradation of polymer solutions. SPE Res. Eng., v. 3, no. 1, p. 349–352 (LBL-20788).

A rigorous but simple deterministic model is presented to quantify chemical degradation of high-molecular-weight polymer solutions undergoing random bond scission. Molecular-weight alteration is characterized by a fundamental rate constant, k, whose inverse represents the average lifetime of a polymer chain bond. Evaluation of the proposed random-scission model (RSM) against known Monte Carlo (MC) calculations shows complete agreement.

Given the molecular-weight decline from the RSM, we establish the corresponding polymer solution viscosity loss using the semiempirical Martin equation along with the Mark-Houwink relationship for intrinsic viscosity. Comparison of the RSM viscosity predictions against the chemical degradation data of Shupe for partially hydrolyzed polyacrylamide gives good agreement. Thus, a new tool is available to predict polymer chemical degradation and viscosity loss at reservoir time scales and conditions.

Lam, S.T., Hunsbedt, A., Kruger, P., and Pruess, K., 1988. Analysis of the Stanford geothermal reservoir model experiments using the LBL reservoir simulator. Geothermics, v. 17, no. 4, p. 595–605 (LBL-25957).

This paper describes the results of an analysis of data obtained from a series of heat-sweep experiments performed in the Stanford Geothermal Reservoir Model using the Lawrence Berkeley Laboratory reservoir simulator. The physical reservoir model is an experimental system consisting of a pressure vessel which contains a granite rock matrix with production and recharge capabilities to simulate the heat-sweep process in a fractured hydrothermal reservoir under liquid-phase conditions.

Arrangements were made with the Lawrence Berkeley Laboratory to test their geothermal reservoir simulator on the physical model data. The objectives were to provide insight into the detailed physical process occurring in the relatively complex physical system and to provide feedback to LBL on the capability and possible improvements to the LBL reservoir simulator to model a complex physical system.

The overall conclusion of this work is that the LBL simulator does an excellent job of predicting the physical processes in the Stanford Geothermal reservoir Model experiments for extreme thermal gradient conditions and for a system with very complex boundary conditions. The analysis demonstrates the importance of specifying relevant parameters accurately to provide adequate modeling for the important physical processes.

Lippmann, M.J., and Bodvarsson, G.S., 1987. Convective heat transport in geothermal systems. Rev. Brasileira Geofis., v. 5, p. 301–310 (LBL-26973).

Most geothermal systems under exploitation for direct use or electrical power production are of the hydrothermal type, where heat is transferred essentially by convection in the reservoir, conduction being secondary. In geothermal systems, buoyancy effects are generally important, but often the fluid and heat flow patterns are largely controlled by geologic features (e.g., faults, continuity of layers) and location of recharge and discharge zones. During exploitation, these flow patterns can drastically change in response to pressure and temperature declines, and changes in recharge/discharge patterns.

Convective circulation models of several geothermal systems, before and after start of fluid production, are described, with emphasis on different characteristics of the systems and the effects of exploitation on their evolution. Convective heat transport in geothermal fields is discussed, taking into consideration (1) major geologic features; (2) temperature-dependent rock and fluid properties; (3) fracture-versus porous-medium characteristics; (4) single-versus two-phase reservoir systems; and (5) the presence of noncondensible gases.

Majer, E.L., McEvilly, T.V., Eastwood, F.S., and Myer, L.R., 1988. Fracture detection using *P*-wave and *S*-wave vertical seismic profiling at The Geysers. Geophysics, v. 53, no. 1, p. 76–84 (LBL-20100).

In a pilot vertical seismic profiling study, *P*-wave and cross-polarized *S*-wave vibrators were used to investigate the potential utility of shear-wave anisotropy measurements in characterizing a fractured rock mass. The caprock at The Geysers geothermal field was found to exhibit about an 11 percent velocity variation between *SH*-wave and *SV*-waves generated by rotating the *S*-wave vibrator orientation to two orthogonal polarizations for each survey level in the well. The effect is generally consistent with the equivalent anisotropy expected from the known fracture geometry.

Moreno, L., Tsang, Y.W., Tsang, C.F., Hale, F.V., and Neretnieks, I., 1988. Flow and tracer transport in a single fracture: A stochastic model and its relation to some field observations. Water Resour. Res., v. 24, no. 12, p. 2033–2048 (LBL-25049).

Calculations for the flow and solute transport through a single rough-surfaced fracture were carried out. The fracture plane was discretized into a square mesh to which variable apertures were assigned. The spatially varying apertures of each single fracture were generated using geostatistical methods, based on a given aperture probability density distribution and a specified spatial correlation length. Constant head boundary conditions were assumed for the flow in the x direction of a single fracture with no flow boundaries in the y direction. The fluid potential at each node of the discretization mesh was computed and the steady state flow rates between all the nodes were obtained. Our calculations showed that fluid flow occurs predominantly in a few preferred paths. Hence, the large range of apertures in the single fracture gives rise to flow channeling. The solute transport was calculated using a particle tracking method. Both the spatial and time variations of tracer breakthrough results are presented. The spatial variation of tracer transport between a line of injection points and a line of observation points are displayed in contour plots which we labeled "transfer matrix." Our results indicate that such plots can give information on the spatial correlation length of the heterogeneity in the fracture. The tracer breakthrough curve obtained from a line of point measurements is shown to be controlled by the aperture density distribution and is insensitive to statistical realization and spatial correlation length. These results suggest the importance of making line measurements in the laboratory and the field. Sensitivity of our results on parameter variations was also investigated.

Nichols, E.A., Morrison, H.F., and Clarke, J., 1988. Signals and noise in measurements of low-frequency geomagnetic fields. J. Geophys. Res., v. 93, no. B11, p. 13,743–13,754 (LBL-24325).

The apparent magnetic noise, obtained from the coherency function for two parallel magnetic sensors, generally overestimates sensor noise because the sensors do not measure the same signal. The different signals result from the nonparallel alignment of the sensors and from the additional magnetic signal induced in each sensor by its motion in the Earth's magnetic field. A magnetometer array experiment was completed in Grass Valley, Nevada, to determine the minimum magnetic signal that could be detected in the presence of background natural field variations and motion of the sensor. Superconducting quantum interference device (SQUID) magnetometers with internal biaxial tiltmeters were used to record the magnetic fields and the motion of the sensors. A least squares fitting program enabled the field at one site in the array to be predicted from a remote site and to produce a residual field with a standard deviation of 8 pT over a 1-hour period with a low-pass filter at 0.3 Hz. Consistent field-to-residual ratios of 40–60 dB were achieved, with some ratios exceeding 70 dB. The least squares fit uses only a linear combination of the magnetic and tilt fields at a remote site to predict the observed magnetic field. This procedure allows for correction of calibration and orientation errors as well as the removal of the apparent fields originating from sensor movement. Misalignment and motion of the sensor are shown to be the major sources of magnetic field noise. The orientation error is typically of the same magnitude as the noise induced by sensor motion. In order to achieve ratios better than 20–40 dB one must include both the orthogonal fields and the tiltmeter outputs. Inclusion of a frequency-dependent transfer function should increase the prediction ability of the least squares model, as evidenced by the improvement to 70 dB obtained with simple band limiting of the original data. These techniques should be applicable to any type of artificial source survey where natural field fluctuations are the noise-limiting factor. The ability to describe the observed signals should allow a dramatic increase in one's ability to detect an artificially generated signal, allowing signal-to-to noise improvements of 40–60 dB without increasing transmitter power or the averaging time.

Niemi, A., and Bodvarsson, G.S., 1988. Preliminary capillary hysteresis simulations in fractured rocks, Yucca Mountain, Nevada. J. Contam. Hydrol., v. 3, p. 277–291 (LBL-23974).

Preliminary simulations have been carried out to address the question of how hysteretic (history-dependent) capillary pressure-liquid saturation relations may affect the flow and liquid saturation distribution in a fractured rock system. Using a hysteresis model modified from the theoretically based dependent domain model of Mualem (1984), a system consisting of discrete fractures and rock matrix parts was simulated under periodically occurring infiltration pulses. Comparisons were made between the hysteretic case and the non-hysteretic case using the main drying curve alone. Material properties used represent values reported for the densely welded tuffs at Yucca Mountain, Nevada. Since no actual hysteresis measurements were available for the welded tuffs, the necessary data was derived based on information available in the soils literature. The strongly hysteretic behavior in the uppermost layer of the matrix along with the overall lower matrix capillary suctions, generated higher fracture flows and a more "smeared" matrix liquid saturation vs. depth distribution for the hysteretic case. While the actual amounts of water being absorbed into the matrix were very similar, the distributions of this absorbed water were different and the matrix was affected up to greater depths in the hysteretic case in comparison to the non-hysteretic case.

Nitsche, H., Lee, S.C., and Gatti, R.C., 1988. Determination of plutonium oxidation states at trace levels pertinent to nuclear waste disposal. J. Radioanal. Nucl. Chem., v. 124, no. 1, p. 171–185 (LBL-23158).

A scheme was developed for the determination of oxidation states of plutonium in environmental samples. The method involves a combination of solvent extractions and coprecipitation. It was tested on solutions with both high-level and trace-level concentrations. The scheme was used to determine Pu oxidation states in solutions from solubility experiments in groundwater from a potential nuclear waste disposal site. At steady-state conditions, Pu was found to be soluble predominantly as Pu(V) and Pu(VI).

O'Connell, D.R.H., and Johnson, L.R., 1988. Second-order moment tensors of microearthquakes at The Geysers geothermal field, California. Bull. Seismol. Soc. Am., v. 78, no. 5, p. 1674–1692 (LBL-26966).

The Geysers geothermal field is the site of intense microseismicity which appears to be associated with steam production. It seems that focal mechanisms of earthquakes at The Geysers vary systematically with depth, but *P*-wave first motion focal mechanism studies have been hampered by inadequate resolution. In this study an unconstrained frequency domain moment tensor inversion method is used to over come *P*-wave first-motion focal sphere distribution problems and to investigate microearthquake source properties. A goal was to investigate the feasibility of using waveforms to invert for the second-order moment tensor of microearthquakes in the complex setting of The Geysers. Derived frequency-domain moment tensors for two earthquakes were verified by mechanisms estimated from *P*-wave first motions and required far fewer stations. For one event, 19 *P*-wave first motions were insufficient to distinguish between normal-slip and strike-slip focal mechanisms, but a well-constrained strike-slip solution was obtained from the waveform principal moment inversion using data from six stations. Improved waveform focal mechanism resolution was a direct consequence of using *P*- and *S*-wave data together in a progressive velocity-hypocenter inversion to minimize Green function errors. The effects of hypocenter mislocation and velocity model Green function errors on moment tensor estimates were investigated. Synthetic tests indicate that these errors can introduce serious isotropic and compensated linear vector dipole components as large as 26 per cent for these events, whereas principle moment orientation errors were $< 8°$. In spite of unfavorable recording geometries and large (0.6 km) station elevation differences, the results indicate that waveform moment tensor estimates for microearthquake sources can be robust and constrain source mechanisms using data from a relatively small number of stations.

Pabalan, R.T., and Pitzer, K.S., 1988. Apparent molar heat capacity and other thermodynamic properties of aqueous KCl solutions to high temperatures and pressures. J. Chem. Eng. Data, v. 33, p. 354–362 (LBL-24085).

Heat capacities of KCl solutions have been measured from 413 to 73 K at 200 bar over the molality range of 0.05–3.0 mol kg^{-1}. These were combined with literature data on volumes, heat capacities, enthalpies, and osmotic coefficients up to a temperature of 599 K and a pressure of 500 bar to yield comprehensive equations for the calculation of the thermodynamic properties of KCl(aq) to high temperatures and pressures by using the ion-interaction approach of Pitzer.

Pabalan, R.T., and Pitzer, K.S. 1988. Heat capacity and other thermodynamic properties of Na_2SO_4(aq) in hydrothermal solutions and the solubilities of sodium sulfate minerals in the system Na-Cl-SO_4-OH-H_2O to 300°C. Geochim. Cosmochim. Acta, v. 52, p. 2393–2404 (LBL-24706).

Heat capacities of Na_2SO_4(aq) solutions have been measured from 140°–300°C at 200 bars using a flow-calorimeter over the molality range of 0.05–1.5 mol · kg^{-1}. Using the ion-interaction or virial coefficient approach developed by Pitzer (1973, 1979, 1987) and coworkers, and approximating the pressure-dependencies of the various Na_2SO_4(aq) thermodynamic quantities with those of NaCl(aq) calculated from the equations of Rogers and Pitzer (1982), our measured heat capacities were combined with literature values on heat capacities, enthalpies, and osmotic coefficients at temperatures to 225°C and at pressures mostly at 1 bar or vapor-saturation pressure to yield a comprehensive set of equations for the thermodynamic properties of Na_2SO_4(aq) at temperatures 25°–300°C, pressure to at least 200 bars, and molalities to 3.0 mol · kg^{-1}. Standard state chemical potentials and activity and osmotic coefficients of $Na_2SO_{4(aq)}$ derived from our model, together with standard state properties of the solids available in the literature, permit the calculation of sodium sulfate solubilities in water and in electrolyte mixtures to 300°C. Good agreement between experimental and predicted solubilities in water indicates that the ion-interaction model can be used successfully to predict mineral-solution equilibria to 300°C without an explicit accounting for ion-pairs, and demonstrates that heat capacity measurements can be used to obtain reliable high-temperature and high-pressure activity properties of electrolyte solutions. The binary and ternary mixing parameters θ_{ij} and ψ_{ijk} are required by the ion-interaction model for calculations for multicomponent mixtures. It was found sufficient to adopt previously determined values for θ_{ij} at 25°C without temperature dependence and, from the solubility data, to determine temperature-dependent ψ_{ijk} functions.

Perry, D.L., Phillips, S.L., and Chung, J.D., 1988. Potentiostatic measurement of the diffusion coefficient of UO_2^{2+} in carbonate media. Inorg. Chim. Acta, v. 149, p. 301–304 (LBL-25453).

For more than three decades, an international research program has been in progress to obtain the necessary chemical data for disposal of wastes from nuclear energy used in electric power production, defense, and energy research and development. An important aspect of this research is to understand the chemistry of actinides and other elements falling in the category of waste radionuclides in natural waters. One waste element of interest is uranium, since spent reactor fuel is largely comprised of uranium oxide. Uranium exists in its highest oxidation state in aqueous systems as the dioxouranium(VI), or uranyl ion, UO_2^{2+} complexed with a variety of different anions. Extensive studies, for example, have been conducted on the chemistry of hydrolyzed uranyl salts precipitated from water. Spectroscopic studies have been made on uranyl sufates and uranyl carbonate. Additionally, detailed analytical research on the measurement of uranyl ion in aqueous solution has been reported, and even discrete, air-stable uranyl hydrolysis dimers have been documented.

While much more experimental data are needed to obtain a truly complete picture of the aqueous solution chemistry of UO_2^{2+}, the work described here was limited to measurement of the diffusion coefficient of UO_2^{2+} in carbonate media. Previous research on the carbonate system has shown that the species in 1 M Na_2CO_3 is the tris(carbonato)-dioxouranium(VI) ion, or $UO_2(CO_3)_3^{4-}$. In a saturated carbonate solution, the uranyl ion will achieve its maximum equatorial coordination number ('coordinatively saturated') by being surrounded by three bidentate carbonate ligands. Besides the value of the diffusion coefficient reported here, information has been reported previously concerning the reaction kinetics of the uranium(VI)–carbonate system in aqueous carbonate solutions.

Persoff, P., and Thomas, J.F., 1988. Estimating Michaelis-Menten or Langmuir isotherm constants by weighted nonlinear least squares. Soil Sci. Soc. Am. J., v. 52, no. 3, p. 886–889 (LBL-21220 Rev.).

We derive a nonlinear least squares fitting method for determining either Michaelis-Menten equation or Langmuir adsorption isotherm constants from experimental data. Data points can be weighted unequally if their relative precisions are known. Comparison of this method with the commonly used linearization methods, using simulated data sets containing normally distributed random errors, showed that this method yields more accurate and precise estimates of the constants than any of the linearizations. A short BASIC program to facilitate computation is presented.

Pruess, K., 1988. SHAFT, MULKOM, TOUGH: A set of numerical simulators for multiphase fluid and heat flow. Geotermia, Rev. Mex. Geoenergia, v. 4, no. 1, p. 185–202 (LBL-24430).

Numerical simulation of fluid and heat flow has become a widely accepted technique for studying and evaluating geothermal reservoirs and other subsurface flow systems. This article discusses several interrelated simulation codes which were developed at Lawrence Berkeley Laboratory with a capability to model Multiphase flow and phase change effects. We review some of the early concepts in geothermal reservoir simulation, and summarize the development of the SHAFT79 and MULKOM codes. We also describe the architecture of MULKOM and TOUGH and give a detailed statement of the governing equations.

Pyrak-Nolte, L.J., and Cook, N.G.W., 1988. Fluid percolation through single fractures. Geophys. Res. Lett., v. 15, no. 11, p. 1247–1250 (LBL-25714).

Large deviations from "cubic-law" dependence of laminar fluid flow through fractures on the apparent mechanical aperture of a fracture can be explained by assuming: 1) cubic-law dependence of flow on the actual local aperture at the microscopic level; 2) conservation of rock volume when deforming the fracture; and 3) macroscopic flow properties are dominated by the critical neck (the smallest aperture along the path of highest aperture through the fracture).

Ransohoff, T.C., and Radke, C.J., 1988. Laminar flow of a wetting liquid along the corners of a predominantly gas-occupied noncircular pore. J. Colloid Interface Sci., v. 121, no. 2, p. 392–401 (LBL-22045).

The problem of low Reynolds number wetting liquid flow in a noncircular capillary occupied predominantly by a nonwetting gas phase is separated into individual corner flow problems and solved numerically. The solution is presented in terms of a dimensionless flow resistance, β, which is tabulated as a function of corner geometry (half angle and degree of roundedness), surface shear viscosity, and contact angle. The effect of corner geometry and contact angle is to change the cross-sectional area available for flow, while the surface shear viscosity affects the boundary condition at the gas-liquid interface. The dimensionless flow resistance is shown to increase with increasing half angle, degree of roundedness, surface shear viscosity, and contact angle. Finally, it is demonstrated that the error resulting from the use of the hydraulic-diameter approximation for the corner flow problem is on the order of 50% or higher.

Ransohoff, T.C., and Radke, C.J., 1988. Mechanisms of foam generation in glass-bead packs. SPE Res. Eng., v. 3, no. 2, p.573–585 (LBL-26739).

The fundamental, pore-level mechanisms of foam generation are investigated in monodisperse bead packs. First, direct visual observations identify the following generation mechanisms: lamella leave-behind, gas-bubble snap-off, and lamella division. Then, to ascertain the relative importance of these mechanisms, quantitative experiments are pursued on the role of bead-pack permeability (bead sizes from 0.25 to 1 mm [0.01 to 0.04 in.]), gas-phase velocity (0.001 to 0.8 cm/s [0.0004 to 0.3 in./sec]), gas-phase fractional flow (0.60 to 1.0), permeability variations, and surfactant type [sodium dodecyl benzene sulfonate (SDBS), sodium dodecyl sulfate (SDS), Chevron Chaser SD1000™, and Suntech IV 1035™]. We discover a critical velocity, above which a "strong" foam is generated and below which only "weak" foam is formed. The snap-off mechanism is the primary mechanism responsible for the formation of the strong foam. A simple model, based on the concept of a "germination site," is developed to predict the onset of snap-off at higher gas velocities. New experimental data obtained in the homogeneous glass-bead packs for the critical capillary number necessary to form a strong foam are in excellent agreement with the proposed germination-site model.

Standifer, E.M., and Nitsche, H., 1988. First evidence for hexagonal $AmOHCO_3$. Lanthanide Actinide Res., v. 2, p. 383–383 (LBL-25624).

Americium, like neodymium, forms two hydroxycarbonates with hexagonal and orthorhombic crystal structures. Both forms were synthesized and identified by X-ray powder diffraction measurements. This is the first report of hexagonal $AmOHCO_3$.

Thornton, S.D., and Radke, C.J., 1988. Dissolution and condensation kinetics of silica in alkaline solution. SPE Res. Eng., v. 3, no. 2, p. 743–752 (LBL-26740).

Chemical loss through long-term rock reactions is a major impediment for practical application of alkaline waterflooding. This paper addresses the viability of soluble silicates reducing hydroxide consumption by siliceous rock reactions. A convenient differential rate method is used to obtain new experimental kinetic data for the dissolution/condensation rates of quartz at 23 and 70°C [73 and 158°F] and amorphous silica at 23°C [73°F] over the pH range from 11 to 12 and in 1 *M* NaCl. The role of added silicates is studied from zero solution concentration to considerably above the solubility limit.

Silica dissolution rates are observed to slow as the solubility limit is reached and become negative (i.e., net precipitation occurs) above the solubility limit. The kinetic rates decrease with increasing solution silicate in a parabolic fashion. Most important, the solubility limit of quartz (amorphous silica) controls the deposition rate of quartz (amorphous silica) over the range of pH values and temperatures investigated. That is, crystalline quartz grows directly on solid quartz particles, rather than deposition of amorphous silica with subsequent alteration to the crystalline habit. This means that relatively small amounts of soluble silicates, approaching the solubility limit of quartz, can protect against hydroxide consumption by quartzitic rock reactions.

A molecular dissolution/condensation reaction scheme is proposed, based on equilibrium adsorption of unionized silicic acid. With this reaction path, a mathematical model is developed that agrees quite well with the measured kinetic rate data.

Tokunaga, T.K., 1988. Laboratory permeability errors from annular wall flow. Soil Sci. Soc. Am. J., v. 52, no. 1, p. 24–27 (LBL-23794).

Laboratory saturated hydraulic conductivity measurement errors introduced by permeameter fluid flow within gaps between sample cores and permeameter walls are estimated through a simple model that idealizes gap flow as occurring within a smooth annulus. The inner annulus boundary fluid velocity is matched to the Darcy velocity within the sample core. The ratio of flow within the annulus to that within the core, Q_{gap}/Q_{core}, is shown to have both cubic and linear dependence on the gap width. Q_{gap}/Q_{core} is also shown to be inversely dependent on both the core permeability and the permeameter radius. Although the model is very idealized, the strong possibility of overestimating permeabilities in laboratory cores is demonstrated. Related concerns include flow in fractured porous media, and potential errors in interpreting solute travel times in laboratory columns and field lysimeters.

Tralli, D.M., and Johnson, L.R., 1987. Epicentral confidence regions of nuclear test events at teleseismic distances. Bull. Seismol. Soc. Am., v. 77, p. 2212–2217 (LBL-23935).

Disclosed nuclear test events in the Nevada Test Site and presumed nuclear tests in Eastern Kasakh in the Soviet Union are located using estimates of tectonically regionalized *P* travel-time functions. Epicentral confidence regions are calculated. A site calibration using the NTS events is undertaken by determining a slowness-dependent travel-time bias appropriate for source regions with characteristic crustal and shallow-mantle velocity structure similar to that at NTS. The problem of constraining focal depth estimates is not approached, as only teleseismic *P*-wave data are used. However, bounds on epicenters may be achieved sufficiently tight at the 95% confidence level to supplement other discrimination criteria. The mean area of the confidence ellipses is on the order of 50 km^2 at NTS, given about 150 observing stations. At Eastern Kasakh, with about 200 stations, the mean area is 90 km^2. The small uncertainties suggest that regionalized travel times are an effective characterization of lateral velocity variations in the Earth.

Tsang, Y.W., Tsang, C.F., Neretnieks, I., and Moreno, L., 1988. Flow and tracer transport in fractured media: A variable aperture channel model and its properties. Water Resour. Res., v. 24, no. 12, p. 2049–2060 (LBL-25048).

Field evidences indicate that the bulk of water flow in fractured crystalline rock often occurs in preferred flow paths, or channels. A theoretical approach was proposed by Tsang and Tsang (1987) to interpret flow and transport through a two- or three-dimensional fractured medium in terms of a system of statistically equivalent one-dimensional channels. The apertures along the flow channels are characterized by an aperture density distribution and a spatial correlation length. In this paper, we present detailed studies on the properties of these channels: channel volume, channel residence time, and channel volumetric flow rate. We also calculated the dispersion in tracer transport through groups of statistically equivalent channels. The one-dimensional channel model is then applied to breakthrough data from transport in a two-dimensional single fracture (Moreno et al., this issue) in both a forward and an inverse calculation. We show from the inverse calculation that the aperture density distribution parameters of the one-dimensional flow channels may be estimated from the dispersion and mean residence time of the traer data. The tracer breakthrough curve should be obtained from line measurements with tracer sampled over several spatial correlation lengths of the variable apertures. This is in contrast to conventional point tracer measurements which are expected to fluctuate with statistical realization and may not yield pertinent information on the flow system. Based on the insight gained in such calculations, design and analysis of field measurements are discussed. Both tracer breakthrough measurements and flow rate measurements alone are controlled by the small constrictions along the flow paths and therefore do not yield a good measure of the mean aperture in channel.

Tucker, D.B., Standifer, E.M., Nitsche, H., and Silva, R.J., 1988. Data acquisition and feedback control system for solubility studies of the nuclear waste elements neptunium and plutonium. Lanthanide Actinide Res., v. 2, p. 279–287 (LBL-23541).

A pH control system ("pH-stat") was designed to maintain aqueous actinide solutions at constant temperatures and pH values for solubility measurements relevant to the assessment of a potential repository for nuclear waste. The pH-stat recorded and adjusted the pH values of groundwater solutions of Np and Pu over periods of 15 to 18 weeks. the solutions' temperatures during these experiments were controlled at 60.0° ± 0.3°C, while their pH values were measured to be 6.0, 7.0, and 8.5, with standard deviations generally not exceeding 0.1 pH unit. The pH-stat was employed in solubility measurements of Np(V) and Pu(IV) from supersaturation. the major solid phase in the Np(V) solutions was $NaNpO_2CO_3 \cdot H_2O$; its log(solubility product) is -10.3 ± 0.5 under the experimental conditions (I = 0.14 ± 0.05 M; 60°C). The solubility-limiting solid in the plutonium solutions was amorphous Pu(IV) polymer. High plutonium valences were measured in the steady-state solutions, with Pu(V) predominating at pH 8.5.

Vasco, D.W., Johnson, L.R., and Goldstein, N.E., 1988. Using surface displacement and strain observations to determine deformation at depth, with an application to Long Valley caldera, California. J. Geophys. Res., v. 93, no. B4, p. 3232–3242 (LBL-22809).

We present a method for the inversion of surface displacement and strain to determine six independent combinations of the strain components at depth. These six combinations represent three mutually perpendicular double forces without moment and three pairs of double forces with moment. Furthermore, they may be directly related to a moment tensor density distribution for static strain. The method is linear and, unlike other methods, does not depend on an a priori source model. Due to the linearity of the formulation, methods such as generalized inversion or l^1 residual norm minimization may be used to determine models of deformation at depth. The methods presented are applicable to a variety of available geodetic data sets. The technique is applied to repeat leveling data taken between 1982 and 1985 in Long Valley caldera. We determined a model of the magma intrusion suspected to have occurred beneath the caldera. The model derived minimized the l^2 norm of the difference between the predicted and observed data subject to the constraint that only intrusion occur. The model indicates that most volume expansion took place in the caldera region above 8 km ± 2 km. In the 0–4 km depth range the expansion is widely distributed with a maximum value of 0.005 km^3. Deeper, 4–8 km, there is a concentration of intrusion in the central portion of the caldera. The maximum volume increase here is 0.030 km^3.

Verma, A., and Pruess, K., 1988. Thermohydrological conditions and silica redistribution near high-level nuclear wastes emplaced in saturated geological formations. J. Geophys. Res., v. 90, no. B2, p. 1159–1173 (LBL-21613).

Evaluation of the thermohydrological conditions near high-level nuclear waste packages is needed for the design of the waste canister and for overall repository design and performance assessment. Most available studies in this area have assumed that the hydrologic properties of the host rock are not changed in response to the thermal, mechanical, or chemical effects caused by waste emplacement. However, the ramifications of this simplifying assumption have not been substantiated. We have studied dissolution and precipitation of silica in liquid-saturated hydrothermal flow systems, including changes in formation porosity and permeability. Using numerical simulation, we compare predictions of thermohydrological conditions with and without inclusion of silica redistribution effects. Two cases were studied, namely, a canister-scale problem, and a repository-wide thermal convection problem and different pore models were employed for the permeable medium (fractures with uniform or nonuniform cross sections). We find that silica redistribution in water-saturated conditions does not have a sizable effect on host rock and canister temperatures, pore pressures, or flow velocities.

Wang, J.S.Y., Mangold, D.C., and Tsang, C.F., 1988. Thermal impact of waste emplacement and surface cooling associated with geologic disposal of high-level nuclear waste. Environ. Geol. Water Sci., v. 11, no. 2, p. 183–239 (LBL-22615).

This article is a study of the thermal effects associated with the emplacement of aged radioactive high-level wastes in a geologic repository, with emphasis on the following subjects: waste characteristics, repository structure, and rock properties controlling the thermally induced effects; thermal, thermomechanical, and thermohydrologic impacts, determined mainly on the basis of previous studies that assume 10-yr-old wastes; thermal criteria used to determine the repository waste loading densities; and technical advantages and disadvantages of surface cooling of the wastes prior to disposal as a means of mitigating the thermal impacts. Waste loading densities determined by repository designs for 10-yr-old wastes are extended to older wastes using the near-field thermomechanical criteria based on room stability considerations. Also discussed are the effects of long surface cooling periods determined on the basis of far-field thermomechanical and thermohydrologic considerations. Extension of the surface cooling period from 10 yr to longer periods can lower the near-field thermal impact but have only modest long-term effects for spent fuel. More significant long-term effects can be achieved by surface cooling of reprocessed high-level waste.

Wang, J.S.Y., Narasimhan, T.N., and Scholz, C.H., 1988. Aperture correlation of a fractal fracture. J. Geophys. Res., v. 93, no. B3, p. 2216–2224 (LBL-22494).

A rough-walled fracture is modeled by fractal geometry. In the fractal fracture model, the rock surfaces are characterized by a fractal dimension D between 2 and 3 with lower D for smoother surfaces and higher D for rougher surfaces. The mismatch due to shear displacement between two mirror-image fractal surfaces determines the fracture aperture distribution. An analytic equation is derived for the variogram $\gamma_l(r)$ describing the spatial correlation of the aperture of a fractal fracture. The aperture of a smooth fracture with low D is highly correlated over distances much larger than the shear displacement. The aperture of a rough fracture with high D becomes uncorrelated within a range shorter than the shear displacement. Near the origin, $r = 0$, of the variogram, the variogram is proportional to r^{6-2D}. For the special case of Brownian fractal with $D = 2.5$, the variogram is proportional to r, which is the same r dependence exhibited by the spherical model widely used in geostatistical analyses.

Weres, O., Newton, A.S., and Tsao, L., 1988. Hydrous pyrolysis of alkanes, alkenes, alcohols and ethers. Org. Geochem., v. 12, no. 5, p. 433–444 (LBL-23178 Rev.).

The decomposition reactions of alkanes, alkenes and related compounds have been systematically studied under conditions of hydrous pyrolysis: 3–5 days at 317°C, in the presence of simulated oil field brine and clay. *n*-Hexadecane slowly cracks to give *n*-alkanes and *n*-alkenes C-2 through C-14. Ethers and alcohols rapidly hydrolyze and dehydrate producing alkenes. Alkenes add to hexadecane to give branched alkanes. Tetrahydronaphthalene inhibits the cracking and alkylation of hexadecane both. *n*-Hexadecene cracks like *n*-hexadecane, but a large fraction of it dimerizes.

Most though not all reactions observed may be explained in terms of free radical chain mechanisms. For example, there is little evidence for the rearrangement of carbon skeletons, and the distribution of cracking products obtained from squalane is also consistent with a free radical chain reaction. However, the dehydration of alcohols may involve carbonium ions, and extensive migration of double bonds in alkenes was observed.

These results demonstrate why alkenes are insignificant in natural oils, while they are commonly present in artificial shale oil. Even at 317°C, the rate of alkylation is comparable to the rate of cracking. Because the activation energy for alkylation is smaller than for cracking, the probability of alkylation increases relative to cracking at lower temperature. Therefore, alkylation will be much faster than cracking in petroleum source beds and reservoirs, and the steady concentration of alkenes will be very small. In the low pressure, high temperature pyrolysis of oil shale a fraction of the alkenes produced boil off together with the alkanes before they are able to react, and appear in the product distillate.

Wu, Y.S., and Pruess, K., 1988. A multiple-porosity method for simulation of naturally fractured petroleum reservoirs. SPE Res. Eng., v. 2, no. 1, p. 327–336 (LBL-27236).

This paper describes the application of the method of "Multiple Interacting Continua" (MINC) to the simulation of oil recovery in naturally fractured reservoirs. A generalization of the double-porosity technique, the MINC method permits a fully transient description of interporosity flow by numerical methods. We present examples to demonstrate the utility for the MINC method for modeling oil-recovery mechanisms by water imbibition and field applications for five-spot waterflooding and water coning problems in fractured reservoirs. All results show that the MINC method provides accurate predictions of the behavior of naturally fractured reservoirs, while requiring only a modest increase in computation work compared with the double-porosity method. The double-porosity method may result in large errors for matrix blocks of low permeability or large size.

APPENDIX B: OTHER PUBLICATIONS

TOPICAL REPORTS

LBL-21022
Wang, J.S.Y., and Narasimhan, T.N., 1986. Hydrologic mechanisms governing partially saturated fluid flow in fractured welded units and porous nonwelded units at Yucca Mountain.

LBL-21121
Ahn, J., Chambré, P.L., and Pigford, T.H., 1985. Radionuclide migration through fractured rock: Effects of multiple fractures and two-member decay chains.

LBL-21482
Apps, J.A., Neil, J.M., and Jun, C.-H., 1988. Thermochemical properties of gibbsite, bayerite, boehmite, diaspore, and the aluminate ion between 0 and 350°C.

LBL-21814
Vasco, D.W., 1986. Inversion of static displacement of the earth's surface (Ph.D. thesis).

LBL-22280
O'Connell, D.R., 1986. Seismic velocity structure and microearthquake source properties at The Geysers, California, geothermal area (Ph.D. thesis).

LBL-22361
Noorishad, J., Carnahan, C.L., and Benson, L.V., 1986. Development of the non-equilibrium reactive chemical transport code CHMTRNS.

LBL--23096
Tsang, C.F., 1987. A borehole fluid conductivity logging method for the determination of fracture inflow parameters.

LBL-23546
Bjornsson, G., 1988. A multi-feedzone geothermal wellbore simulator (M.S. thesis).

LBL-23848
Phillips, S.L., Hale, F.V., and Tsang, C.-F., 1988. Groupings of organic waste chemicals based on sorption, biotransformation and hydrolysis at standard conditions for application to the deep subsurface environment.

LBL-23888
Severson, L.K., 1987. Interpretation of shallow crustal structure of the Imperial Valley, California, from seismic reflection profiles (Master's thesis).

LBL-23986
Zavoshy, S.J., Chambré, P.L., Ahn, J., Pigford, T.H., and Lee, W.W.-L., 1987. Steady-state radionuclide transfer from a cylinder intersected by a fissure.

LBL-23987
Lung, H.-C., Chambre, P.L., Pigford, T.H., and Lee, W.W.-L., 1987. Transport of radioactive decay chains in finite and semi-infinite porous media.

LBL-24453
Muralidhar, K., and Long, J.C.S., 1987. A scheme for calculating flow in fractures using numerical grid generation in three-dimensional domains of complex shapes.

LBL-24657
Goldstein, N.E., Alumbaugh, D., and Benson, S.M., 1988. Ground conductivity measurements adjacent to the Kesterson ponds 1, 2, and 5.

LBL-24661
Daley, T., 1987. Analysis of P- and S-wave VSP data from the Salton Sea geothermal field.

LBL-24700
Myer, L.R., and Christian, T.L., 1987. Permeability of shale at elevated temperature and pressure: Test methodology and preliminary results.

LBL-24735
Cummins, P., 1987. Seismic body waves and the earth's inner core.

LBL-24796
Mishra, S., Bodvarsson, G.S., and Attanayake, M.P., 1987. Estimating properties of unsaturated fractured formations from injection and falloff tests.

LBL-24914
Billaux, D., Bodea, S., and Long, J., 1988. FMG, RENUM, LINEL, ELLFMG, ELLP, and DIMES: Chain of programs for calculating and analyzing fluid flow through two-dimensional fracture networks—Theory and design.

LBL-24928
Hale, F.V., and Tsang, C.F., 1988. A code to compute borehole fluid conductivity profiles with multiple feed points.

LBL-25594
Ahn, J., 1988. Mass transfer and transport of radionuclides in fractured porous rock (Ph.D. thesis).

LBL-25783
Pruess, K., and Wu, Y.S., 1988. On PVT-data, well treatment, and preparation of input data for an isothermal gas-water-foam version of MULKOM.

LBL-25870
Lee, W.-W.L., Pigford, T.H., and Chambré, P.L., 1988. Release rates of soluble species at Yucca Mountain: A preliminary mass transfer analysis.

LBL-25874
Long, R.H., 1988. An analysis of selenium and chloride movement through a pond sediment at Kesterson Reservoir (M.S. thesis).

LBL-25971
Doughty, C., and Bodvarsson, G.S., 1988. Some design considerations for the proposed Dixie Valley tracer test.

LBL-26542
Yates, C.C., 1988. Analysis of pumping test data of a leaky and layered aquifer with partially penetrating wells.

CONFERENCE PAPERS

Ahn, J., Chambré, P.L., and Pigford, T.H., 1988. Transient diffusion from a waste solid into fractured porous rock. Presented at the Annual Meeting of the American Nuclear Society, San Diego, California, June 12–16, 1988. Trans. Am. Nucl. Soc., v. 56, p. 173–174 (LBL-24576).

Apps, J.A., and Neil, J.M., 1988. Correlation of the solubilities of aluminum hydroxides and oxyhydroxides in alkaline solutions with the thermodynamic properties of $AL(OH)_4^-$. Presented at the American Chemical Society Symposium "Chemical Modeling in Aqueous Systems II," Los Angeles, California, September 25–30, 1988 (LBL-26506).

Bodvarsson, G.S., Bjornsson, S., Gunnarsson, A., Gunnlaugsson, E., Sigurdsson, O., Stefansson, V., and Steingrimsson, B., 1988. A summary of modeling studies of the Nesjavellir geothermal field, Iceland. Presented at the Thirteenth Workshop on Geothermal Reservoir Engineering, Stanford, California, January 19–21, 1988 (LBL-24675).

Carnahan, C.L., 1987. Some effects of data base variations on numerical simulations of uranium migration. Presented at the International Conference on Chemistry and Migration Behavior of Actinides and Fission Products in the Geosphere, Munich, Federal Republic of Germany, September 14–18, 1987 (LBL-24537).

Carnahan, C.L., 1988. Simulation of effects of redox and precipitation on diffusion of uranium solution species in backfill. *In* M.J. Apted and R.E. Westerman (eds.), Scientific Basis for Nuclear Waste Management XI, Boston, Massachusetts, November 30–December 3, 1987. Materials Research Society Symposia Proceedings (Vol. 112). Materials Research Society, Pittsburgh, Pennsylvania, p. 293–302 (LBL-24538).

Carnahan, C.L., 1988. Coupling of precipitation/dissolution reactions to mass diffusion. *In* Chemical Modeling in Aqueous Systems II, Proceedings, 196th Annual Meeting of the American Chemical Society, Division of Geochemistry, Los Angeles, California, September 25–30, 1988 (LBL-26183).

Chambré, P.L., Hwang, Y., W.W.-L. Lee, and Pigford, T.H., 1987. Release rates from waste packages in a salt repository. Presented at the American Nuclear Society Winter Meeting, Los Angeles, California, November 15–19, 1987. Trans. Am. Nucl. Soc., v. 55, p. 132–133 (LBL-23638).

Chambré, P.L., Kang, C.H., Lee, W.W.-L., and T.H. Pigford, 1987. Waste dissolution with chemical reaction, diffusion, and advection. Presented at the American Nuclear Society Winter Meeting, Los Angeles, California, November 15–19, 1987. Trans. Am. Nucl. Soc., v. 55, p. 130–131 (LBL-23640).

Chambré, P.L., Kang, C.H., Lee, W.W.-L., and Pigford, T.H., 1988. The role of chemical reaction in waste-form performance. *In* Scientific Basis for Nuclear Waste Management XI, Boston, Massachusetts, November 30–December 3, 1987. Materials Research Society Symposia Proceedings (Vol. 112). Materials Research Society, Pittsburgh, Pennsylvania, p. 285–291 (LBL-23641).

Cox, B.L., Pruess, K., and McKibbin, R., 1988. Mathematical modeling of near-critical convection. Presented at the Thirteenth Workshop on Geothermal Reservoir Engineering, Stanford, California, January 19–21, 1988 (LBL-24774).

Ewy, R.T., Cook, N.G.W., and Myer, L.R., 1988. Hollow cylinder tests for studying fracture around underground openings. Presented at the 29th Annual U.S. Symposium on Rock Mechanics, Minneapolis, Minnesota, June 13–15, 1988 (LBL-25308).

Gaulke, S.W., and Bodvarsson, G.S., 1987. Analysis of pressure, enthalpy and CO_2 transients in well BR21, Ohaaki, New Zealand. Presented at the 1987 Annual Meeting of the Geothermal Resources Council, Sparks, Nevada, October 12–14, 1987. Geoth. Resour. Counc. Trans., v. 11, p. 535–539 (LBL-23718).

Ginley, G.M., and Radke, C.J., 1988. The influence of soluble surfactants on the flow of long bubbles through a cylindrical capillary. Presented at the Third Chemical Congress of the North American Continent and 195th Meeting of the American Chemical Society, Symposium on Advances in Oil Chemistry, Toronto, Canada, June 5–11, 1988 (LBL-24370).

Goldstein, N.E., 1987. Introduction: Potential field and electromagnetic studies. Presented at the Symposium on the Long Valley Caldera: A Pre-Drilling Data Review, Berkeley, California, March 17–18, 1987 (LBL-24570).

Hwang, Y., Chambré, W.W.-L. Lee, and T.H. Pigford, 1987. Pressure-induced brine migration in consolidated salt in a repository. Presented at the American Nuclear Society Winter Meeting, Los Angeles, California, November 15–17, 1987. Trans. Am. Nucl. Soc., v. 55, p. 132–133 (LBL-23637).

Hwang, Y., Chambré, W.W.-L. Lee, and T.H. Pigford, 1987. Pressure-induced brine migration into an open borehole in a salt repository. Presented at the American Nuclear Society Winter Meeting, Los Angeles, California, November 15–17, 1987. Trans. Am. Nucl. Soc., v. 55, p. 133–134 (LBL-23636).

Jacobsen, J.S., and Carnahan, C.L., 1987. Numerical simulation of alteration of sodium bentonite by diffusion of ionic groundwater components. Presented at the Materials Research Society Fall Meeting, Symposium P: Scientific Basis for Nuclear Waste Management XI, Boston, Massachusetts, November 30–December 3, 1987 (LBL-24494).

Jiménez, A.I., and Radke, C.J., 1987. Dynamic stability of foam lamellae flowing through a periodically constricted tube. Presented at the Third Chemical Congress of the North American Continent and 195th National Meeting of the American Chemical Society, Symposium on Advances in Oil Chemistry, Toronto, Canada, June 5–11, 1988 (LBL-24369).

Kang, C.H., Chambré, P.L., Lee, W.W.-L., and T.H. Pigford, 1987. Time-dependent nuclide transport through backfill into a fracture. Presented at the American Nuclear Society Winter Meeting, Los Angeles, California, November 15–19, 1987. Trans. Am. Nucl. Soc., v. 55, p. 134–136 (LBL-23639).

Kim, C.-L., Light, W.B., Lee, W.W.-L., Chambré, P.L., and Pigford, T.H., 1988. Variable temperature effects on release rates of readily soluble nuclides. Presented at the American Nuclear Society International Topical Meeting, SPECTRUM '88, Nuclear and Hazardous Waste Management, Pasco, Washington, September 11–15, 1988 (LBL-24805).

Leary, P.C., Henyey, T.L., and McEvilly, T.V., 1988. A pilot vertical seismic profiling experiment at the Cajon Pass deep scientific drillhole. *In* A. Bodén and K.G. Eriksson (eds.), Deep Drilling in Crystalline Bedrock. Vol. 2: Review of Deep Drilling Projects, Technology, Sciences and Prospects for the Future. Proceedings of the Third International Symposium on Observation of the Continental Crust through Drilling, Mora and Orsa, Sweden, September 7–10, 1987. Springer-Verlag, New York, p. 417–427 (LBL-27531).

Light, W.B., Chambré, P.L., Lee, W.W.-L., and Pigford, T.H., 1988. The effect of a stationary precipitation front on nuclide dissolution and transport: Analytic solutions. Presented at the American Nuclear Society International Topical Meeting, SPECTRUM '88, Nuclear and Hazardous Waste Management, Pasco, Washington, September 11–15, 1988 (LBL-24803).

Lippmann, M.J., 1987. The geothermal program at Lawrence Berkeley Laboratory. Presented at the 1987 Annual Meeting of the Geothermal Resources Council, Sparks, Nevada, October 11–14, 1987. Geoth. Resour. Counc. Trans., v. 11, p. 559–564 (LBL-23608).

Lippmann, M.J., 1988. Reducing long-term reservoir performance uncertainty. *In* Proceedings, DOE Geothermal Program Review VI, San Francisco, California, April 19–21, 1988, Conf.-880477, p. 39–43 (LBL-25245).

Lippmann, M.J. (ed.), 1988. Proceedings of the Technical Review "Advances in Geothermal Reservoir Technology—Research in Progress," Lawrence Berkeley Laboratory, Berkeley, California, June 14–15, 1988 (LBL-25635).

Lippmann, M.J., Bodvarsson, G.S., Benson, S.M., and Pruess, K., 1987. Recent geothermal reservoir engineering activities at Lawrence Berkeley Laboratory. *In* Proceedings, International Symposium on the Development and Exploitation of Geothermal Resources, Cuernavaca, Mexico, October 5–9, 1987, p. 262–269 (LBL-24033).

Long, R.H., Benson, S., Alavi, M., and Narasimhan, T.N., 1988. Transport of a conservative solute through a shallow pond bottom. *In* H.J. Morel-Seytoux and D.G. DeCoursey (eds.), Proceedings of the Eighth Annual AGU Front Range Branch Hydrology Days, Fort Collins, Colorado, April 19–21, 1988 (LBL-25217).

Long, J.C.S., Billaux, D., Hestir, K., Majer, E.L., Peterson, J., Karasaki, K., Nihei, K., Gentier, S., and Cox, L., 1988. Characterization of fracture networks for fluid flow analysis. Presented at the Fourth Canadian/American Conference on Hydrogeology, Banff, Alberta, Canada, June 21–24, 1988 (LBL-26868).

McGuinness, M.J., and Pruess, K., 1987. Unstable heat pipes. Proc., 9th New Zealand Geothermal Workshop, Auckland, New Zealand, November 4–6, 1987, p. 147–151 (LBL-24092).

McKibbin, R., and Pruess, K., 1988. Some effects of non-condensible gas in geothermal reservoirs with steam-water counterflow. Presented at the Thirteenth Workshop on Geothermal Reservoir Engineering, Stanford, California, January 19–21,1988 (LBL-24973).

Meike, A., 1987. Specimen cage modification for TEM *in-situ* shearing. Presented at the Materials Research Society Fall Meeting, Symposium W: Specimen Preparation for Transmission Electron Microscopy of Materials, Boston, Massachusetts, November 30–December 5, 1987 (LBL-24145).

Pabalan, R.T., and Pitzer, K.S., 1988. Models for aqueous electrolyte mixtures for systems extending from dilute range to the fused salt—Evaluation of parameters to high temperatures and pressures. Presented at the American Chemical Society Annual Meeting (Chemical Modeling in Aqueous Systems II), Anaheim, California, September 25–30, 1988 (LBL-26468).

Pigford, T.H., and Chambré, P.L., 1988. Near-field mass transfer in geologic disposal systems: A Review. *In* M.J. Apted and R.E. Westerman (eds.), Scientific Basis for Nuclear Waste Management XI, Boston, Massachusetts, November 30–December 3, 1987. Materials Research Society Symposia Proceedings (Vol. 112). Materials Research Society, Pittsburgh, Pennsylvania, p. 125–141 (LBL-23689).

Pigford, T.H., Chambré, P.L., and Lee, W.W.-L., 1988. Mass transfer and transport in geologic repositories: Analytical studies and applications. Presented at the Annual Meeting of the American Nuclear Society, San Diego, California, June 12–16, 1988. Trans. Am. Nucl. Soc., v. 56, p. 169 (LBL-24599, LBL-24599 Rev.).

Pruess, K. and Narasimhan, T.N., 1988. Numerical modeling of multiphase and nonisothermal flow in fractured media. Presented at the International Conference on Fluid Flow in Fractured Rocks, Atlanta, Georgia, May 15–19, 1988 (LBL-25547).

Pruess, K., and Wu, Y.S., 1988. A semi-analytical method for heat sweep calculations in fractured reservoirs. Presented at the Thirteenth Workshop on Geothermal Reservoir Engineering, Stanford, California, January 19–21, 1988 (LBL-24463).

Ripperda, M., and Bodvarsson, G.S., 1988. Analysis of internal wellbore flow. *In* Proceedings, Thirteenth Workshop on Geothermal Reservoir Engineering, Stanford, California. Report SGP-TR-113, p. 269–272 (LBL-26826).

Sammel, E.A., and Benson, S., 1987. An analysis of the hydrologic effects of proposed test drilling in the Winema National Forest near Crater Lake, Oregon. Presented at the 1987 Annual Meeting of the Geothermal Resources Council, Sparks, Nevada, October 12–14, 1987. Geoth. Resour. Counc. Trans., v. 11 p. 293–303 (LBL-23721).

Tsang, C.-F., 1988. Tracer travel time and model validation. To be presented at the 1988 Annual Meeting of the American Nuclear Society, San Diego, California, June 12–16, 1988. *In* Trans. Am. Nucl. Soc., v. 56, p. 157–158 (LBL-24751).

Tsang, C.F., Tsang, Y.W., and Hale, F.V., 1988. Tracer transport in fractured rocks. *In* Proceedings, International Conference on Fluid Flow in Fractured Rocks, Atlanta, Georgia, May 15–17, 1988 (LBL-25657).

Tsang, Y.W., and Hale, F.V., 1988. A study of the application of mercury porosimetry method to a single fracture. *In* Proceedings, International Conference on Fluid Flow in Fractured Rocks, Atlanta, Georgia, May 15–17, 1988 (LBL-25489).

Wu, Y.-S., and Pruess, K., 1988. An analytical solution for wellbore heat transmission in layered formations. Presented at the 1988 California Regional Meeting of the Society of Petroleum Engineers, Long Beach, California, March 23–25, 1988 (LBL-25056). [Feb 1989]

Zheng, Z., Myer, L.R., and Cook, N.G.W., 1988. Borehole breakout and stress measurements. Presented at the 29th Annual U.S. Symposium on Rock Mechanics, Minneapolis, Minnesota, June 13–15, 1988 (LBL-25655).

Zhou, Q., Goldstein, N.E., and Becker, A., 1988. Crosshole electromagnetic responses of multiple thin conductors. *In* Proceedings, Society of Exploration Geophysicists Annual Meeting, Anaheim, California, October 30–November 3, 1988 (LBL-25319A).

Zhou, W., Ahn, J., Lee, W.W.-L., and Chambré, P.L., 1988. Dissolution/precipitation of a two-member chain at a dissolving waste matrix. Presented at the American Nuclear Society International Topical Meeting, SPECTRUM '88, Nuclear and Hazardous Waste Management, Pasco, Washington, September 11–15, 1988 (LBL-24804).

☆ U. S. GOVERNMENT PRINTING OFFICE: 1989 685-213 : 1001

LAWRENCE BERKELEY LABORATORY
TECHNICAL INFORMATION DEPARTMENT
1 CYCLOTRON ROAD
BERKELEY, CALIFORNIA 94720